NUREG/CR-0238
TREE-1230
for U.S. Nuclear Regulatory Commission

POWER-COOLING-MISMATCH TEST SERIES
TEST PCM-4
POSTIRRADIATION EXAMINATION

STEPHEN L. SEIFFERT TERRENCE F. COOK

July 1978

EG&G Idaho, Inc.

IDAHO NATIONAL ENGINEERING LABORATORY

DEPARTMENT OF ENERGY

IDAHO OPERATIONS OFFICE UNDER CONTRACT EY-76-C-07-1570

Available from
National Technical Information Service
Springfield, Virginia 22161
Price Codes:
Microfiche $3.00
Printed Copy A14

The price of this document for requesters outside of the North American continent can be obtained from the National Technical Information Service.

NUREG/CR-0238

TREE-1230

POWER-COOLING-MISMATCH TEST SERIES

TEST PCM-4

POSTIRRADIATION EXAMINATION

Approved:

P. E. MacDonald, Manager
Thermal Fuels Behavior Division

H. J. Zeile, Manager
Thermal Fuels Behavior Program

L. J. Ybarrondo, Director
Water Reactor Research

NUREG/CR-0238
TREE-1230
R3

POWER-COOLING-MISMATCH TEST SERIES

TEST PCM-4

POSTIRRADIATION EXAMINATION

by

Stephen L. Seiffert
Terrence F. Cook

EG&G IDAHO, INC.

July 1978

PREPARED FOR THE
U.S. NUCLEAR REGULATORY COMMISSION
AND THE
DEPARTMENT OF ENERGY
IDAHO OPERATIONS OFFICE
UNDER CONTRACT NO. EY-76-C-07-1570

ACKNOWLEDGMENTS

The authors extend their thanks to the Hot Cell Branch personnel whose support has made the completion of this examination possible. Special thanks is extended to W. H. Love and P. B. Reed for assistance during the metallurgical examinations. The authors acknowledge the assistance of 3. A. Ploger in the preliminary postirradiation examination, and R. R. Hobbins for technical assistance. The contributions of G. A. Reymann, D. H. Malin, and P. B. Reed for computer analysis and data reduction are gratefully acknowledged.

ABSTRACT

This report presents the results of the postirradiation examination of Test PCM-4 fuel rods in the Power-Cooling-Mismatch Test Series administered under the Thermal Fuels Behavior Program by EG&G Idaho, Inc., for the Nuclear Regulatory Commission. The purpose of the test was to investigate fuel rod behavior during film boiling operation.

Test PCM-4, conducted in a pressurized water reactor (PWR) test loop in the Power Burst Facility at the Idaho National Engineering Laboratory, used four 1.01-m-long, unirradiated PWR-type zircaloy-clad fuel rods. The four rods were subjected to a preconditioning period, followed by four separate flow-reduction, departure from nucleate boiling test cycles performed at linear rod peak powers up to an average of 69 kW/m and at minimum coolant mass fluxes of 600 kg/(s·m^2). All four rods were operated in film boiling conditions during the fourth (final) test cycle for times varying up to 140 s prior to manual reactor shutdown.

The four test fuel rods exhibited evidence of surface damage characterized by cladding collapse and surface oxide spalling along the portion of each rod experiencing film boiling. All four rods remained intact during reactor shutdown and subsequent postirradiation handling. The rods operated at temperatures above the zircaloy cladding beta-phase transformation temperature of 1245 K. Internal and external cladding oxidation, and fuel melting occurred.

The overall conditions and changes in the fuel and cladding that occurred as a consequence of film boiling operation are discussed. Cladding temperatures estimated for various circumferential and axial positions along the film boiling region of each test rod are presented. Cladding deformation from collapse and bowing are reported. Cladding embrittlement associated with high temperature cladding oxidation reaction with the coolant and the fuel is evaluated and comparisons with fuel failure criteria are presented. Effects of film boiling on fuel restructuring are also presented.

SUMMARY

Postirradiation examinations were performed on four pressurized water reactor type fuel rods following testing in the Power-Cooling-Mismatch (PCM) Test 4. This test was the fourth in-pile investigation in the Power-Cooling-Mismatch Test Series conducted by the Thermal Fuels Behavior Program of EG&G Idaho, Inc. The test series, sponsored by the United States Nuclear Regulatory Commission's Fuel Behavior Research Program to define nuclear fuel rod behavior during transient abnormal reactor operating conditions, is directed toward providing an experimental data base useful for the development and verification of computer models of fuel rod behavior. The major objective of Test PCM-4 was to investigate effects of cladding temperatures, stabilized in the alpha + beta two-phase zircaloy range (1105 to 1245 K) during film boiling operation, on the fuel rod mechanical and chemical behavior. The postirradiation examination was performed to obtain data on cladding and fuel microstructural changes induced by the high temperature test operation to complement the test instrumentation results presented in the companion test results report.

The four unirradiated, zircaloy-clad, fuel rods (Rods UTA-0014, UTA-0015, UTA-0016, and A-0017) were tested in a simulated pressurized water reactor environment, within the in-pile test loop of the Power Burst Facility reactor. Each rod was 1.01 m long and contained unirradiated UO_2 fuel (20% enriched at 93% theoretical density) with an active fuel column length of 0.915 m. All four fuel rods were prepressurized with a helium and argon gas mixture, one rod at 3.79 MPa and three rods at 2.49 MPa. Each rod was contained in a separate flow shroud which effectively isolated fuel rods in the assembly from thermal and hydraulic interaction.

The test sequence consisted of a preconditioning phase and the departure from nucleate boiling (DNB) testing. Four separate flow-reduction DNB test cycles were preformed at linear rod peak powers up to an average of 69 kW/m with minimum coolant mass fluxes to 600 kg/(s·m^2). All fuel rods experienced film boiling conditions during the fourth (final) test cycle. The time in film boiling of the individual rods varied up to a maximum of about 140 s prior to the reactor being manually shut down. All four rods remained intact during reactor operation, shutdown, and subsequent posttest handling. Surface damage induced by film boiling, as characterized by oxide spalling, was observed on all four test rods. A surface coating of black oxide was observed on the portions of each rod outside the film boiling zone. The film boiling zone was characterized by the observable collapse, waisting (collapse into the gap between fuel pellets), and heavy surface oxidation from the coolant-cladding reaction. Bowing was observed on only two of the rods, Rods UTA-0015 and UTA-0016.

The four fuel rods operated during film boiling at temperatures above the beta-phase zircaloy transformation temperature of 1245 K. The cladding temperature distribution was evaluated using measured thicknesses of surface oxide and the outer diameter cladding reaction layer of oxygen-stabilized alpha microstructures to establish peak temperatures and isothermal effective temperatures at various circumferential orientations and axial positions

along the film boiling zones of the rods. Peak cladding temperatures of 1620, 1700, 1740, and 1570 K were calculated for Rods UTA-0014, UTA-0015, UTA-0016, and A-0017, respectively. Isometric plots of the peak and isothermal effective temperatures exhibited temperature reductions at thermocouple locations attributable to a local cooling fin effect. No temperature variation associated with rod bowing inside the flow shroud was noted.

Cladding deformation was characterized by collapse along the film boiling zone and by rod bowing. The collapse exhibited an ovality of generally 1.007 over the film boiling zone, compared with the nominal ovality of 1.003 outside the zone. Diametral reductions in the collapse region up to 93% of the cold gap were measured. Cladding waisting occurred over 60 to 79% of the collapse zones of the rods. Posttest void volumes compared favorably with pretest values.

Contact between the cladding and coolant during film boiling led to rapid external oxidation of the cladding. Oxygen diffusion from the surface oxide layer resulted in the formation of oxygen-stabilized alpha-zircaloy from the parent beta phase. Contact between the UO_2 fuel and cladding, as a result of collapse of the cladding toward the fuel column and thermal expansion of the fuel at film boiling temperatures, promotes oxygen diffusion across the fuel-cladding interface. For the film boiling times employed, a layer of oxygen-stabilized alpha forms at the inner cladding surface at temperatures well above the beta-phase transformation temperature. This reaction is accompanied by a U-Sn-Zr intermetallic reaction layer at the interface when no inner surface ZrO_2 is present.

Embrittlement of the cladding in the high temperature film boiling zone by internal and external oxidation arising from UO_2-zircaloy reactions was evaluated from estimated effective cladding temperatures and test exposure time in film boiling, using the critical oxidation time criteria and the 17% equivalent cladding reacted embrittlement criterion. The absence of failure of the rods during the test by oxygen embrittlement was correctly predicted by both criteria.

Cladding samples examined from the film boiling zones of all fuel rods exhibited varying degrees of hydriding. The hydriding was dispersed within the cladding alpha + beta two-phase and prior beta-phase fields in the cladding interior, away from the oxygen rich alpha-phase material at the outer and inner cladding surfaces. The structural integrity of the cladding was not affected by the hydriding. An alpha + beta two-phase structure was also observed in some cladding samples between the outer and inner oxygen-stabilized alpha layers and the parent beta-phase material. Hydriding was prevalent at the boundaries between the alpha + beta two-phase region and the parent beta phase. These structures are attributed both to a change in terminal hydrogen solubility during oxygenation and to posttest quenching.

Examination of fuel microstructures from samples within the film boiling zone revealed equiaxed grain growth in three of the four rods, Rods UTA-0014, UTA-0015, and UTA-0016. Reaction of the UO_2 fuel with the centerline tantlum sheathed thermocouples of Rods UTA-0014 and UTA-0016 introduced a local melt region. The tantalum-UO_2

melting affected the performance of the centerline thermocouples of these two rods, inducing erractic response prior to the final film boiling test cycle and failure during the final test cycle. The restructuring apparent in the fuel of Rod A-0017 was due to fuel melting, central void formation and molten fuel slumping, and redistribution of porosity outside the molten zone. Fuel restructuring in this rod did not affect the fuel rod structural integrity. Limited granular fracturing (shattering) of the UO_2 fuel was observed near the outer pellet edges and near the central restructured regions. Fracturing near the outer pellet edges occurred in regions of mechanical contact between fuel fragments and the cladding. Fracturing near the center of the fuel pellets was associated with fragments in mechanical contact with major fuel cracks. Grain sizes of approximately 20 μm (lower limit) associated with the granular fracturing were noted. The shattering was localized in the film boiling zone.

CONTENTS

FIGURES

TABLES

POWER-COOLING-MISMATCH-TEST SERIES

TEST PCM-4

POSTIRRADIATION EXAMINATION

I. INTRODUCTION

Fuel behavior studies are being conducted in the Thermal Fuels Behavior Program by EG&G Idaho, Inc., as part of the Nuclear Regulatory Commission's Water Reactor Safety Research Fuel Behavior Program[1] define the behavior of fuel rods during transient reactor conditions. The power-coolin mismatch (PCM) experiments are being performed in conjunction with similar tests on adiated fuel rods, and are designed to determine the effects of film boiling on unirradiated fuel rod behavior. The PCM Test Series is directed toward providing experimental data for verification of analytical models developed to predict the behavior of light water reactor nuclear fuels under normal and postulated accident conditions.

The tests proposed for the PCM testing program were determined on the basis of an analysis that included (a) a parametric study of a pressurized water reactor (PWR) type fuel rod subjected to a variety of postulated PCM conditions to help identify modes of post-DNB (departure from nucleate boiling) fuel rod behavior, and (b) a sensitivity study to determine the relative effect of variations in basic fuel rod design parameters and the uncertainty in the cladding-to-coolant heat transfer coefficient on the post-DNB fuel rod behavior. Results of the parametric study indicated that, due to the unique variation of zircaloy cladding ductility with temperature, the post-DNB cladding behavior will depend on the phase of the zircaloy. Zircaloy cladding ductility increases with increasing temperature in the alpha-phase and reaches a maximum at the beginning of the alpha + beta two-phase transformation (T = 1105 K). The ductility then decreases with increasing temperature, reaching a minimum ductility approximately midway through the two-phase region. The ductility again increases with increasing temperature toward the beta-phase transformation (T = 1245 K). At cladding temperatures above 1245 K, the external zircaloy-water and the internal zircaloy-fuel chemical reactions result in cladding oxygenation. Oxygen uptake strengthens but embrittles the cladding. The extent of the zircaloy-water and zircaloy-fuel chemical reaction is primarily determined by the time at temperature. Thus, the cladding ductility at a given temperature in the beta phase progresses from high to low, decreasing as oxygenation occurs. At beta-phase temperatures above about 1650 K, oxygen uptake occurs very rapidly. On the basis of variations in the zircaloy cladding ductility with temperature and exposure, five categories of post-DNB fuel rod behavior can occur from a PCM event. These five categories are summarized in Table I, together with the potential modes of fuel rod failure.

TABLE I

CATEGORIES OF POST-DNB FUEL BEHAVIOR DURING PCM TRANSIENTS

Category	Stabilized Cladding Temperature Range (K)	Stabilized Zircaloy Cladding Material Phase	Zircaloy-Water Reaction	Cladding Ductility	Potential Fuel Rod Failure Modes
1	<920	Mixed stress-relieved and preequiaxed alpha	None	Normal	
2	920 - 1105	Recrystallized alpha	None	High	Large deformations[a]
3	1105 - 1245[b]	Alpha + beta two-phase	Minimal	Low	Small deformations[a]
4	1245 - 1650	Low temperature beta	Severe	High-low[c]	Cladding oxygen embrittlement
5	>1650	High temperature beta	Severe	Low	Cladding and possibly fuel melting

[a] Cladding outward deformation is possible in a LWR only after sufficient gaseous fission product accumulation has increased the internal rod pressure to values above the system pressure.

[b] This temperature range is intended to bound the minimum for cladding ductility occurring through the alpha + beta phase transition.

[c] The cladding ductility, initially high in beta-phase zircaloy, will decrease rapidly as the zircaloy becomes embrittled by oxidation and oxygen absorption.

Results of the sensitivity study performed to determine the relative effect of variations in basic fuel rod design parameters and the uncertainty in the cladding-to-coolant heat transfer coefficient on post-DNB fuel rod behavior indicated that design parameter variations have less influence on post-DNB fuel rod thermal behavior than the uncertainty in the post-DNB film boiling heat transfer coefficient. Thus, only one test fuel rod design was required for the PCM test program.

The tests currently identified for the PCM program are summarized in Table II. three of the major classifications for the tests are fuel rod prepressurization, duration of film boiling, and temperature stabilization (based on film boiling temperature). These parameters essentially determine the mode of cladding failure. The film boiling time and temperature determine what variations occur in cladding ductility or the extent of embrittlement, and the fuel rod internal prepressurization determines whether the cladding will balloon or collapse.

The PCM test program consists of single-rod tests and nine-rod cluster tests. Prior to the current phase of the PCM program, four single-rod tests, not listed in Table II, were completed. Tests PCM-2A (single-rod), PCM-2 (four-rod), and PCM-3 (four-rod) have been completed. The results of these tests are described in References 2 through 6.

This report contains data on the physical and metallurgical state of the cladding and fuel obtained from postirradiation examinations of the four Test PCM-4 fuel rods, Rods UTA-0014, UTA-0015, UTA-0016, and A-0017. The four test rods were mounted in the central test space of the Power Burst Facility (PBF) reactor. These rods, contained in individual flow shrouds, were tested simultaneously under the same nominal PWR operating conditions. The purpose of Test PCM-4 was to investigate fuel rod mechanical, chemical, and thermal behavior when the maximum film boiling cladding temperatures stabilized in the alpha + beta two-phase temperature range (1105 to 1245 K). Due to a sparsity of data from previous PCM tests in this temperature range (previous PCM tests had exceeded the scheduled temperatures), the objectives were changed from those defined in Tables I and II to expand the data base in the two-phase temperature range.

The test consisted of a thermal-hydraulic power calibration, a preconditioning operation during which the gap conductance was measured, a fuel rod aging period, and the DNB portion of the test. Four separate flow reduction DNB test cycles were performed at linear rod peak powers up to 69 kW/m. The test was initially programmed for rod powers up to 52 kW/m, but due to a calibration error the desired linear ratings were exceeded so that the fuel rods stabilized in film boiling at temperatures above the beta-phase zircaloy transformation temperature of 1245 K. The test thus exceeded the scheduled temperatures of the test objectives. Additional information useful to Category 4, defined in Tables I and II, was obtained from the test.

On-line data obtained during the test included cladding surface temperature measurements, fuel centerline temperature, rod internal pressure, and rod axial elongation data. The time in film boiling was determined from the fuel rod axial elongation and from

TABLE II

PCM TEST PROGRAM DESCRIPTION

Test Parameters	PCM-2A	PCM-2	PCM-3	PCM-4	PCM-5	PCM-6	PCM-7
Number of test rods	1	4[a]	4[a]	4[a]	9	9	9
Temperature[b] stabilization ategory	2	2	3	4	4	2	4
Predicted cladding response	collapse	collapse	collapse	collapse	collapse	balloon	balloon
Maximum duration of stable film boiling (s)	210	105	60	160	300	300	300
Maximum linear peak power (kW/m)	58	46	46	63	52	52	52
Fuel rod cold internal pressure (MPa)	2.49	2.49/ 3.79	2.49/ 3.79	2.49/ 3.79	2.59	5.52	5.52
Coolant inlet temperature (K)	600	600	600	600	600	616	616
Flow shroud inside diameter (mm)	16.3	16.3	16.3	16.3	[c]	[c]	[c]

[a] Four test rods situated in a square array with individual flow shrouds which thermally and hydraulically isolated the rods from each other.

[b] Category
2. Maximum cladding temperatures stabilized below 1105 K (alpha-phase zircaloy, no zircaloy-water reaction; high ductility; deformation failure expected in high pressure rods after large deformation).
3. Maximum cladding temperature stabilized between 1105 - 1245 K (alpha + beta two-phase zircaloy; little zircaloy-water reaction; low ductility; deformation failure expected in high pressure rods).
4. Maximum cladding temperature stabilized above 1245 K (beta-phase zircaloy; severe zircaloy-water reaction; high ductility, changing to very low ductility; melting, embrittlement, or deformation failure expected depending on rod power and pressure).

[c] Nine rods situated in a square array with a 14.3-mm pitch and a flow shroud surrounding the bundle.

cladding surface temperature results. The film boiling temperatures were not accurately indicated by the cladding surface thermocouples, since the thermocouples significantly perturbed the cladding surface temperature (up to 150 K). Therefore, the film boiling temperatures were determined from microstructural temperature estimates and estimates based on the kinetic analysis of oxidation reaction layer thicknesses.

The objectives of the postirradiation examination of Test PCM-4 fuel rods were to:

(1) Provide a best estimate of the film boiling time-temperature history for the four fuel rods and determine the extent of film boiling

(2) Determine the fuel rod deformation

(3) Quantify the embrittlement from internal and external cladding oxygenation and hydriding

(4) Determine the fuel restructuring as a result of film boiling.

The experimental configuration and test conduct are summarized in Section II. Details of the test rod parameters relevant to the test, and instrumation used in the test are discussed.

Observations of the effects of film boiling operation on the four test rods are presented in Section III. The overall appearance and gross damage to the test rods is discussed. The film boiling zone for each rod is defined.

The cladding axial and circumferential temperature distributions within the film boiling zones of the test rods are presented in Section IV. Temperatures determined from cladding microstructures and reaction layer thicknesses are discussed. The temperature-related cladding deformation is discussed in Section V.

Cladding chemical reactions from coolant-cladding and cladding-fuel interaction are discussed in Section VI. The cladding embrittlement from oxidation is assessed and the influence of hydrogen and thermal quenching on microstructure and cladding hardening is discussed.

Fuel restructuring within the film boiling zone is assessed in Section VII. Fuel centerline melting associated with the tantalum thermocouple sheath reaction is investigated and discussed. Granular fracturing of the fuel is also discussed.

The many measurements and calculations made to characterize the posttest conditions of the test fuel rods are presented in Appendices A through F. Appendix A contains descriptions of the experimental irradiation and axial power profile determination necessary to understand the overall thermal history of the test fuel rods. The as-built fuel rod material

characterizations required for analytical model evaluation and posttest comparisons are contained in Appendix B. Results of the cladding collapse measurements are presented in Appendix C. Posttest information on cladding phase transformations and fuel restructuring are contained in Appendix D. Results of examinations of special cladding and fuel microstructural features by electron microprobe, scanning electron microscopy, and microhardness tests on the cladding are also presented in Appendix D. Appendix E presents results of the metallographic examinations of selected thermocouple junctions from the test rods. Cladding surface temperature estimates based on oxidation reaction layer thicknesses are tabulated and discussed in Appendix F.

II. EXPERIMENT CONFIGURATION AND TEST CONDUCT

Test PCM-4 was performed in the Power Burst Facility (PBF) pressurized water reactor in-pile test loop. The PBF driver core test space was designed to operate as a neutron flux trap which permits high power densities in tested fuel rods relative to the active core power density.

During testing, each fuel rod was rigidly fixed in a flow shroud at the top end cap and was free to expand axially downward onto a length change transducer. The flow shrouds directed the coolant upwards over the fuel rods and effectively thermally and hydraulically isolated the rods from interacting. The rod shrouds were symmetrically positioned in the PBF in-pile tube. Details of the experiment design are presented in Appendix A. Fuel rod materials and parameters relevant to Test PCM-4, instrumentation used in this test, and experiment conduct are summarized in this section.

1. EXPERIMENT CONFIGURATION

Each test fuel rod used in Test PCM-4 was composed of ceramic UO_2 pellets contained in a zircaloy-4 cladding tube. The 0.915-m-long fuel stack contained 60 UO_2 pellets (20% enriched UO_2 at 93% theoretical density), each nominally 9.30 mm in diameter and 15.40 mm long (pellets at the bottom of each stack were fractional lengths). The cladding tubes were nominally 10.75 mm on the outside diameter and had 0.61-mm wall thicknesses. The nominal fuel-cladding diametral gap was 0.190 mm. The pretest void volumes of Rods UTA-0014, UTA-0015, UTA-0016, and A-0017 were 9.6 ± 0.3, 9.0 ± 0.3, 8.8 ± 0.3, and 7.2 ± 0.3 x $10^{-2} m^3$, respectively. Rods UTA-0014, UTA-0015, and UTA-0016 were prepressurized with helium gas at ambient temperature to 2.49 ± 0.01 MPa, whereas Rod A-0017 was prepressurized to 3.79 ± 0.07 MPa. Detailed pretest characterization data for Test PCM-4 fuel rods are presented in Appendix B.

The fuel rod instrumentation consisted of an ultrasonic fuel centerline thermometer in Rod UTA-0015 and a tantlum sheathed centerline thermocouple in Rods UTA-0014 and UTA-0016. A plenum gas pressure transducer and titanium sheathed cladding surface thermocouples completed the instrumentation on these rods. Rod A-0017 was uninstrumented.

2. EXPERIMENT CONDUCT

Test PCM-4 began with a thermal-hydraulic rod power calibration to determine the rod powers relative to the in-pile tube neutron flux. The rod powers were determined during the power calibration (when single-phase coolant conditions were maintained) from coolant flow and temperature rise measurements at 12 different fuel rod peak powers up to a maximum of 69 kW/m. During the power calibration phase, the nominal coolant mass flux

through each shroud, pressure, and inlet temperature were 3400 kg/(s·m^2), 15.16 MPa, and 585 K, respectively. The power calibration was followed by a preconditioning period to obtain an operating history of the test fuel rods and to allow for pellet cracking and partial restructuring of the UO_2 fuel. Nominal coolant conditions were adjusted to 2125 kg/(s·m^2), 15.0 MPa, and 600 K during the preconditioning operation. The reactor was operated for 15 h to induce fuel cracking and partial fuel restructuring. Four cycles were performed during the 15-h preconditioning operation in which the rod powers were initially increased to 43 kW/m at a nominal rate of 1 kW/(m·min), held at power for three hours, and decreased to 3 kW/m at a rate of 1 kW/(m·min). The rod powers were cycled up after 20 min of operation at 3 kW/m. Subsequent to this operation, it was determined that the fuel rods operated under sustained nucleate boiling conditions during the preconditioning period. Gap conductance measurements were made during the preconditioning operation, both at steady state ($\int$kdT) power and under transient power oscillation conditions.

Following the preconditioning operation, the coolant flow conditions were adjusted to obtain nucleate boiling along the test fuel rods. Nucleate boiling conditions "age" the cladding surface by removing residual gases, thereby eliminating the possibility of premature DNB. Nominal coolant inlet conditions used during the aging operation were 220 kg/(s·m^2), 15.1 MPa, and 600 K. The fuel rod powers were increased from 3 kW/m to approximately 72 kW/m at an average rate of 3 kW/(m·min) during this operation. The fuel rods were operated under these conditions for one hour.

The experimental portion of the test consisted of four sequential flow reduction test cycles to achieve film boiling conditions. During the first two cycles the reactor power was manually reduced and the coolant flow was manually increased when DNB occurred, to prevent high post-DNB cladding temperatures. During the third cycle the coolant flow was manually increased, while the rod powers were held constant, until DNB was eliminated. During the fourth, and final test cycle, the reactor was manually scrammed after cladding temperatures equilibrated in film boiling for up to 40 s. DNB Cycles 1, 2, 3, and 4 were performed for average rod powers of approximately 69, 69, 60, and 69 kW/m, respectively, at minimum coolant mass fluxes on the order of 1600 kg/(s·m^2). Additional details of the experimental irradiation and axial rod power determination are presented in Appendix A.

III. EFFECTS OF FILM BOILING OPERATION ON TEST PCM-4 FUEL RODS

This section presents an overview of the posttest condition of the four irradiated Test PCM-4 fuel rods. Changes in the appearance of the cladding surface are useful in characterizing the extent of film boiling. The film boiling zone is defined and discussed in this section together with supplementary data on the permanent changes induced by film boiling operation in the cladding and fuel structures.

The posttest appearances of the Test PCM-4 fuel rods are shown in Figures 1 through 8, viewed in separate rod orientations 180° apart. All four rods exhibited cladding collapse at fuel pellet interfaces (waisting), heavy surface oxidation, and spalling of the surface oxide due to the high temperature operation (above 920 K). The axial region of collapse along each fuel rod was identified as the film boiling zone. The collapse data are summarized in Table III. Outside diameter measurements characterizing the cladding collapse are discussed in Section V and are presented in Appendix C.

The film boiling region extended between 0.58 and 0.88 m from the bottom of the rod along Rod UTA-0014, and between 0.54 and 0.88 m along Rod UTA-0015. The observable film boiling zone along Rods UTA-0016 and A-0017 was between 0.56 and 0.84 m, and 0.57 and 0.84 m, respectively. All of the rods exhibited a black oxide outside the film boiling zone.

The rods were neutron radiographed following testing to characterize changes in the condition of the fuel columns. Composite neutrographs of the test fuel stacks are presented in Figure 9 for Rods UTA-0014 and UTA-0015, and in Figure 10 for Rods UTA-0016 and A-0017.

A small fuel melt zone was identified near the center of fuel pellets within the film boiling zones of Rods UTA-0014, UTA-0016, and A-0017. The melt zones are within the film boiling region of each rod. In Rods UTA-0014 and UTA-0016, the melt zone was associated with the length of the tantalum sheathed centerline thermocouples that extended into the film boiling region.

Fuel cracking (major crack formation) over the entire length of the column was common to all four test fuel stacks. An open fuel gap was observed in each of the fuel stacks. The position of the gap in the fuel column along the rods corresponds with the approximate lowest extent of film-boiling-induced collapse and the approximate region of maximum collapse of the cladding as summarized in Table IV. The gaps probably occurred as a result of locking of the thermally expanded fuel by the cladding collapse during test operation and subsequent contraction of the lower portion of the fuel column following cooldown.

Overall views of the transverse and longitudinal metallographic samples examined and discussed in this report are presented in Figure 11 for Rods UTA-0014 and UTA-0015, and

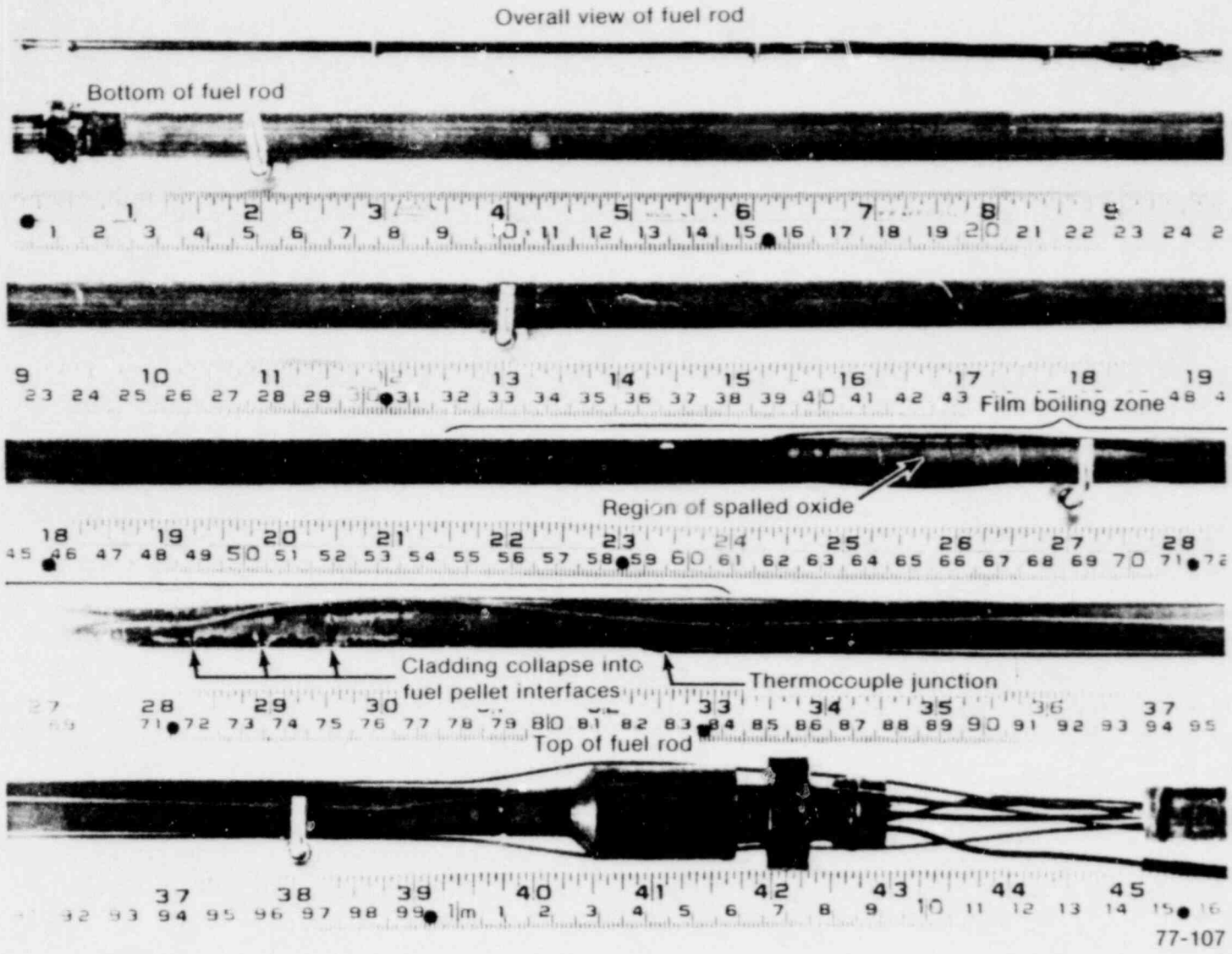

Fig. 1 Rod UTA-0014, showing the posttest condition at the 0° orientation.

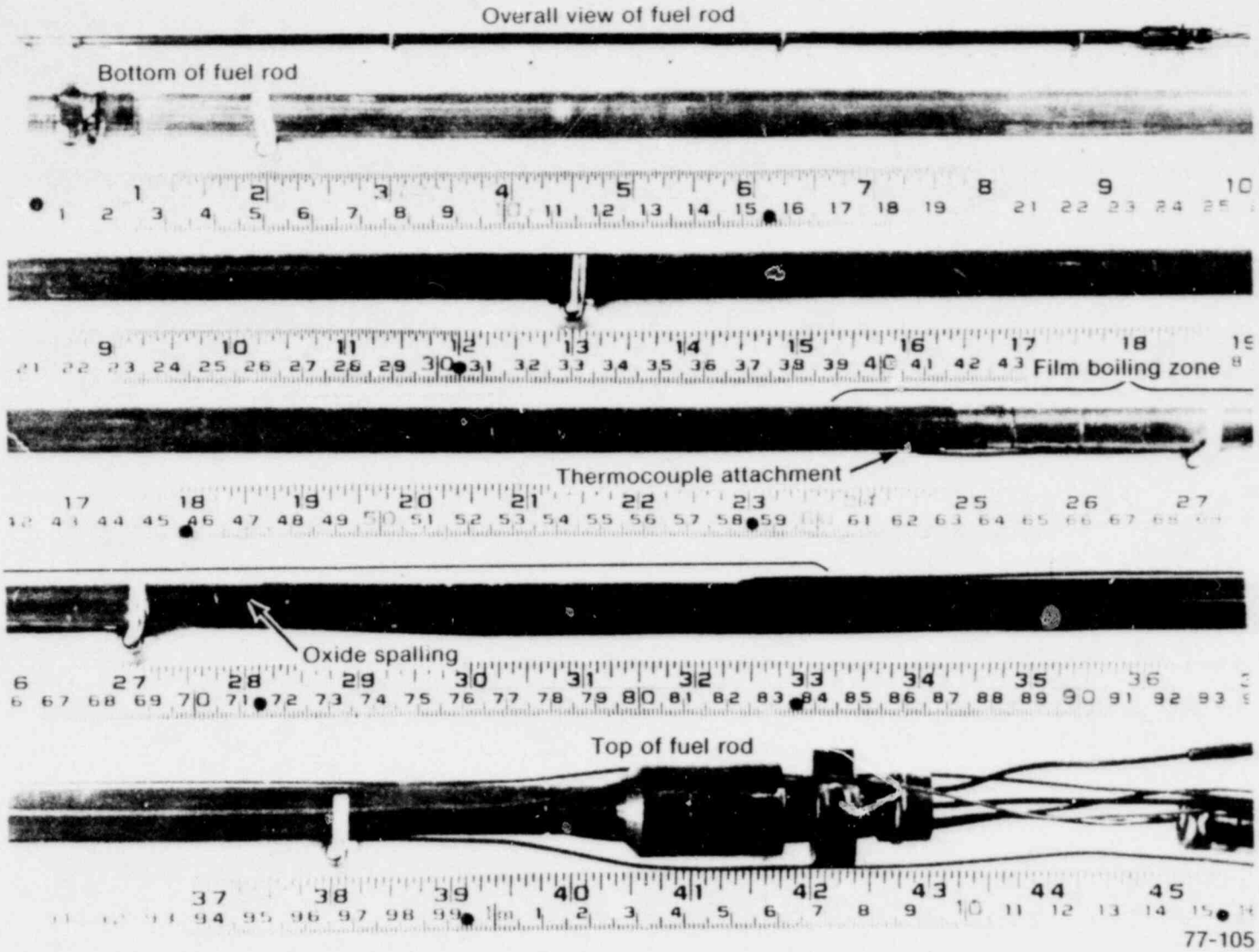

Fig. 2 Rod UTA-0014, showing the posttest condition at the 180° orientation.

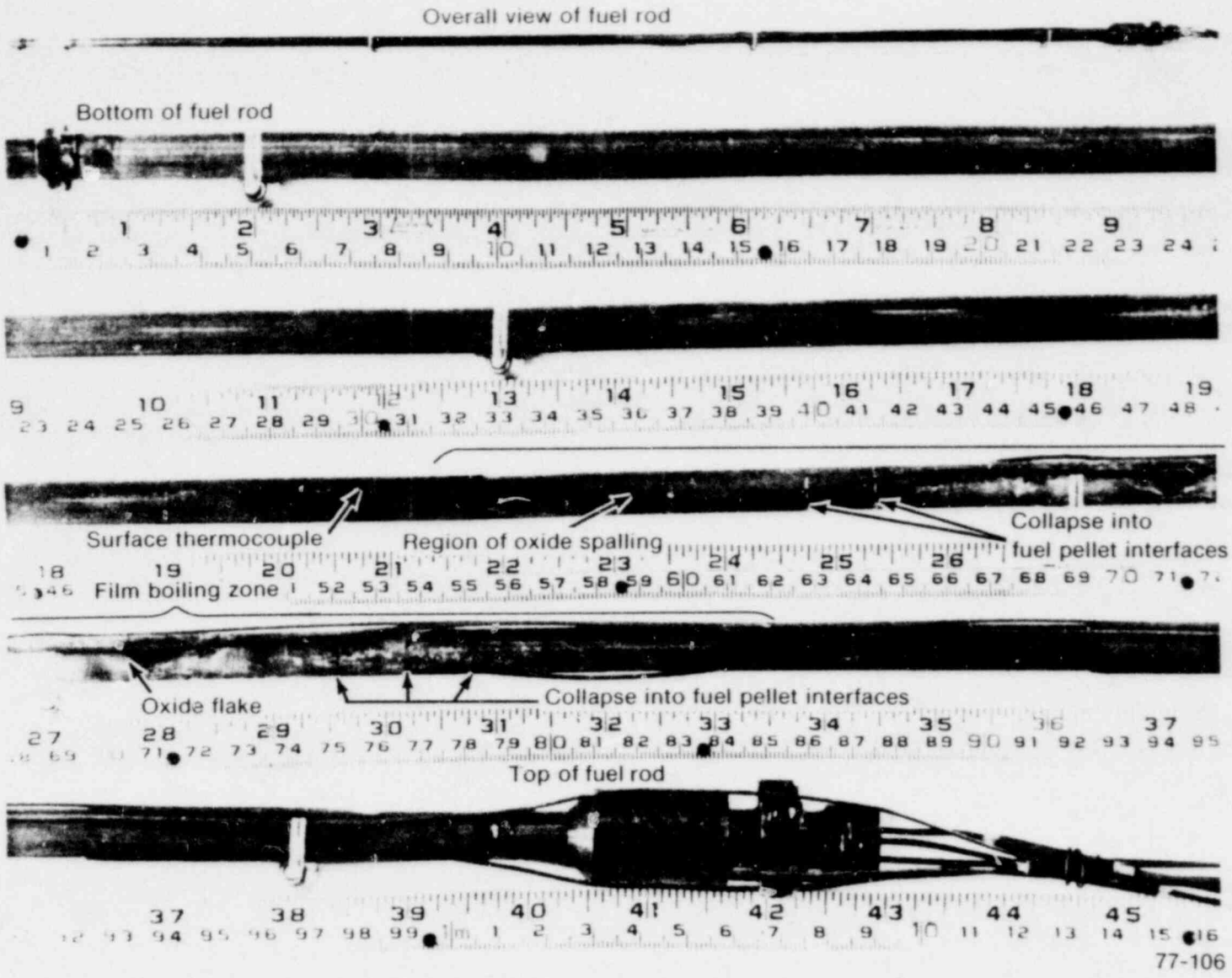

Fig. 3 Rod UTA-0015, showing the posttest condition at the 0° orientation.

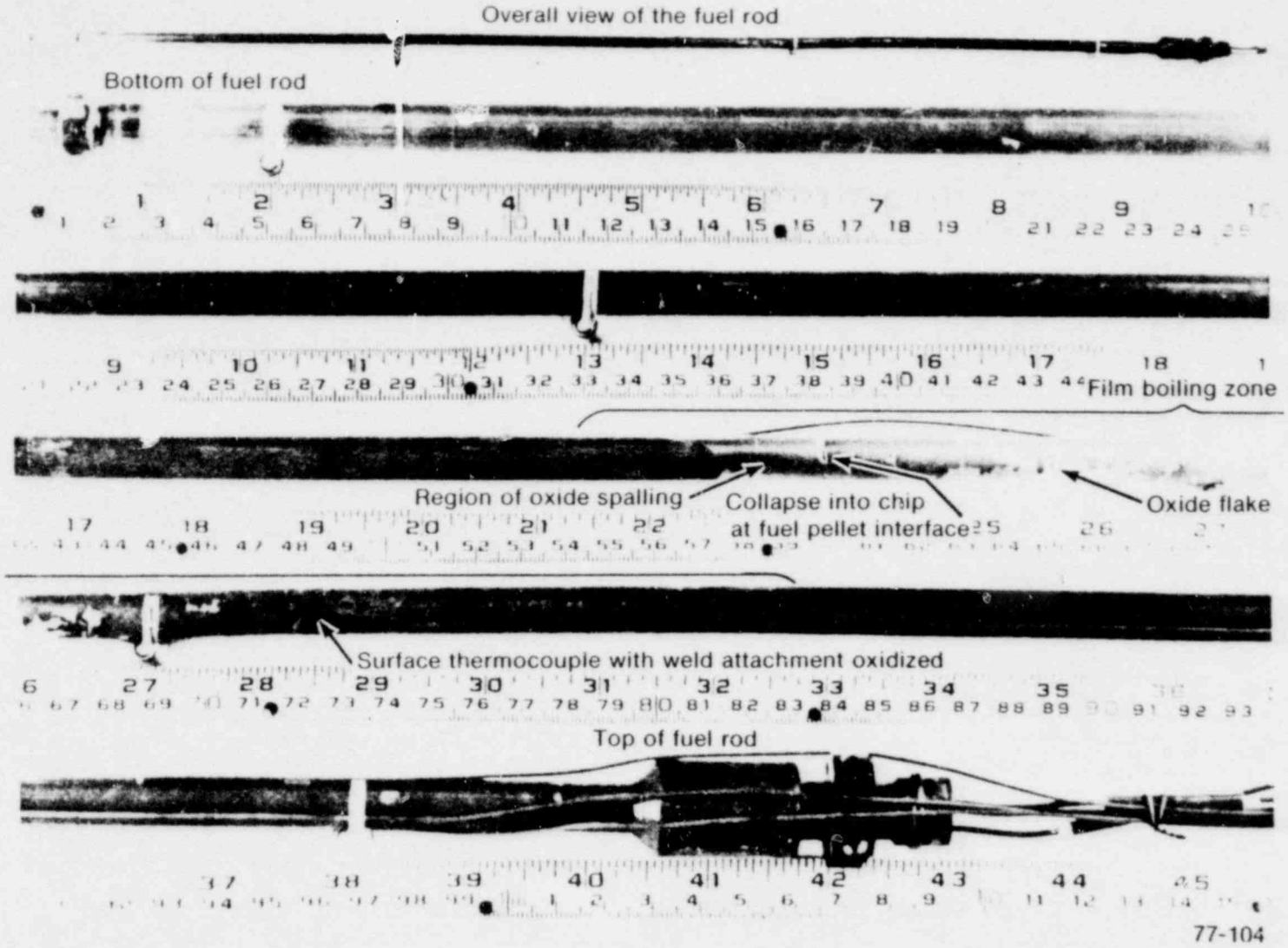

Fig. 4 Rod UTA-0015, showing the posttest condition at the 180° orientation.

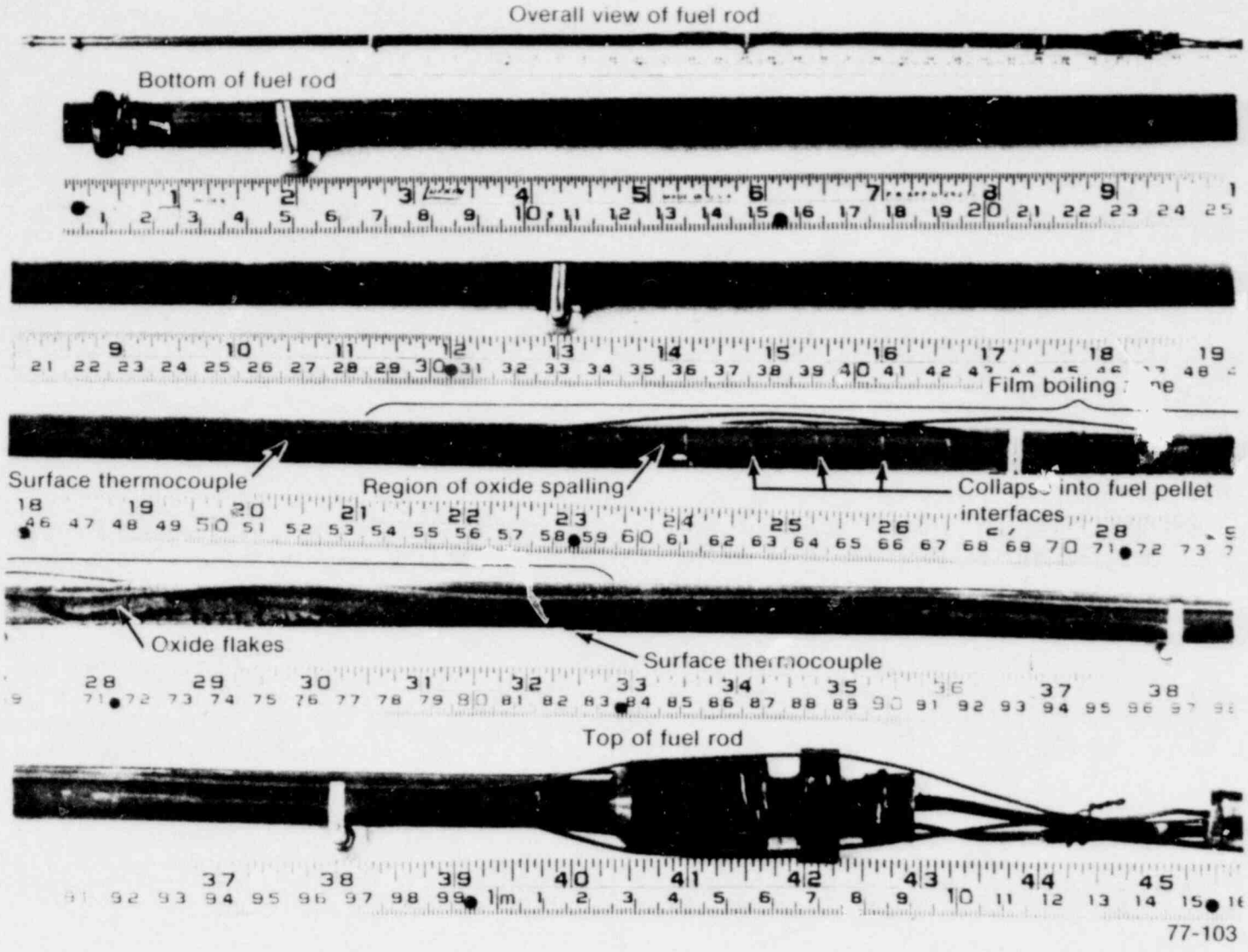

Fig. 5 Rod UTA-0016, showing the posttest condition at the 0° orientation.

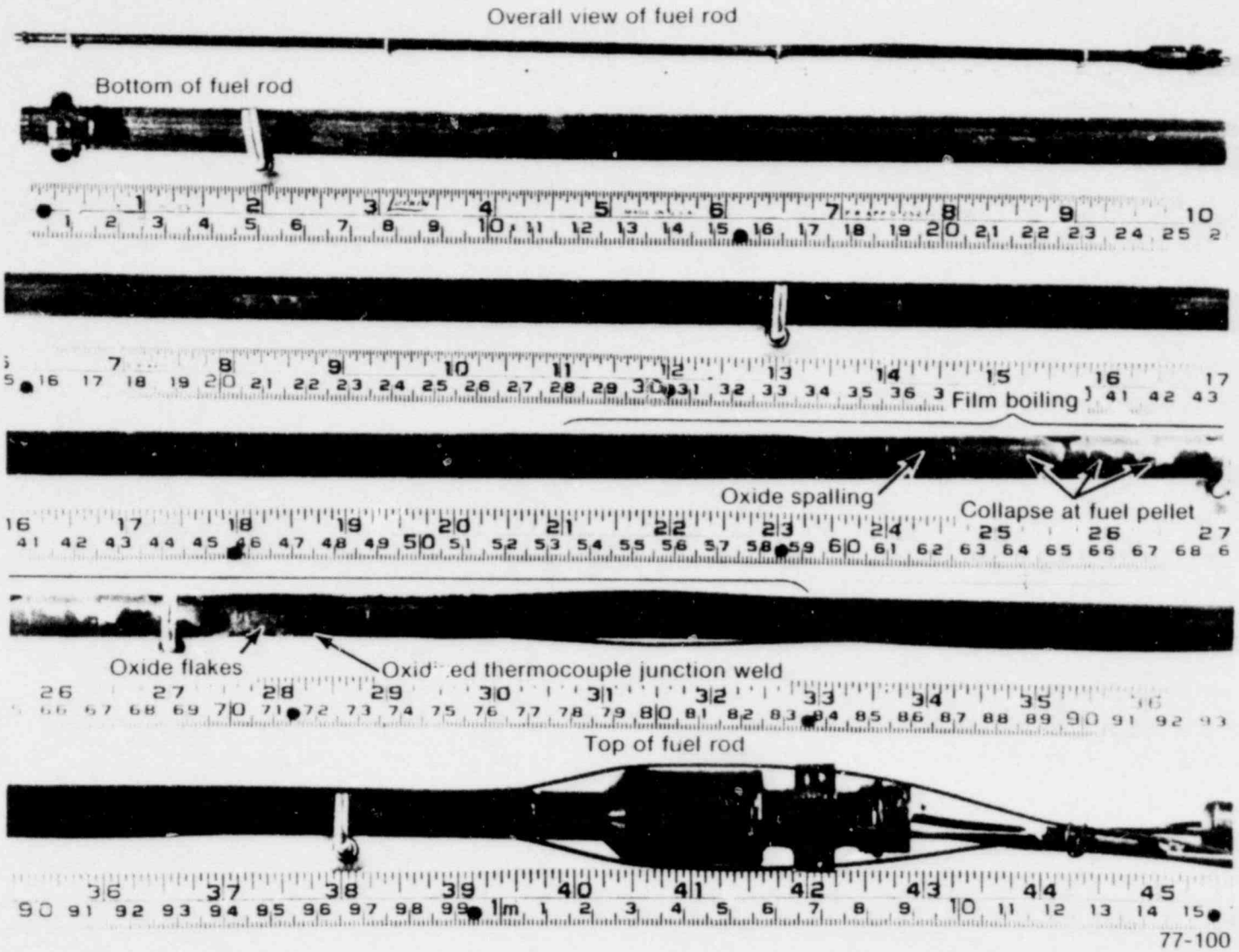

Fig. 6 Rod UTA-0016, showing the posttest condition at the 180° orientation.

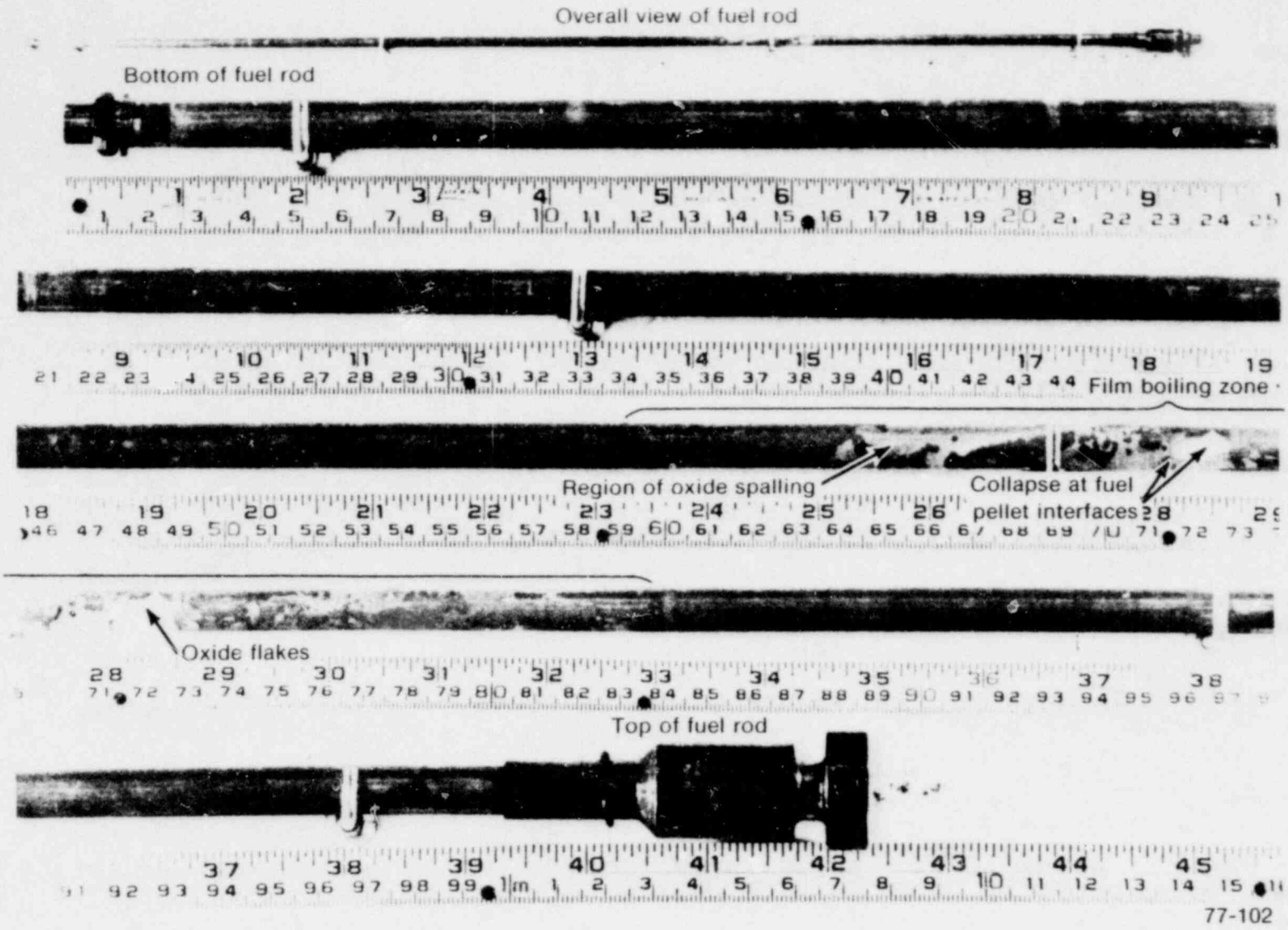

Fig. 7 Rod A-0017, showing the posttest condition at the 0° orientation.

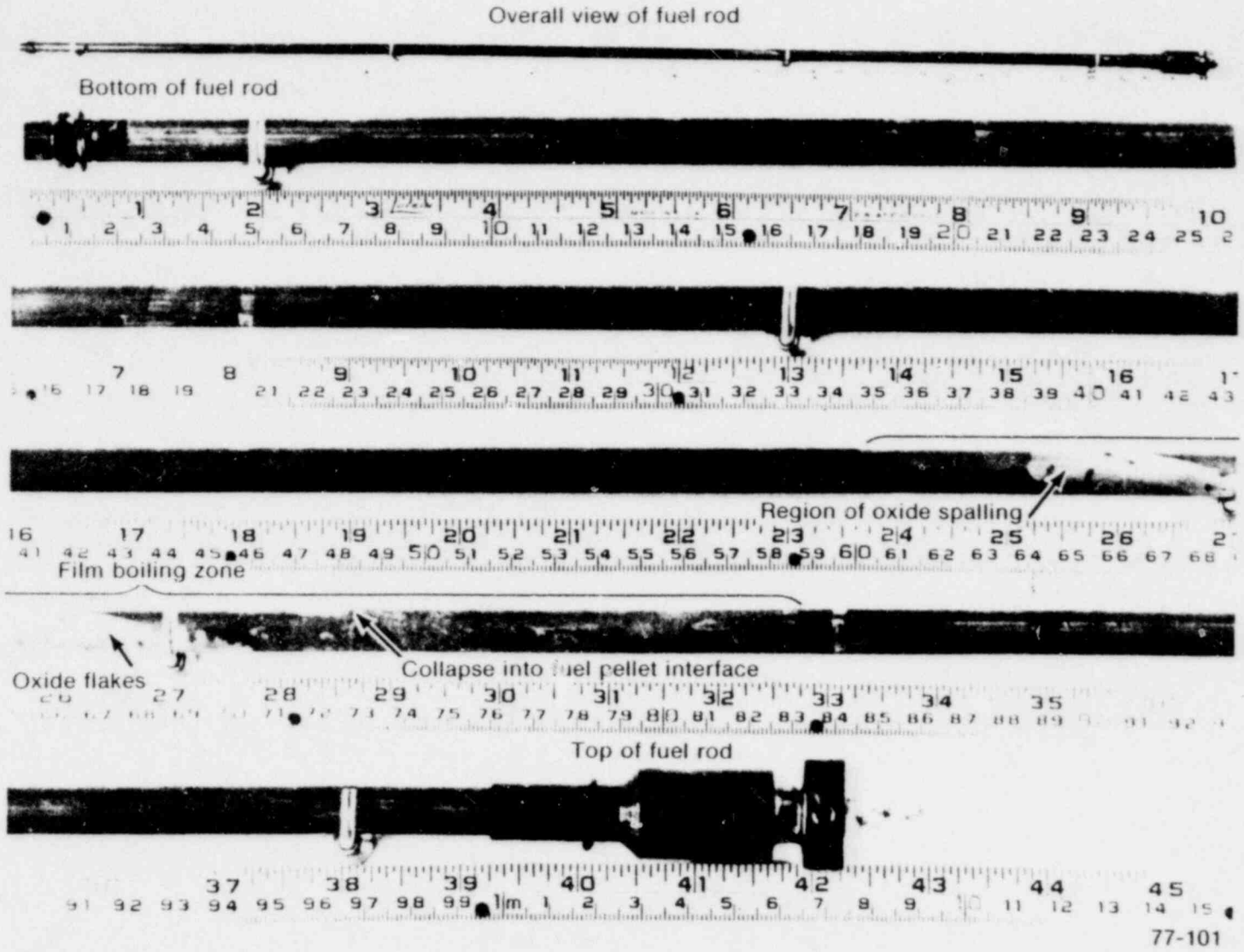

Fig. 8 Rod A-0017, showing the posttest condition at the 180° orientation.

TABLE III

FILM BOILING ZONES FOR TEST PCM-4 FUEL RODS

Rod	Film Boiling Zone	
	Location from Bottom of Rod (m)	Location from Bottom of Fuel Stack (m)[a]
UTA-0014	0.58 to 0.88	0.54 to 0.84
UTA-0015	0.54 to 0.88	0.50 to 0.84
UTA-0016	0.56 to 0.84	0.52 to 0.80
A-0017	0.57 to 0.84	0.53 to 0.80

[a] The bottom of the fuel stack was 0.035 m above the bottom of the fuel rod.

in Figure 12 for Rods UTA-0016 and A-0017. The samples were sectioned from various regions near the peak power location at midlength, regions that remained at cooler operating temperatures during testing, regions of various cladding thermocouple locations, and regions of film-boiling-induced cladding collapse. These regions were determined from the extent of surface oxidation, measured collapse, and thermocouple data indicating surface temperatures greater than 730 K (approximate DNB condition). The sample locations are identified with respect to the bottom of the fuel rod, which is 35 mm from the bottom of the fuel stack.

The predominant features apparent in the photomacrographs are the regions of fuel restructuring and melting near centerline thermocouples as evidenced by the coloration change (dark to light) toward the center of the fuel pellets, the fuel fracturing, fuel slumping into pellet-to-pellet interfacial dishes, central void formation at the pellet center, and regions of cladding collapse into fuel pellet interfaces (waisting).

Knowledge of the detailed cladding temperature distributions along the individual fuel rods is important to the understanding of cladding structural changes, oxidation, and subsequent embrittlement. During Test PCM-4, cladding temperatures were only approximately known from test instrumentation. Cladding temperatures were initially evaluated by posttest metallographic examination using microstructural characteristics such as the stress-relieved condition ($T < 920$ K), recrystallized alpha-zircaloy ($920 < T < 1105$ K), the alpha + beta two-phase zircaloy ($1105 < T < 1245$ K), and the prior beta-phase zircaloy ($T > 1245$ K). Microstructures established from the metallographic examination, together with associated temperature estimates, are summarized in Section IV. Details of the metallographic examination are presented in Appendix D.

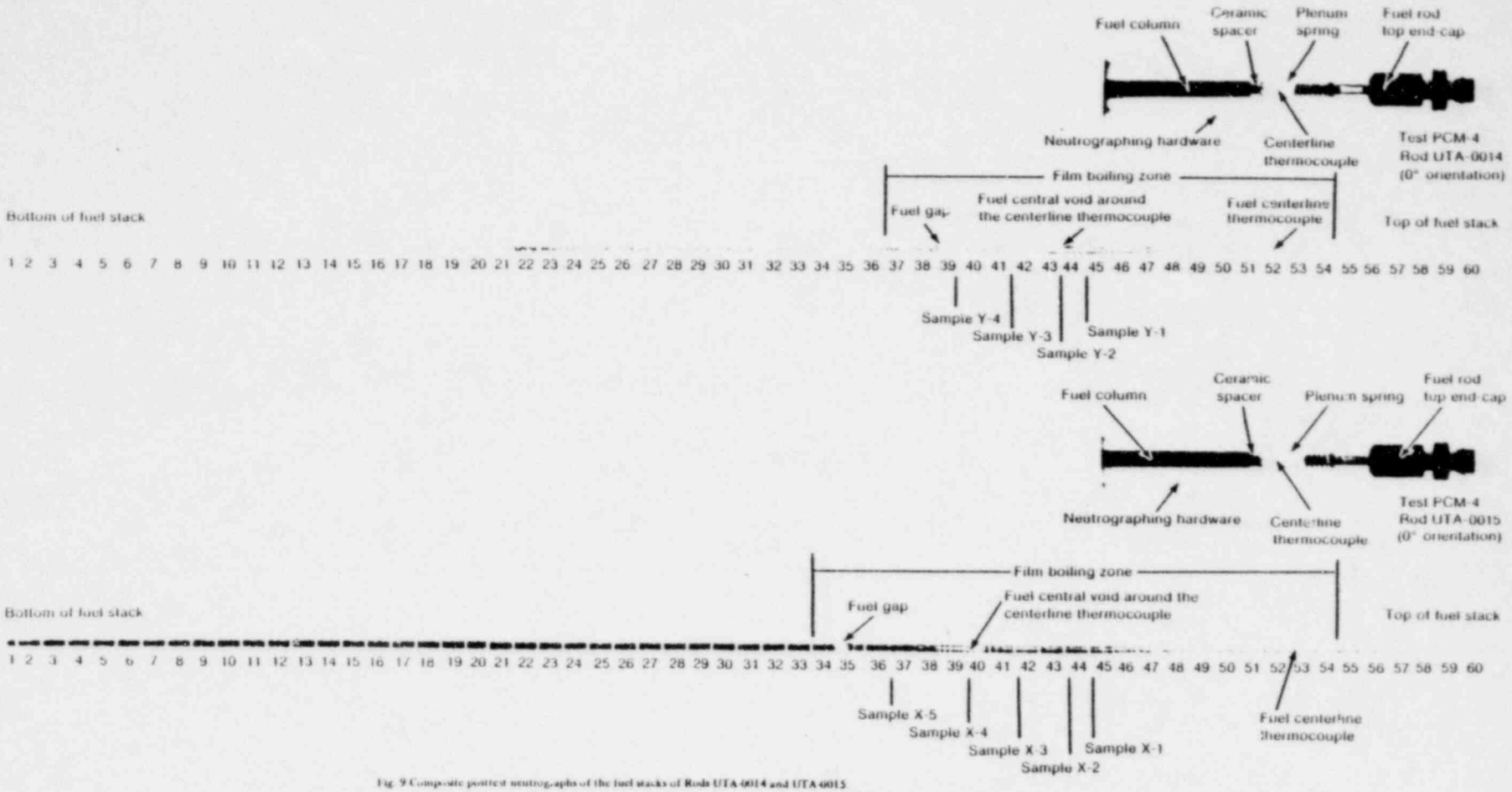

Fig. 9 Composite posttest neutrographs of the fuel stacks of Rods UTA-0014 and UTA-0015.

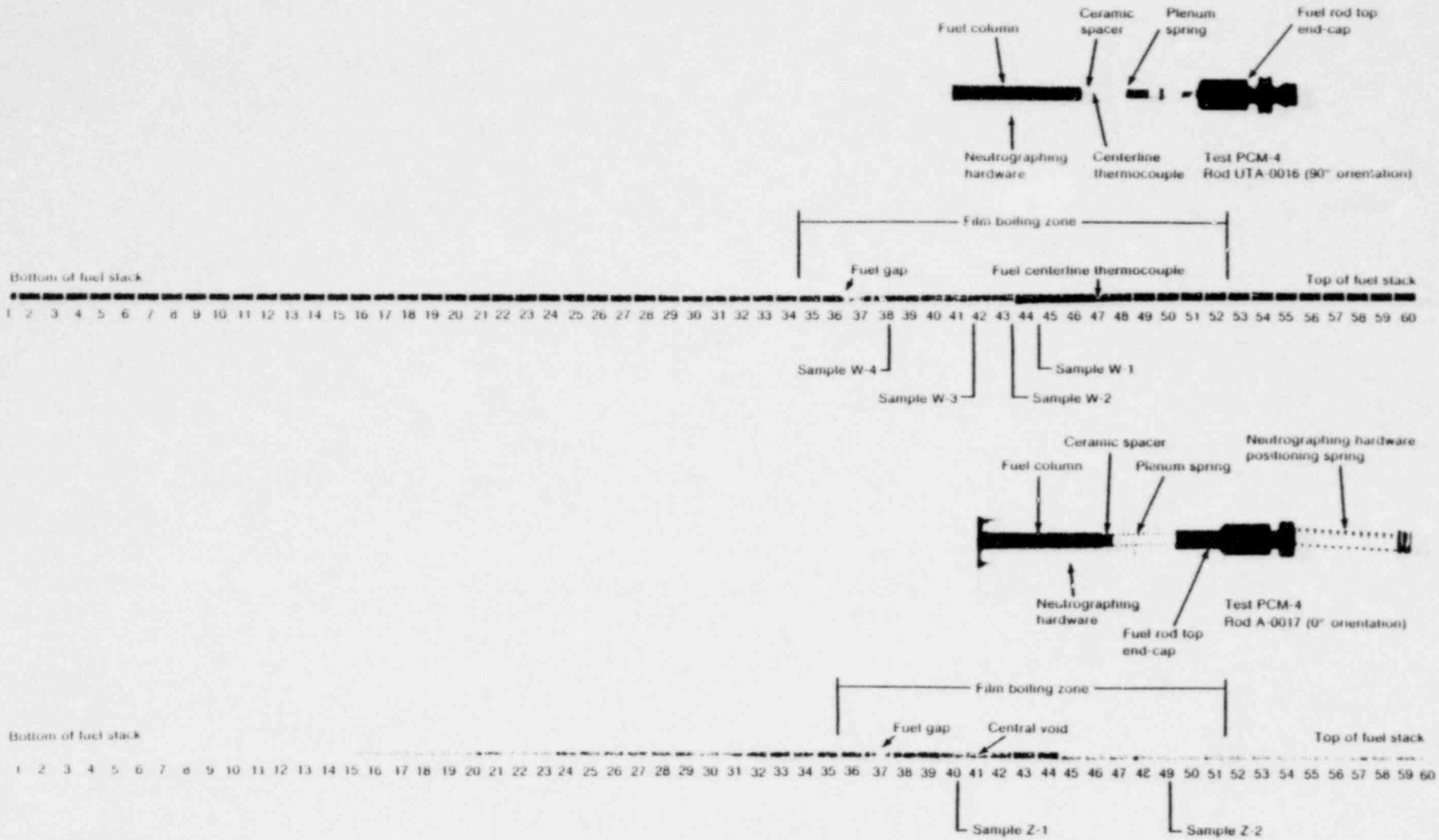

Fig. 10 Composite postfest neutrographs of the fuel stacks of Rods UTA-0016 and A-0017.

TABLE IV

COMPARISON OF FUEL PELLET GAP LOCATION WITH FILM BOILING ZONE

Rod	Pellet Gap Location			Region of Maximum Collapse (m)	Film Boiling Zone Location from Bottom of Fuel Stack (m)
	Pellet Number from Bottom of Stack	Pellet Number From Top of Stack	Distance from Bottom of Stack (m)		
UTA-0014	38	22	0.59	0.55 to 0.65	0.54 to 0.84
UTA-0015	34	26	0.53	0.55 to 0.75	0.50 to 0.84
UTA-0016	35 to 36	25 to 24	0.54 to 0.56	0.60 to 0.70	0.52 to 0.80
A-0017	36	24	0.56	0.55 to 0.75	0.53 to 0.80

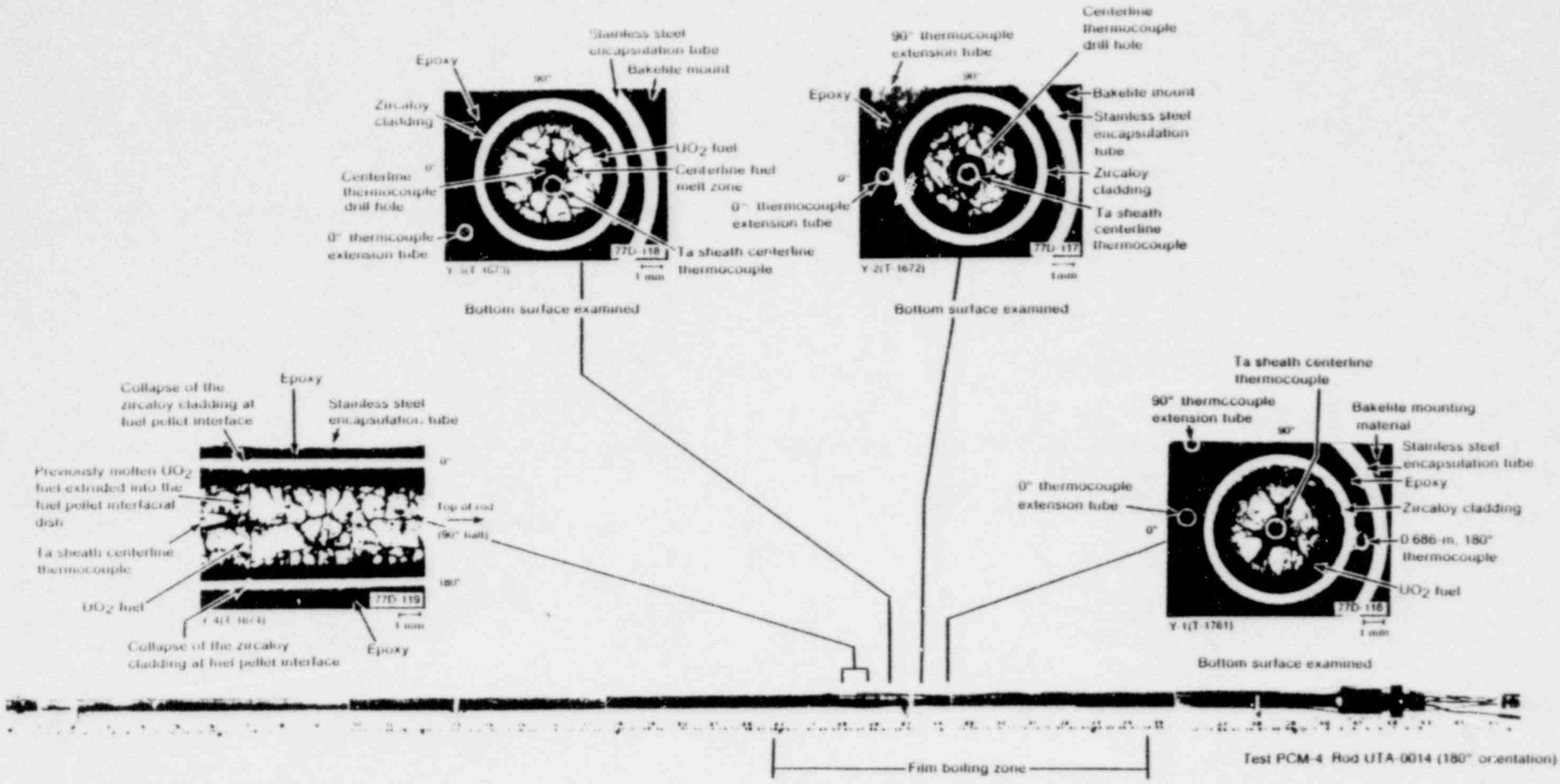

Fig. 11 Overall posttest view of Rods UTA-0014 and UTA-0015.

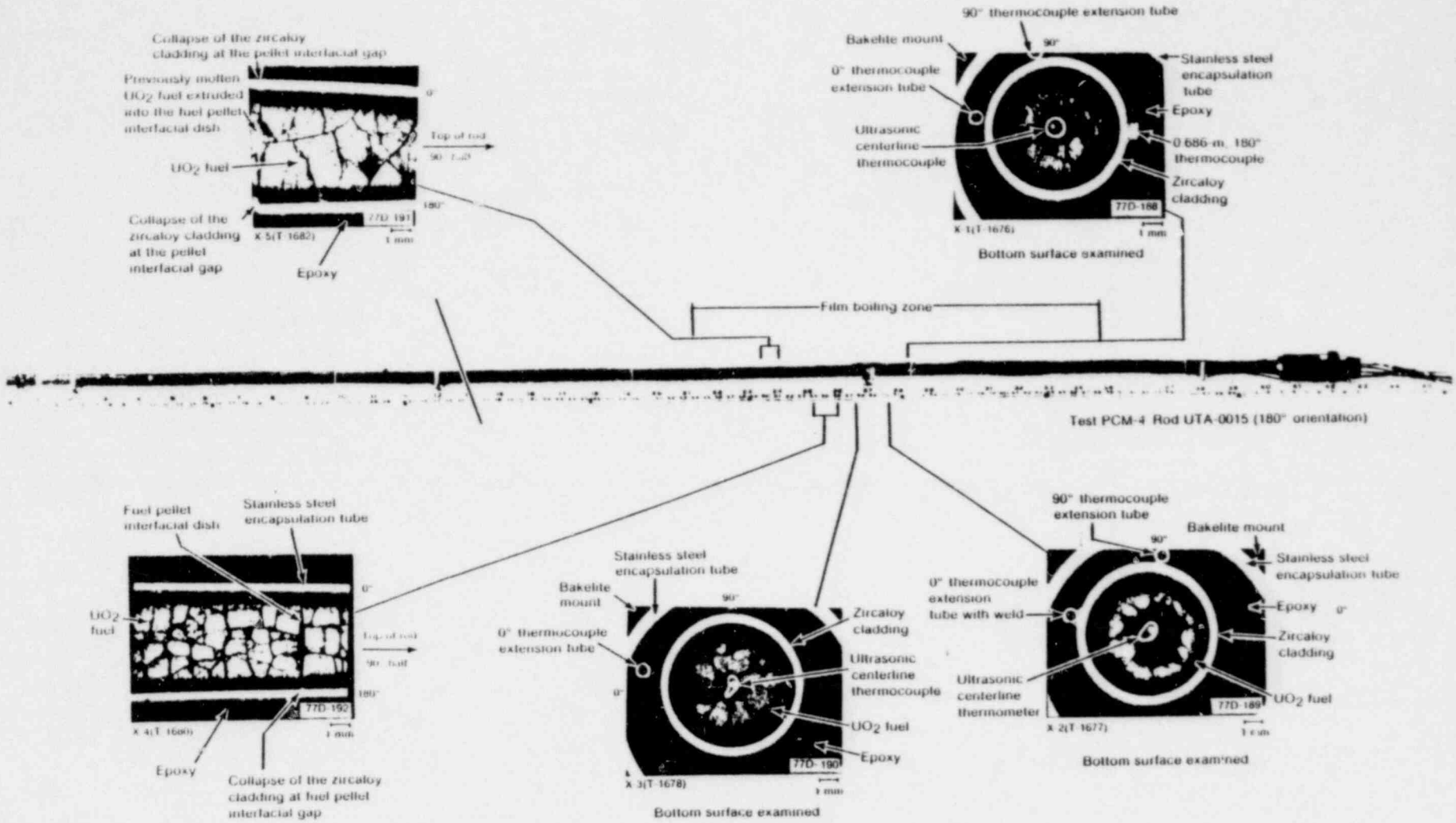

Fig. 11 (continued)

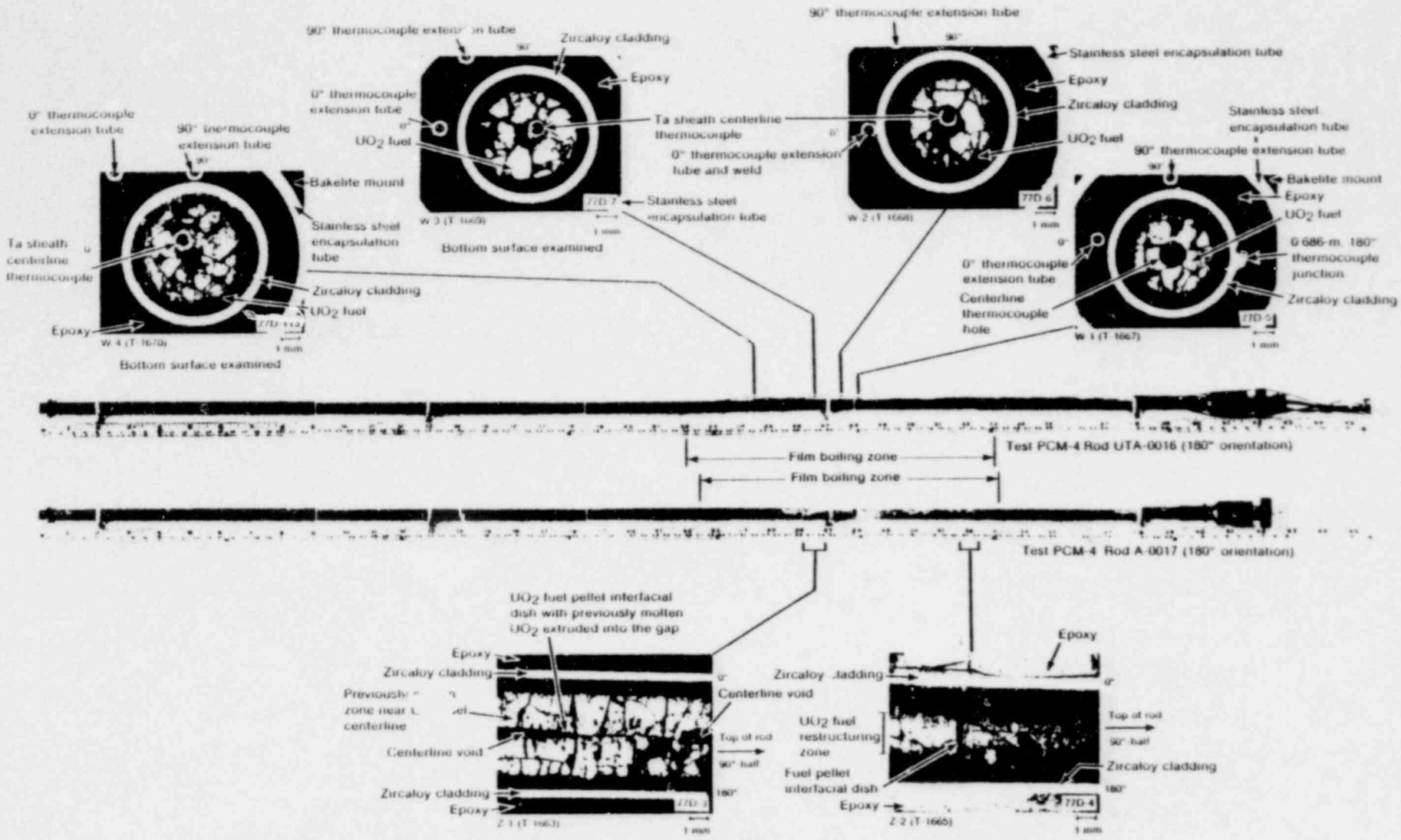

Fig. 12 Overall posttest view of Rods UTA-0016 and A-0017.

Peak and effective cladding temperatures representative of the duration of the transient have been calculated and are presented in the next section.

IV. CLADDING TEMPERATURE DISTRIBUTION

Post-DNB fuel rod cladding phase changes and oxygenation by zircaloy-water reaction and fuel-cladding reaction are processes that influence the cladding ductility. The principal variables controlling these processes are time in film boiling and the cladding temperature.

In-pile measurements of temperatures from cladding thermocouples do not give an accurate indication of film boiling temperatures due to a large ΔT (temperature lowering) associated with a cooling fin effect. The thermocouple responses do give an accurate profile of the temperature changes over the duration of the temperature transient. To obtain the cladding temperature distribution, temperatures were calculated using two methods, both based on parabolic rate law correlations. These calculated temperatures were used to establish circumferential temperatures at selected axial locations along the film boiling zone. (Cladding surface temperature calculations are discussed in detail in Appendix F.)

The two methods used for estimating the cladding surface temperatures were (a) the BUILD5[a] computer code modified to give peak cladding temperatures and (b) an isothermal temperature method which establishes an effective temperature. A constant cladding surface temperature is calculated for the time at temperature in the isothermal temperature method, as distinguished from the modified BUILD5 code which uses a time-dependent temperature representative of the film boiling transient as input. The time-dependent temperatures established by the modified BUILD5 computer code are the best-estimate values of the cladding peak temperature distribution. The isothermal method calculates a single effective temperature to account for the oxidation measured for the total exposure time experienced. The isothermal effective temperature is used in comparing in-pile transient test reaction layer formation (from both zircaloy-water and zircaloy-fuel reactions) with out-of-pile isothermal reaction layer kinetics. The results of the calculations used to estimate the cladding temperature distributions are presented and discussed in the following sections.

1. PEAK CLADDING TEMPERATURES (MODIFIED BUILD5 COMPUTER CODE CALCULATIONS)

Cladding temperatures were only approximately measured during testing since the surface thermocouple junctions, attached at various axial and circumferential positions, protruded into the coolant, effectively acting as cooling fins. The resultant lowering in temperature indicated by the thermocouples was several hundred degrees Kelvin. However, the thermocouples indicated relative time-temperature responses which correspond well

[a] The BUILD5 computer code was developed by R. Pawel at the Oak Ridge National Laboratory, and is based on the mathematical analyses of oxygen diffusion in beta-zircaloy[7,8].

with the linear variable differential transformer (LVDT) length change indications for initiation and termination of the film boiling conditions.

A modified version of the BUILD5 computer code[a] was used to correct these temperatures and establish a best-estimate temperature distribution. Thermocouple time-temperature responses were linearized over segments for input into the modified code. The modified BUILD5 program calculates the buildup of combined thicknesses of oxide and oxygen-stabilized alpha-zircaloy (the ξ-layer) by numerical integration over successive time steps. A series of calculated ξ-layer thicknesses are determined by augmenting the individual temperature response profiles by a multiplicative factor (*FAC). The best-estimate peak cladding temperatures are determined by matching calculated ξ-layer thicknesses with those obtained metallographically. In some cases, only an oxygen-stabilized alpha layer existed and was used for the matching comparison.

Since the test temperature responses are available only from thermocouple locations, approximate responses at other circumferential and axial locations were extrapolated for the analysis from composite thermocouple time-temperature profiles, taking into account the time adjustment for axial progression of film boiling along the rod. The progression of film boiling is indicated by the thermocouple response along each of the instrumented rods. The progression was estimated from the thermocouple responses for the three instrumented rods and the LVDT data for Rod A-0017 (uninstrumented). Plots of film boiling progression and of linearized thermocouple responses and extrapolated curves are presented in Appendix F.

Peak cladding temperatures were calculated for Rods UTA-0014, UTA-0015, UTA-0016, and A-0017, and are plotted in Figures 13, 14, 15, and 16, respectively. The temperatures were plotted isometrically as a function of both the circumferential and axial positions along the rod. Curves have been sketched to connect the 0, 90, 180, and 270° data points for each axial position represented. Dotted line curves were sketched to represent positions where no metallographic data were available for comparison. Locations of the metallurgical mounts and the thermocouple positions are indicated.

The isometric plots of the temperatures in Figures 13, 14, 15, and 16 are presented as the best-estimate representation of the cladding peak temperature distribution along the film boiling zones of the rods. Maximum cladding temperatures of 1620 K (0.600 m), 1700 K (0.606 m), 1740 K (0.667 m), and 1570 K (0.628 m) were calculated for Rods UTA-0014, UTA-0015, UTA-0016, and A-0017, respectively. These peak cladding temperatures are consistent with temperatures inferred from cladding microstructures as indicated in Tables V through VIII for each rod. Variations in temperature along each fuel rod may be interpreted from the contours where lower temperatures associated with the thermocouple positions on the instrumented rods indicate a local cooling fin effect.

---

[a] The modified BUILD5 computer code listing is presented in Appendix F, Table F-XIV.

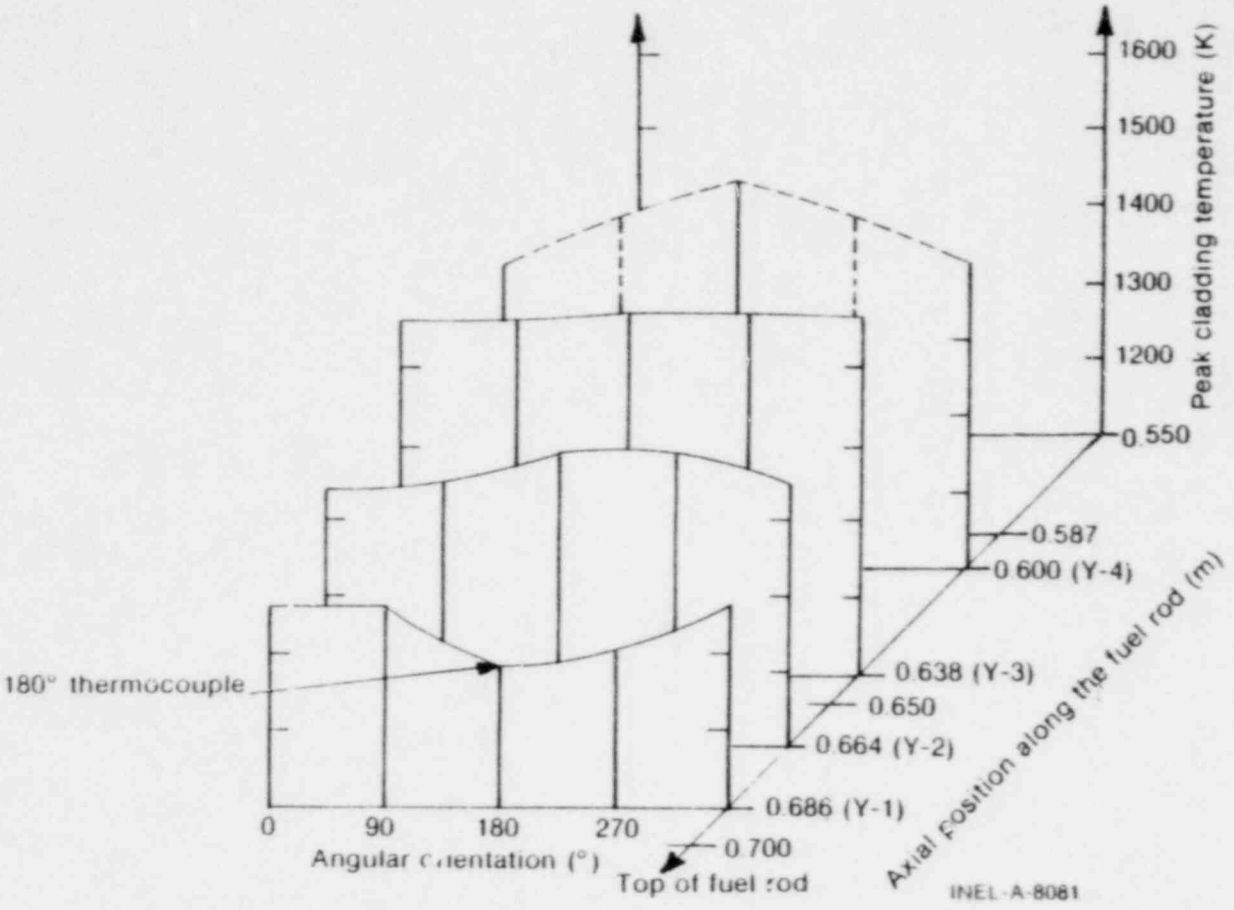

Fig. 13 Isometric plot of the modified BUILD5 peak cladding temperature as a function of angular orientation and axial position for Rod UTA-0014.

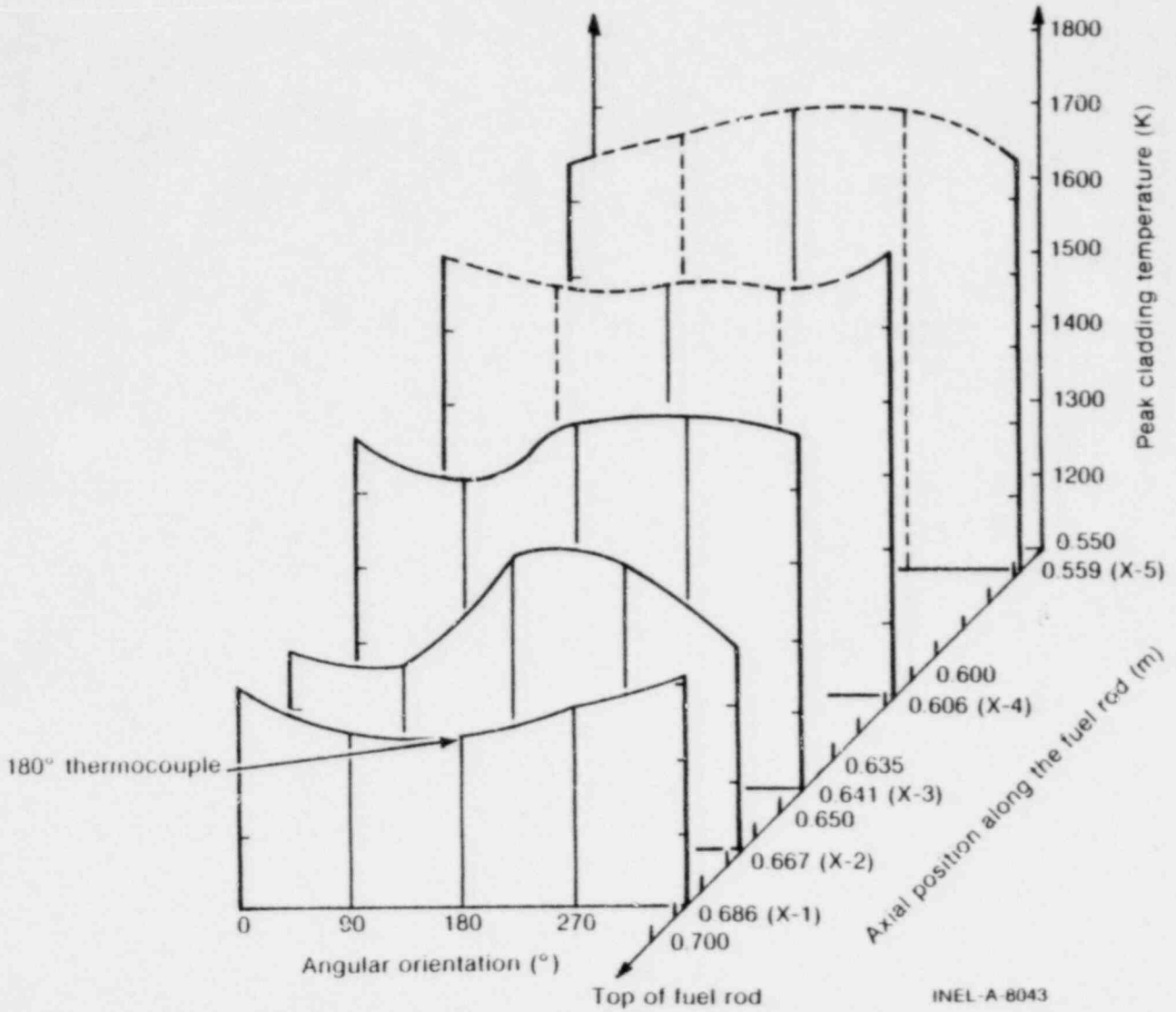

Fig. 14 Isometric plot of the modified BUILD5 peak cladding temperature as a function of angular orientation and axial position for Rod UTA-0015.

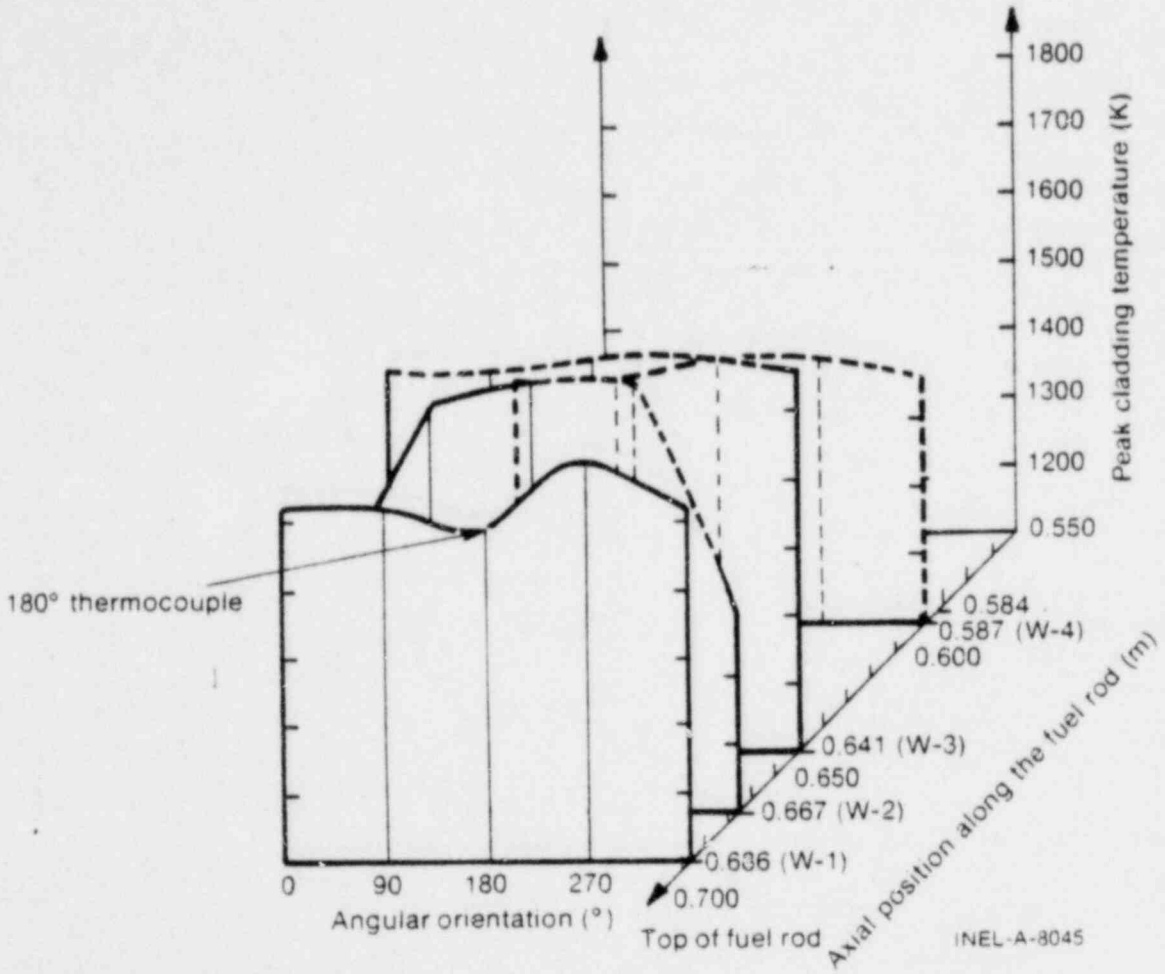

Fig. 15 Isometric plot of the modified BUILD5 peak cladding temperature as a function of angular orientation and axial position for Rod UTA-0016.

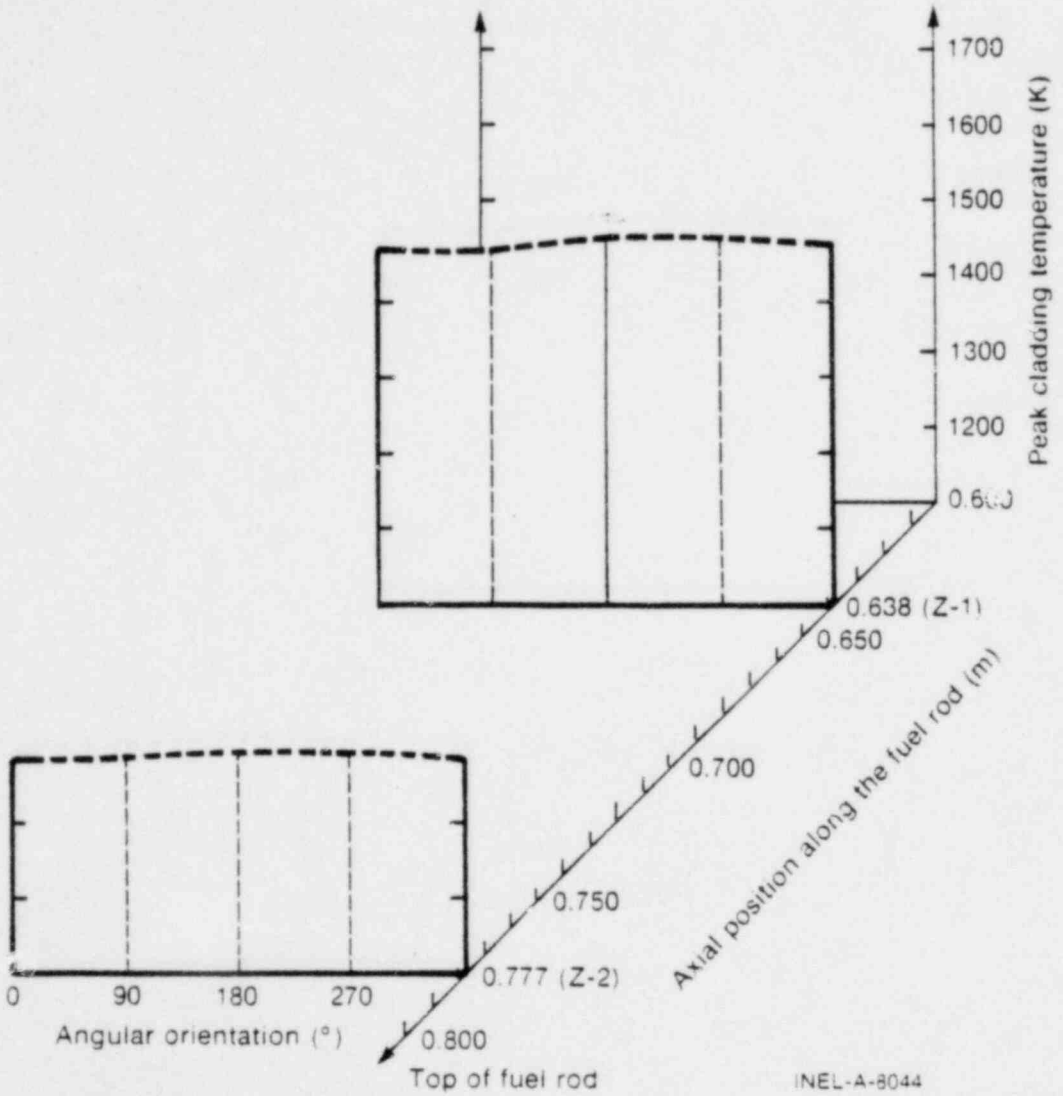

Fig. 16 Isometric plot of the modified BUILD5 peak cladding temperature as a function of angular orientation and axial position for Rod A-0017.

MICROSTRUCTURE KEY FOR TABLES V THROUGH VIII.

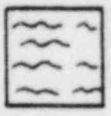

- The 'as-received' stress-relieved microstructure characterized by ropy (stringer) alpha structure

- Transition zone boundary

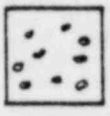

- Recrystallized (equiaxed) alpha-zircaloy

- Transformed prior beta-phase zircaloy

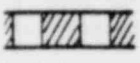

- Oxygen-stabilized alpha-zircaloy

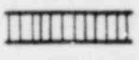

- Surface corrosion (oxide) ZrO_2

- UO_2 fuel pellet

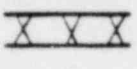

- UO_2-zircaloy duplex interaction layer

INEL-A-8682

TABLE V

OBSERVED MICROSTRUCTURES AND ESTIMATED TEMPERATURES AT VARIOUS LOCATIONS ALONG ROD UTA-0014

Sample	Y-1	Y-2	Y-3	Y-4
Location from bottom of fuel stack (m)	0.686	0.664	0.638	0.600
Cladding microstructure	Prior beta-zircaloy	Prior beta-zircaloy	Prior beta-zircaloy	Prior beta-zircaloy
	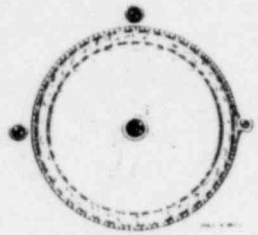	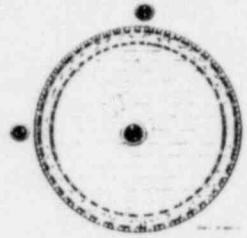	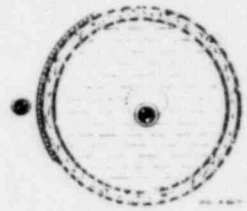	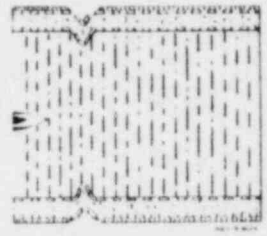
Circumferential cladding temperature range from microstructure (K)	> 1245	> 1245	> 1245	> 1245
Peak temperature[a]				
Maximum (K)	1360	1460	1560	1620
Minimum (K)	1280	1440	1530	1500
Isothermal effective temperature[b]				
Maximum (K)	1290	1390	1460	1480
Minimum (K)	1210	1380	1430	1360

[a] Calculated using the modified BUILD5 computer code.

[b] From extent of oxidation.

TABLE VI

OBSERVED MICROSTRUCTURES AND ESTIMATED TEMPERATURES AT VARIOUS LOCATIONS ALONG ROD UTA-0015

Sample	X-1	X-2	X-3	X-4	X-5
Location from bottom of fuel stack (m)	0.686	0.667	0.641	0.606	0.559
Cladding microstructure	Prior beta- zircaloy	Prior beta with some alpha + beta two-phase zircaloy near 0°	Prior beta-zircaloy	Prior beta-zircaloy	Prior beta-zircaloy
	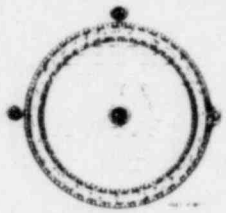	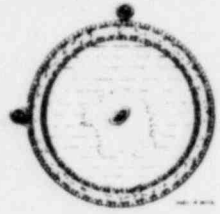	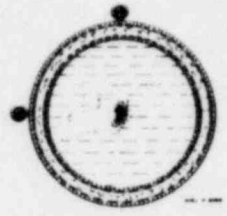	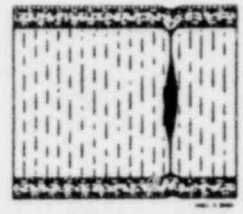	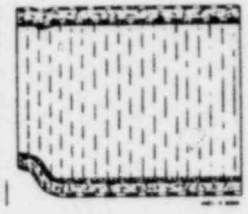
Circumferential cladding temperature range from microstructure (K)	> 1245	1105 < T < 1245 near 0°, > 1245 remainder	> 1245	> 1245	> 1245
Peak temperature[a]					
Maximum (K)	1410	1500	1600	1700	1270
Minimum (K)	1330	1360	1200	1280	1240
Isothermal effective temperature[b]					
Maximum (K)	1340	1430	1520	1620	1600
Minimum (K)	1270	1300[c]	1440	1610	1540

[a] Calculated using the modified BUILD5 computer code.

[b] From extent of oxidation.

[c] The minimum temperature was calculated in association with a position away from 0° and correctly reflects the adjacent prior beta microstructure.

TABLE VII

OBSERVED MICROSTRUCTURES AND ESTIMATED TEMPERATURE AT VARIOUS LOCATIONS ALONG ROD UTA-0016

Sample	W-1	W-2	W-3	W-4
Location from bottom of fuel stack (m)	0.686	0.667	0.641	0.587
Cladding microstructures	Prior beta-zircaloy 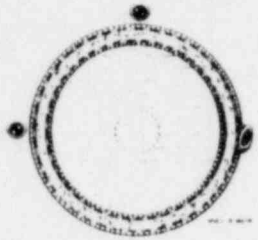	Prior beta-zircaloy 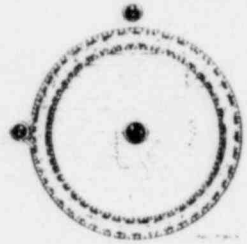	Prior beta-zircaloy 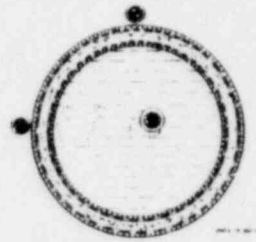	Prior beta-zircaloy 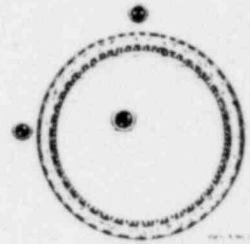
Circumferential cladding temperature range from microstructure (K)	> 1245	> 1245	> 1245	> 1245
Peak temperature[a]				
Maximum (K)	1690	1740	1690	1560
Minimum (K)	1590	1670	1600	1490
Isothermal effective temperature[b]				
Maximum (K)	1410	1490	1520	1450
Minimum (K)	1350	1440	1440	1350

[a] Calculated using the modified BUILD5 computer code.

[b] From extent of oxidation.

TABLE VIII

OBSERVED MICROSTRUCTURES AND ESTIMATED TEMPERATURES AT VARIOUS LOCATIONS ALONG ROD A-0017

Sample	Z-1	Z-2
Location from bottom of fuel stack (m)	0.629	0.768
Cladding microstructures	Prior beta-zircaloy	Alpha + beta zircaloy
	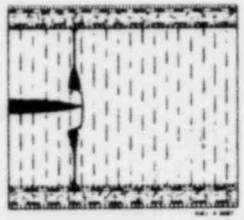	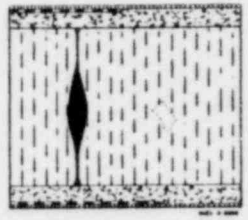
Circumferential cladding temperature range from microstructure (K)	> 1245	1105 < T < 1245
Peak temperatures[a]		
Maximum (K)	1570	1390[c]
Minimum (K)	--	1380[c]
Isothermal effective temperature[b]		
Maximum (K)	1530	1320[c]
Minimum (K)	1520	1310[c]

[a] Calculated using the modified BUIL05 computer code.

[b] From extent of oxidation.

[c] These values are inconsistent with the existing microstructures observed in the cladding. The cladding exhibits hydrogen-modified alpha-zircaloy.

7. ISOTHERMAL EFFECTIVE TEMPERATURE CALCULATIONS

Isothermal effective temperatures were calculated for all four test fuel rods using the oxide, oxygen-stabilized alpha, and ξ layers for comparison with embrittlement results and microstructural estimates of the cladding temperature. These calculations utilized corrected film boiling times for each axial location along the rods to account for the progession of film boiling (Appendix F). The results are presented isometrically in Figures 17, 18, 19, and 20 for Rods UTA-0014, UTA-0015, UTA-0016, and A-0017, respectively. Maximum isothermal effective temperatures of 1480 K (0.600 m), 1620 K (0.606 m), 1490 K (0.667 m), and 1530 K (0.628 m) were calculated for Rods UTA-0014, UTA-0015, UTA-0016, and A-0017, respectively. The general contour features are very similar to those of the peak temperatures plotted from the modified BUILD5 calculations (Figures 13-16).

The results are generally consistent with microstructurally estimated temperatures as observed from Tables V through VIII. Calculational methods are discussed and the results are presented in Appendix F.

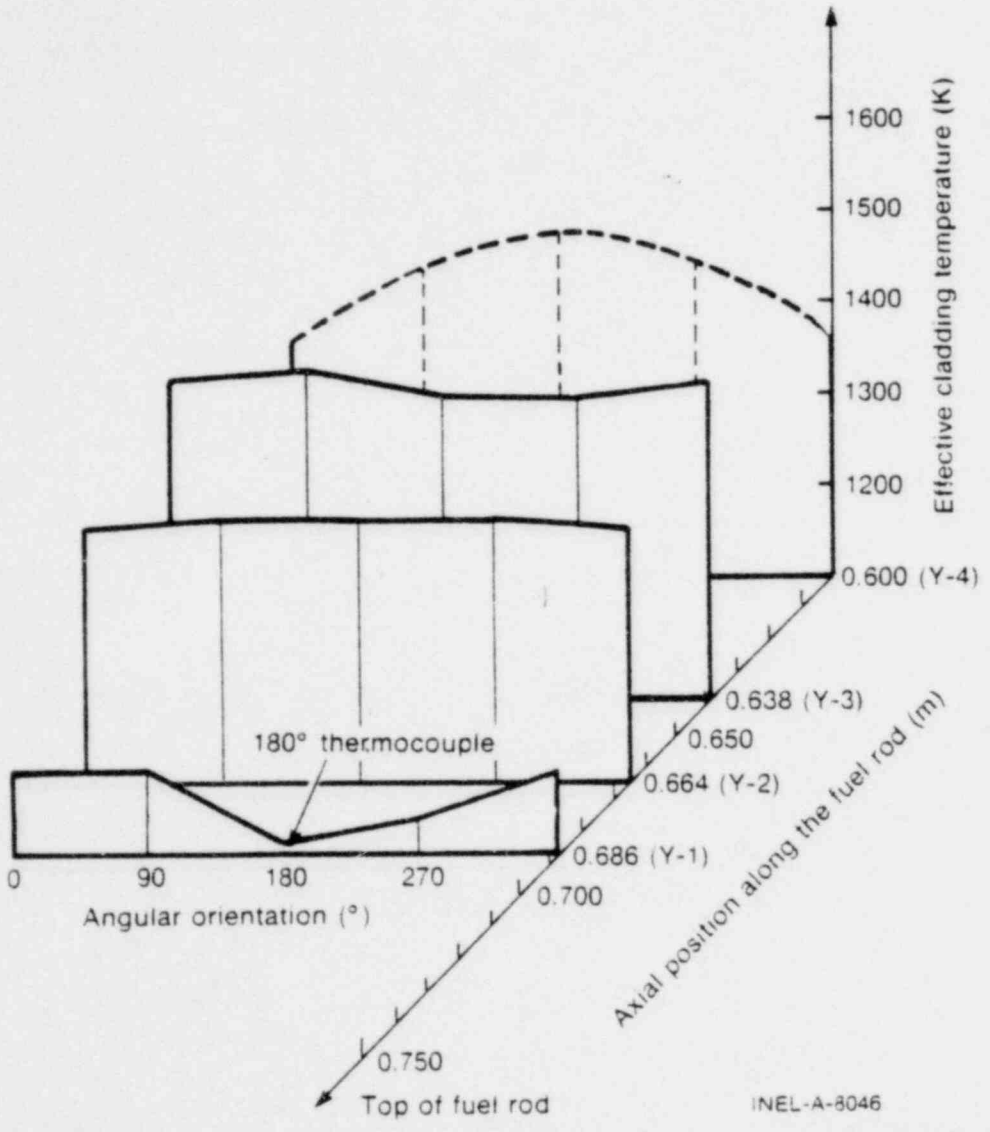

Fig. 17 Isometric plot of the isothermal effective cladding temperature as a function of angular orientation and axial position for Rod UTA-0014.

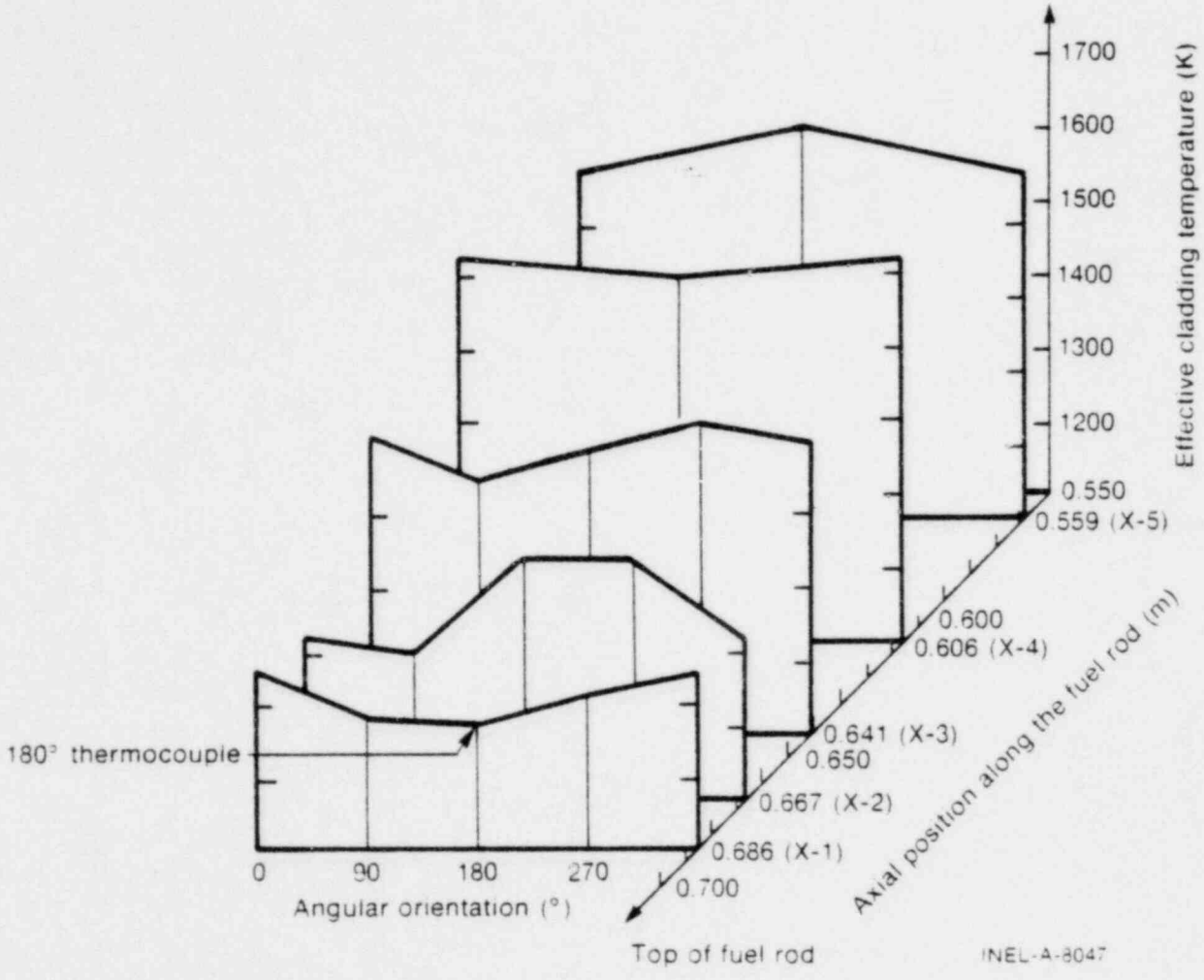

Fig. 18 Isometric plot of the isothermal effective cladding temperature as a function of angular orientation and axial position for Rod UTA-0015.

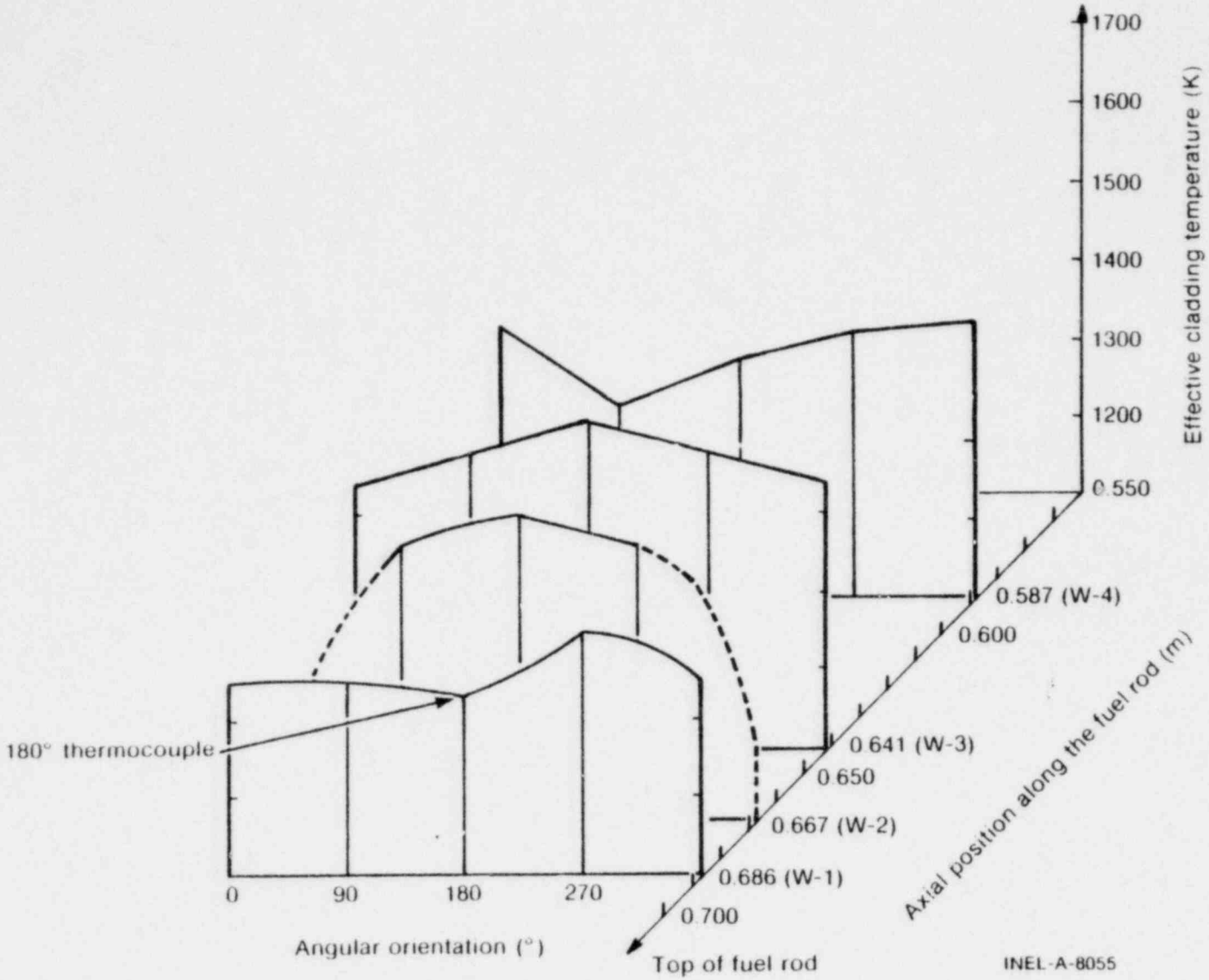

Fig. 19 Isometric plot of the isothermal effective cladding temperature as a function of angular orientation and axial position for Rod UTA-0016.

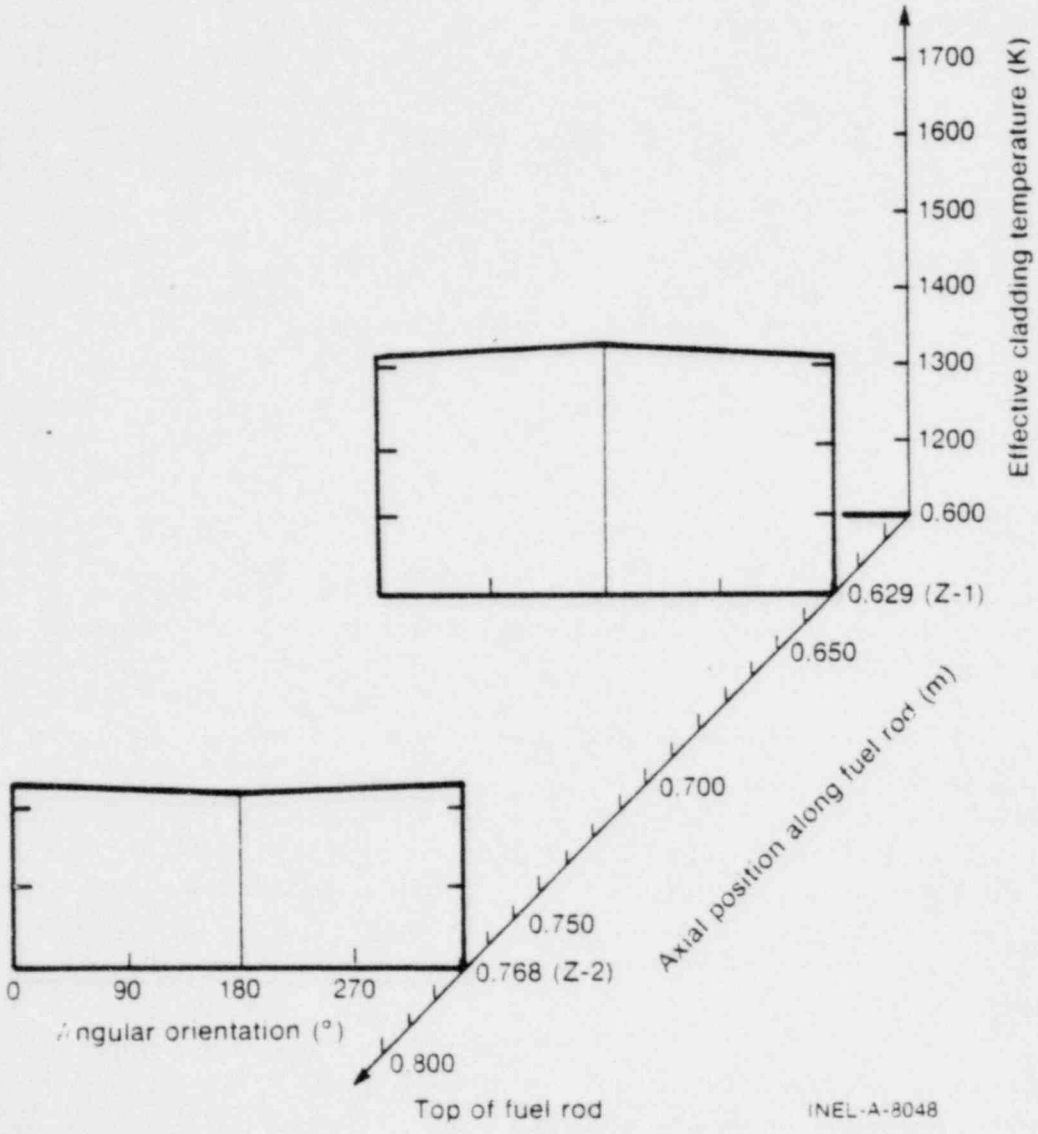

Fig. 20 Isometric plot of the isothermal effective cladding temperature as a function of angular orientation and axial position for Rod A-0017.

V. CLADDING DEFORMATION

Cladding geometry changes (primarily collapse, waisting, and bowing) occur at the high temperatures associated with the film boiling transient due to the temperature dependence of the fuel and cladding mechanical properties. The cladding deformations discussed in this section are postulated to have occurred relatively early in the film boiling transient. Previous tests have indicated that deformation can occur in recrystallized alpha material ($T \sim 920$ K)[3]. Later, under sustained high temperatures, oxidation stengthens and embrittles the cladding, thus impeding deformation. Characterization of cladding geometry changes is important to evaluating the FRAP-T (Fuel Rod Analysis Program-Transient) computer code[9], which is used for predicting fuel rod response under transient conditions. External cladding geometry changes associated with Test PCM-4 and summarized in this section are collapse along the film boiling zone, and rod bowing.

1. CLADDING COLLAPSE

All four fuel rods exhibited a region of collapse, as determined from posttest diametral measurements (Appendix C), in the high temperature zone ($T > 920$ K), located about midlength along each rod.

The outside diameter measurements of each fuel rod are plotted versus the fuel column length in Figure 21 for Rod UTA-0014, Figure 22 for Rod UTA-0015, Figure 23 for Rod UTA-0016, and Figure 24 for Rod A-0017. The pretest outside cladding diameter of each rod was nominally 10.7 mm and the diametral gap between the fuel and the cladding was 0.2 mm. These values may be compared with the posttest values resulting from collapse of each fuel rod. The reduction in diameter is approximately the same (nominally 93% diametral cold gap closure) for all four rods, as seen in Table IX.

The diameter reduction in Rods UTA-0014 and A-0017 was somewhat ovular, being eccentric, or elliptical, across the diameter in the regions of collapse. The ovality (maximum outer diameter/minimum outer diameter) for these rods was nominally 1.003 outside the collapse region and 1.007 within the collapse zone. The diameters were more uniform along the regions of maximum collapse; however, local peaks occurred near the center of the film boiling zone in Rod A-0017. Rod UTA-0015 has an ovality of 1.007 only near the center of the collapse zone, varying to 1.003 outside the collapse region. Similar results were found for Rod UTA-0016.

Cladding waisting (collapse into the fuel pellet interfacial gaps) occurred in Rod UTA-0014 between 0.58 and 0.76 m from the bottom of the fuel stack, which was over 60% of the extent of the collapse zone. For Rod UTA-0015, waisting was observed over 79% of the collapse zone, from 0.52 to 0.81 m. Cladding waisting was the most pronounced in Rod UTA-0016. It occurred from 0.54 to 0.76 m, and encompassed 79% of the collapse

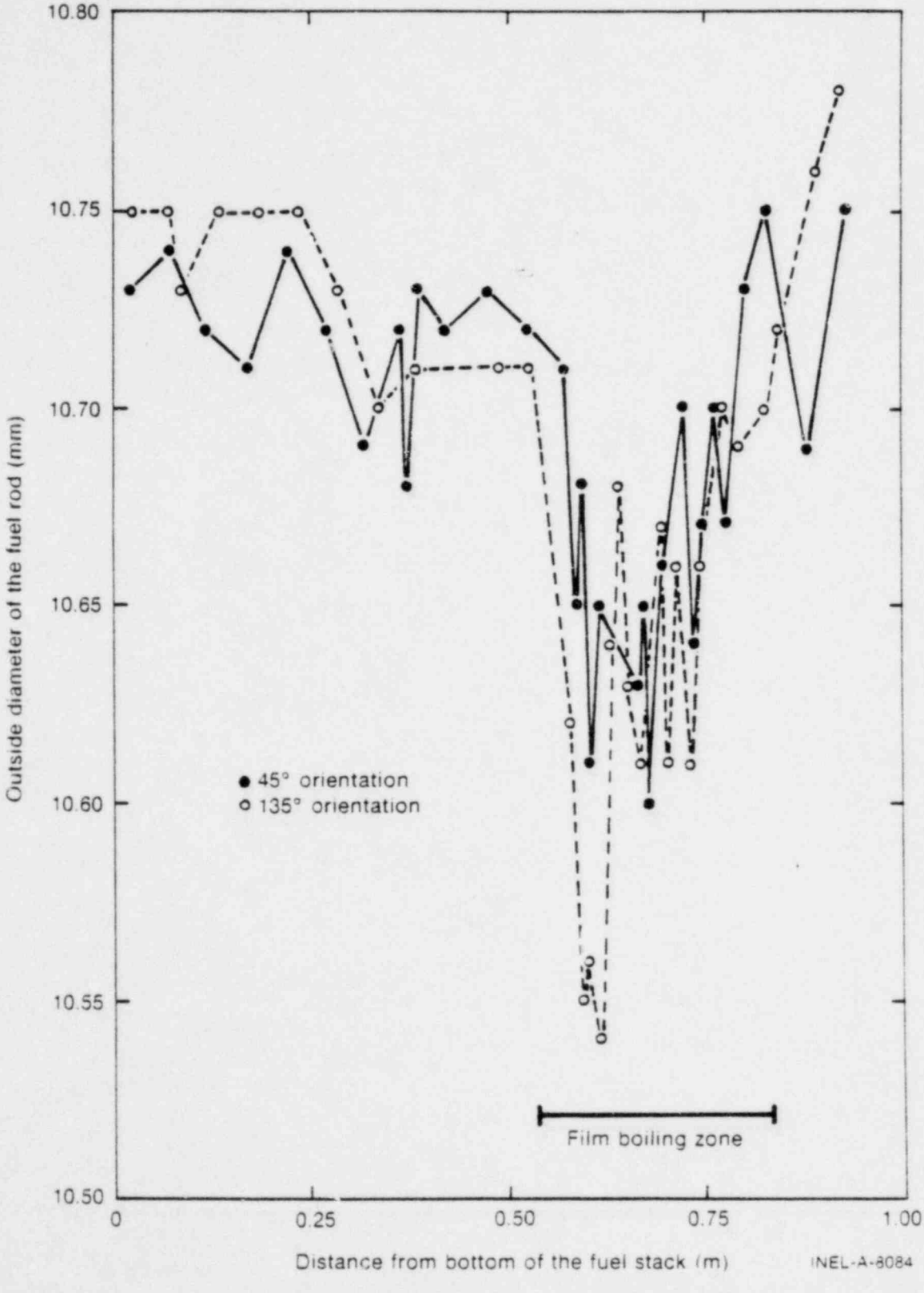

Fig. 21 Diametral measurements of collapse for Rod UTA-0014.

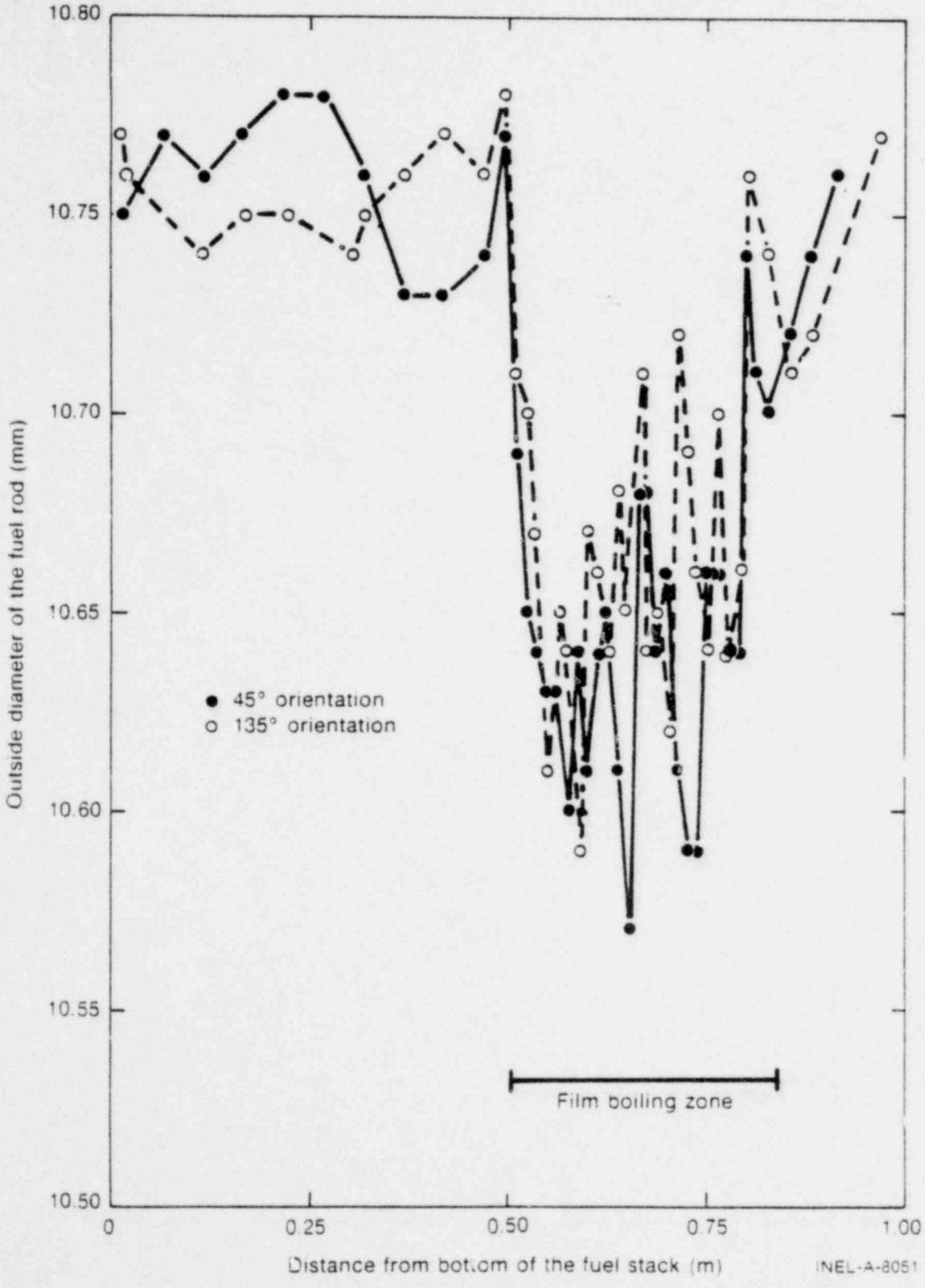

Fig. 22 Diametral measurements of collapse for Rod UTA-0015.

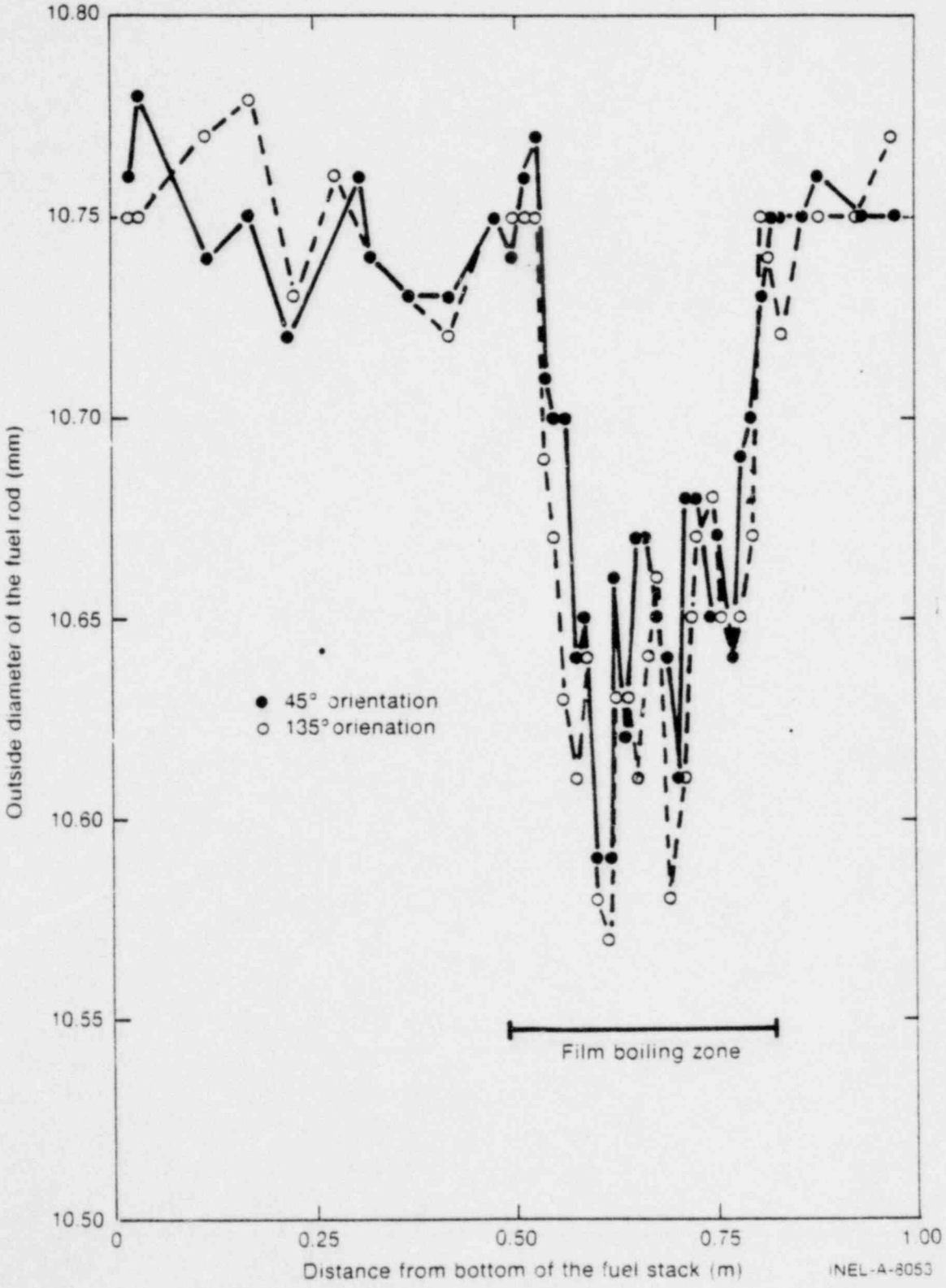

Fig. 23 Diametral measurements of collapse for Rod UTA-0016.

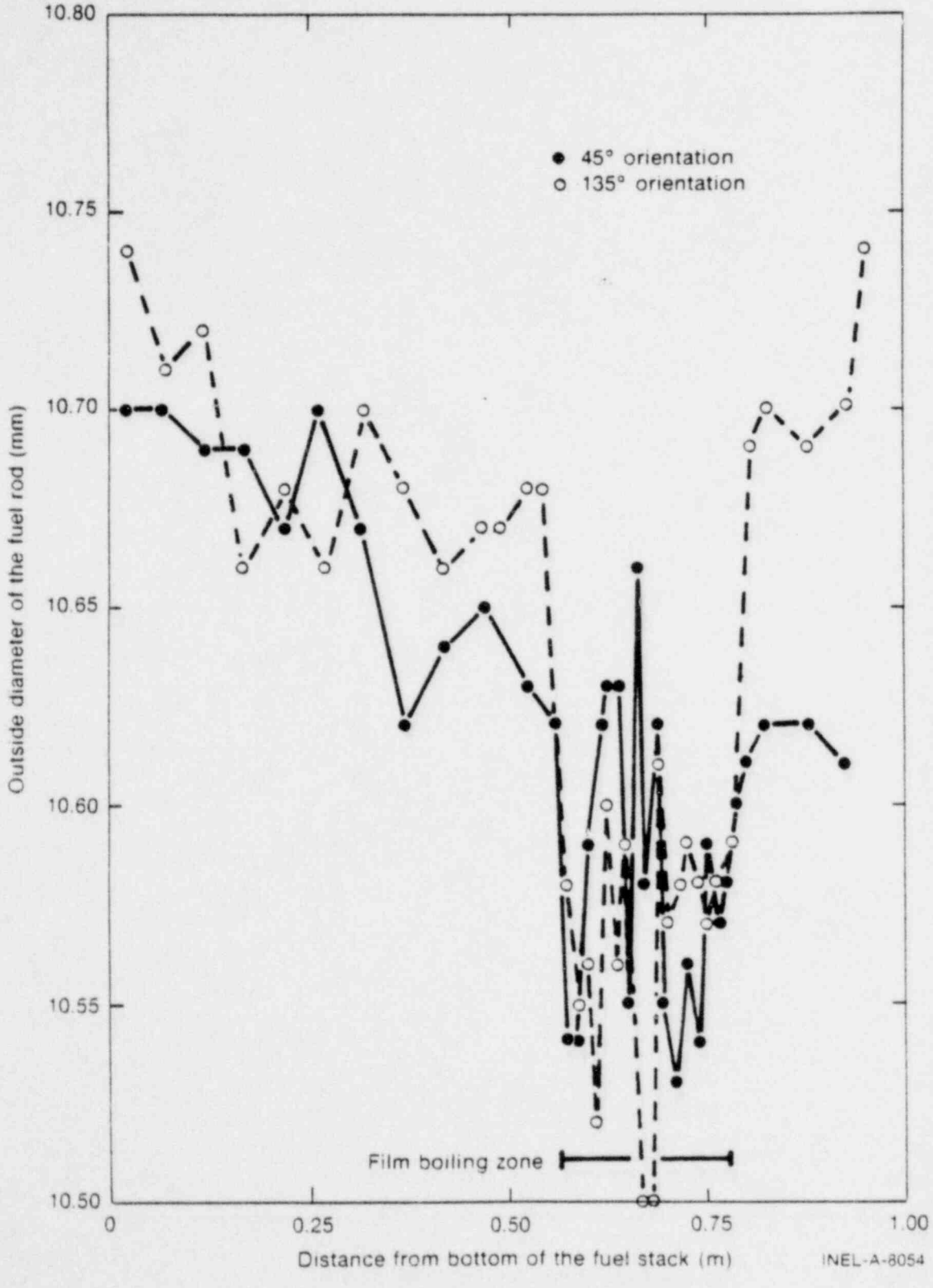

Fig. 24 Diametral measurements of collapse for Rod A-0017.

TABLE IX

AXIAL EXTENT OF FUEL ROD DIAMETER REDUCTION

Rod	Extent of Collapse[a] (m)	Magnitude of Maximum Collapse (mm)	Portion of Fuel-Cladding Gap Closed (%)	Location of Maximum Collapse (m)
UTA-0014	0.54 to 0.84	0.17	85	0.55 to 0.65
UTA-0015	0.50 to 0.84	0.20	100	0.55 to 0.75
UTA-0016	0.52 to 0.80	0.18	90	0.60 to 0.70
A-0017	0.53 to 0.80	0.19	95	0.55 to 0.75

[a] These axial positions are referenced with respect to the bottom of the fuel stack, which is 35 mm above the bottom of the fuel rod.

zone. Waisting was observed at only two interfaces in Rod A-0017, near 0.69 m. Since Rods UTA-0014 and A-0017 operated at approximately the same temperatures ($\Delta T \sim 50$ K) the difference in the amount of waisting observed may be due to the higher prepressurization of Rod A-0017 (3.79 MPa, compared with 2.59 MPa for the other three rods), giving a smaller differential pressure between the system overpressure and rod internal pressure during the test. A similar effect was noted in Test PCM-3[6].

The measured posttest void volumes for Rods UTA-0014, UTA-0015, UTA-0016, and A-0017 were 9.3, 9.6, 9.2, and 7.2 x 10^{-6} m^3, respectively, with a measurement uncertainty of $\pm 0.2 \times 10^{-6}$ m^3. These values compare favorably to measured pretest values of 9.6 ± 0.3, 9.0 ± 0.3, 8.8 ± 0.3, and $7.2 \pm 0.3 \times 10^{-6}$ m^3. Even though certain of these measurements indicate a small void volume change, uncertainties in the calculational and measurement methods preclude a critical analysis of the changes.

Rod A-0017 was laser punctured and the internal fill gas was collected and analyzed. No significant gaseous fission products were detected to have built up as a result of the test. The gas composition is presented in Table X. Rod A-0017 was internally pressurized pretest to 3.79 ± 0.07 MPa, with a nominally 90% He and 10% Ar mixture. The total posttest gas collected, at standard temperature and pressure, was $237.0 \pm 2.4 \times 10^{-6}$ m^3. The posttest gas volume together with the void volume gives a calculated rod pressure of 3.34 ± 0.10 MPa. Although the posttest rod pressure had decreased from the original value, there was no indication that this rod leaked. No drop in pressure due to void volume change was detected; the pre- and posttest void volumes were identical. The discrepancy apparently resulted from uncertainties in the fill gas volume or pretest pressure, or both.

TABLE X

FILL GAS ANALYSIS FOR ROD A-0017

Elemental gas constituents	H_2	He	$CO + N_2$	O_2	Ar	CO_2	Kr	Xe
Analysis (mean concentration) (mole %)	<0.01	93.23	0.03	<0.01	6.72	0.01	<0.01	0.01

2. CLADDING BOWING

Estimates of the magnitude and direction of free bowing were made for all four fuel rods. Figure 25 shows a schematic representation (not to scale) of the bowing observed for each rod. The orientation of the in-pile tube test assembly is referenced with respect to the reactor core. The rod bow was characterized by centerline free deflection. Skew was noted visually, using the 0 to 90° right-hand symmetry indicated in the schematic when viewing the rod from the top-end, down along the rod length. The arrow in the figure indicates the direction of maximum measured posttest end displacement of the fuel rod from the centerline as a result of bowing. The fuel rods (10.7-mm diameter) were retained in the 16.3-mm inside diameter flow shroud by positioning screws at 0.21 and 0.84 m from the bottom of the rod, and they bowed inside the shroud between these points during testing. The positioning screws prevented the rods from bowing against the flow shroud wall.

Rods UTA-0014 and A-0017 displayed no observable bowing. Rod UTA-0015 was bowed parallel to the 0 to 180° plane with the side displacement of the bottom end of the rod in the 0° direction. The smoothly curved free bow extended from 0.61 m to the top of the rod, and had a maximum estimated free deflection of 10 mm, which is more than can be accommodated by the flow shroud. The bow of Rod UTA-0016 extended from 0.46 to 0.71 m, parallel to the 0 to 180° plane. The maximum lateral deflection of the bottom end of the rod (in the 180° direction) was estimated to be 5 mm, which is about half the amount noted in Rod UTA-0015.

The magnitude of skewing associated with bowing was not quantified for these rods, although the observed bowing did exhibit some skew toward the bottom ends. Since the severity of the bowing within the shrouds is unknown during film boiling, insufficient information was obtained from posttest measurement to allow a detailed evaluation of the effect of bowing on coolant flow conditions.

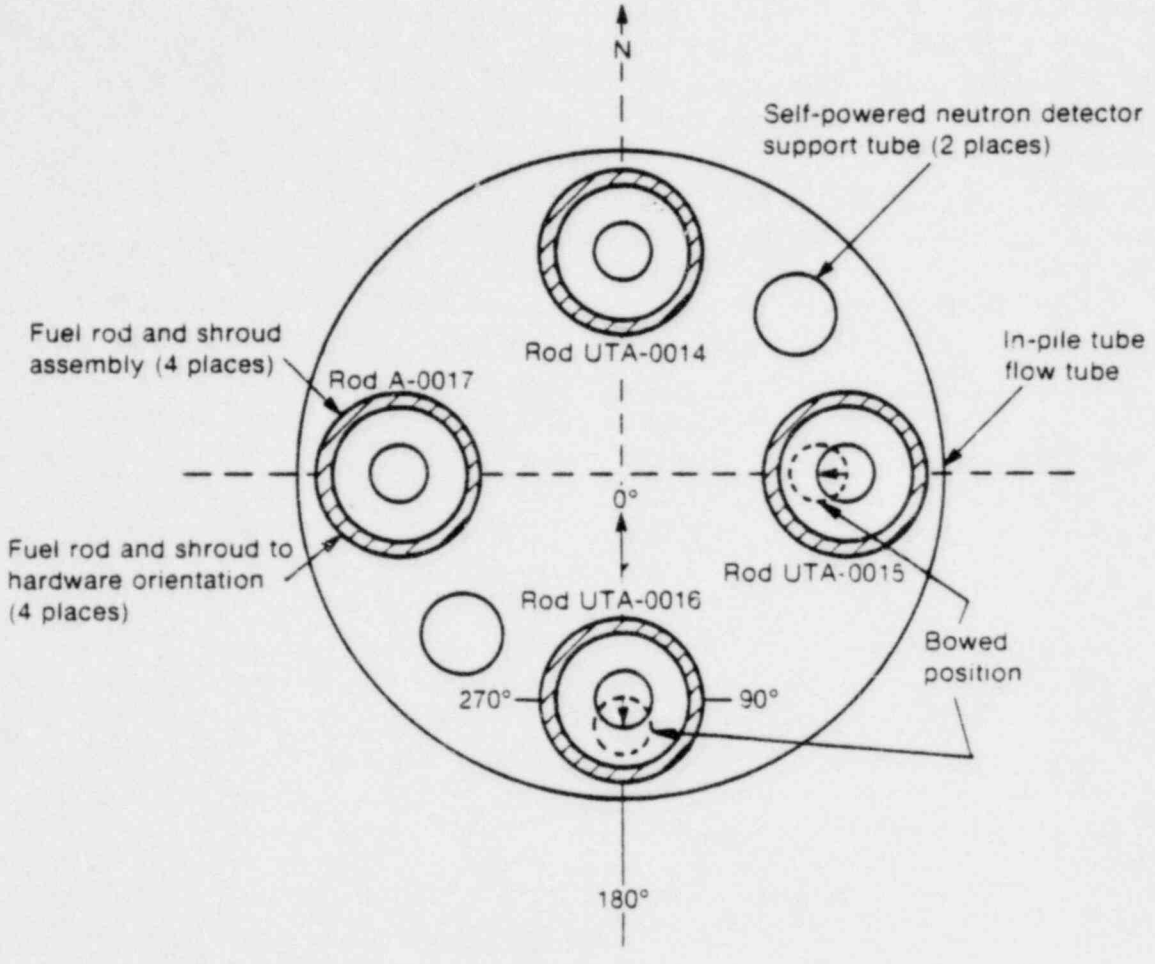

Fig. 25 Fuel rod bowing schematically illustrated for Test PCM-4.

VI. CLADDING CHEMICAL REACTION

The elevated temperatures which occur during film boiling operation induce several forms of cladding chemical reactions. The exterior cladding surface oxidizes as a result of the zircaloy-steam reaction. The oxidation is characterized by development of surface oxide layers and the formation of an oxygen-stabilized alpha-zircaloy layer in cladding material which has transformed to beta-phase zircaloy ($T > 1245$ K). Oxidation reactions may also be found on the inner cladding surface as a result of reactions between the zircaloy cladding and the UO_2 fuel. Hydrogen uptake may also accompany the zircaloy-steam interaction in which free hydrogen may be developed from the film boiling steam blanket.

Oxygen diffusion from the UO_2 into the beta-phase zircaloy occurs, inducing an inner cladding surface layer transformation to oxygen-stabilized alpha-zircaloy. Frequently, when the fuel and cladding are in contact at high temperature, a duplex reaction layer, formed from UO_2-zircaloy reaction, will develop together with the oxygen-induced transformation of beta-phase material to oxygen-stabilized alpha-zircaloy. No duplex reaction layer will form near the beta transformation temperature ($T \sim 1245$ K), for the transient film boiling times represented here, and none will form if ZrO_2 is present on the cladding inner surface. The duplex layer consists of a uranium-rich layer adjacent to the cladding and a zirconium-rich layer adjacent to the fuel[5]. The various reaction layers are characterized in the following sections. Representative examples only are presented; a complete description is contained in Appendix D. Cladding embrittlement from oxidation is assessed and discussed. The effects of hydrogen uptake are characterized in this section primarily as microstructural variations, with hardening indistinguishable from the oxygen embrittlement.

1. CHARACTERIZATION OF CLADDING REACTION LAYERS

Extensive external ZrO_2 buildup on the exterior of the zircaloy cladding of all the test fuel rods was observed. Thin black oxide (< 10 μm) formed outside the film boiling zone. Thicker, multilayered (up to 46 μm) grey-to-white oxide films were found in samples cut from the film boiling region. Similar thicknesses of oxygen-stabilized alpha layers were also found inside the cladding at both the inner and outer cladding surfaces. Such reaction layers are typical of the film boiling zones of the Test PCM-4 fuel rods and are characterized below. Detailed reaction layer thicknesses measured from cladding samples of the test fuel rods are presented in Appendix F.

1.1 Zircaloy-Water Reaction

Thick oxide layers of the type observed on all the metallurgical samples taken from the film boiling zones of Test PCM-4 fuel rods are illustrated in Figure 26. The multilayered oxide illustrated has a grey-to-white appearance in cross section (peak cladding temperature about 1590 K). Cyclic film boiling conditions as a result of either cyclic testing or variations

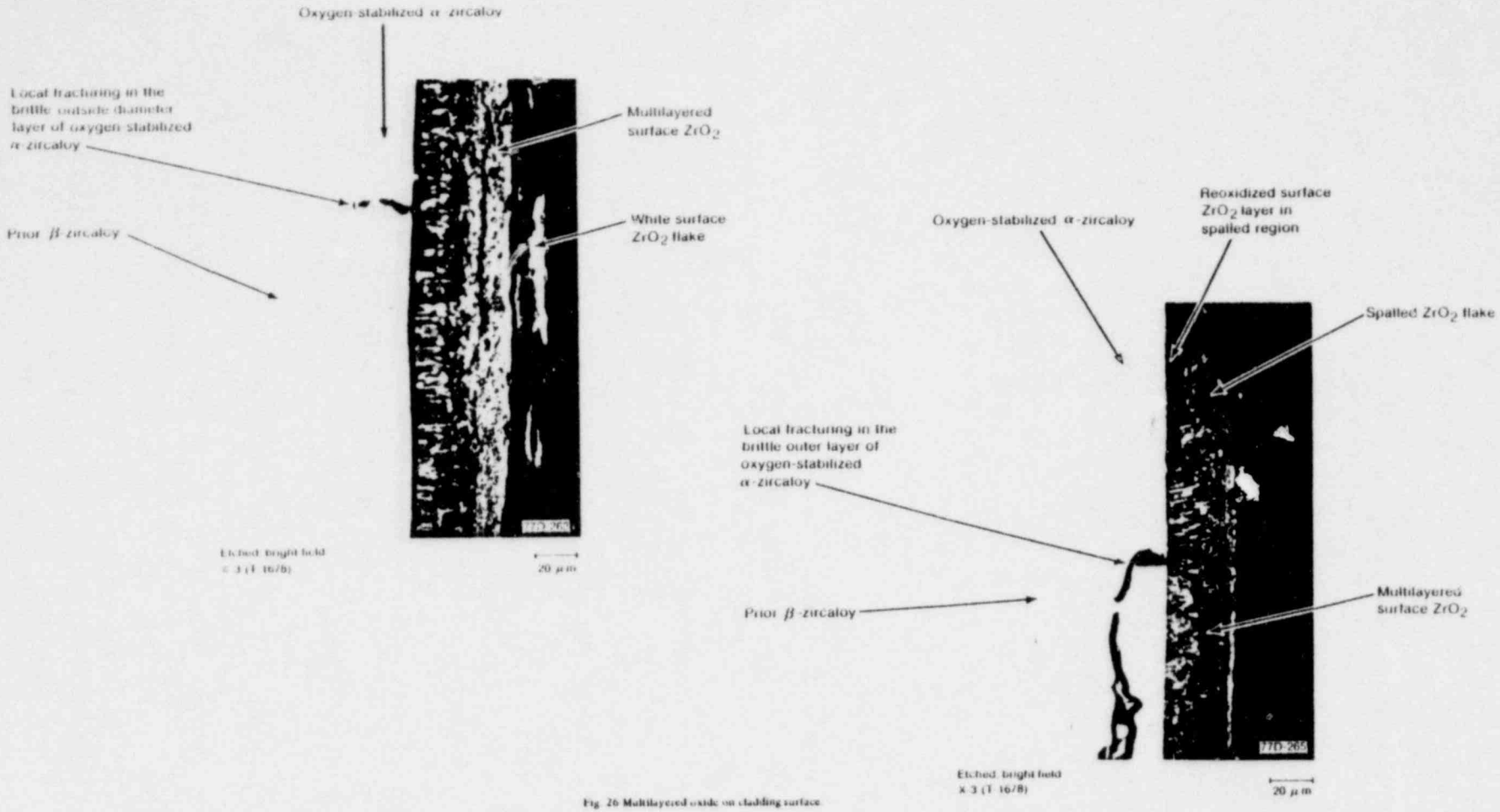

Fig. 26 Multilayered oxide on cladding surface

associated with transition film boiling modes may induce the multiple layer formation. Such oxide layers fracture and spall with laminar separation when mechanically stressed. Examples of the surface oxide spalling are illustrated in Figures 27 and 28. Locally anomalous corrosion (nodular) and oxide layer growth at surface defects and layer disturbances were observed, similar to that found in previous PCM tests[6], but are not illustrated here. Hydriding of the alpha material at prior beta grain boundaries was also observed as illustrated in Figure 28.

A remnant flake of surface ZrO_2 was observed in the collapse indentation as illustrated in Figure 29. The collapse into the gap between fuel pellets occurred prior to significant oxidation, and the ZrO_2 film follows the identation contour. Electron microprobe analysis of the multilayer oxide flake indicates detectable levels of Sn in the oxide layers (Appendix D). The surrounding oxide coating at the collapse shoulders spalled off as a result of mechanical stressing, probably associated with cooldown of the rod following testing. Cladding oxidation is characterized by the development of outer and inner diameter bands of oxygen-stabilized alpha-zircaloy at the periphery of the prior beta field as shown in Figure 29.

1.2 Fuel-Cladding Reaction

The oxygenation-induced beta-phase to alpha-phase transformation is often accompanied by the formation of an intermetallic zone at the fuel-cladding interface where contact is maintained during film boiling operation. The region of such contact has been identified in previous tests as the length of cladding near rod midlength which experiences collapse[3,5,6]. The intermetallic zone has been identified from both in-pile[3,5] and out-of-pile[10,12] tests as a uranium-zirconium two-phase alloy. Grossman and Rooney[10] identified δ-UZr_2 plus a solid solution of γ-U and beta-zircaloy within the two-phase metallic layer at the fuel-cladding interface at 1263 K for a long anneal of 144 hours. The zirconium-uranium dioxide reaction was studied by Mallett[11,12], who identified two metallic layers as the result of U-Zr interdiffusion accompanied by alpha-phase formation in the oxygenated zirconium. Between 970 and 1400 K, reaction bands form, beginning in the fuel, and cross the interface to form

$$[UO_2] \rightarrow [\alpha\text{-}Zr(O) + \alpha\text{-}U]\ \text{Zr-rich} \rightarrow$$

$$[U\ (\alpha\text{-}U\ \text{when heated near 1400 K and}\ \delta\text{-}UZr_2\ \text{when heated near}$$

$$1000\ K) + \alpha\text{-}Zr(O)]\ \ \text{U-rich} \rightarrow [\alpha\text{-}Zr(O)] \rightarrow [\beta\text{-}Zr] \qquad (1)$$

reaction layers at the fuel-cladding interface. Hofmann[13] reported reaction layers in the form

$$UO_2 \rightarrow [\alpha\text{-}Zr(O)] \rightarrow [U\ \text{or}\ (U, Zr)\ \text{alloy}] \rightarrow [\alpha\text{-}Zr(O)] + [\beta\text{-}Zr] \qquad (2)$$

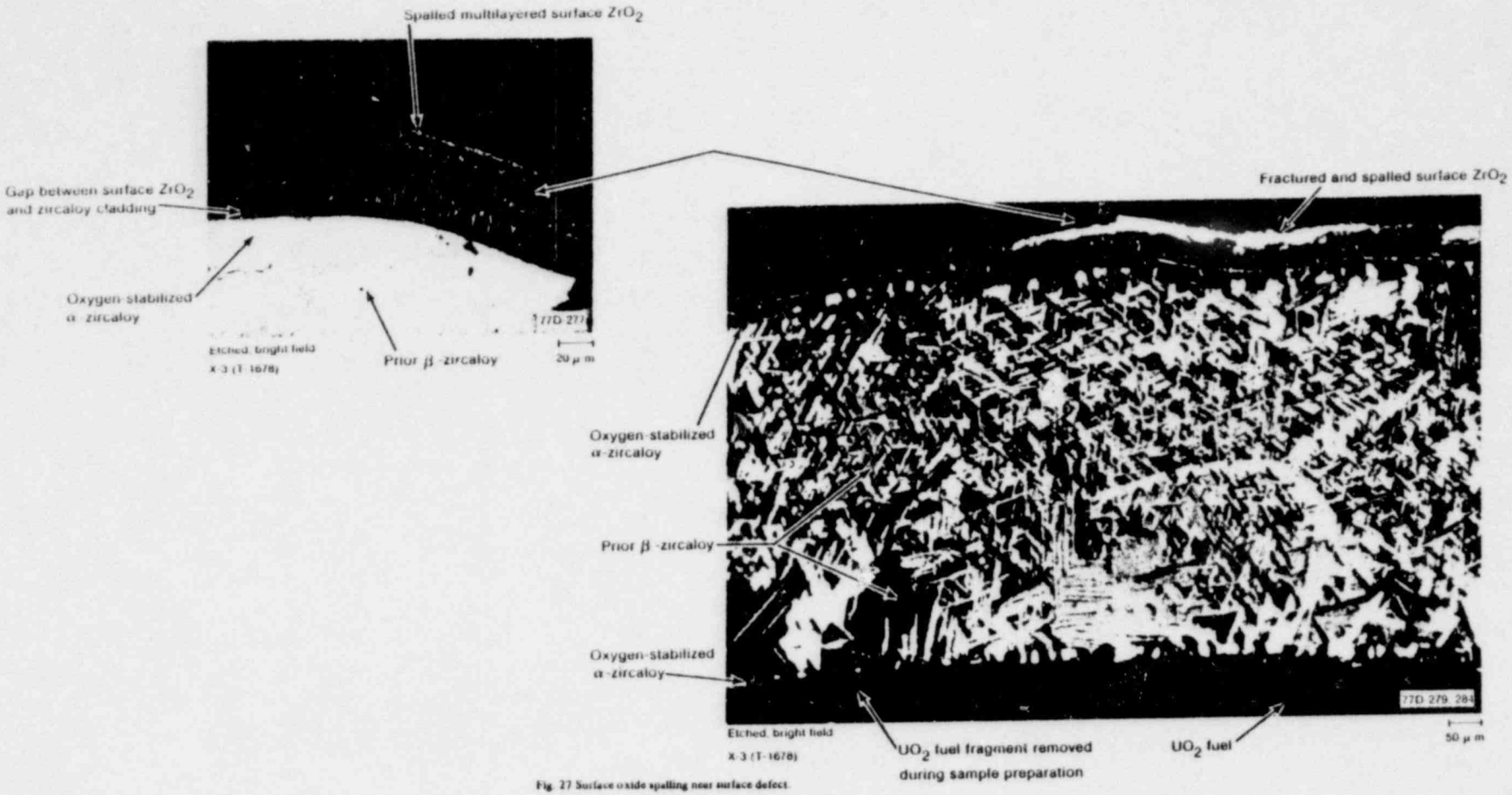

Fig. 27 Surface oxide spalling near surface defect.

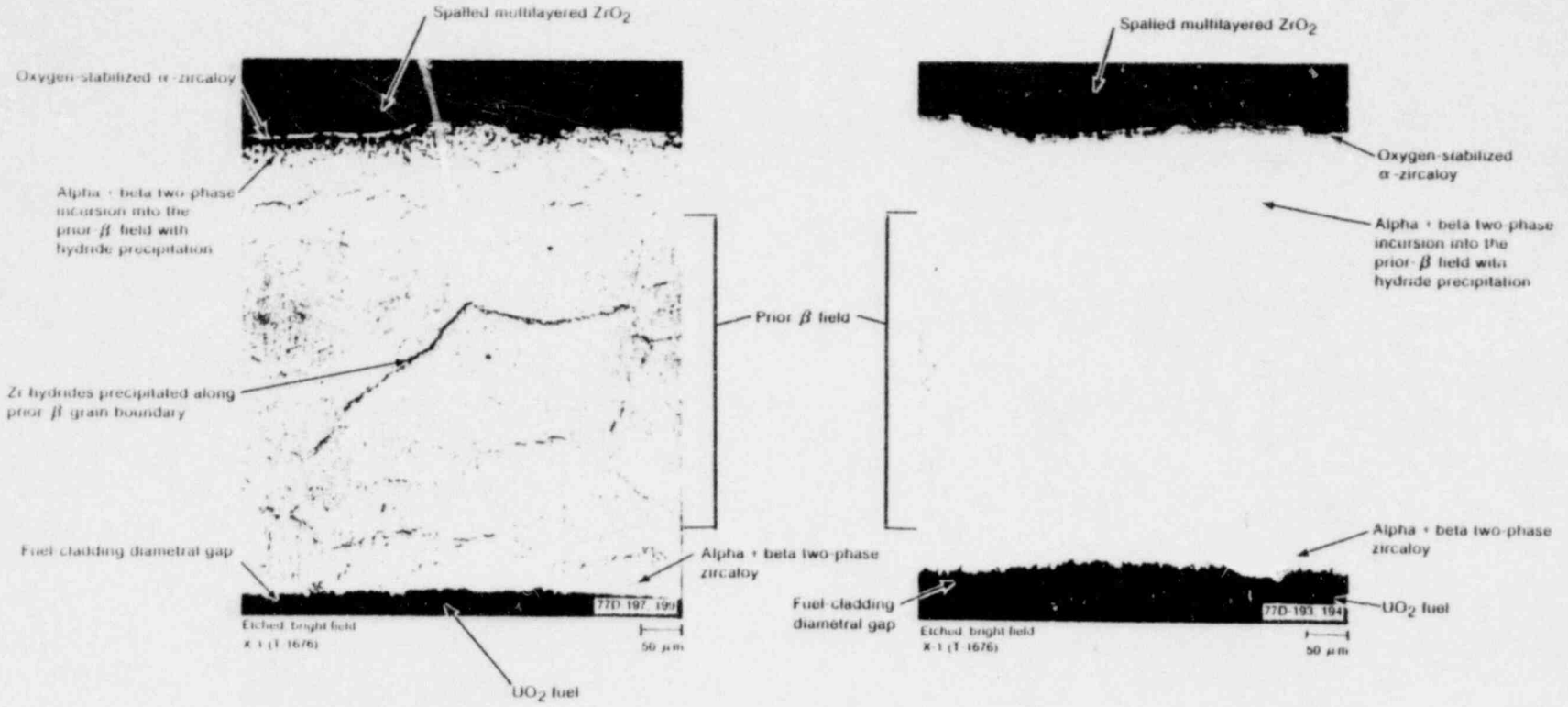

Fig. 28 Spalling of multilayered surface oxide.

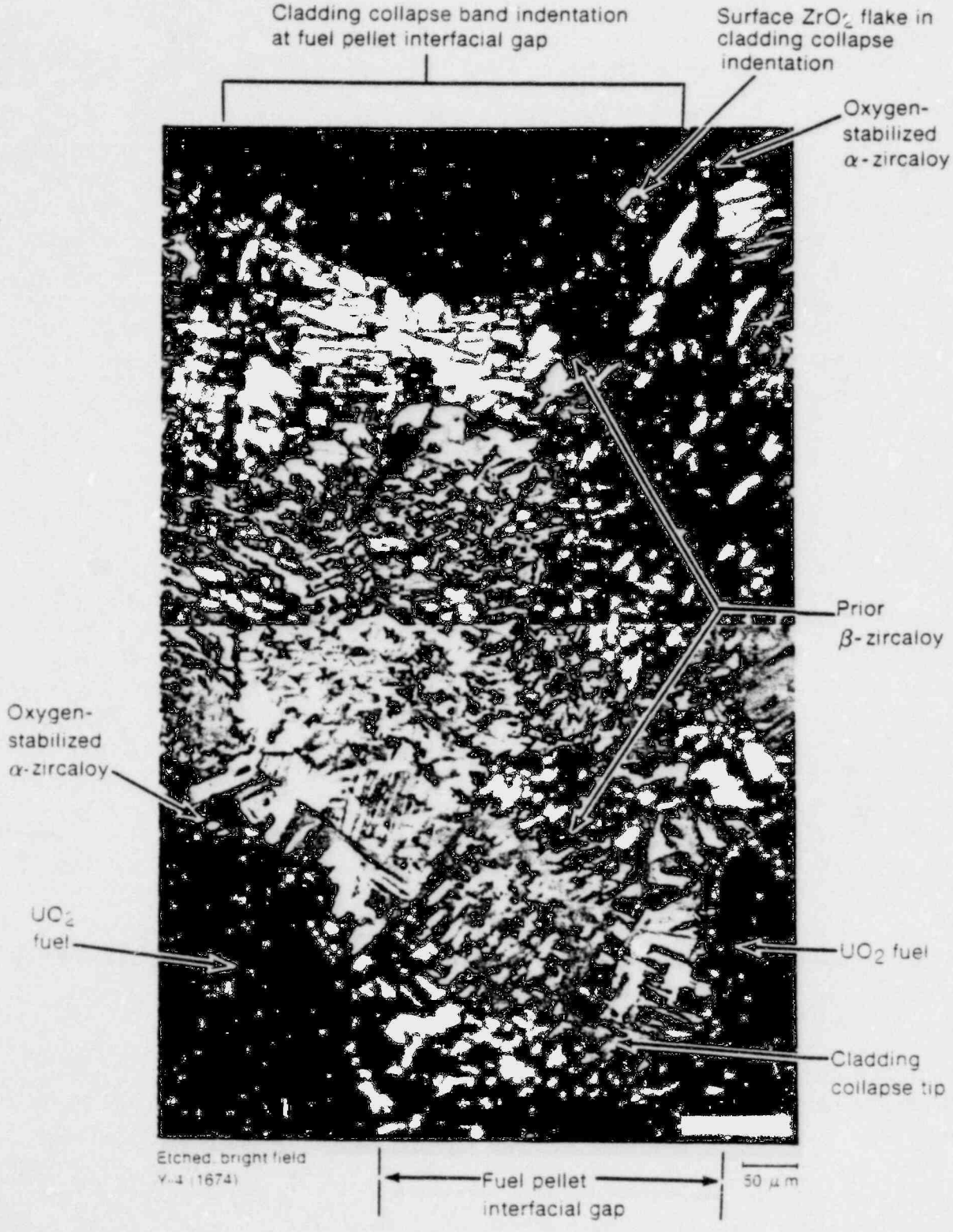

Fig. 29 Surface oxide flake attached to the cladding waisted region at a fuel pellet interfacial gap.

for reaction at 1673 K and 30 min with fuel-cladding contact pressure of about 7.09 MPa. Constituent reaction layer formation similar to those observed by Grossman-Rooney, Mallett et al, and Hofmann are discussed below for the Test PCM-4 fuel rods.

The reaction at the interface between fuel and cladding at several locations on the various test rods is illustrated in Figures 30, 31, and 32. In Figures 30 and 31, the internal UO_2-zircaloy reaction layer is composed of two principal layers. As verified by electron microprobe analysis in previous tests[3,5,6], the layer adjacent to the cladding has been identified to be low in Zr, but contains a significant quantity of U, together with a measurable quantity of Sn (designated a U-rich, U-Sn-Zr alloy). The layer adjacent to the fuel at the interface has been identified to be low in Sn and U, but contains a large quantity of Zr (designated a Zr-rich, U-Zr alloy). The constituent form of the metallic layers at the fuel-cladding interface is identified as

$$[UO_2] \rightarrow [\alpha\text{-}Zr(O) + U]\ \text{Zr-rich} \rightarrow [U \text{ or } (U, Zr) \text{ alloy} + Sn]\ \text{U-rich} \rightarrow [\alpha\text{-}Zr(O)] \rightarrow [\beta\text{-}Zr]. \quad (3)$$

The tin present in the reaction layer adjacent to the cladding is probably the result of a small amount of depletion of the zircaloy at the interface. The composition changes, as material is deposited along fuel cracks farther out into the fuel, to a U-rich, U-Zr alloy with no tin present.

Fuel fragments were observed attached to the inner cladding surface at various locations by the UO_2-zircaloy reaction layers. Thermal contraction of the fuel following quenching from test temperatures shatters the fuel pellet along the periphery at regions where the fuel has reacted at the pellet-cladding interface, leaving the attached fuel fragments. Fuel fracturing transverses the brittle reaction layer and initiates cracking and intergranular attack of the adjacent layer of oxygen-stabilized alpha in the cladding. If brittle cracking of the inner oxygen-stabilized alpha layer occurs early during the cyclic testing, cavity defects of the type illustrated in Figure 32 may form.

1.3 Evaluation of the Interior Reaction Layer Kinetics

To evaluate the reaction kinetics of the zircaloy cladding from UO_2 fuel-cladding contact, microstructural layer thicknesses of oxygen-stabilized alpha and the duplex reaction layer at the interface were compared with kinetic correlations developed by various investigations. The oxygen-stabilized alpha-zircaloy reaction layer growth at the UO_2 fuel-cladding interface was studied by Grossman and Rooney[10] and Mallett[11,12]. The ZrO_2 and oxygen-stabilized alpha layer growth from zircaloy-steam reaction was studied by Cathcart[14]. These investigators showed that their out-of-pile isothermal data followed a parabolic growth relationship in which oxygen penetration into the zircaloy was proportional to $t^{1/2}$. Curves (solid and dashed lines) following the isothermal analyses of these investigations for oxygen uptake are presented in Figure 33, where the reaction layer

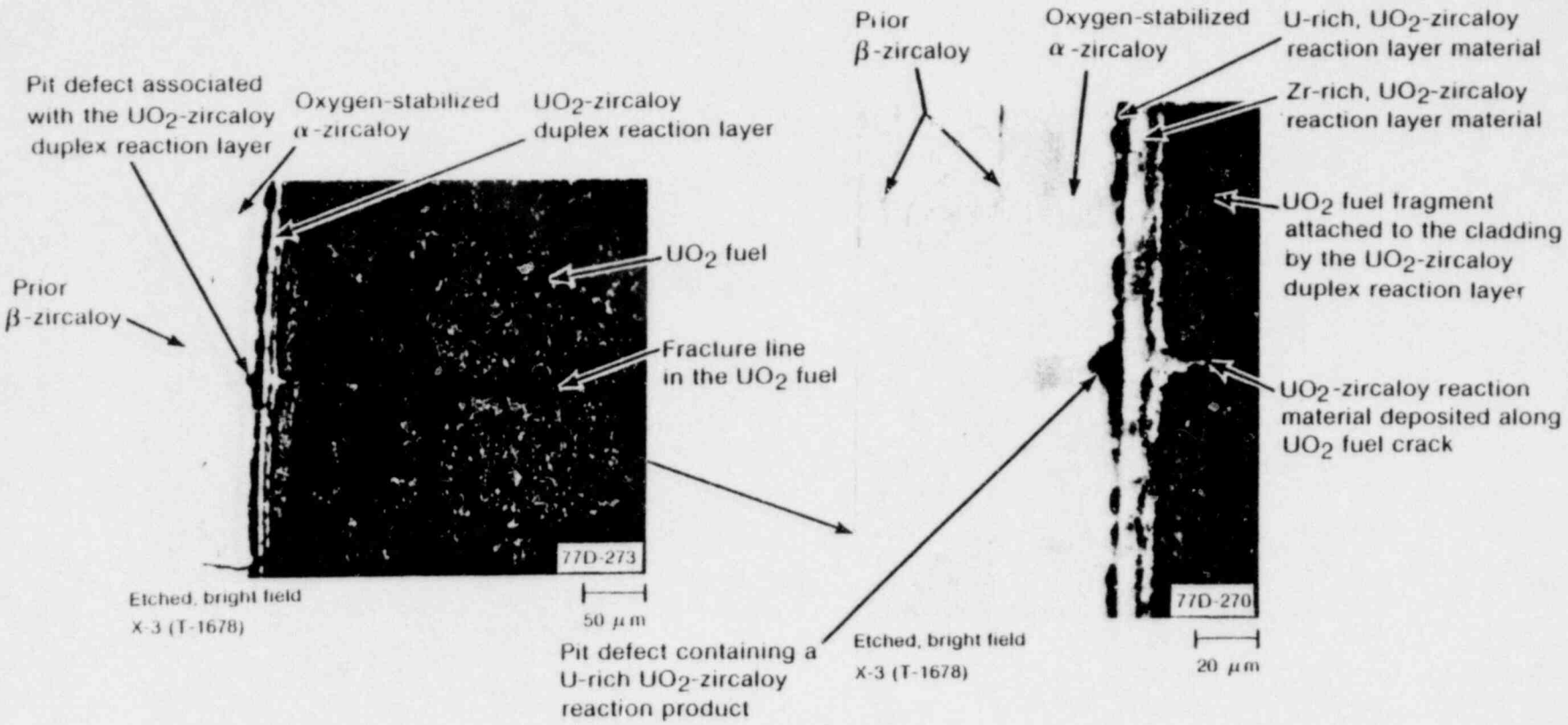

Fig. 30 Inner cladding surface UO_2-zircaloy reaction layer development.

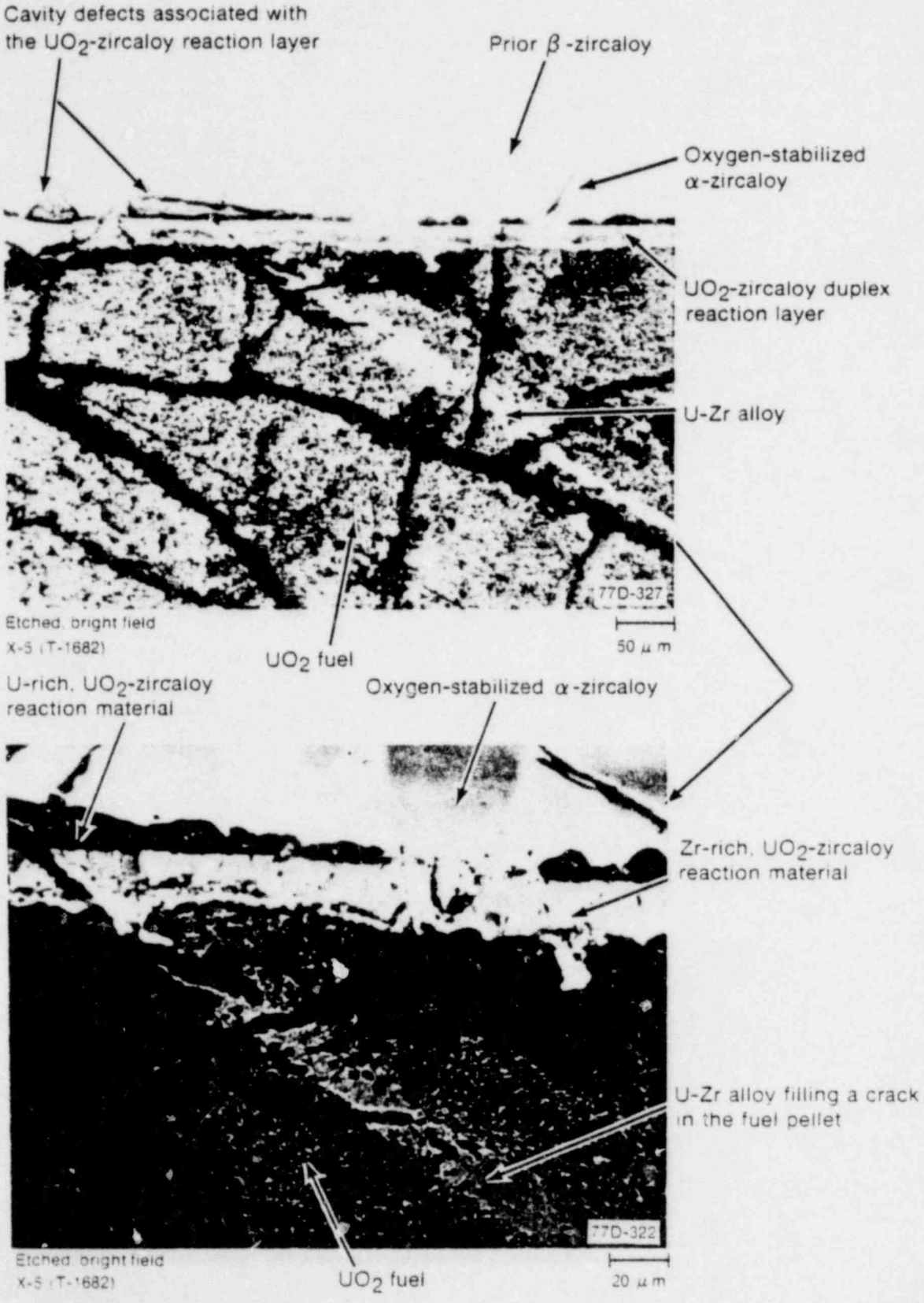

Fig. 31 Example of UO_2-zircaloy reaction layer associated with fuel crack filling by reaction material.

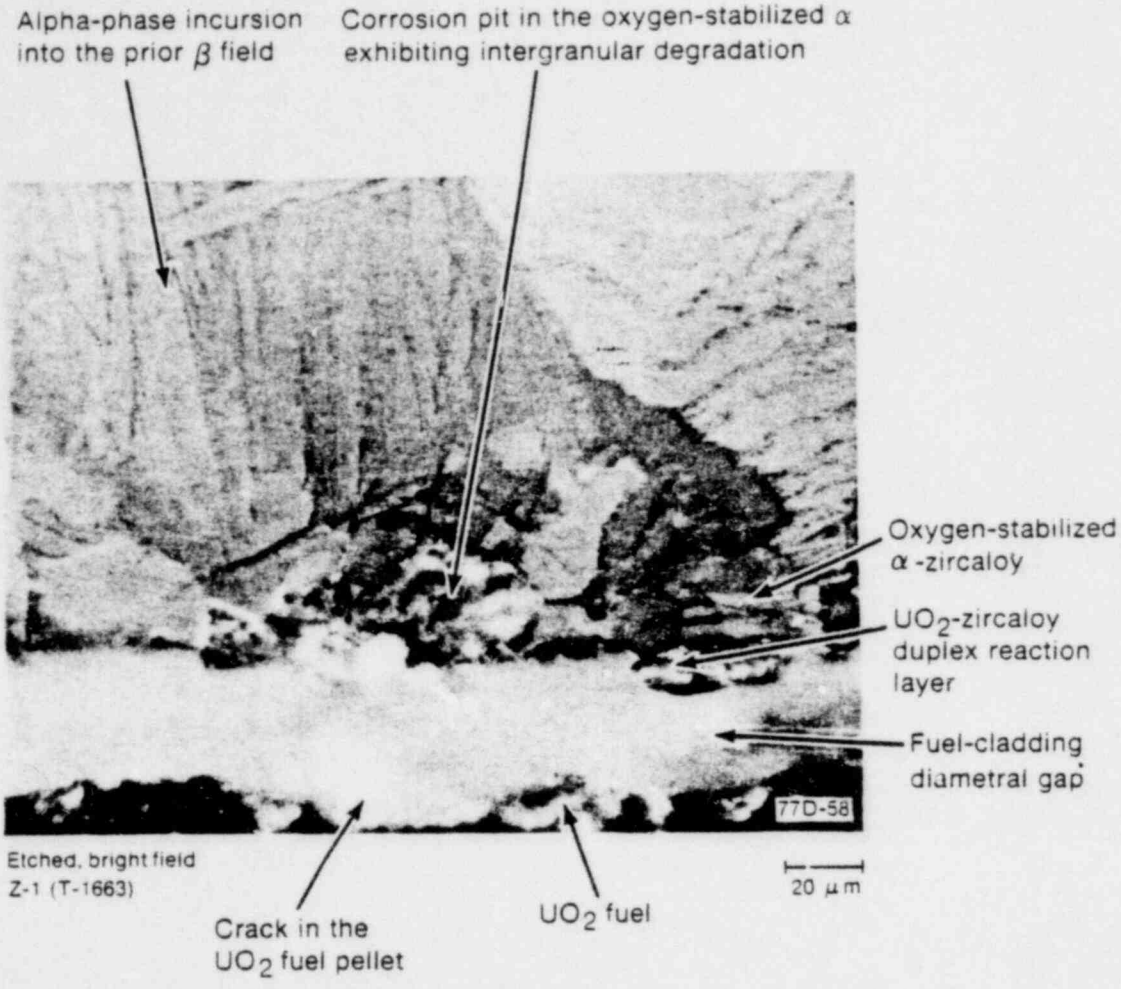

Fig. 32 Intergranular corrosion of the cladding and pit defect at the fuel-cladding interface.

growth kinetic parameter χ^2/t (cm^2/s) is plotted as a function of the reciprocal temperature. The Grossman and Rooney and Mallett curves are for oxygen-stabilized alpha layer growth at the inner cladding surface, and, for comparison, the Cathcart curve represents the outer cladding surface oxide plus oxygen-stabilized alpha (ξ) layer growth.

Inside diameter reaction layer thicknesses at the UO_2-cladding interface of Test PCM-4 fuel rods were measured metallographically. The microstructural layer thicknesses were compared with the isothermal analyses of Grossman and Rooney, Mallett, and Cathcart are plotted in Figure 33, as solid- and dashed-line curves, to determine the oxygenation kinetics for the interfacial reaction layer development. Calculated values of the kinetic parameter χ^2/t, determined from reaction layer thicknesses tabulated in Appendix F, are plotted in Figure 33 as a function of the reciprocal isothermal temperature of the outer cladding surface. The small ΔT across the cladding wall was not taken into account.

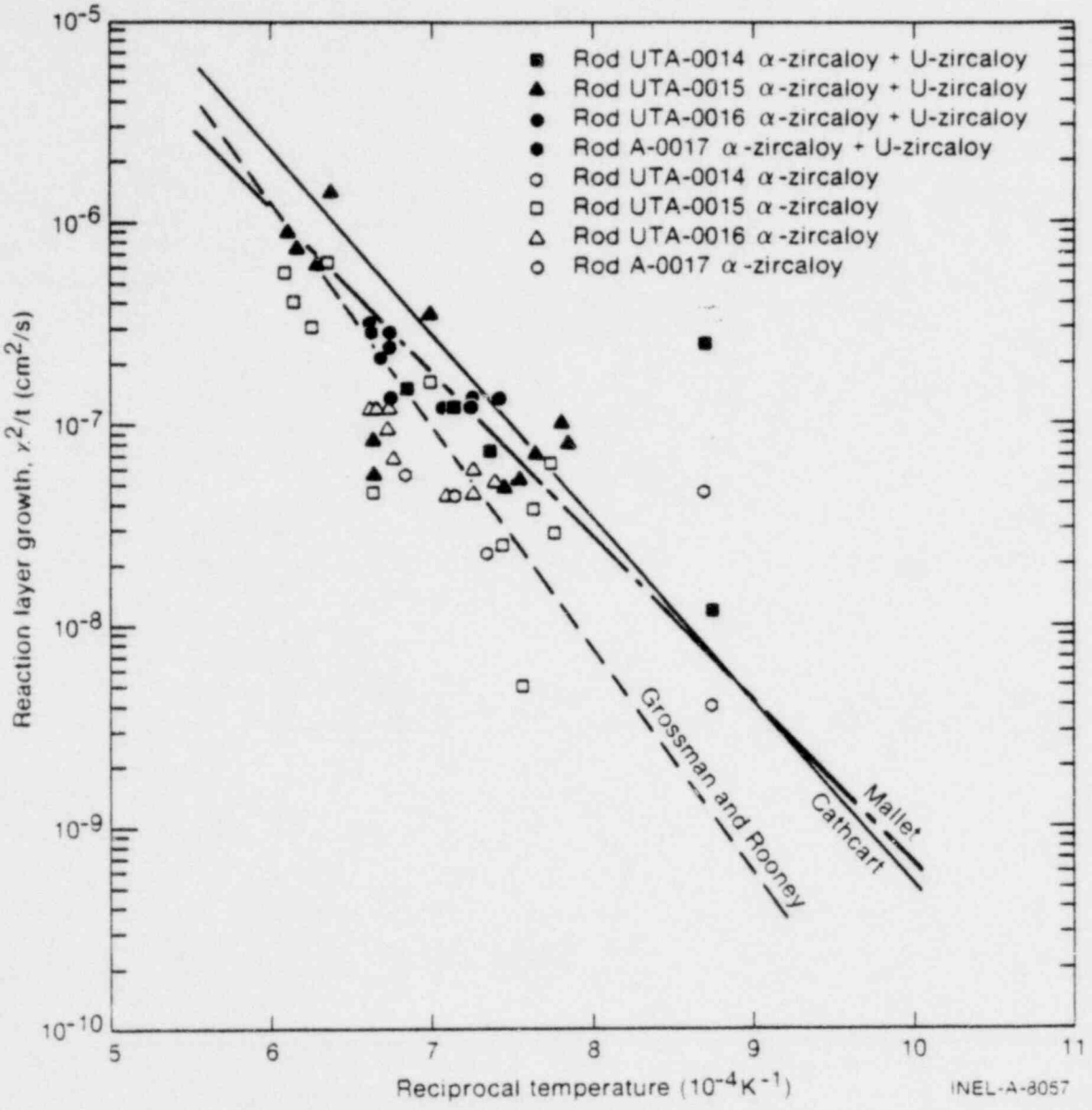

Fig. 33. Determination of the oxidation kinetics of cladding from fuel-cladding and metal-water reaction.

The results for the four rods indicate that the combined two-phase U-zircaloy reaction layer and cladding inner layer of oxygen-stabilized alpha growth kinetics generally scatter above and below the Mallett and Grossman and Rooney results. Test PCM-4 data tend to follow below the Cathcart isothermal analysis which was based on metal-steam (water) reaction. A similar result was demonstrated in previous Test PCM-3[6].

The previous PCM tests indicate that the chemical reaction of fuel and cladding in contact during film boiling can lead to oxygen-induced embrittlement of the cladding, similar to that induced by metal-steam (water) reaction. Cronenberg and El Genk[15] have

presented an analytical model to assess the extent and kinetics of oxygen uptake in zircaloy cladding from UO_2 reaction. Their model considers the oxygen uptake in terms of simple oxygen diffusion and they present a solution involving coupled two-media diffusion with a moving boundary, arising from the beta- to alpha-zircaloy phase change. The analytical results are presented in Figure 34 as an upper and lower limit for the reaction layer development. The upper limit is associated with the growth of the oxygen-stabilized alpha layer and the oxygen-diffusion front in the fuel. The lower limit represents only the oxygen-stabilized layer growth. These bounds are given as

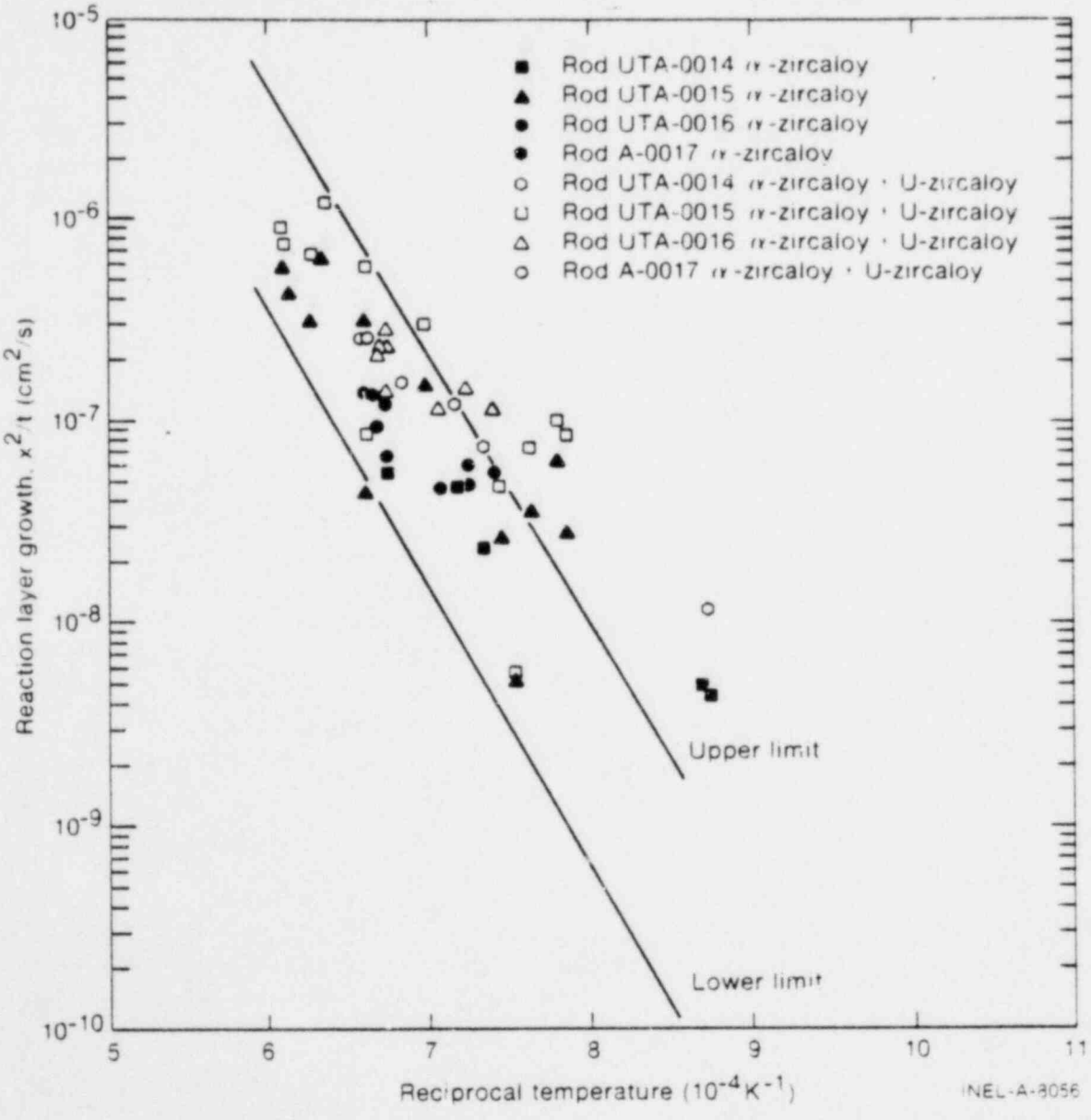

Fig. 34 Comparison of the experimental reaction layer growth with the theoretical results of the coupled-media diffusion model proposed by Cronnenberg and El Genk.

$$\delta^2/t + 4D_1 = \text{upper limit } (cm^3/s) \quad (4)$$

and

$$\delta^2/t = \text{lower limit } (cm^3/s) \quad (5)$$

where

δ = position of alpha/beta phase front.

t = real time in seconds.

D_1 = oxygen diffusion coefficient in the fuel.

Experimental reaction layer thicknesses are plotted in Figure 34 as the kinetic parameter χ^2/t for comparison with the Cronenberg-El Genk analysis. The comparison indicates that both the single oxygen-stabilized alpha layer growth and the combined oxygen-stabilized alpha plus uranium-zircaloy layer growth fall within the upper and lower bounds set by the prediction for isothermal temperatures above the 1245 K (alpha + beta) two-phase transition temperature to prior beta-zircaloy.

2. CLADDING EMBRITTLEMENT

Pawel[7,8] has shown that the beta-phase oxygen content and distribution has an effect on the mechanical properties of oxidized zircaloy. The response of oxidized cladding will depend on (a) the oxygen concentration within the beta field, (b) the amount of remaining beta-phase material, and (c) the amount of alpha-phase incursion into the prior beta field. The embrittlement of oxidized cladding at room temperature from Test PCM-4 fuel rods was evaluated using criteria investigated by Pawel for establishing failure based on time (the critical oxidation time) of high temperature cladding oxidation in steam. The criterion proposed by Scatena for failure by oxygen embrittlement from equivalent cladding reacted (surface oxide and oxygen-stabilized alpha) is 17%[16].

2.1 Cladding Oxidation

Optical metallography of the cladding samples demonstrated that the amount of oxygen-stabilized alpha material and alpha-phase incursions constituted only a few percent of the wall thickness of the cladding beta material. Considering the limits of oxygen concentration in the beta material suggested by Pawel for room temperature embrittlement of zircaloy (95% saturation of 0.7 wt%), insufficient oxygen appears to have been present to critically embrittle the cladding.

The results of the critical oxidation time calculations are summarized in Table XI for Test PCM-4 using the embrittlement criteria of Pawel. Pawel's criteria are in graphical form

TABLE XI

COMPARISON OF MAXIMUM CLADDING EXPOSURE CONDITIONS WITH THE CRITICAL OXIDATION TIME FOR EMBRITTLEMENT AND EQUIVALENT CLADDING REACTED

Rod	Maximum Cladding Temperature[a] (K)	Time in Film Boiling[b] (s)	Critical Oxidation Time (corrected) (s)	Equivalent Cladding Reacted (%)	Failure During or Following Test
UTA-0014	1480	55	241	4	No
UTA-0015	1620	67	100	8	No
UTA-0016	1520	112	230	6	No
A-0017	1530	96	200	6	No

[a] Maximum cladding temperatures were determined by calculations using isothermal correlations.

[b] Times in film boiling were determined from the axial progression of film boiling along the fuel rod.

where curves of critical oxidation time versus cladding temperature are given for the cladding wall thickness of 0.686 mm used in the Oak Ridge experiment[7,8]. A correction factor of 0.79, determined by the relative wall thicknesses and given by the ratio

$$\left[\frac{\text{PCM test fuel rod wall thickness (0.610 m)}}{\text{experimental cladding wall thickness (0.686 m)}}\right]^2$$

has been applied to the critical time for each fuel rod to account for a thinner cladding wall used in the PCM tests. It is apparent, from Table XI, that the exposure time in film boiling for Test PCM-4 fuel rods was well below the critical exposure time for room temperature embrittlement of the cladding.

The equivalent cladding reacted to ZrO_2 was calculated for each fuel rod as a percentage of the initial wall thickness at the position of the maximum measured reaction layer thicknesses on the inner and outer cladding surfaces[16,17]. The results of these calculations are presented in Table XI. The values are well below the embrittlement criterion based on 17% equivalent cladding reacted[16] indicating that no embrittlement failure for Test PCM-4 fuel rods would be expected.

2.2 Cladding Hydriding

A factor in the hardening of zircaloy is hydrogen uptake from the zircaloy-steam interaction. The hydrogen dissolution reaction in zircaloy follows a relationship of the form

$$\frac{1}{2}\ H_2\ (g) = H.\ (\text{dissolved in zircaloy}). \qquad (6)$$

All four tested fuel rods exhibited varying degrees of cladding hydriding, although no failure of the test rods was indicated, both during in-pile testing and by the posttest examination. The influence of hydrogen on the Test PCM-4 cladding is discussed in this section.

A typical example of the hydride structures in the cladding sectioned from the film boiling zone is illustrated in Figure 35. The hydrides remain basically dispersed within the cladding parent beta phase. Hydrides appearing in the cladding at lower temperatures are generally circumferentially oriented[5,6]. Hydrides appearing in the beta phase appear to have randomly reoriented when quenched from test temperatures well above the beta transus temperature (1245 K). The hydrides tend to precipitate intergranularly in the beta quenched condition in association with the alpha-phase platelet material nucleated inside prior beta grains or along the prior beta grain boundaries. The hydrides tend to form outside the oxygen-stabilized alpha reaction layer regions. In Figure 35, a band of alpha + beta two-phase material is found between the oxygen-stabilized alpha interfaces and the parent beta-phase material. Hydriding is prevalent at the alpha + beta to beta interfaces. Such structures are discussed in Appendix D and are thought to arise both from changes in hydrogen solubility during oxygenation and from posttest quenching effects.

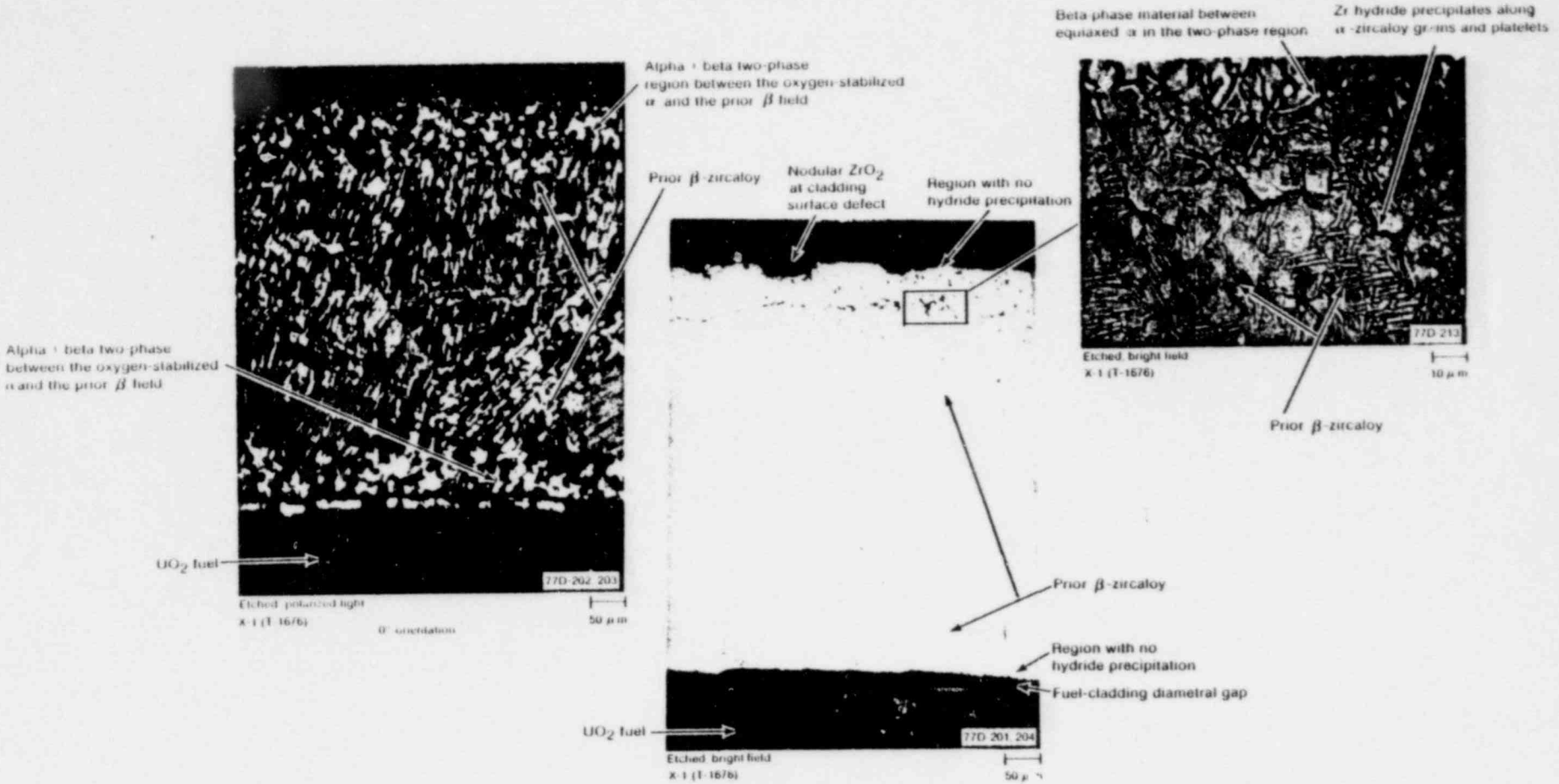

Fig. 35 Hydride precipitation at 0.686-m and 0° circumferential orientation in Rod UTA-0013.

The hydriding observed in the metallurgical samples examined from the film boiling zones of the test rods is greater than would be expected from the nominally <10 ppm pretest hydrogen content of the cladding. Although weld penetration and degradation was identified metallographically in the instrumented fuel rods (to > 75% of the cladding wall thickness without observable perforation, as described in Appendix E), no leaks were encountered in measuring the posttest void volumes, suggesting that none of the rods contained cladding perforations allowing coolant access to the interior of the rods before, during, or following DNB testing. Similarly, posttest void volume and pressure data obtained from the uninstrumented rod, Rod A-0017, indicated it was also unfailed. Free hydrogen generated by steam during transition film boiling or sustained film boiling conditions may be a possible source of the additional hydrogen taken up by the cladding, particularly if stagnant conditions form from a thick film blanket, or if fluctuations in the distribution of the film blanket exist. It was impossible to differentiate, by microhardness measurements (discussed in Appendix D), the effects of hydriding from the overriding oxygen-related hardening. Apparently, the level of hydrogen uptake and subsequent hydriding of the beta-quenched cladding was not sufficient to significantly influence the microhardness.

VII. FUEL RESTRUCTURING

The film boiling transient conditions result in thermal restructuring of the UO_2 fuel. The restructuring evidenced in Test PCM-4 fuel rod samples was, in general, characterized by limited grain growth near the pellet centers, with grain sizes up to more than 60 μm, and scattered equiaxed grains exceeding 100 μm. In addition to the grain enlargement observed near the center of fuel pellets examined from the film boiling zones, a small fuel melt zone was identified near the center of Rods UTA-0014, UTA-0016, and A-0017. Rods UTA-0014 and UTA-0016 were instrumented with tantalum sheathed centerline thermocouples which reacted with the UO_2 fuel to form the melt zone in these rods.

Fuel fracturing, shattering, and fragmenting accompanied the cyclic rapid heating and cooling of the test operation. The largest fuel pellet cracks were radially oriented, growing narrower in width toward the outer pellet edges. The fracturing occurred in both inter- and transgranular modes. Fracturing near the outer pellet edge where grain sizes were small (4 to 12 μm) was commonly transgranular and often followed lines of porosity. Isolated evidence of crack healing was also observed near the pellet peripheries. Fracturing near the pellet centers generally exhibited both inter- and intragranular fracturing. Details of these observations are presented in the following sections.

1. EQUIAXED GRAIN GROWTH

Estimates of the fuel temperature characteristic of the boundary between unrestructured and equiaxed grain zones is that T ∿1900 K is required for grain enlargement to occur[18]. The temperature at which columnar grain growth occurs varies from 1970 to 2400 K, depending on the temperature gradient in the fuel. Typical fuel centerline temperatures measured within the film boiling zone during the test were T ∿2000 to 2200 K for the instrumented fuel rods.

Fuel restructuring and relative grain sizes measured near the center and outer diameter of the examined rod samples are presented in Tables XII, XIII, XIV, and XV, for Rods UTA-0014, UTA-0015, UTA-0016, and A-0017, respectively. Rod UTA-0014 exhibited limited equiaxed fuel grain growth. Although a localized central molten zone developed, associated with the reaction of the tantalum sheathed centerline thermocouple with the UO_2, no columnar grained region was observed between the equiaxed grain zone and the molten region. Rod UTA-0015 showed only equiaxed grain growth at the fuel center in the film boiling zone. Rod UTA-0016 contained a central molten zone of fuel, also associated with the reaction between UO_2 and the tantalum sheathed centerline thermocouple. The molten zone developed in the equiaxed grain region. No columnar grains were observed. Rod A-0017 exhibited a central molten zone. A region of columnar grain growth was observed between the central molten fuel and the region of equiaxed grain growth.

TABLE XII

UO_2 FUEL RESTRUCTURING IN ROD UTA-0014

	Sample			
	Y-1	Y-2	Y-3	Y-4
Location from bottom of fuel stack (m)	0.686	0.664	0.638	0.600
UO_2 fuel grain size[a]				
Near center (μm)[b]	>40	>45	>42	>110
Near edge (μm)	--	4 to 6	∿7	--
Approximate percent of restructuring[c]	65	75	78	71

[a] Uncertainty in these measurements is ± 2.5 μm.

[b] Values measured in regions adjacent to the molten central zone.

[c] Measured by the fractional radius for equiaxed grain growth.

TABLE XIII

UO_2 FUEL RESTRUCTURING IN ROD UTA-0015

	Sample				
	X-1	X-2	X-3	X-4	5
Location from bottom of fuel stack	0.686	0.667	0.641	0.606	0.559
UO_2 fuel grain size[a]					
Near center (μm)	~18	--	>60	30 to 40[b]	40 to 50[b]
Near edge (μm)	4 to 6	6	5	6 to 8	4 to 6
Approximate percent of restructuring[c]	71	68	78	79	74

[a] Uncertainty in these measurements is ± 2.5 μm.

[b] Some individual grains were greater than 60 μm in the adjacent regions near the fuel pellet center.

[c] Measured by the fractional radius for equiaxed grain growth.

TABLE XIV

UO_2 FUEL RESTRUCTURING IN ROD UTA-0016

	Sample			
	W-1	W-2	W-3	W-4
Location from bottom of fuel stack (m)	0.686	0.667	0.641	0.587
UO_2 fuel grain[a] size				
Near center (μm)	20 to 30	30 to 40[b]	~40[b]	30 to 40[b]
Near edge (μm)	5 to 6	4	6	<4
Approximate percent of restructuring[c]	67	68	78	71

[a] Uncertainty in these measurements is ± 2.5 μm.

[b] Measured by the fractional radius for equiaxed grain growth.

[c] Scattered grains in these regions had grain sizes exceeding 70 μm.

TABLE XV

UO_2 FUEL RESTRUCTURING IN ROD A-0017

	Sample	
	Z-1	Z-2
Location from bottom of fuel stack (m)	0.629	0.803
UO_2 fuel grain size[a]		
Near center (μm)	30 to 60[b,c]	~4
Approximate percent of restructuring[d]	80	41

[a] Uncertainty in these measurements is ± 2.5 μm.

[b] Values measured in regions adjacent to the columnar grain and molten central zones.

[c] Some individual grains had measured average diameters exceeding 100 μm adjacent to the columnar grain zone.

[d] Measured by the fractional radius for equiaxed grain growth.

2. FUEL MELTING

Fuel melting occurs at fuel temperatures near 3100 K[19], and results in the formation of a central void and large grains upon solidification. The effects of fuel melting in Rod A-0017 are illustrated in Figure 36. The columnar grained region between the equiaxed zone and the central solidified region exhibits macropore migration and coalescence as seen in the figure. A portion of one of the lenticular central voids formed at several locations (additionally apparent in the posttest neutrographs in Figure 10) is also noted in Figure 36.

The fuel melting observed in Rods UTA-0014 and UTA-0016 was uncommon to the normally expected fuel restructuring. The molten zone developed in the equiaxed grain region without columnar grain formation. The reaction of tantalum, from the thermocouple sheaths, with the UO_2 to form the molten zone was confirmed by the identification of elemental tantalum inclusions within the melt zone by electron microprobe. The tantalum reacted with the UO_2 to form low melting temperature products in the fuel. Selected structures from the tantalum and UO_2 melt zones in Rods UTA-0014 and UTA-0016 are illustrated in Figures 37 and 38. The several localized structures and patterns observed in the figures suggest simple eutectic or monotectic-like morphologies. Details of the tantalum-UO_2 reaction are presented in Appendix D. The reaction of tantalum and UO_2 is primarily of interest only for instrumented test fuel. The importance of the tantalum-UO_2 melting to Test PCM-4 was the loss of centerline temperature data late in the test when rod temperatures were expected to reach maximum test values. Both Rods UTA-0014 and UTA-0016 experienced erratic centerline thermocouple response prior to the final DNB test cycle and failed during the final test cycle.

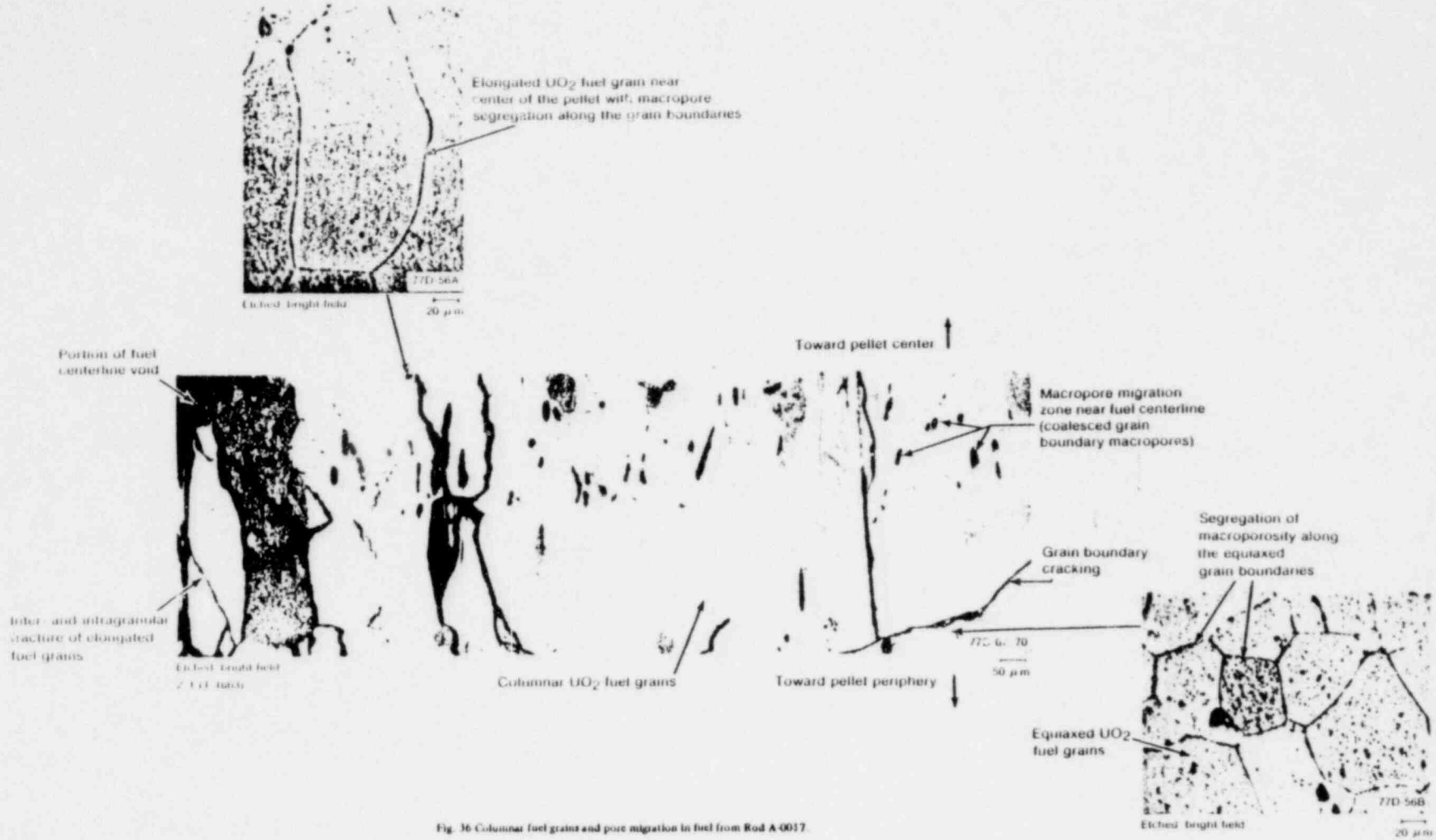

Fig. 36 Columnar fuel grains and pore migration in fuel from Rod A-0017

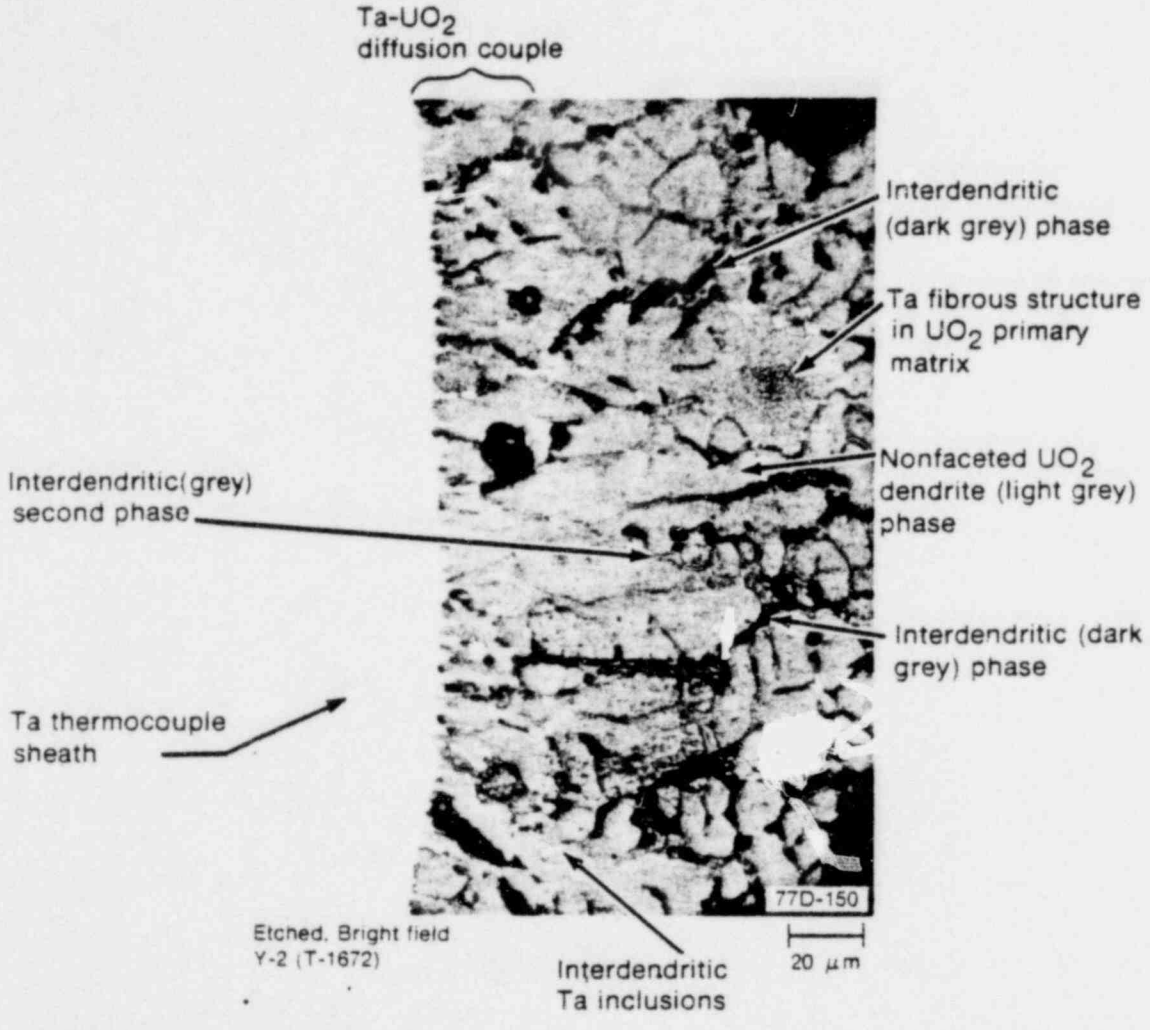

Fig. 37 Tantalum and UO_2 diffusion couple with eutectic-like fibrous structures of tantalum in the UO_2 matrix.

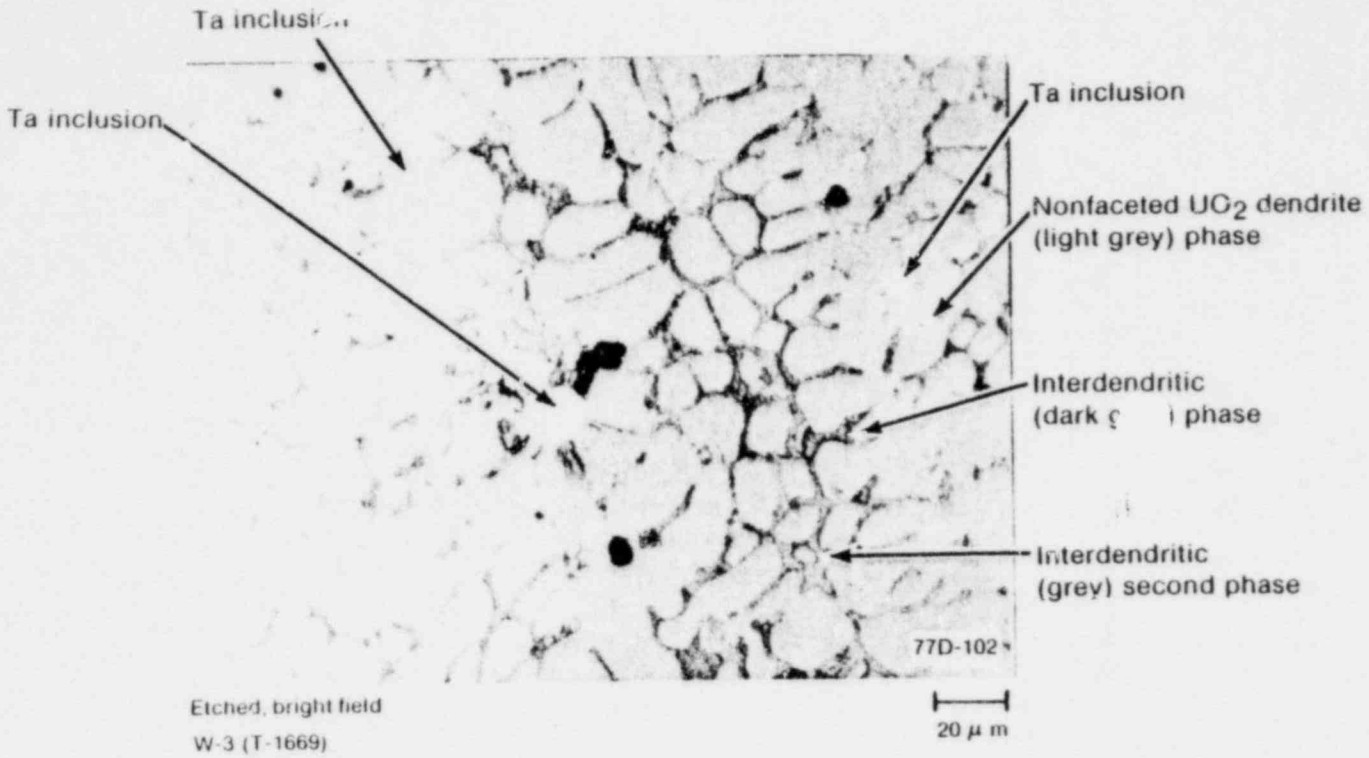

Fig. 38 Nonfaceted UO_2 dendrites with interdendritic tantlum inclusions in the tantalum UO_2 melt zone.

3. FUEL SHATTERING

Fuel fracturing and fragmenting in Test PCM-4 fuel rods occurred with the characteristic pellet-to-pellet propagation of the major fracture lines along the length of the fuel column as expected from the preconditioning operation and verified by posttest neutrography[3,5,6]. Radial fracture patterns were dominant in metallurgical samples examined from the film boiling zones. Circumferential intergranular cracking was limited to the periphery of the pellets in conjunction with fuel-cladding attachment by the UO_2-Zr intermetallic reaction layer. Where no UO_2-Zr reaction was observed, transgranular cracking of the unrestructured UO_2 was prevalent. Both inter- and transgranular fracturing was observed in the restructured regions near pellet centers.

Fuel shattering (granular fracturing) was noted in localized regions near the center and periphery of fuel examined from within the film boiling zone. The intergranular form of this localized grain fracturing is illustrated in Figure 39 for fracturing near the fuel-cladding interface. The shattering and granular separation of enlarged grains occurred in association with major pellet cracks, suggesting that mechanical stressing at the interfaces is important. Nominal grain sizes in the fuel in this region of approximately 20 μm or larger were noted. These grain sizes are distinguished from normal unrestructured fuel (typically 2 to 8 μm in diameter) in these tests. Apparently, some fuel grain growth in the vicinity of major fuel cracks does occur out to the fuel pellet periphery, but has not been firmly characterized from the posttest metallographic examination.

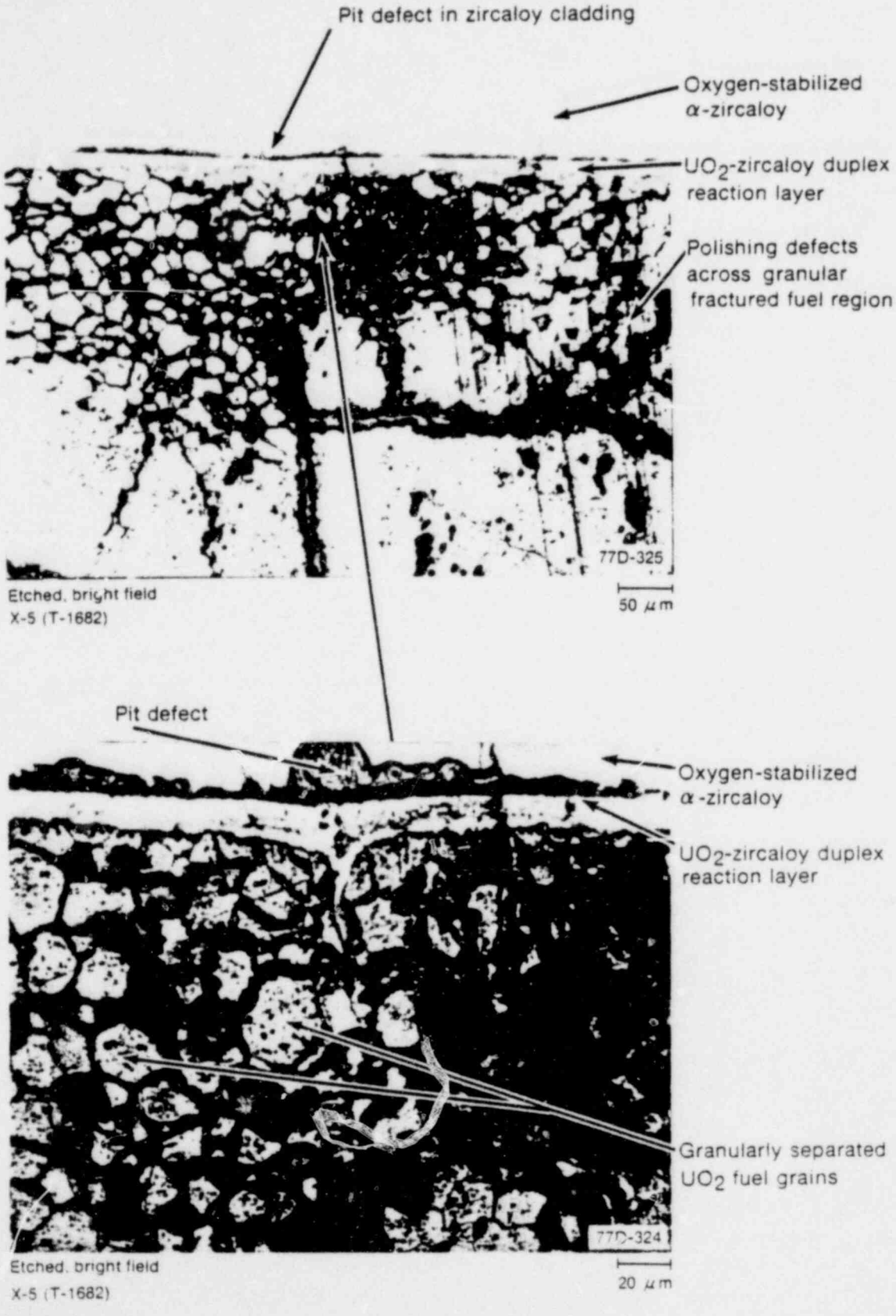

Fig. 39 Granular fracture of UO_2 fuel.

VIII. CONCLUSIONS

The results of the posttest visual and metallographic examination presented in this report indicate that despite evidence of structural damage from rod bowing, cladding collapse (including collapse into the interfaces between pellets) within the film boiling zone, an oxide spalling along the region of collapse, the test rods operated under severe cladding oxidizing film boiling conditions without failure during nuclear operation, shutdown, and subsequent posttest handling. Cladding oxidation data are consistent with previous PCM test data and both the critical oxidation time embrittlement criteria of Pawel and the 17% equivalent cladding reacted embrittlement criterion correctly predicted nonfailure of the fuel rods. Specific observations and conclusions are as follows:

(1) Film boiling operation resulted in damage to both the cladding and fuel of Test PCM-4 fuel rods. For the instrumented rods, the regions identified with severe cladding surface oxidation and cladding collapse correlate well with the regions over which the cladding surface thermocouples indicated that sustained film boiling conditions had occurred. Collapse up to 93% of the diametral cold gap was measured posttest with ovality up to 1.007 found throughout the collapse zone, compared to nominally 1.003 measured outside the collapse zone. Rod free bowing (up to a 10-mm deflection from the centerline) was determined to be greater than could be accommodated in the flow shroud, but due to retention by positioning screws along the shroud, rod bowing did not exert a discernible effect on the test coolant flow.

Evidence of fuel-cladding contact and locking of the fuel column was indicated by the gap in the fuel column observed by posttest neutrography, thermal cracking which extends into the inner cladding wall as a result of collapse into pellet interfaces, and fuel-cladding reaction layer development.

(2) Peak cladding temperatures ranged from 1570 to 1740 K. Such temperatures induced cladding phase transformation to the prior beta-phase and oxidation reactions with the coolant and the fuel during nuclear operation. Experimental reaction layer thicknesses for both the cladding-water and the cladding-fuel reactions were found to be consistent with out-of-pile isothermal kinetic data for zircaloy-water reaction. The time at such temperatures was insufficient to result in fuel rod failures by oxygen embrittlement. Cladding surface thermocouples induced circumferential temperature gradients of up to 130 K, and typically recorded temperatures more than 450 K below temperatures estimated from existing microstructures.

(3) Internal cladding hydriding was dispersed in the beta-quenched condition. The cladding hydriding was not sufficient to affect the cladding integrity. Outer and inner regions of alpha + beta two-phase zircaloy were observed between the oxygen-stabilized alpha and parent beta-phase in some of the samples examined. The development of such structures is attributed to changes in the hydrogen terminal solubility in the presence of oxygenation and quenching effects.

(4) Fuel restructuring was primarily limited to equiaxed grain growth up to 60 μm in diameter toward the fuel pellet centers for fuel examined from the film boiling zones of Rods UTA-0014, UTA-0015, and UTA-0016. A thin central melt zone observed in Rods UTA-0014 and UTA-0016 was the result of reaction between the UO_2 fuel and the tantalum sheath of the centerline thermocouple. The fuel in the film boiling zone of Rod A-0017 exhibited typical fuel restructuring with a central melt zone, central voids, a columnar grained region, an equiaxed grained region, and finally, near the pellet periphery, an unrestructured region. Granular fracturing was observed in fuel near the outer pellet edge in regions of mechanical contact with cracked fuel fragments and the cladding. Fuel grain sizes in the granular fractured regions were typically $\sim$20 μm and larger. The granular fracturing was localized to the cladding collapse zone.

IX. REFERENCES

1. United States Nuclear Regulatory Commission, Reactor Safety Research Program, *A Description of Current and Planned Reactor Safety Research Sponsored by the Nuclear Regulatory Commission's Division of Reactor Safety Research*, NUREG-75/058 (June 1975).

2. G. W. Cawood et al, *Power-Cooling-Mismatch Test Series, Test PCM-2A Test Results Report*, ANCR-NUREG-1347 (September 1976).

3. S. L. Seiffert and G. R. Smolik, *Postirradiation Examination for the Power-Cooling-Mismatch Test - 2A*, TREE-NUREG-1029 (February 1977).

4. Z. R. Martinson and R. K. McCardell, *Power-Cooling-Mismatch Test Series, Test PCM-2, Test Results Report*, TREE-NUREG-1038 (February 1977).

5. S. L. Seiffert, *Power-Cooling-Mismatch Test Series, Test PCM-2, Postirradiation Examination*, TREE-NUREG-1069 (March 1977).

6. S. L. Seiffert, *Power-Cooling-Mismatch Test Series, Test PCM-3, Postirradiation Examination*, TREE-NUREG-1187 (December 1977).

7. R. E. Pawel, "Diffusion in a Finite System with a Moving Boundary," *Journal of Nuclear Materials, 49* (1974) pp 281-290.

8. R. E. Pawel, "Oxygen Diffusion in Beta Zircaloy During Steam Oxidation," *Journal of Nuclear Materials, 50* (1974) pp 247-258.

9. J. A. Dearien et al, *FRAP-T2: A Computer Code for the Transient Analysis of Oxide Fuel Rods*, TREE-NUREG-1040 (March 1977).

10. L. N. Grossman and D. M. Rooney, *Interfacial Reaction Between UO_2 and Zircaloy-2*, GEAP 4679 (EURAEC) (April 1965).

11. M. W. Mallet, "Solid State Reactions of Uranium Dioxide," in *Uranium Dioxide: Properties and Nuclear Applications*, J. Belle (Ed.) Section 7.4, pp 342-371, U.S. Government Printing Office, 1961.

12. M. W. Mallett et al, *The Kinetics of the Zirconium-Uranium Dioxide Reaction*, BMI-1028 (August 1955).

13. P. Hoffman, "Investigation of the Influence of Oxide Fuel and Fission Products on the Mechanical Properties of Zry-4 Cladding Tubes under LWR Transient Conditions," *Proceedings of the American Nuclear Society Topical Meeting on Thermal Reactor Safety*, CONF-770708 (January 1978).

14. J. V. Cathcart et al, *Zirconium Metal-Water Oxidation Kinetics IV, Reaction Rate Studies*, ORNL/NUREG-17 (August 1977).

15. A. W. Cronenberg and M. S. El Genk, *An Assessment of Oxygen Diffusion During UO_2-Zircaloy Interaction*, TREE-NUREG-1192 (January 1978).

16. C. J. Scatena, *Fuel Cladding Embrittlement During Loss-of-Coolant Accident*, NEDO-10674 (October 1972).

17. A. S. Mehner et al, *Postirradiation Examination Results for the Irradiation Effects Scoping Test 1*, ANCR-NUREG-1336 (September 1976).

18. D. R. Olander, *Fundamental Aspects of Reactor Fuel Elements*, TID-26711-PI (April 1976).

19. G. A. Reymann (comp.), *MATPRO-Version 10: A Handbook of Materials Properties for Use in the Analysis of Light Water Reactor Fuel Rod Behavior*, ed. S. A. Letson TREE-NUREG-1180 (February 1978).

APPENDIX A

EXPERIMENTAL IRRADIATION AND AXIAL POWER PROFILE

APPENDIX A

EXPERIMENTAL IRRADIATION AND AXIAL POWER PROFILE

A summary of the experimental irradiation and power profile necessary to understand the overall thermal history of the test fuel rods is presented in this Appendix.

1. EXPERIMENTAL IRRADIATION – EXPERIMENTAL DESIGN AND CONDUCT

All tests were performed in-pile in the Power Burst Facility (PBF) reactor. The PBF driver core is designed to contain a centrally located tubular test region which operates as a neutron flux trap, permitting high power densities in tested fuels relative to the active core[A-1]. Test fuel rod shrouds are positioned in a heavy-walled Inconel 718 tube designed to protect the driver core from potential fuel rod failure and to facilitate in-pile insertion and removal of experiments. The associated water loop simulates the operating conditions of a pressurized water reactor.

The test was performed with four fuel rods, each contained in a separate flow shroud, positioned radially in the PBF in-pile tube (IPT). The fuel rods are effectively thermally and hydraulically isolated from each other by the separate flow shrouds. Radial positioning is illustrated in Figure A-1 for the four-rod assembly. The assembly is designed to position the four fuel rods symmetrically and to allow easy removal following irradiation.

The test assembly was instrumented for measurement of coolant conditions, fuel rod power, fuel rod length change, fuel rod internal pressure, fuel centerline temperature, cladding surface temperature, and instantaneous and integrated relative neutron flux in the region of the fuel rod cluster. An instrumented fuel rod mounted inside its flow shroud is shown in Figure A-2.

The experimental assembly is shown installed in the PBF in-pile tube test space in Figure A-3. Each fuel rod is rigidly fixed into the assembly at the top end cap during testing, but is free to expand axially downward against a transducer to measure length changes. The coolant flow is directed upward through the flow shrouds over the test fuels. The unrestricted annular coolant flow area is 118.6 mm^2. The coolant flow area around the surface thermocouples was reduced to 114.2 mm^2.

The basic test sequence consisted of a thermal hydraulic calibration of fuel rod power versus the in-pile tube neutron flux, a preconditioning operation, fuel rod aging, and the sequential departure from nucleate boiling (DNB) testing. The objective of the power calibration was to measure the maximum linear heat rating of each fuel rod.

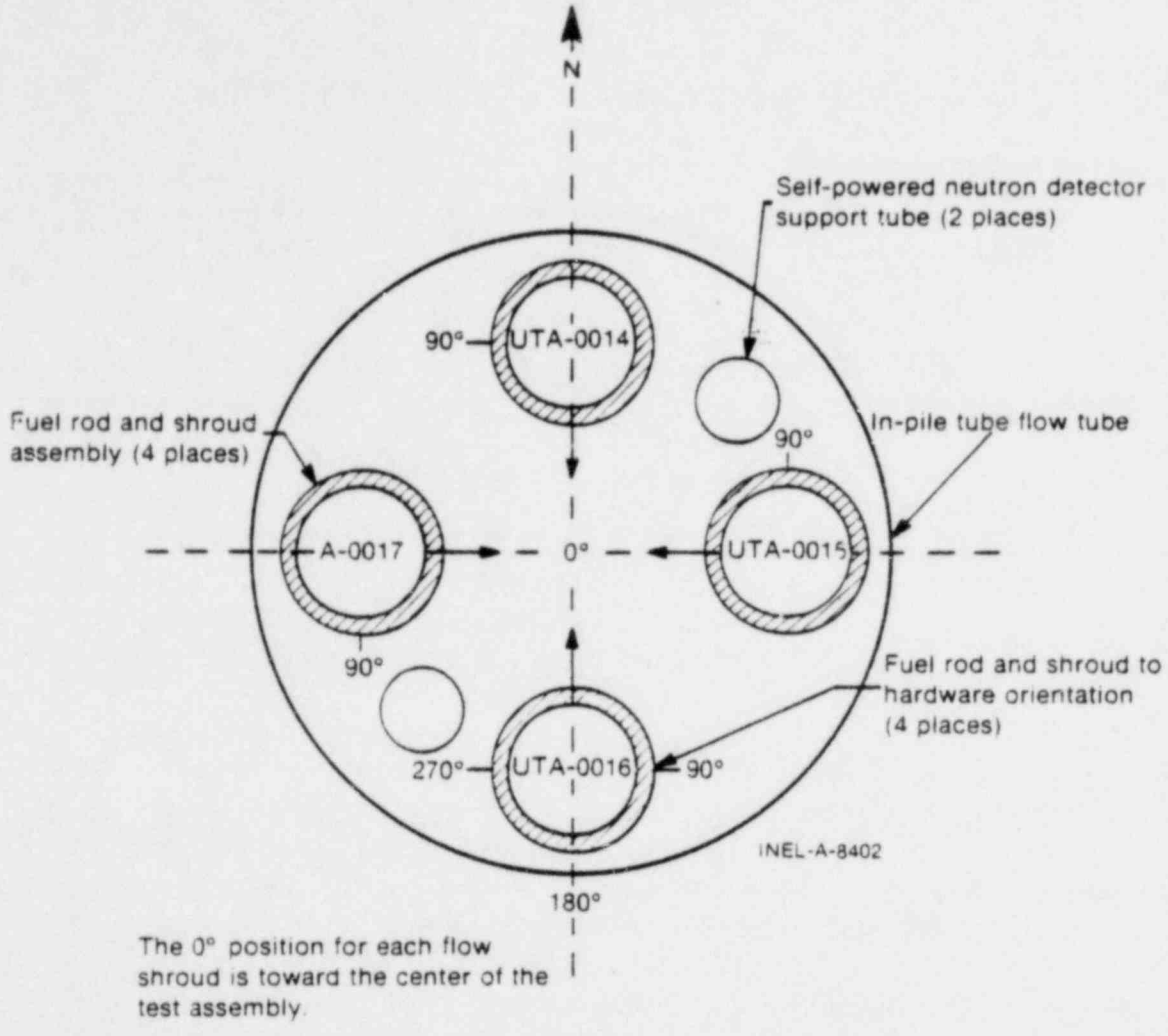

Fig. A-1. Fuel rod circumferential orientation in the PBF in-pile tube test space for Test PCM-4.

The rod powers were determined during the power calibration (when single-phase coolant conditions were maintained) from coolant flow and temperature rise measurements at 12 different fuel rod peak powers (0 to approximately 69 kW/m). During the power calibration phase, the nominal coolant mass flux, pressure, and inlet temperature were 3400 kg/(s·m^2), 15.16 MPa, and 585 K, respectively. A small variation in the coolant mass flux of about 5% from the rod with maximum flow to the rod with minimum flow for the total loop flow was noted. The flow variation was attributed to small differences in inlet orificing and flow restriction arising from rod instrumentation. The fuel rod power relative to the PBF core power[A-2] is discussed in Section 2 of this appendix. The preconditioning operation was performed to obtain an operating history of the test fuel and to allow pellet cracking and partial restructuring of the fuel. Gap conductance tests were performed during the preconditioning operation, both at steady state power ($\int$kdt) and under transient power oscillation conditions.

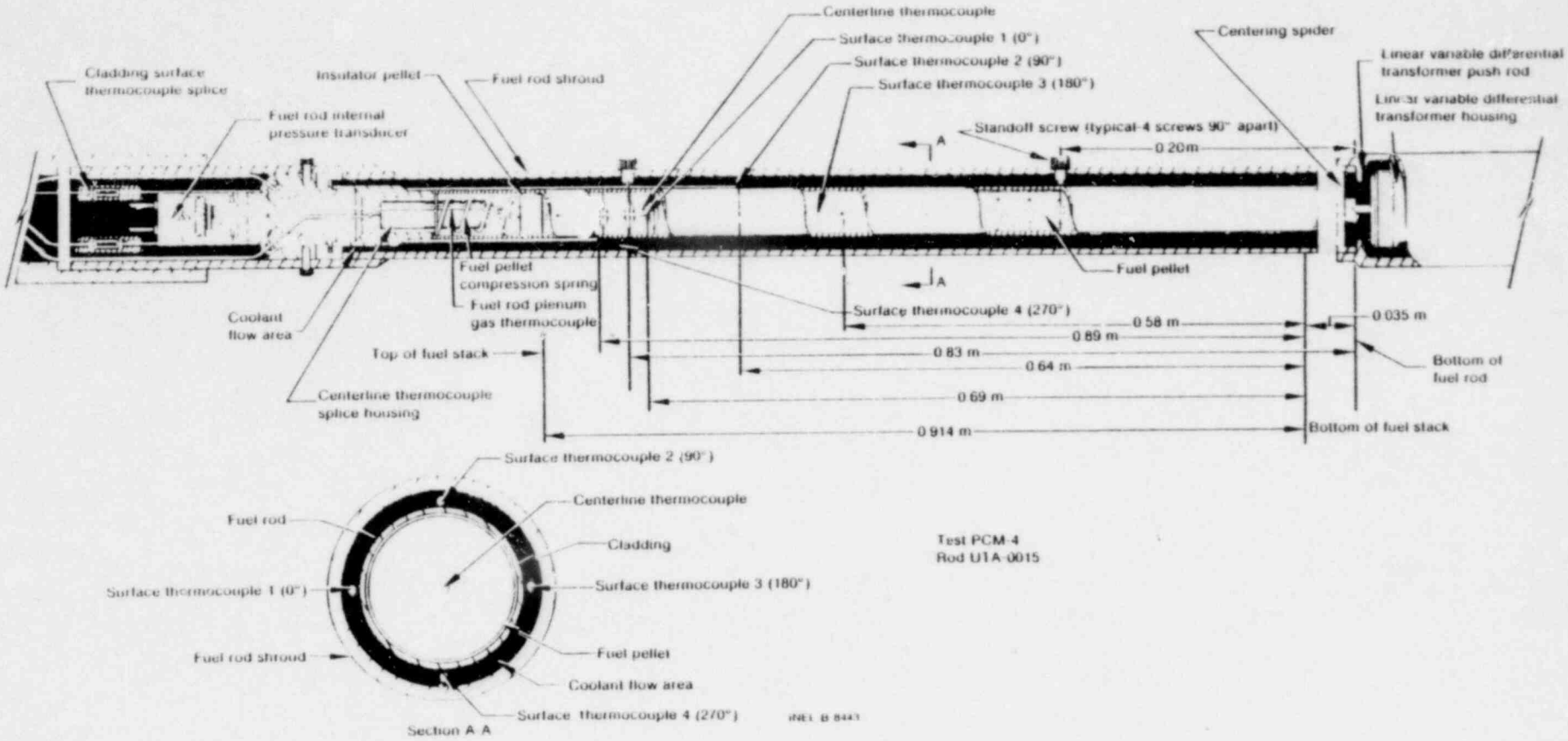

Fig. A-2 Test PCM-4 fuel rod and instrumentation shown installed in the flow shroud.

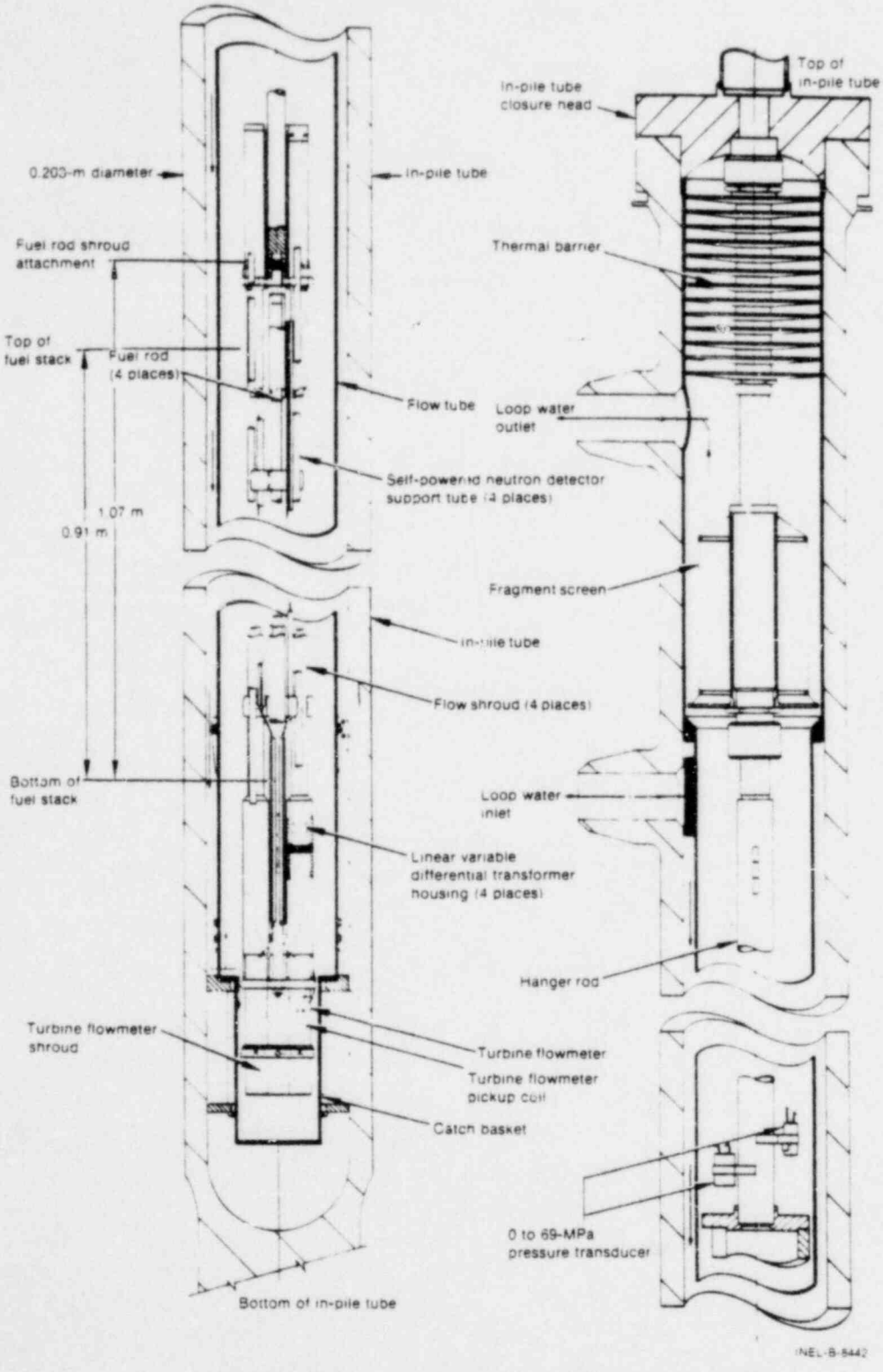

Fig. A-3 Test PCM-4 fuel rod and shroud assembly shown installed in the PBF in-pile test space

Nominal coolant conditions were adjusted to 2125 kg/(s·m^2), 15.0 MPa, and 600 K during the preconditioning operation. The reactor was operated for 15 h to induce fuel cracking and partial fuel restructuring. Four cycles were performed during the 15-h operation where the rod powers were initially increased to 43 kW/m at a nominal rate of 1 kW/(m·min), held at power for three hours and decreased to 3 kW/m at a rate of 1 kW/(m·min). The rod powers were cycled up after 20 min of operation at 3 kW/m.

After the power calibration and preconditioning operations were completed, the coolant inlet conditions and rod power were adjusted to perform cladding surface "aging" during nucleate boiling. Nominal coolant inlet conditions used during the aging operation were 2200 kg/(s·m^2), 15.1 MPa, and 600 K. The fuel rod powers were increased from 3 kW/m to a predetermined value at an average rate 3 kW/(m·min). The predetermined value was set at 47 kW/m, but due to a calibration error the rods exceeded the desired power level by 23 kW/m where DNB initiated. The rod powers were adjusted downward and the coolant flow was corrected to complete the aging operation. The power calibration error extended into all the pretest phases, and, as a result, the fuel rods were operated for the previous 15-h preconditioning phase under sustained nucleate boiling conditions.

DNB conditions were obtained by decreasing the coolant flow rate in small increments of approximately 5% at 60-s intervals while maintaining a nearly constant fuel rod power level (nominally 69 kW/m) until DNB was indicated. Four sequential flow reduction DNB test cycles were performed. Power, coolant inlet temperature, fuel centerline temperature, and coolant flow versus time for the test operation phases are illustrated in Figure A-4. DNB Cycles 1, 2, 3, and 4 were performed for rod powers of approximately 69, 69, 60, and 69 kW/m, respectively. Shortly after DNB was initiated during Cycles 1 and 2, DNB was eliminated by decreasing fuel rod powers and increasing the coolant mass flux to approximately 3000 kg/(s·m^2). DNB was eliminated in Cycle 3 by increasing the coolant mass flux while the rod powers were held constant.

During the first two DNB cycles, DNB was eliminated shortly after it occurred to prevent high post-DNB cladding temperatures by decreasing the fuel power and increasing the coolant mass flux to offset the boiling conditions. During Cycle 3, DNB was eliminated by increasing the coolant mass flux while the rod powers were held approximately constant. The fourth, and final, DNB cycle was performed by a step increase in the rod power at nominally constant coolant flow conditions. Cladding temperatures were allowed to equilibrate at values above 730 K for times in film boiling of 115 to 140 s before the reactor was scrammed to quench the DNB conditions. A summary of the experimental operating conditions and results is presented in Table A-1.

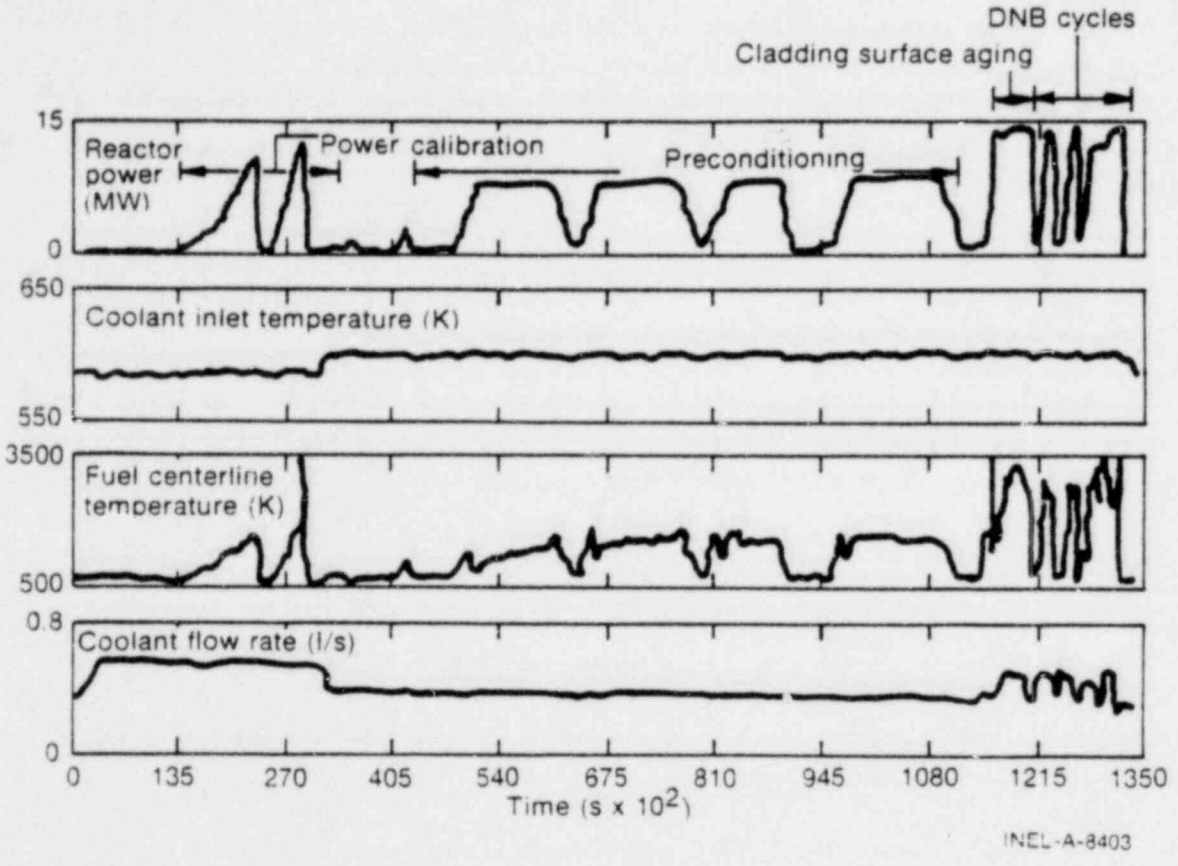

Fig. A-4 Composite plot of Test PCM-4 experimental conduct as a function of time during testing.

TABLE A-I

SUMMARY OF DNB TEST RESULTS FOR TEST PCM-4

DNB Cycle	Fuel Rod	Fuel Rod Peak Power (kw/m)	DNB Occurrence	Coolant Mass Flux at Onset of DNB [kg/(s·m^2)]	Minimum Coolant Mass Flux [kg/(s·m^2)]	Time in Film Boiling[a] (s)	Time after DNB(s)	Maximum Indicated Cladding Surface Temperature (K)	Location of Maximum Cladding Temperature (m)	Maximum Indicated Fuel Centerline Temperature (K)	Cladding Elongation After DNB (m)	Increase in Rod Internal Pressure After DNB (MPa)
Fuel Rod Aging	UTA-0014	74	Yes	2174	2114	0	75	660	0.483	[c]	0.0	--
	UTA-0015	70	Yes	2093	2049	0	45	729	0.635	[c]	0.090	--
	UTA-0016	71	Yes	2091	2062	0	25	660	0.686	2225	0.031	--
	A-0017	73	Yes	2073	2039	0	45	[b]	[b]	[b]	0.051	--
1	UTA-0014	71	No	[d]	1982	0	0	631	0.584	[c]	0	--
	UTA-0015	68	Yes	2043	1932	0	35	731	0.635	2000	0.052	--
	UTA-0016	68	No	[d]	1929	0	0	633	0.584	2350	0	--
	A-0017	70	Yes	2021	1906	0	245	[b]	[b]	[b]	0.027	--
2	UTA-0014	71	No	[d]	1952	0	0	632	0.584	[c]	0	--
	UTA-0015	68	Yes	1971	1899	0	140	703	0.635	2000	0.097	--
	UTA-0016	68	No	[d]	1906	0	0	633	0.584	2340	0	--
	A-0017	70	Yes	2021	1894	0	150	[b]	[b]	[b]	0.048	--
3	UTA-0014	61	No	[d]	1772	0	0	630	0.584	[c]	0	--
	UTA-0015	58	Yes	1777	1716	120	180	738	0.686	1720	0.009	--
	UTA-0016	59	No	[d]	1721	0	0	631	0.584	2110	0	--
	A-0017	60	No	[d]	1704	0	0	[b]	[b]	[b]	0	--
4	UTA-0014	71	Yes	1862	1658	115	160	930	0.584	[c]	0.116	0.24
	UTA-0015	67	Yes	2027	1610	160	280	1100	0.686	[c]	0.185	0.40
	UTA-0016	68	Yes	1848	1617	130	170	1005	0.584	2800	0.197	0.38
	A-0017	70	Yes	2044	1582	[b]	290	[b]	[b]	[b]	0.175	[b]

[a] Time that indicated cladding surface temperature exceeded 730 K.

[b] Fuel rod not instrumented.

[c] Instrumentation not functioning properly or erratic, or both.

[d] Fuel rod did not indicate DNB.

2. AXIAL POWER PROFILE

Power generation for each Test PCM-4 rod was determined by two methods: (a) a thermal hydraulic energy balance[A-2], dependent on single-phase coolant flow, pressure, inlet coolant temperature, coolant temperature rise, and the neutron flux axial profile; and (b) the posttest radiochemical analysis of selected fuel rod segments. A summary of the approximate steady state results obtained during the preconditioning operation is presented in Table A-II.

The fuel rod axial power profiles were determined using the activity profiles obtained by (a) radiochemical analysis of fuel samples from each rods, (b) gross gamma scans of one of the fuel rods from the test, and (c) the cobalt flux wire activation.

2.1 Radiochemical Analysis

The results of radiochemical analysis of one fuel sample from each test fuel rod are presented in Table A-III. The fissions per kilogram of total uranium, (T_U), based on the Zr-95 isotope, are converted in the table to burnup in fissions per cubic meter of UO_2 fuel and to megawatt days per metric ton of uranium (MWd/t). The burnup calculations were based on a value of 182.8 MeV/fission for the heat per fission that is released in the fuel.

2.2 Gross Gamma Scans

Rod A-0017 was gamma scanned horizontally in the 0 and 180° orientations to measure the relative level of gamma ray activity as a function of distance along the fuel stack. The scan was accomplished using a NaI scintillation detector coupled to a multichannel pulse height analyzer and strip chart recorder.

A Slo-Sync stepping motor provided the rod scanning drive and positioning mechanism, which allowed setting the test interval to ±,0.03 mm. The fuel rod was situated in front of the NaI collimator slit (0.051 x 1.270 mm) and the output of the NaI detector was recorded on the strip chart recorder as the fuel rod was driven past the detector-collimator window at a slow, constant rate. The strip chart recording speed was matched to the positioning rate (8.46 mm/s) of the fuel rod past the collimator. A standard Cs-137 source was monitored before and after the gamma scan to determine whether any electronic drift occurred during the scan.

The top and bottom of the fuel stack was identified by gamma counting, as the upper and lower ends of the fuel stack were step-scanned. A rapid change in the gamma ray intensity occurred at the end of the fuel stack. The fuel stack measured in this manner was 0.914 ± 0.005 m, compared with the 0.914 ± 0.003 m measured during fuel rod fabrication. Within the uncertainties of these measurements, no significant change in the fuel stack length was noted between the pre- and posttest values.

TABLE A-II

APPROXIMATE STEADY STATE TEST RESULTS OBTAINED DURING TEST PCM-4 PRECONDITIONING PERIOD

Preconditioning Cycle	Fuel Rod	Fuel Rod Peak Power (kW/m)	Average Coolant Mass Flux [kg/(s·m²)]	Coolant Inlet Temperature (K)	Coolant Temperature Rise (K)	Maximum Cladding Elongation (mm)	Change in Fuel Rod Internal Pressure (MPa)	Fuel Centerline Temperature (K)	Cladding Surface Temperature (K)					
									0.483-m 0°	0.584-m 90°	0.635-m 90°	0.686-m 180°	0.787-m 270°	0.889-m 270°
1	UTA-0014	44	2287	599.5	15.5	0.033	1.0	[a]	616	625	[b]	620	617	[b]
	UTA-0015	42	2200	599.5	15.0	0.033	2.91	1550	619	[b]	622	619	[b]	620
	UTA-0016	42	2241	599.5	15.0	0.050	1.87	1625	621	626	[b]	624	622	[b]
	A-0017	43	2206	599.5	15.4	[a]	[b]	[b]	[b]	[b]	[b]	[b]	[b]	[b]
2	UTA-0014	44	2241	599.5	13.7	0.023	0.84	[a]	615	624	[b]	620	617	[b]
	UTA-0015	42	2160	599.5	13.2	0.031	2.49	1550	619	[b]	622	619	[b]	620
	UTA-0016	42	2200	599.5	13.2	0.037	1.43	1640	621	626	[b]	624	621	[b]
	A-0017	43	2171	599.5	13.7	[a]	[b]	[b]	[b]	[b]	[b]	[b]	[b]	[b]
3	UTA-0014	44	2183	599.7	13.7	0.035	0.84	[a]	[a]	615	623	[b]	616	[b]
	UTA-0015	42	2091	599.7	13.5	0.031	2.50	1590	624	[b]	622	619	[b]	618
	UTA-0016	42	2131	599.7	13.6	0.025	1.44	1650	622	526	[b]	623	620	[b]
	A-0017	43	2102	599.7	14.0	[a]	[b]	[b]	[b]	[b]	[b]	[b]	[b]	[b]
4	UTA-0014	44	2166	599.7	15.0	0.027	1.0	[a]	615	623	[b]	619	617	[b]
	UTA-0015	42	2073	599.7	15.0	0.036	2.90	1600	619	[b]	623	620	[a]	619
	UTA-0016	42	2114	599.7	15.1	0.044	1.79	1660	622	627	[b]	624	622	[b]
	A-0017	43	2085	599.7	15.2	[a]	[b]	[b]	[b]	[b]	[b]	[b]	[b]	[b]

[a] Not functioning properly or erratic or both.

[b] Fuel rod not instrumented.

TABLE A-III

RADIOCHEMICAL ANALYSIS RESULTS

Rod	Distance from Bottom of Fuel Stack (m)	Isotopic Composition (at %)				Fissions per kg of T_U	Fissions per m^3 of UO_2 Fuel	Burnup (MWd/t)
		U-234	U-235	U-236	U-238			
UTA-0014	0.441-0.453	0.092	20.23	0.202	79.47	$1.73 (\pm 7.76 \times 10^{17}) 10^{20}$	$16.23 (10^{23})$	58.6[a]
UTA-0015	0.441-0.453	0.091	19.93	0.201	79.78	$1.78 (\pm 1.27 \times 10^{18}) 10^{20}$	$16.71 (10^{23})$	60.3
UTA-0016	0.441-0.453	0.091	19.79	0.201	79.92	$1.78 (\pm 1.27 \times 10^{18}) 10^{20}$	$16.71 (10^{23})$	60.3
A-0017	0.441-0.453	0.091	20.02	0.200	79.75	$1.53 (\pm 7.96 \times 10^{18}) 10^{20}$	$14.36 (10^{23})$	51.8

[a] Based on 182.8 MeV/fission.

In order to minimize the effects of bowing, Rod A-0017 was gamma scanned at two different orientations 180° apart, each normal to the plane of bow. Figures A-5 and A-6 present the results of the gross gamma scans for the two orientations, 0 and 180°, respectively. The activity profiles appear generally consistent with the expected axial power distribution. The periodic deviations from a smooth cosine curve in the gamma activity along the scan denote locations of fuel pellet interfaces. The presence of an axial gap in the fuel column would appear as a large negative deviation in the gamma activity at that location. A gap in the fuel column observed in the posttest neutrograph at Pellet 37 (between 0.562 and 0.569 m from the bottom of the fuel stack) was identified in the gross gamma scans of this fuel rod.

Results of the relative gamma activity along the scans compared with the average activity are presented in Tables A-IV and A-V. The fuel rod axial power profile obtained from the gamma scan data is related to the axial neutron flux profile, an important input parameter to the Fuel Rod Analysis Program-Transient (FRAP-T) code[A-4]. The axial peak-to-average ratio data from Tables A-IV and A-V indicate that the peak was located near 0.50 m from the bottom of the fuel stack, with a peak-to-average activity ratio of 1.22.

2.3 Flux Wire Gamma Scan

A 0.510% Co-Al flux wire was attached to the fuel rod and shroud assembly of Rod A-0017 for in-pile monitoring of the relative axial irradiation flux profile. After the test, the flux wire was removed and the gamma intensity was measured in 7.6-mm increments for one-minute-per-measurement intervals along the length of the wire, beginning at the bottom. The mean background count rate was 80 counts per minute. Table A-VI lists the cobalt flux wire scan data.

The thermal neutron fluence is determined by measuring the Co-60 activity induced by the activation of Co-59 in the wire. Since the wire is an alloy, the activity is corrected to yield disintegrations per second per mg of cobalt. The net rate of production of increase in Co-60 activity during reactor irradiation is given by

$$N = N_0 \sigma \phi \Delta t = N_0 \sigma F \qquad \text{(A-1)}$$

where

N = number of Co-60 atoms per unit volume following irradiation

Δt = incremental time (s)

N_0 = number of original Co-59 per unit volume

σ = cross section of Co-59 (37.3 barns)

ϕ = thermal neutron flux [$n/(cm^2 \cdot s)$].

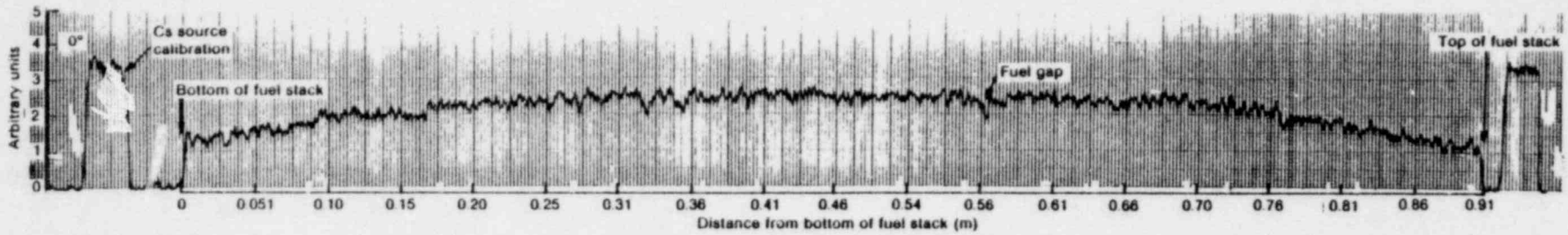

Fig. A-5 Gross gamma scan of Rod A-0017 at 0° orientation.

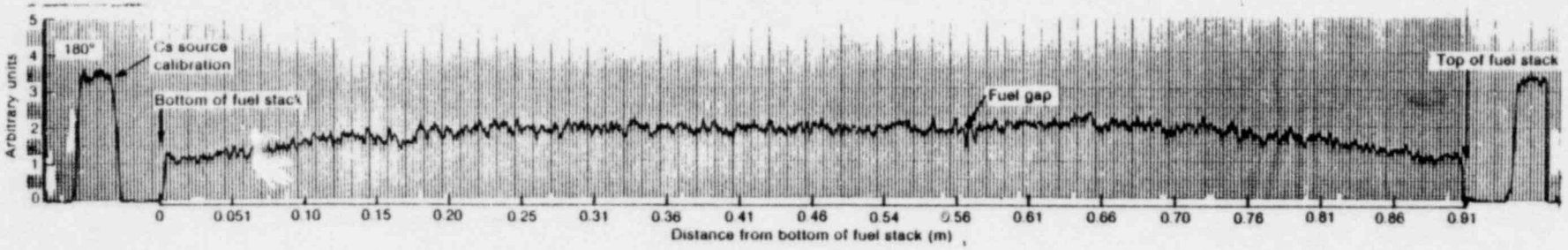

Fig. A-6 Gross gamma scan of Rod A-0017 at 180° orientation.

TABLE A-IV

GROSS GAMMA SCAN FOR ROD A-0017, 0° ORIENTATION

Distance from Bottom of Fuel Stack (m)	Peak Height (arbitrary units)	Peak Activity/ Average Activity[a]
0.0	0.0	0.0
0.0254	1.200	0.5622
0.0508	1.400	0.6559
0.0762	1.600	0.7495
0.1016	1.750	0.8198
0.1270	1.900	0.8901
0.1524	2.100	0.9838
0.1778	2.200	1.0306
0.2032	2.300	1.0775
0.2286	2.350	1.1009
0.2540	2.370	1.1103
0.2794	2.400	1.1243
0.3048	2.450	1.1477
0.3302	2.500	1.1712
0.3556	2.500	1.1712
0.3810	2.500	1.1712
0.4064	2.500	1.1712
0.4318	2.500	1.1712
0.4572	2.500	1.1712
0.4826	2.550	1.1946
0.5080	2.600	1.2180
0.5334	2.500	1.1712
0.5588	2.500	1.1712
0.5842	2.500	1.1712
0.6096	2.500	1.1712
0.6350	2.450	1.1477
0.6604	2.400	1.1243
0.6858	2.300	1.0775
0.7112	2.200	1.0306
0.7366	2.150	1.0072
0.7620	2.000	0.9369
0.7874	2.000	0.9369
0.8128	1.900	0.8901
0.8382	1.700	0.7964
0.8636	1.600	0.7495
0.8890	1.550	0.7261
0.9144	0.0	0.0

[a] The average gamma activity is 2.1346 arbitrary units.

TABLE A-V

GROSS GAMMA SCAN FOR ROD A-0017, 180° ORIENTATION

Distance from Bottom of Fuel Stack (m)	Peak Height (Arbitrary Units)	Peak Activity/ Average Activity[a]
0.0	0.0	0.0
0.0254	1.200	0.6750
0.0508	1.300	0.7313
0.0762	1.400	0.7875
0.1016	1.600	0.9000
0.1270	1.750	0.9844
0.1524	1.750	0.9844
0.1778	1.900	1.0688
0.2032	1.950	1.0969
0.2286	1.950	1.0969
0.2540	1.950	1.0969
0.2794	1.950	1.0969
0.3048	1.950	1.0969
0.3302	1.950	1.0969
0.3556	2.000	1.1250
0.3810	2.000	1.1250
0.4064	2.000	1.1250
0.4318	2.000	1.1250
0.4572	2.000	1.1250
0.4826	2.000	1.1250
0.5080	2.000	1.1250
0.5334	2.000	1.1250
0.5588	1.950	1.0969
0.5842	1.950	1.0969
0.6096	2.000	1.1250
0.6350	2.000	1.1250
0.6604	2.000	1.1250
0.6858	2.000	1.1250
0.7112	2.000	1.1250
0.7366	1.950	1.0969
0.7620	1.850	1.0406
0.7874	1.750	0.9844
0.8128	1.700	0.9563
0.8382	1.500	0.8438
0.8636	1.300	0.7313
0.8890	1.100	0.6188
0.9144	0.0	0.0

[a] The average gamma activity is 1.778 arbitrary units.

TABLE A-VI

FLUX WIRE GAMMA SCAN

Distance from Bottom of Wire (m)	Counts per Minute (10^4)	Distance from Bottom of Wire (m)	Counts per Minute (10^4)
0.025	1.434	0.353	3.753
0.033	1.512	0.361	3.771
0.041	1.572	0.368	3.779
0.048	1.616	0.376	3.779
0.056	1.709	0.384	3.782
0.064	1.771	0.391	3.775
0.071	1.834	0.399[a]	3.854
0.079	1.914	0.406	3.850
0.086	1.999	0.414	3.879
0.094	2.061	0.422	3.849
0.102	2.108	0.429	3.856
0.109	2.195	0.437	3.877
0.117	2.230	0.444	3.838
0.125	2.299	0.452	3.852
0.132	2.375	0.460	3.851
0.140	2.426	0.467	3.857
0.147	2.427	0.475	3.819
0.155	2.508	0.483	3.809
0.163	2.623	0.490	3.801
0.170	2.672	0.498	3.749
0.178	2.799	0.506	3.710
0.185	2.848	0.513	3.719
0.193	2.986	0.521	3.682
0.201	2.951	0.528	3.673
0.208	3.024	0.536	3.613
0.216	3.063	0.544	3.556
0.224	3.131	0.551	3.589
0.231	3.192	0.559	3.587
0.239	3.230	0.566	3.520
0.246	3.273	0.574	3.447
0.254	3.325	0.582	3.424
0.262	3.406	0.589	3.455
0.269	3.429	0.597	3.356
0.277	3.476	0.605	3.360
0.285	3.507	0.612	3.311
0.292	3.519	0.620	3.271
0.299	3.616	0.627	3.249
0.307	3.585	0.635	3.187
0.315	3.651	0.643	3.131
0.323	3.656	0.650	3.132
0.330	3.713	0.658	3.094
0.338	3.698	0.666	3.070
0.345	3.704	0.673	3.021

TABLE A-VI (continued)

Distance from Bottom of Wire (m)	Counts per Minute (10^4)	Distance from Bottom of Wire (m)	Counts per Minute (10^4)
0.681	2.958	0.795	2.071
0.688	2.896	0.803	2.001
0.696	2.836	0.810	1.936
0.704	2.769	0.818	1.903
0.711	2.743	0.826	1.827
0.719	2.683	0.833	1.781
0.726	2.647	0.841	1.706
0.734	2.568	0.848	1.649
0.742	2.531	0.856	1.590
0.749	2.454	0.864	1.502
0.757	2.395	0.871	1.454
0.765	2.334	0.879	1.396
0.772	2.259	0.887	1.333
0.780	2.212	0.894	1.286
0.787	2.121		

[a] $k_n = 4.374 \times 10^{13}$ (nvt)/counts per minute evaluated at this point.

The thermal neutron flux is proportional to the induced radioactivity of the cobalt flux wire. The time-integrated neutron flux

$$F = \phi \Delta t = \eta A \ (n/cm^2) \qquad \text{(A-2)}$$

was determined for a data point (0.399 m from the bottom of the wire), and was used to establish a conversion factor, K_n, for the scanned measurements, where A is the actual Co-60 activity [d/(mg·s)] and $\eta = 1.239 \times 10^{14}$ for 0.510% Co-Al wire. The K_n (nvt) factor is

$$K_n = \eta A/R$$
$$= F/R \qquad \text{(A-3)}$$

where R is the relative count monitored. The F(nvt) at 0.399 m was divided by the total counts per minute of the interval $K_n = 4.374 \times 10^{13}$. The ratio of (nvt) at a point along the wire to the total counts per minute at that point has been assumed to remain constant over the flux wire. To obtain thermal neutron fluence in neutrons/cm^2, K_n is multiplied by R (counts per minute).

Results of the normalization of the scan are presented in Table A-VII, which lists the normalized axial neutron flux profile determined from the ratio of the local neutron flux compared with the average flux along the wire and smoothed by fitting to a Fourier series curve. A neutron axial peak-to-average ratio of 1.361 was determined from these data, with the axial peak located 0.404 m from the bottom of the fuel stack. The discrepancy between the location and magnitude of the activity peak obtained from the cobalt flux wire and the location obtained from gross gamma scanning of Rod A-0017 is due to fuel rod bowing, since the accuracy of the gamma scan is reduced when the distance from the fuel rod to the scanning detector slit varies. The axial power profile determined from the normalized axial neutron flux is presented in Figure A-7.

TABLE A-VII

AXIAL NEUTRON FLUX PROFILE

Distance from Bottom of Fuel Stack (m)	Local Flux/Average Flux
0.061	0.643
0.0914	0.740
0.1219	0.833
0.1524	0.920
0.1829	1.048
0.2134	1.098
0.2438	1.166
0.2743	1.230
0.3048	1.281
0.3353	1.299
0.3658	1.326
0.3962	1.351
0.4038	1.361
0.4267	1.360
0.4572	1.353
0.4877	1.315
0.5182	1.289
0.5486	1.258
0.5791	1.212
0.6096	1.148
0.6401	1.099
0.6706	1.038
0.7010	0.962
0.7315	0.888
0.7620	0.792
0.7925	0.702
0.8230	0.625
0.3534	0.527
0.8839	0.451

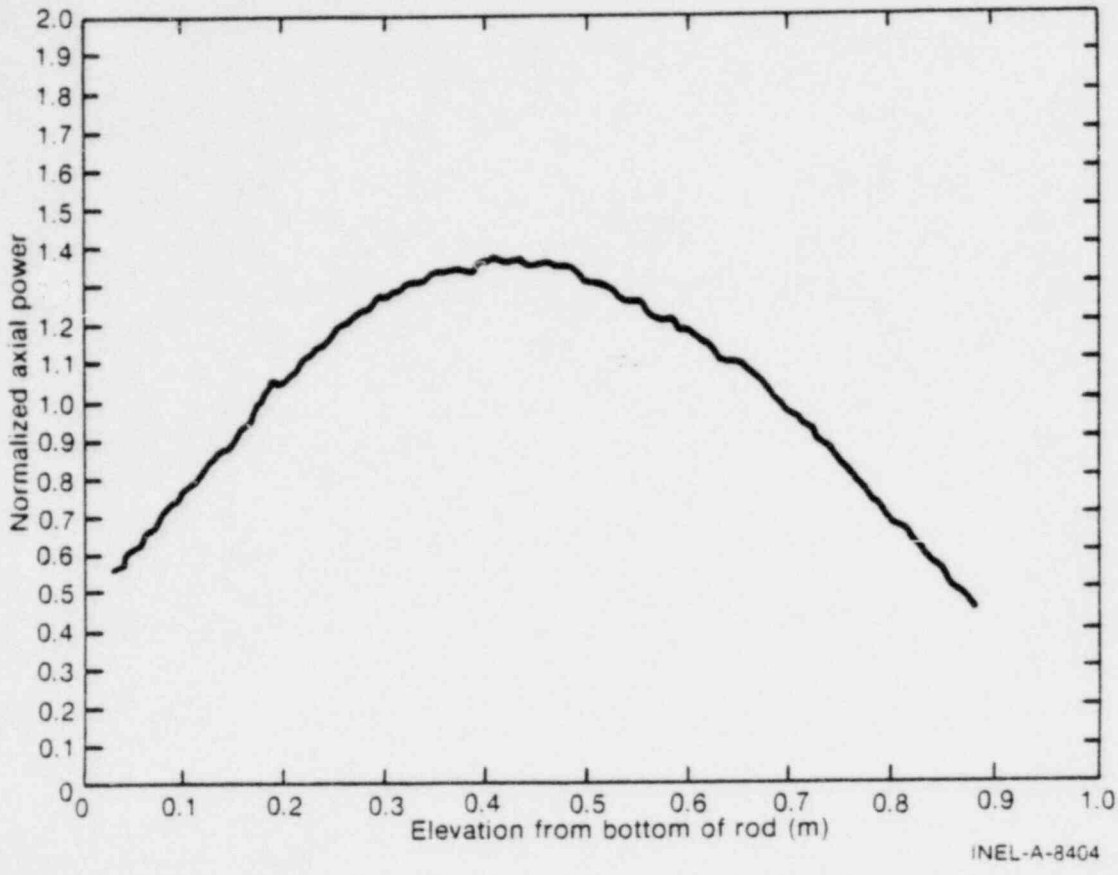

Fig. A-7 Axial power profile for Test PCM-4 determined from cobalt flux wire activation.

3. REFERENCES

A-1. T. G. Odekirk, *Detailed Test Plan Report for PBF Test Series, PCM-20: The Behavior of Unirradiation PWR Fuel Rods Under Power-Cooling-Mismatch Conditions*, ANCR-1095 (April 1974).

A-2. R. K. McCardell et al, *Thermal Fuels Behavior Program Test Results Report: Power-Coolant-Mismatch Series, Power Calibration Test*, ANCR-1248 (July 1975).

A-3. R. B. Remer, "The Effects of Power Transients on the Peak Heat Flux," *International Journal of Heat and Mass Transfer, 12* (1969) pp 953-964.

A-4. J. A. Dearien et al, *FRAP-T2: A Computer Code for the Transient Analysis of Oxide Fuel Rods*, TREE-NUREG-1040.

APPENDIX B

PRETEST FUEL ROD CHARACTERIZATION

APPENDIX B

PRETEST FUEL ROD CHARACTERIZATION

Preirradiation fuel rod characterization provides as-built referential information required for analytical model evaluation and for posttest comparison. Pretest measurements were made to characterize three of Test PCM-4 fuel rods, Rod UTA-0014, UTA-0015, and UTA-0016. The nominal physical characteristics of the fuel rod components are presented in this appendix to aid in posttest identification and evaluation, and for analytical model verification. The test fuel rod design data (nominal values) are presented in Table B-I.

The test fuel rods contained a 0.915-m-long fuel stack composed of 60 ceramic fuel pellets (93% theoretical density, 20% enriched UO_2) each nominally 9.30 mm in diameter and 15.49 mm long (the bottom pellets in each stack were partial pellets). The pellets were enclosed in a zircaloy-4 cladding tube of nominally 10.7-mm outside diameter and 0.61-mm wall thickness. The nominal fuel-cladding diametral gap was 0.2 mm.

The cladding inside diameters were measured at angular orientations of 0 to 90° at increments of 25.4 mm on each of the three characterized fuel rods. The cladding outside diameters were measured at two angular orientations (0 and 90°) at elevations of 0.025, 0.304, 0.609, and 0.914 m above the bottom of the cladding tube. The cladding inside diameter measurements were made with an air gauge (accuracy ± 2.5 μm) and the cladding outside diameter measurements were made with a micrometer (accuracy 0.03 mm). The cladding diameter measurements are presented for the three characterized rods in Tables B-II, B-III, and B-IV.

The physical dimensions (diameter, length, weight, and density) of the 60 pressurized water reactor type fuel pellets comprising the three characterized fuel rods are presented in Tables B-V, B-VI, and B-VII. The pellet data listed in these tables were obtained by measuring the length between the upper and lower dish shoulder of each pellet. Both the diametral and length measurements were preformed using a Bausch and Lomb optical gauge, Model BR-25. The measurements are accurate to ± 0.005 m. An analytical balance, accurate to ± 1 mg, was used to provide pellet mass data.

Pretest radiographs of the fuel columns in Rods UTA-0014, UTA-0015, and UTA-0016 are presented in Figures B-1, B-2, and B-3, respectively. The fuel pellets are numbered from the bottom of the stack in the sequence corresponding to that found in Tables B-V through B-VII.

TABLE B-I

TEST PCM-4 FUEL ROD COMPONENT NOMINAL DESIGN DATA

Fuel

Ceramic grade, dished and sintered uranium dioxide pellets.

Enrichment (wt% U-235 of total U)	19.87 ± 0.03
Uranium content (wt% U)	88.1 ± 0.2
Density (Mg/m^3)	10.2 ± 0.3
Pellet diameter (mm)	9.30 ± 0.01
Pellet length (mm)	15.5 ± 0.3
Dish depth (mm)	0.33 (nominal)
Total impurities (ppm)	>364
O:U ratio	2.002 ± 0.002

Cladding

Zircaloy-4 alloy manufactured to ASTM Standard B 353-69; Grade RA-2; 50% cold-worked and stress relieved; nominal values.

Inside diameter (mm)	9.49
Wall thickness (mm)	0.61
Yield strength (0.2% offset, MPa)	558
Tensile strength (MPa)	744
Elongation (%)	18
Hardness (R_B)	96

End Cap Rod Stock

Zircaloy-2 alloy manufactured to ASTM Standard B 351-67; Grade RA-1; annealed; nominal values.

Yield strength (0.2% offset, MPa)	341
Tensile strength (MPa)	531
Elongation (%)	25
Hardness (BHN)	176

TABLE B-I (continued)

Compression Springs

Oil-tempered, chromium-vanadium alloy spring steel manufactured to ASTM Standard A 231-68; nominal values.

Wire diameter (mm)	1.04
Tensile strength (MPa)	2041
Spring outside diameter (mm)	9.02
Free length (cm)	6.03
Total number coils	17

Insulating End Spacers

Coors Porcelain Co.; ceramic grade sintered alumina; nominal values.

Density (Mg/m^3)	3.90
Compressive strength (MPa)	2496
Length (mm)	6.35
Diameter (mm)	9.27

TABLE B-II

CLADDING INSIDE AND OUTSIDE DIAMETER DATA FOR ROD UTA-0014

Distance from Bottom of Cladding[a] (cm)	Cladding Inside Diameter (cm)		Cladding Outside Diameter (cm)	
	0°	90°	0°	90°
2.54	0.9496	0.9491	1.0751	1.0749
5.08	0.9496	0.9490		
7.62	0.9495	0.9492		
10.16	0.9499	0.9491		
12.70	0.9494	0.9489		
15.24	0.9493	0.9490		
17.78	0.9496	0.9490		
20.32	0.9495	0.9491		
22.86	0.9495	0.9488		
25.40	0.9495	0.9490		
27.94	0.9494	0.9493		
30.48	0.9493	0.9490	1.0750	1.0750
33.02	0.9495	0.9492		
35.56	0.9496	0.9492		
38.10	0.9494	0.9490		
40.64	0.9492	0.9491		
43.18	0.9493	0.9492		
45.72	0.9495	0.9492		
48.26	0.9492	0.9489		
50.80	0.9495	0.9491		
53.34	0.9493	0.9494		
55.88	0.9489	0.9490		
58.42	0.9494	0.9492		
60.96	0.9496	0.9489	1.0752	1.0748
63.50	0.9495	0.9487		
66.04	0.9495	0.9488		
68.58	0.9498	0.9489		
71.12	0.9494	0.9487		
73.66	0.9496	0.9487		
76.20	0.9496	0.9490		
78.74	0.9497	0.9491		
81.28	0.9497	0.9485		
83.82	0.9495	0.9487		
86.36	0.9496	0.9488		
88.90	0.9494	0.9488		
91.44	0.9495	0.9490	1.0747	1.0748
93.98	0.9492	0.9493		
96.52	0.9491	0.9493		

[a] The total tube length for Rod UTA-0014 was 99.358 cm.

TABLE B-III

CLADDING INSIDE AND OUTSIDE DIAMETER DATA FOR ROD UTA-0015

Distance from Bottom of Cladding[a] (cm)	Cladding Inside Diameter (cm)		Cladding Outside Diameter (cm)	
	0°	90°	0°	90°
2.54	0.9491	0.9493	1.0700	1.0704
5.08	0.9496	0.9490		
7.62	0.9497	0.9488		
10.16	0.9495	0.9491		
12.70	0.9495	0.9489		
15.24	0.9494	0.9490		
17.78	0.9497	0.9488		
20.32	0.9494	0.9489		
22.86	0.9492	0.9492		
25.40	0.9494	0.9489		
27.94	0.9492	0.9488		
30.48	0.9488	0.9491	1.0698	1.0706
33.02	0.9489	0.9492		
35.56	0.9495	0.9489		
38.10	0.9491	0.9493		
40.64	0.9491	0.9491		
43.18	0.9491	0.9495		
45.72	0.9494	0.9492		
48.26	0.9491	0.9496		
50.80	0.9492	0.9495		
53.34	0.9489	0.9495		
55.88	0.9489	0.9497		
58.42	0.9488	0.9495		
60.96	0.9491	0.9492	1.0698	1.0704
63.50	0.9492	0.9489		
66.04	0.9494	0.9490		
68.58	0.9495	0.9488		
71.12	0.9493	0.9492		
73.66	0.9495	0.9491		
76.20	0.9495	0.9491		
78.74	0.9495	0.9491		
81.28	0.9494	0.9490		
83.82	0.9493	0.9492		
86.36	0.9495	0.9488		
88.90	0.9492	0.9490		
91.44	0.9492	0.9493	1.0692	1.0699
93.98	0.9488	0.9491		
96.52	0.9490	0.9492		

[a] The total tube length for Rod UTA-0015 was 99.863 cm.

TABLE B-IV

CLADDING INSIDE AND OUTSIDE DIAMETER DATA FOR ROD UTA-0016

Distance from Bottom of Cladding[a] (cm)	Cladding Inside Diameter (cm)		Cladding Outside Diameter (cm)	
2.54	0.9499	0.9492	1.0757	1.0757
5.08	0.9499	0.9495		
7.62	0.9498	0.9492		
10.16	0.9497	0.9492		
12.70	0.9496	0.9494		
15.24	0.9498	0.9494		
17.78	0.9488	0.9494		
20.32	0.9495	0.9495		
22.86	0.9497	0.9496		
25.40	0.9493	0.9496		
27.94	0.9491	0.9495		
30.48	0.9493	0.9499	1.0758	1.0760
33.02	0.9496	0.9499		
35.56	0.9492	0.9499		
38.10	0.9493	0.9500		
40.64	0.9493	0.9499		
43.18	0.9493	0.9503		
45.72	0.9491	0.9501		
48.26	0.9490	0.9500		
50.80	0.9497	0.9498		
53.34	0.9495	0.9498		
55.88	0.9493	0.9498		
58.42	0.9495	0.9502		
60.96	0.9493	0.9501	1.0758	1.0759
63.50	0.9495	0.9499		
66.04	0.9495	0.9498		
68.58	0.9498	0.9498		
71.12	0.9498	0.9496		
73.66	0.9495	0.9496		
76.20	0.9494	0.9500		
78.74	0.9497	0.9497		
81.28	0.9498	0.9495		
83.82	0.9496	0.9497		
86.36	0.9495	0.9498		
88.90	0.9497	0.9497		
91.44	0.9496	0.9495	1.0760	1.0755
93.98	0.9496	0.9499		
96.52	0.9498	0.9501		

[a] The total tube length for Rod UTA-0016 was 99.860 cm.

TABLE B-V

PHYSICAL CHARACTERIZATION DATA FOR ROD UIA-0014

Pellet[a]	Diameter (cm)				Length (cm)			Weight (g)	Geometric Density (g/cm^3)	Immersion Density (g/cm^3)	Centerline Hole Diameter (cm)	
	Top	Center	Bottom	Average	0°	90°	Average				Top	Bottom
1	0.9299	0.9299	0.9299	0.9299	0.6495	0.6248	0.6372	4.3258	10.2768	--	0.0	0.0
2	0.9289	0.9294	0.9286	0.9290	1.5400	1.5390	1.5395	10.6144	10.2888	--	0.0	0.0
3	0.9301	0.9301	0.9296	0.9300	1.5392	1.5349	1.5371	10.5733	10.2426	--	0.0	0.0
4	0.9301	0.9301	0.9301	0.9301	1.5347	1.5326	1.5337	10.5258	10.2159	--	0.0	0.0
5	0.9301	0.9304	0.9301	0.9302	1.5413	1.5377	1.5395	10.6440	10.2891	10.3429	0.0	0.0
6	0.9299	0.9301	0.9299	0.9300	1.5359	1.5377	1.5368	10.5950	10.2653	--	0.0	0.0
7	0.9301	0.9296	0.9299	0.9299	1.5400	1.5420	1.5410	10.6190	10.2622	--	0.0	0.0
8	0.9291	0.9296	0.9296	0.9295	1.5372	1.5387	1.5380	10.5794	10.2538	--	0.0	0.0
9	0.9296	0.9296	0.9299	0.9297	1.5395	1.5408	1.5401	10.5949	10.2436	--	0.0	0.0
10	0.9299	0.9294	0.9296	0.9296	1.5448	1.5479	1.5464	10.6443	10.2564	10.3160	0.0	0.0
11	0.9299	0.9301	0.9307	0.9302	1.5380	1.5392	1.5386	10.5736	10.2270	--	0.0	0.0
12	0.9304	0.9307	0.9301	0.9304	1.5357	1.5387	1.5372	10.5693	10.2284	--	0.0	0.0
13	0.9301	0.9304	0.9299	0.9301	1.5344	1.5372	1.5358	10.5828	10.2566	--	0.0	0.0
14	0.9301	0.9304	0.9301	0.9302	1.5370	1.5392	1.5381	10.5963	10.2524	--	0.0	0.0
15	0.9291	0.9291	0.9289	0.9290	1.5354	1.5362	1.5358	10.5450	10.2445	10.2909	0.0	0.0
16	0.9296	0.9299	0.9299	0.9298	1.5380	1.5403	1.5391	10.5961	10.2548	--	0.0	0.0
17	0.9301	0.9309	0.9301	0.9304	1.5370	1.5400	1.5385	10.5547	10.2058	--	0.0	0.0
18	0.9281	0.9286	0.9279	0.9282	1.5395	1.5418	1.5406	10.5610	10.2464	--	0.0	0.0
19	0.9296	0.9301	0.9299	0.9299	1.5474	1.5502	1.5488	10.6848	10.2735	--	0.0	0.0
20	0.9304	0.9307	0.9304	0.9305	1.5362	1.5395	1.5378	10.5591	10.2124	10.2794	0.0	0.0
21	0.9291	0.9291	0.9289	0.9290	1.5481	1.5494	1.5488	10.6486	10.2576	--	0.0	0.0
22	0.9304	0.9304	0.9301	0.9303	1.5420	1.5438	1.5429	10.6453	10.2653	--	0.0	0.0
23	0.9299	0.9304	0.9307	0.9303	1.5359	1.5395	1.5377	10.6093	10.2656	--	0.0	0.0
24	0.9307	0.9307	0.9307	0.9307	1.5288	1.5309	1.5298	10.5586	10.2622	--	0.0	0.0
25	0.9299	0.9301	0.9296	0.9299	1.5286	1.5301	1.5293	10.5362	10.2608	10.3085	0.0	0.0
26	0.9304	0.9307	0.9307	0.9306	1.5372	1.5387	1.5380	10.6421	10.2900	--	0.0	0.0
27	0.9304	0.9304	0.9299	0.9302	1.5331	1.5347	1.5339	10.6021	10.2863	--	0.0	0.0
28	0.9304	0.9307	0.9304	0.9305	1.5352	1.5372	1.5362	10.6268	10.2891	--	0.0	0.0
29	0.9304	0.9307	0.9304	0.9305	1.5321	1.5339	1.5330	10.5603	10.2461	--	0.0	0.0
30	0.9299	0.9301	0.9299	0.9300	1.5415	1.5428	1.5422	10.6014	10.2356	10.3085	0.0	0.0
31	0.9296	0.9296	0.9299	0.9297	1.5314	1.5326	1.5320	10.5864	10.2954	--	0.0	0.0
32	0.9301	0.9304	0.9304	0.9303	1.5362	1.5387	1.5375	10.6015	10.2598	--	0.0	0.0
33	0.9299	0.9301	0.9299	0.9300	1.5375	1.5395	1.5385	10.6043	10.2632	--	0.0	0.0
34	0.9299	0.9301	0.9299	0.9300	1.5337	1.5359	1.5348	10.5664	10.2513	--	0.0	0.0
35	0.9301	0.9307	0.9301	0.9303	1.5397	1.5408	1.5403	10.6244	10.2631	10.3259	0.0	0.0
36	0.9307	0.9307	0.9301	0.9305	1.5354	1.5372	1.5363	10.6221	10.2837	--	0.0	0.0
37	0.9307	0.9299	0.9286	0.9297	1.5296	1.5334	1.5315	10.5682	10.2811	--	0.0	0.0

TABLE B-V (continued)

Pellet[a]	Diameter (cm)				Length (cm)			Weight (g)	Geometric Density (g/cm^3)	Immersion Density (g/cm^3)	Centerline Hole Diameter (cm)	
	Top	Center	Bottom	Average	0°	90°	Average				Top	Bottom
38	0.9299	0.9301	0.9301	0.9301	1.5481	1.5512	1.5497	10.6864	10.2653	--	0.0	0.0
39	0.9299	0.9299	0.9299	0.9299	1.5380	1.5395	1.5387	10.1757	10.2479	10.1602	0.1829	0.1854
40	0.9299	0.9299	0.9299	0.9299	1.5397	1.5420	1.5409	10.1219	10.1966	10.1748	0.1854	0.1905
41	0.9296	0.9296	0.9296	0.9296	1.5331	1.5354	1.5343	10.1330	10.2407	10.0793	0.1829	0.1854
42	0.9296	0.9296	0.9296	0.9296	1.5347	1.5372	1.5359	10.1218	10.2298	10.2367	0.1854	0.1880
43	0.9296	0.9291	0.9291	0.9293	1.5375	1.5400	1.5387	10.1459	10.2374	10.2454	0.1829	0.1880
44	0.9296	0.9296	0.9296	0.9296	1.5344	1.5372	1.5358	10.1410	10.2500	10.2769	0.1854	0.1880
45	0.9291	0.9291	0.9291	0.9291	1.5357	1.5370	1.5363	10.1261	10.2433	10.2764	0.1854	0.1880
46	0.9296	0.9296	0.9296	0.9296	1.5405	1.5423	1.5414	10.1790	10.2222	10.3102	0.1778	0.1829
47	0.9294	0.9294	0.9294	0.9294	1.5461	1.5491	1.5476	10.1958	10.2033	10.3157	0.1778	0.1829
48	0.9291	0.9291	0.9291	0.9291	1.5375	1.5390	1.5382	10.1307	10.2469	10.2835	0.1880	0.1905
49	0.9296	0.9296	0.9296	0.9296	1.5433	1.5453	1.5443	10.1744	10.2441	10.3511	0.1880	0.1930
50	0.9296	0.9296	0.9296	0.9296	1.5377	1.5392	1.5385	10.1487	10.2113	10.2914	0.1778	0.1829
51	0.9294	0.9294	0.9294	0.9294	1.5380	1.5395	1.5387	10.1617	10.2399	10.3129	0.1803	0.1854
52	0.9294	0.9294	0.9294	0.9294	1.5352	1.5370	1.5361	10.0369	10.1606	10.2632	0.1880	0.1905
53	0.9299	0.9299	0.9299	0.9299	1.5375	1.5400	1.5387	10.1836	10.2277	10.3078	0.1727	0.1829
54	0.9294	0.9299	0.9299	0.9297	1.5400	1.5436	1.5418	10.1602	10.2157	10.3188	0.1803	0.1880
55	0.9289	0.9289	0.9289	0.9289	1.5410	1.5433	1.5422	10.1190	10.2086	10.2455	0.1880	0.1880
56	0.9294	0.9294	0.9294	0.9294	1.5405	1.5433	1.5419	10.1663	10.2463	10.2851	0.1854	0.1905
57	0.9294	0.9294	0.9294	0.9294	1.5362	1.5377	1.5370	10.1391	10.2580	10.2900	0.1880	0.1905
58	0.9294	0.9294	0.9294	0.9294	1.5349	1.5370	1.5359	10.1621	10.2591	10.2514	0.1778	0.1880
59	0.9294	0.9294	0.9294	0.9294	1.5364	1.5392	1.5378	10.1358	10.2370	10.2709	0.1854	0.1880
60	0.9294	0.9294	0.9294	0.9294	1.5296	1.5370	1.5333	10.1011	10.2327	10.2860	0.1829	0.1905

[a] Pellets are numbered from bottom to top of fuel stack.

TABLE B-VI

PHYSICAL CHARACTERIZATION DATA FOR ROD UTA-0015

Pellet[a]	Diameter (cm)				Length (cm)			Weight (g)	Geometric Density (g/cm^3)	Immersion Density (g/cm^3)	Centerline Hole Diameter (cm)	
	Top	Center	Bottom	Average	0°	90°	Average				Top	Bottom
1	0.9286	0.9286	0.9286	0.9286	0.6754	0.6894	0.6824	4.6591	10.3451	--	0.0	0.0
2	0.9289	0.9289	0.9289	0.9289	1.5349	1.5367	1.5358	10.5162	10.2202	--	0.0	0.0
3	0.9304	0.9304	0.9304	0.9304	1.5420	1.5441	1.5430	10.5939	10.2130	--	0.0	0.0
4	0.9307	0.9304	0.9304	0.9305	1.5326	1.5344	1.5335	10.5406	10.2236	--	0.0	0.0
5	0.9299	0.9301	0.9304	0.9301	1.5352	1.5380	1.5366	10.5868	10.2553	10.3051	0.0	0.0
6	0.9304	0.9304	0.9304	0.9304	1.5382	1.5418	1.5400	10.5882	10.2279	--	0.0	0.0
7	0.9301	0.9299	0.9299	0.9300	1.5448	1.5469	1.5458	10.6620	10.2693	--	0.0	0.0
8	0.9304	0.9304	0.9301	0.9303	1.5425	1.5446	1.5436	10.6087	10.2257	--	0.0	0.0
9	0.9307	0.9307	0.9307	0.9307	1.5400	1.5430	1.5415	10.5965	10.2201	--	0.0	0.0
10	0.9299	0.9301	0.9304	0.9301	1.5339	1.5354	1.5347	10.5491	10.2316	10.2835	0.0	0.0
11	0.9304	0.9301	0.9301	0.9302	1.5430	1.5453	1.5442	10.6483	10.2615	--	0.0	0.0
12	0.9299	0.9307	0.9307	0.9304	1.5387	1.5400	1.5394	10.5775	10.2219	--	0.0	0.0
13	0.9304	0.9304	0.9304	0.9304	1.5326	1.5334	1.5330	10.5453	10.2334	--	0.0	0.0
14	0.9296	0.9294	0.9291	0.9294	1.5347	1.5367	1.5357	10.5274	10.2207	--	0.0	0.0
15	0.9301	0.9301	0.9301	0.9301	1.5453	1.5481	1.5467	10.6686	10.2659	10.3373	0.0	0.0
16	0.9304	0.9304	0.9304	0.9304	1.5309	1.5329	1.5319	10.5543	10.2499	--	0.0	0.0
17	0.9301	0.9301	0.9301	0.9301	1.5400	1.5428	1.5414	10.6352	10.2696	--	0.0	0.0
18	0.9296	0.9294	0.9294	0.9295	1.5370	1.5405	1.5387	10.5869	10.2560	--	0.0	0.0
19	0.9304	0.9304	0.9304	0.9304	1.5375	1.5420	1.5397	10.6253	10.2655	--	0.0	0.0
20	0.9301	0.9301	0.9319	0.9307	1.5342	1.5375	1.5358	10.5716	10.2325	10.3044	0.0	0.0
21	0.9304	0.9304	0.9304	0.9304	1.5339	1.5359	1.5349	10.5839	10.2580	--	0.0	0.0
22	0.9299	0.9301	0.9301	0.9301	1.5314	1.5337	1.5325	10.5867	10.2846	--	0.0	0.0
23	0.9304	0.9304	0.9304	0.9304	1.5331	1.5364	1.5348	10.5753	10.2505	--	0.0	0.0
24	0.9301	0.9301	0.9301	0.9301	1.5395	1.5423	1.5409	10.6101	10.2488	--	0.0	0.0
25	0.9299	0.9299	0.9299	0.9299	1.5395	1.5420	1.5408	10.5960	10.2417	10.3020	0.0	0.0
26	0.9299	0.9299	0.9299	0.9299	1.5326	1.5392	1.5359	10.5577	10.2371	--	0.0	0.0
27	0.9304	0.9304	0.9304	0.9304	1.5281	1.5311	1.5296	10.5651	10.2759	--	0.0	0.0
28	0.9301	0.9304	0.9304	0.9303	1.5359	1.5387	1.5373	10.5753	10.2353	--	0.0	0.0
29	0.9299	0.9299	0.9299	0.9299	1.5354	1.5413	1.5384	10.5974	10.2593	--	0.0	0.0
30	0.9301	0.9301	0.9296	0.9300	1.5413	1.5423	1.5418	10.6576	10.2924	10.3634	0.0	0.0
31	0.9291	0.9291	0.9291	0.9291	1.5390	1.5430	1.5410	10.5516	10.2140	--	0.0	0.0
32	0.9294	0.9294	0.9294	0.9294	1.5410	1.5433	1.5422	10.5739	10.2222	--	0.0	0.0
33	0.9299	0.9299	0.9299	0.9299	1.5362	1.5387	1.5375	10.5765	10.2450	--	0.0	0.0
34	0.9291	0.9291	0.9289	0.9290	1.5354	1.5377	1.5366	10.5128	10.2081	--	0.0	0.0
35	0.9299	0.9304	0.9304	0.9302	1.5375	1.5385	1.5380	10.5900	10.2471	10.2392	0.0	0.0
36	0.9296	0.9296	0.9296	0.9296	1.5420	1.5456	1.5438	10.6090	10.2394	--	0.0	0.0
37	0.9291	0.9291	0.9291	0.9291	1.5359	1.5387	1.5373	10.0729	10.1712	10.3017	0.1829	0.1854

TABLE B-VI (continued)

Pellet[a]	Diameter (cm)				Length (cm)			Weight (g)	Geometric Density (g/cm^3)	Immersion Density (g/cm^3)	Centerline Hole Diameter (cm)	
	Top	Center	Bottom	Average	0°	90°	Average				Top	Bottom
38	0.9296	0.9296	0.9296	0.9296	1.5347	1.5372	1.5359	10.1190	10.2154	10.2887	0.1829	0.1854
39	0.9289	0.9289	0.9289	0.9289	1.5359	1.5377	1.5368	10.1221	10.2418	10.2667	0.1854	0.1880
40	0.9296	0.9296	0.9296	0.9296	1.5415	1.5430	1.5423	10.1759	10.2358	10.2690	0.1829	0.1880
41	0.9294	0.9294	0.9294	0.9294	1.5372	1.5390	1.5381	10.1377	10.2314	10.2857	0.1829	0.1880
42	0.9294	0.9294	0.9294	0.9294	1.5362	1.5410	1.5386	10.1292	10.2137	10.2468	0.1829	0.1854
43	0.9294	0.9296	0.9296	0.9296	1.5339	1.5375	1.5357	10.1579	10.2584	10.2034	0.1829	0.1854
44	0.9289	0.9296	0.9296	0.9294	1.5385	1.5415	1.5400	10.1338	10.2204	10.2515	0.1854	0.1880
45	0.9291	0.9291	0.9291	0.9291	1.5392	1.5428	1.5410	10.1336	10.2135	10.2471	0.1854	0.1854
46	0.9291	0.9291	0.9291	0.9291	1.5362	1.5382	1.5372	10.1430	10.2429	10.2764	0.1829	0.1854
47	0.9296	0.9296	0.9296	0.9296	1.5283	1.5301	1.5292	10.0877	10.2349	10.2926	0.1829	0.1880
48	0.9294	0.9294	0.9294	0.9294	1.5408	1.5430	1.5419	10.1782	10.2466	10.3331	0.1829	0.1880
49	0.9291	0.9291	0.9291	0.9291	1.5359	1.5385	1.5372	10.1442	10.2384	10.2755	0.1803	0.1854
50	0.9296	0.9296	0.9296	0.9296	1.5337	1.5359	1.5348	10.1496	10.2483	10.2560	0.1803	0.1854
51	0.9289	0.9289	0.9294	0.9290	1.5425	1.5443	1.5434	10.1819	10.2365	10.3253	0.1778	0.1880
52	0.9289	0.9289	0.9289	0.9289	1.5392	1.5405	1.5399	10.1713	10.2479	10.3036	0.1778	0.1854
53	0.9296	0.9296	0.9296	0.9296	1.5347	1.5382	1.5364	10.1590	10.2354	10.2937	0.1778	0.1829
54	0.9296	0.9296	0.9296	0.9296	1.5479	1.5514	1.5497	10.2483	10.2420	10.2900	0.1778	0.1854
55	0.9294	0.9294	0.9294	0.9294	1.5557	1.5585	1.5571	10.3250	10.2800	10.3421	0.1803	0.1854
56	0.9296	0.9294	0.9294	0.9295	1.5339	1.5357	1.5348	10.1511	10.2538	10.2836	0.1803	0.1854
57	0.9294	0.9294	0.9294	0.9294	1.5324	1.5354	1.5339	10.1317	10.2421	10.2514	0.1803	0.1854
58	0.9291	0.9291	0.9291	0.9291	1.5504	1.5524	1.5514	10.2485	10.2421	10.2871	0.1778	0.1854
59	0.9294	0.9294	0.9294	0.9294	1.5433	1.5469	1.5451	10.1726	10.2140	10.3190	0.1829	0.1854
60	0.9284	0.9291	0.9291	0.9289	1.5301	1.5334	1.5317	10.0917	10.2337	10.2809	0.1829	0.1854

[a] Pellets are numbered from bottom to top of fuel stack.

TABLE B-VII

PHYSICAL CHARACTERIZATION DATA FOR ROD UTA-0016

Pellet[a]	Diameter (cm)				Length (cm)			Weight (g)	Geometric Density (g/cm^3)	Immersion Density (g/cm^3)	Centerline Hole Diameter (cm)	
	Top	Center	Bottom	Average	0°	90°	Average				Top	Bottom
1	0.9299	0.9299	0.9299	0.9299	0.5456	0.5667	0.5561	3.7979	10.3796	--	0.0	0.0
2	0.9301	0.9307	0.9307	0.9305	1.5334	1.5357	1.5345	10.6122	10.2861	--	0.0	0.0
3	0.9284	0.9299	0.9301	0.9295	1.5329	1.5362	1.5345	10.5594	10.2576	--	0.0	0.0
4	0.9294	0.9301	0.9301	0.9299	1.5372	1.5392	1.5382	10.5943	10.2571	--	0.0	0.0
5	0.9299	0.9299	0.9294	0.9297	1.5344	1.5380	1.5362	10.6147	10.2944	10.3353	0.0	0.0
6	0.9307	0.9304	0.9299	0.9303	1.5334	1.5359	1.5347	10.5629	10.2412	--	0.0	0.0
7	0.9284	0.9294	0.9301	0.9293	1.5494	1.5524	1.5509	10.6603	10.2488	--	0.0	0.0
8	0.9301	0.9304	0.9304	0.9303	1.5392	1.5413	1.5403	10.6035	10.2429	--	0.0	0.0
9	0.9304	0.9307	0.9307	0.9306	1.5453	1.5497	1.5475	10.7023	10.2837	--	0.0	0.0
10	0.9309	0.9312	0.9307	0.9309	1.5344	1.5370	1.5357	10.6013	10.2584	10.3323	0.0	0.0
11	0.9301	0.9304	0.9304	0.9303	1.5314	1.5337	1.5325	10.5540	10.2472	--	0.0	0.0
12	0.9309	0.9309	0.9304	0.9307	1.5278	1.5293	1.5286	10.5569	10.2673	--	0.0	0.0
13	0.9304	0.9307	0.9304	0.9305	1.5334	1.5357	1.5345	10.5712	10.2464	--	0.0	0.0
14	0.9309	0.9307	0.9304	0.9307	1.5291	1.5309	1.5300	10.5712	10.2736	--	0.0	0.0
15	0.9307	0.9309	0.9307	0.9307	1.5329	1.5359	1.5344	10.6031	10.2725	10.3321	0.0	0.0
16	0.9307	0.9304	0.9296	0.9302	1.5375	1.5390	1.5382	10.5828	10.2384	--	0.0	0.0
17	0.9304	0.9309	0.9301	0.9305	1.5311	1.5334	1.5323	10.5405	10.2320	--	0.0	0.0
18	0.9304	0.9299	0.9291	0.9298	1.5382	1.5397	1.5390	10.5562	10.2170	--	0.0	0.0
19	0.9301	0.9304	0.9304	0.9303	1.5489	1.5519	1.5504	10.6800	10.2484	--	0.0	0.0
20	0.9296	0.9304	0.9307	0.9302	1.5410	1.5448	1.5429	10.6412	10.2632	10.3177	0.0	0.0
21	0.9289	0.9289	0.9291	0.9290	1.5349	1.5367	1.5358	10.5146	10.2168	--	0.0	0.0
22	0.9296	0.9301	0.9304	0.9301	1.5339	1.5359	1.5349	10.5583	10.2407	--	0.0	0.0
23	0.9299	0.9294	0.9281	0.9291	1.5357	1.5382	1.5370	10.5950	10.2834	--	0.0	0.0
24	0.9304	0.9307	0.9281	0.9297	1.5385	1.5410	1.5397	10.6000	10.2561	--	0.0	0.0
25	0.9309	0.9312	0.9307	0.9309	1.5367	1.5390	1.5378	10.5224	10.2159	10.2799	0.0	0.0
26	0.9291	0.9301	0.9304	0.9299	1.5392	1.5403	1.5397	10.6135	10.2654	--	0.0	0.0
27	0.9299	0.9301	0.9304	0.9301	1.5316	1.5331	1.5324	10.5341	10.2325	--	0.0	0.0
28	0.9299	0.9304	0.9304	0.9302	1.5438	1.5471	1.5455	10.6475	10.2522	--	0.0	0.0
29	0.9304	0.9304	0.9304	0.9304	1.5443	1.5474	1.5458	10.6490	10.2473	--	0.0	0.0
30	0.9301	0.9304	0.9301	0.9302	1.5306	1.5349	1.5328	10.5816	10.2742	10.2973	0.0	0.0
31	0.9296	0.9304	0.9301	0.9301	1.5352	1.5387	1.5370	10.6010	10.2684	--	0.0	0.0
32	0.9296	0.9299	0.9296	0.9297	1.5448	1.5461	1.5455	10.6335	10.2501	--	0.0	0.0
33	0.9299	0.9304	0.9304	0.9302	1.5296	1.5314	1.5305	10.5483	10.2573	--	0.0	0.0
34	0.9248	0.9294	0.9304	0.9282	1.5334	1.5344	1.5339	10.5777	10.3081	--	0.0	0.0
35	0.9301	0.9307	0.9301	0.9303	1.5306	1.5324	1.5315	10.5496	10.2498	10.2950	0.0	0.0
36	0.9299	0.9301	0.9307	0.9302	1.5364	1.5397	1.5381	10.5849	10.2413	--	0.0	0.0
37	0.9304	0.9307	0.9307	0.9306	1.5387	1.5408	1.5397	10.6190	10.2556	--	0.0	0.0

TABLE B-VII (continued)

Pellet[a]	Diameter (cm)				Length (cm)			Weight (g)	Geometric Density (g/cm^3)	Immersion Density (g/cm^3)	Centerline Hole Diameter (cm)	
	Top	Center	Bottom	Average	0°	90°	Average				Top	Bottom
38	0.9299	0.9304	0.9304	0.9302	1.5347	1.5372	1.5359	10.5908	10.2616	--	0.0	0.0
39	0.9289	0.9289	0.9289	0.9289	1.5329	1.5344	1.5337	10.1154	10.2506	10.2810	0.1829	0.1880
40	0.9289	0.9289	0.9289	0.9289	1.5382	1.5413	1.5397	10.1730	10.2677	10.3512	0.1829	0.1880
41	0.9291	0.9291	0.9291	0.9291	1.5375	1.5390	1.5382	10.1161	10.2204	10.2755	0.1854	0.1880
42	0.9291	0.9291	0.9291	0.9291	1.5474	1.5512	1.5493	10.2404	10.2541	10.2853	0.1803	0.1854
43	0.9291	0.9291	0.9291	0.9291	1.5491	1.5524	1.5508	10.2591	10.2513	10.2948	0.1778	0.1829
44	0.9294	0.9294	0.9294	0.9294	1.5390	1.5423	1.5406	10.1814	10.2469	10.2014	0.1803	0.1854
45	0.9299	0.9299	0.9299	0.9299	1.5405	1.5446	1.5425	10.2090	10.2558	10.2870	0.1829	0.1854
46	0.9294	0.9294	0.9294	0.9294	1.5425	1.5446	1.5436	10.1453	10.2082	10.2748	0.1829	0.1905
47	0.9296	0.9296	0.9296	0.9296	1.5375	1.5397	1.5386	10.1557	10.2460	10.2707	0.1829	0.1905
48	0.9294	0.9291	0.9291	0.9292	1.5430	1.5453	1.5442	10.1571	10.2434	10.3182	0.1905	0.1930
49	0.9294	0.9294	0.9294	0.9294	1.5443	1.5479	1.5461	10.1766	10.2285	10.2513	0.1854	0.1905
50	0.9294	0.9294	0.9294	0.9294	1.5408	1.5418	1.5413	10.1564	10.2405	10.3090	0.1829	0.1930
51	0.9296	0.9296	0.9296	0.9296	1.5372	1.5403	1.5387	10.1556	10.2451	10.2967	0.1854	0.1880
52	0.9299	0.9299	0.9296	0.9298	1.5268	1.5291	1.5279	10.0765	10.2282	10.2730	0.1829	0.1880
53	0.9291	0.9294	0.9294	0.9293	1.5387	1.5418	1.5403	10.0937	10.1861	10.2486	0.1854	0.1905
54	0.9294	0.9294	0.9294	0.9294	1.5352	1.5375	1.5363	10.1297	10.2411	10.2789	0.1829	0.1905
55	0.9289	0.9291	0.9294	0.9291	1.5329	1.5342	1.5335	10.1059	10.2359	10.2152	0.1829	0.1880
56	0.9294	0.9294	0.9294	0.9294	1.5377	1.5405	1.5391	10.1483	10.2353	10.2684	0.1829	0.1880
57	0.9291	0.9291	0.9291	0.9291	1.5370	1.5382	1.5376	10.1360	10.2332	10.2362	0.1829	0.1854
58	0.9296	0.9296	0.9296	0.9296	1.5377	1.5415	1.5396	10.1454	10.2230	10.1297	0.1829	0.1880
59	0.9294	0.9289	0.9289	0.9290	1.5502	1.5535	1.5518	10.2428	10.2472	10.2526	0.1829	0.1854
60	0.9294	0.9294	0.9294	0.9294	1.5446	1.5479	1.5462	10.2162	10.2387	10.1972	0.1778	0.1854

[a] Pellets are numbered from bottom to top of fuel stack.

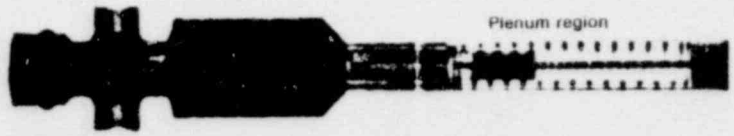

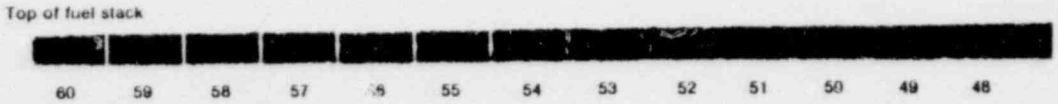

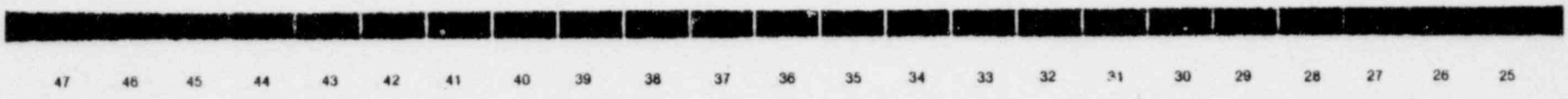

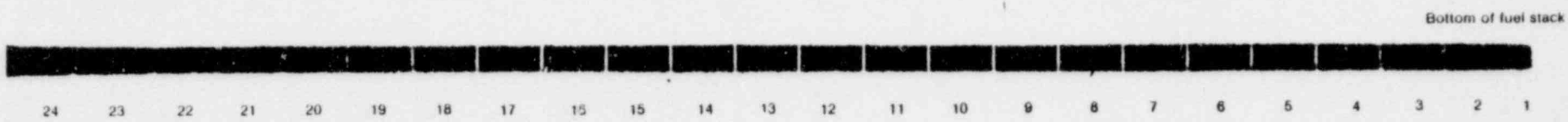

Rod UTA-0014

Fig. B-1 Picture radiograph of Rod UTA-0014.

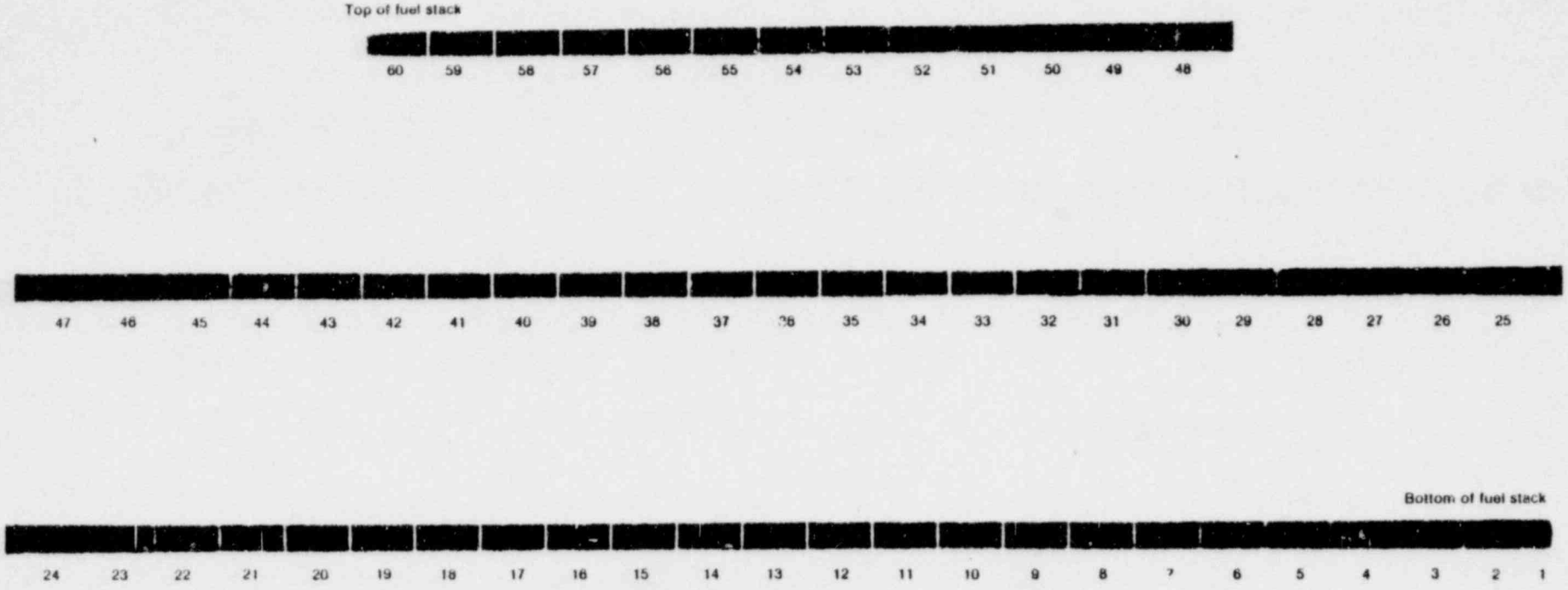

Rod UTA-0015

Fig. B-2 Pretest radiograph of Rod UTA-0015.

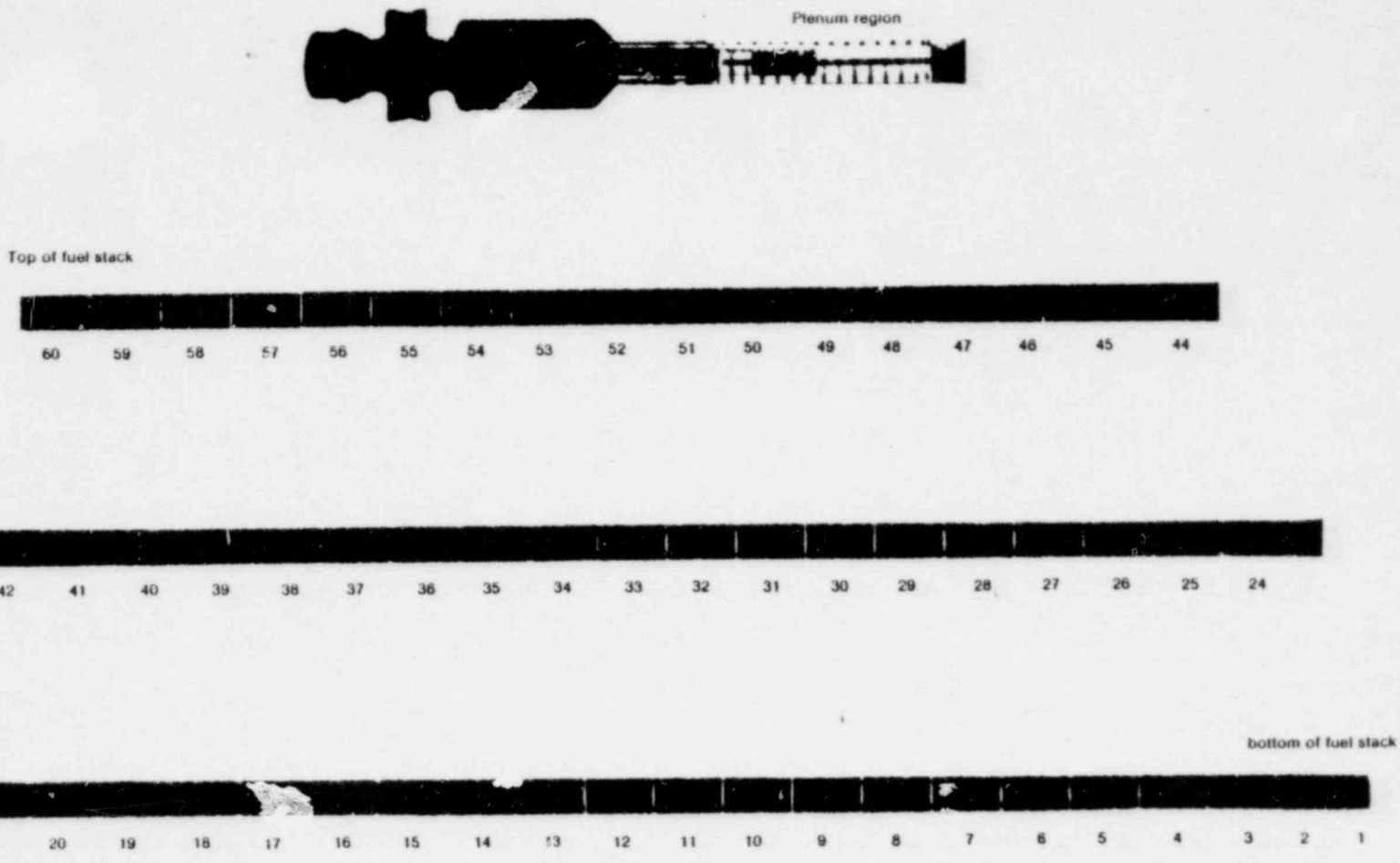

Rod UTA-0016

Fig. B-3 Pretest radiograph of Rod UTA-0016.

APPENDIX C

FUEL ROD POSTTEST DIAMETRAL MEASUREMENTS

APPENDIX C

FUEL ROD POSTTEST DIAMETRAL MEASUREMENTS

Fuel rod diameters were measured posttest to determine the amount of cladding deformation. The cladding deformation consisted of collapse along the central region of the fuel rod and is assumed to define the film boiling zone.

To characterize the region of cladding collapse along each of the Test PCM-4 fuel rods, detailed posttest cladding outside diameter measurements were made along the rods for two angular orientations (45 and 135°). These measurements are presented in Tables C-I for Rod UTA-0014, C-II for Rod UTA-0015, C-III for Rod UTA-0016, and C-IV for Rod A-0017. The measurements were adjusted with reference to the bottom of the fuel stack, which was located 0.035 m from the bottom of the fuel rod end cap. A systematic error (varying between 0.13 and 0.19 mm for the various rods), introduced by the test method and involving use of the in-cell manipulators, has been accounted for in the Tables C-I through C-IV. Measurements were taken using a to 25.4 mm micrometer, with an estimated precision of ± 0.03 mm, at 50-mm increments outside the film boiling zone and at 12-mm increments inside the film boiling zones. The film boiling zone extended from near 0.54 to 0.84 m along Rod UTA-0014. Along Rod UTA-0015, the film boiling zone extended between 0.50 and 0.84 m from the bottom of the fuel stack. The zone extended from 0.52 to 0.80 m, and from 0.53 to 0.80 m along Rods UTA-0016 and A-0017, respectively.

TABLE C-I

DIAMETRAL MEASUREMENTS FOR ROD UTA-0014

Distance from Bottom of Fuel Stack (m)	Diameter at Orientation[a] (mm)	
	45°	135°
0.018	10.73	10.75
0.067	10.74	10.75
0.084		10.73
0.117	10.72	
0.134		10.75
0.168	10.71	
0.184		10.75
0.220	10.74	
0.234		10.75
0.270	10.72	
0.284		10.73
0.318	10.69	
0.336		10.70
0.361	10.72	
0.371	10.68	
0.383		10.71
0.385	10.73	
0.422	10.72	
0.473	10.73	
0.489		10.71
0.524	10.72	
0.526		10.71
0.572	10.71	
0.578		10.62
0.589	10.65	
0.594	10.68	10.55
0.603		10.56
0.608	10.61	
0.616		10.54
0.617	10.65	
0.630		10.64
0.642		10.68
0.653		10.63
0.663	10.63	
0.669		10.61
0.676	10.65	
0.678	10.60	
0.693		10.67
0.694	10.66	
0.706		10.61
0.716		10.66
0.724	10.70	

TABLE C-I (continued)

Distance from Bottom of Fuel Stack (m)	Diameter at Orientation[a] (mm)	
	45°	135°
0.730		10.61
0.737	10.64	
0.745		10.66
0.752	10.67	
0.765	10.70	
0.768		10.70
0.778	10.67	
0.793		10.69
0.806	10.73	
0.824		10.70
0.830	10.75	
0.843		10.72
0.879	10.69	
0.892		10.76
0.923		10.78
0.933	10.75	

[a] Measurements were made using a 0 to 25.4-mm micrometer with an estimated precision of ±0.03 mm.

TABLE C-II

DIAMETRAL MEASUREMENTS FOR ROD UTA-0015

Distance from Bottom of Fuel Stack (m)	Diameter at Orientation[a] (mm)	
	45°	135°
0.014		10.77
0.017	10.75	
0.022		10.76
0.070	10.77	
0.117		10.74
0.120	10.76	
0.168	10.77	
0.171		10.75
0.218	10.78	
0.223		10.75
0.270	10.78	
0.305		10.74
0.319		10.75
0.320	10.76	
0.371	10.73	10.76
0.420	10.73	10.77
0.473	10.74	10.76
0.498	10.77	10.78
0.511		10.71
0.514	10.69	
0.525		10.70
0.526	10.65	
0.535	10.64	
0.536		10.67
0.549	10.63	
0.550		10.61
0.561	10.63	
0.566		10.65
0.575	10.60	10.64
0.589	10.64	10.59
0.600	10.61	
0.602		10.67
0.609		10.66
0.613	10.64	
0.624	10.65	
0.628		10.64
0.638	10.61	
0.640		10.68
0.651		10.65
0.652	10.57	
0.669	10.68	10.71
0.676	10.68	10.64

TABLE C-II (continued)

Distance from Bottom of Fuel Stack (m)	Diameter at Orientation[a] (mm)	
	45°	135°
0.688	10.64	
0.690		10.65
0.702	10.66	
0.707		10.62
0.714	10.61	
0.717		10.72
0.726	10.59	
0.727		10.69
0.738	10.59	
0.740		10.66
0.752	10.66	10.64
0.763	10.66	
0.764	10.66	10.70
0.780	10.64	10.64
0.790	10.64	
0.794		10.66
0.803	10.74	10.76
0.813	10.71	
0.829		10.74
0.830	10.70	
0.854	10.72	
0.858		10.71
0.879	10.74	
0.881		10.72
0.916	10.76	
0.968		10.77

[a] Measurements were made using a 0 to 25.4-mm micrometer with an estimated precision of ±0.03 mm.

TABLE C-III

DIAMETRAL MEASUREMENTS FOR ROD UTA-0016

Distance from Bottom of Fuel Stack (m)	Diameter at Orientation[a] (mm)	
	45°	135°
0.020		10.75
0.022	10.76	
0.032		10.75
0.034	10.78	
0.117		10.77
0.119	10.74	
0.171	10.75	10.78
0.221	10.72	
0.227		10.73
0.276		10.76
0.312	10.76	
0.321	10.74	10.74
0.371	10.73	10.73
0.421	10.73	
0.422		10.72
0.473	10.75	
0.477		10.75
0.498	10.74	
0.501		10.75
0.514		10.75
0.515	10.76	
0.525		10.75
0.528	10.77	
0.538		10.69
0.539	10.71	
0.549		10.67
0.554	10.70	
0.561		10.63
0.563	10.70	
0.576	10.64	
0.577		10.61
0.587	10.65	10.64
0.600		10.58
0.602	10.59	
0.613		10.57
0.618	10.59	
0.625	10.66	
0.627		10.63
0.638	10.62	
0.639		10.63
0.651		10.61
0.653	10.67	

TABLE C-III (continued)

Distance from Bottom of Fuel Stack (m)	Diameter at Orientation[a] (mm)	
	45°	135°
0.663	10.67	10.64
0.676	10.65	10.66
0.688		10.58
0.689	10.64	
0.702	10.61	
0.704		10.61
0.713	10.68	
0.716		10.65
0.727	10.68	10.67
0.743	10.65	
0.745		10.68
0.752	10.67	
0.754		10.65
0.765		10.64
0.768	10.64	
0.780		10.65
0.783	10.69	
0.792	10.70	
0.793		10.67
0.807	10.73	
0.808		10.75
0.815		10.74
0.820	10.75	
0.831	10.75	
0.832		10.72
0.859	10.75	
0.879		10.75
0.882	10.76	
0.930		10.75
0.934	10.75	
0.971		10.77
0.975	10.75	

[a] Measurements were made using a 0 to 25.4-mm micrometer with an estimated precision of ±0.03 mm.

TABLE C-IV

DIAMETRAL MEASUREMENTS FOR ROD A-0017

Distance from Bottom of Fuel Stack (m)	Diameter at Orientation[a] (mm)	
	45°	135°
0.018	10.70	
0.023		10.74
0.065	10.70	
0.069		10.71
0.119		10.72
0.120	10.69	
0.166		10.66
0.169	10.69	
0.219	10.67	10.68
0.267	10.70	
0.270		10.66
0.315	10.67	
0.319		10.70
0.368	10.62	
0.369		10.68
0.418		10.66
0.420	10.64	
0.468		10.67
0.470	10.65	
0.492		10.67
0.522	10.63	
0.524		10.68
0.544		10.68
0.558	10.62	
0.559	10.62	
0.571		10.58
0.573	10.54	
0.587		10.55
0.589	10.54	
0.597		10.56
0.599	10.59	
0.608		10.52
0.616	10.62	
0.620		10.60
0.624	10.63	
0.636	10.63	
0.637		10.56
0.646		10.59
0.651	10.55	
0.660		10.49
0.661	10.66	
0.672	10.58	

TABLE C-IV (continued)

Distance from Bottom of Fuel Stack (m)	Diameter at Orientation[a] (mm)	
	45°	135°
0.675		10.54
0.688	10.62	10.61
0.696	10.55	
0.698		10.57
0.713	10.53	
0.714		10.58
0.726	10.56	10.59
0.738	10.54	10.58
0.751		10.57
0.752	10.59	
0.763		10.58
0.765	10.57	
0.776	10.58	
0.778		10.59
0.788	10.60	
0.789		10.60
0.801	10.61	
0.803		10.69
0.823		10.70
0.829	10.62	
0.873		10.69
0.877	10.62	
0.924	10.61	
0.925		10.70
0.949		10.74

[a] Measurements were made using a 0 to 25.4-mm micrometer with an estimated precision of ±0.03 mm.

APPENDIX D

METALLOGRAPHIC EXAMINATIONS

APPENDIX D

METALLOGRAPHIC EXAMINATIONS

Film boiling temperatures induce phase transformations which modify the microstructures of both fuel and cladding, resulting in changes in the mechanical behavior and the related overall performance of the light water reactor fuel rods. Changes affecting fuel rod performance arise from cladding collapse, from thermal gradients across the fuel, from thermal expansion and contraction of the fuel stack following rapid transient heating and cooling, and from oxygenation of the cladding. Microstructural changes may be deduced from metallographic examination of fuel rod sections. The results of the metallographic examination are presented in this appendix for Rods UTA-0014, UTA-0015, UTA-0016, and A-0017.

1. PREPARATION FOR METALLOGRAPHIC EXAMINATIONS

Each fuel rod was prepared for metallographic examination by epoxy encapsulation into a stainless steel tube. The metallographic samples were selected on the basis of the posttest condition of the fuel rods. The selection was made from the zone of film boiling operation (cladding collapse region).

Epoxy encapsulation was accomplished by positioning the fuel rods inside separate 19.1-mm (inside diameter) stainless steel secondary tubes. A wire had been previously spot welded axially along the outer tube length to establish the 0° reference. A V-notch was vibra-etched axially along the length of the encapsulation tube 90° from the wire reference. The stainless steel tube was scribed with circumferential marks locating and identifying the metallographic sections. Angular orientations of the fuel rods were maintained by aligning the 0° surface thermocouple with the 0° reference wire of the secondary tube during epoxying. Viewed from the top of the fuel rod, angles are measured in the clockwise direction.

The void between the fuel rod and the encapsulation tube was filled with dye-impregnated Armstrong C-7 resin[a]. The epoxy was cured under heat lamps for 12 h and then the upper end cap of the fuel rod was sectioned at the plenum region and removed to allow epoxying of the fuel.

---

[a] Armstrong Products Co., Warsaw, Indiana 46500.

A vent was cut through the encasing tube into the fuel rod just below the bottom sample location. Epoxy was then injected under pressure at the top end until it emerged from the vent. The epoxy was cured under heat lamps for 12 to 16 h prior to sectioning the fuel rod into metallurgical samples.

The encapsulated fuel rod was sectioned using a "Cono" saw with a diamond impregnated blade. Water was used as lubricant for the blade during cutting. The cutting speed of the blade was controlled manually in-cell by a Variac.

The sectioning schedules for the four rods are presented in Tables D-I through D-IV. Portions of the fuel rods identified for burnup analysis were separated from the sectioned metallurgical samples for transfer of the fuel to the Idaho Chemical Processing Plant, at the Idaho National Engineering Laboratory, for radiochemical analysis. The metallographic samples (previously identified by Vibra-tool marking) were marked with black ink on the bottom surface and then transferred to the metallography hot cell for mounting, polishing, and examination. All samples were mounted for examination on the bottom surface (that is, viewed looking toward the upper end of the fuel rod).

The samples were mounted in Bakelite at 422 K and 29 MPa. Samples containing thermocouple junctions scheduled for examination were ground in 0.254-mm intervals and examined alternately through the hot cell periscope until the junctions were located. Final polishing was performed in the Automet together with the other mounted samples.

To prepare the cladding and fuel for study, the samples were ground to a 600-grit finish and then polished in steps to finer grades through "Linde A" aluminum-grade powder on the syntron vibra-polisher and finished in the Automet. Cladding microstructure was revealed by swab-etching with a solution containing 15 ml lactic acid, 5 ml nitric acid, 2 ml hydrofluoric acid, and 5 ml distilled water. Etching times of up to 30 s were used. A fuel etch solution (10% sulfuric acid and 90% hydrogen peroxide) was then applied by swabbing for 1 to 1.5 min to reveal the UO_2 grain structure. The cladding and fuel were then washed in a mild soap solution, rinsed, and quick-dried in hot air. The samples were examined on a metallograph attached to the metallography hot cell, and photomicrographs were obtained at magnifications ranging from 50 to 1000 X, using bright field illumination to illustrate oxide and reaction layers at the fuel-cladding interface, and polarized light to illustrate the various zircaloy microstructures such as in the stress-relieved condition, the recrystallized alpha-phase, prior beta-phase, and the associated oxygen-stabilized alpha-phase layers. The fuel was examined and photomicrographs were made at magnifications ranging from 100 to 1000 X, using bright field illumination. Photomacrographs of the prepared samples were made through the in-cell periscope camera with magnifications of approximately 6 X. The overall magnification of the metallograph was checked several times against a standard during photodocumentation to assure a nominal uncertainty of about 2% in the magnification of photomicrographs.

Grain sizes in the UO_2 fuel structure were determined from photomicrographs of selected samples by the intercept method. The number of grain boundaries on an

TABLE D-I

EXAMINATION SCHEDULE FOR ROD UTA-0014

Sample			Sectioning Location			
Number	Serial Number	Section Geometry	From Bottom of Fuel Rod (m)	From Bottom of Fuel Stack (m)[a]	Surface Examined	Comments
B-1	--	Transverse	0.445 to 0.457	0.410 to 0.422	--	Fission product (burnup) analysis
Y-1	T-1670	Transverse	0.721 to 0.733	0.686 to 0.698	Bottom	Examine thermocouple junction, cladding, and fuel
Y-2	T-1672	Transverse	0.699 to 0.711	0.664 to 0.676	Bottom	Determine fuel and cladding microstructures collapse region of rod
Y-3	T-1673	Transverse	0.673 to 0.686	0.638 to 0.651	Bottom	Same as above
Y-4	T-1674	Longitudinal	0.635 to 0.654	0.600 to 0.619	90° half	Examine region of cladding collapse

[a] Fuel stack is 0.035 m from the bottom of the rod.

TABLE D-II

EXAMINATION SCHEDULE FOR ROD CTA-0015

Sample			Sectioning Location			
Number	Serial Number	Section Geometry	From Bottom of Fuel Rod (m)	From Bottom of Fuel Stack (m)[a]	Surface Examined	Comments
B-2	--	Transverse	0.445 to 0.457	0.410 to 0.422	--	Fission product (burnup) analysis
X-1	T-1676	Transverse	0.721 to 0.733	0.686 to 0.698	Bottom	Examine thermocouple junction, cladding, and fuel
X-2	T-1677	Transverse	0.702 to 0.714	0.667 to 0.679	Bottom	Determine fuel and cladding microstructures in collapse region of rod
X-3	T-1678	Transverse	0.676 to 0.689	0.641 to 0.654	Bottom	Same as above
X-4	T-1680	Longitudinal	0.641 to 0.660	0.606 to 0.625	90° half	Examine region of cladding collapse
X-5	T-1682	Longitudinal	0.594 to 0.606	0.559 to 0.571	90° half	Same as above

[a] Fuel stack is 0.035 m from the bottom of the rod.

TABLE D-III

EXAMINATION SCHEDULE FOR ROD UTA-0016

Sample			Sectioning Location			
Number	Serial Number	Section Geometry	From Bottom of Fuel Rod (m)	From Bottom of Fuel Stack (m)[a]	Surface Examined	Comments
B-3	--	Transverse	0.445 to 0.457	0.410 to 0.422	--	Fission product (burnup) analysis
W-1	T-1667	Transverse	0.721 to 0.733	0.686 to 0.698	Bottom	Examine thermocouple junction, cladding, and fuel
W-2	T-1668	Transverse	0.702 to 0.714	0.667 to 0.679	Bottom	Determine fuel and cladding microstructures in cladding collapse region
W-3	T-1669	Transverse	0.676 to 0.690	0.641 to 0.655	Bottom	Same as above
W-4	T-1670	Transverse	0.622 to 0.635	0.587 to 0.600	Bottom	Examine centerline thermcouple, determine fuel and cladding microstructures

[a] Fuel stack is 0.035 m from the bottom of the rod.

TABLE D-IV

EXAMINATION SCHEDULE FOR ROD A-0017

Sample			Sectioning Location			
Number	Serial Number	Section Geometry	From Bottom of Fuel Rod (m)	From Bottom of Fuel Stack (m)[a]	Surface Examined	Comments
B-4	--	Transverse	0.445 to 0.457	0.410 to 0.422	--	Fission product (burnup) analysis
Z-1	T-1663	Longitudinal	0.664 to 0.683	0.629 to 0.648	90° half	Examine region of collapse; determine fuel and cladding structures
Z-2	T-1665	Longitudinal	0.803 to 0.822	0.768 to 0.787	90° half	Same as above; transition to collapse

[a] Fuel stack is 0.035 m from bottom of the rod.

88 x 113-mm photomicrograph at 200 and 500 X magnifications intercepting a 100-mm line was counted. The average distance between intercepts was then calculated and used as an approximation for the nominal grain diameter. The average value from three observations was used for each grain diameter calculated. Some grain sizes were roughly estimated using a comparison method.

2. RESULTS OF METALLOGRAPHIC EXAMINATIONS

The results of the optical metallographic examinations of cladding and fuel samples sectioned from Rods UTA-0014, UTA-0015, UTA-0016, and A-0017 are presented and discussed in the following subsections.

2.1 Metallographic Examination Results for Rod UTA-0014

All samples sectioned from Rod UTA-0014 for metallographic examination were taken from positions within the approximate region of high temperature test operation located between 0.54 and 0.84 m from the bottom of the fuel stack. The cladding microstructures observed in these samples were all prior beta-phase structures ($T > 1245$ K), bounded on the outer and inner diameters by layers of oxygen-stabilized alpha-zircaloy. An outer diameter surface layer of ZrO_2 in varying thicknesses was present on all of the samples.

Rod UTA-0014 had thermocouple indications of cladding surface temperatures greater than 730 K [departure from nucleate boiling (DNB) conditions] only during the fourth, and final test cycle. DNB was first indicated by the 0.787-m, 270° thermocouple, and 25 s later was indicated by the 0.686-m, 180° thermocouple. Approximately 80 s later, DNB was indicated at the 0.584-m, 90° thermocouple. The 0.483-m, 0° thermocouple (positioned near the axial power peak) did not indicate DNB during the test cycle. Maximum thermocouple readings during the test cycle were 930, 815, and 790 K for the 0.584-m, 90°; 0.686-m, 180°; 0.787-m, 270° thermocouples, respectively. Such temperatures are from 455 to 315 K lower than the 1245 K transformation temperature of the cladding to prior beta-phase zircaloy microstructure. Cladding microstructures observed in the samples from Rod UTA-0014 are outlined in the following discussion.

Cladding microstructures from Sample Y-1 exhibited a prior beta-phase structure bounded on the outer and inner diameters by oxygen-stabilized alpha-zircaloy. The alpha + beta two-phase region found between the oxygen-stabilized alpha and the parent beta-phase may be related to the combined effects of test temperature quench rates and increased solubility of hydrogen in the presence of dissolved oxygen, both of which may change the morphology. These cladding structures, which were observed around the circumference, are illustrated in the photomicrograph of Figure D-1. The UO_2 fuel showed limited equiaxed grain growth toward the center of the pellet, with grain sizes varying up to 40 μm. A thin UO_2 melt zone extending radially 200 to 300 μm was observed near the

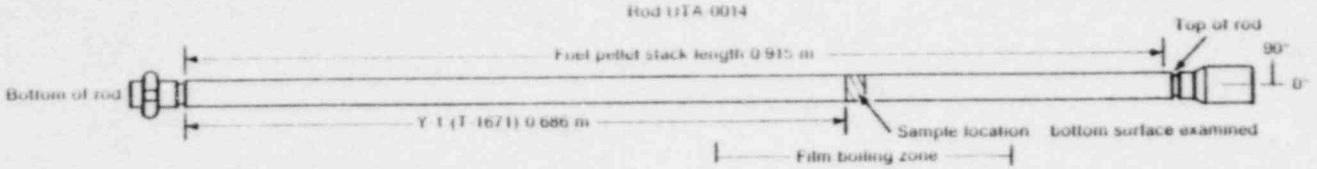

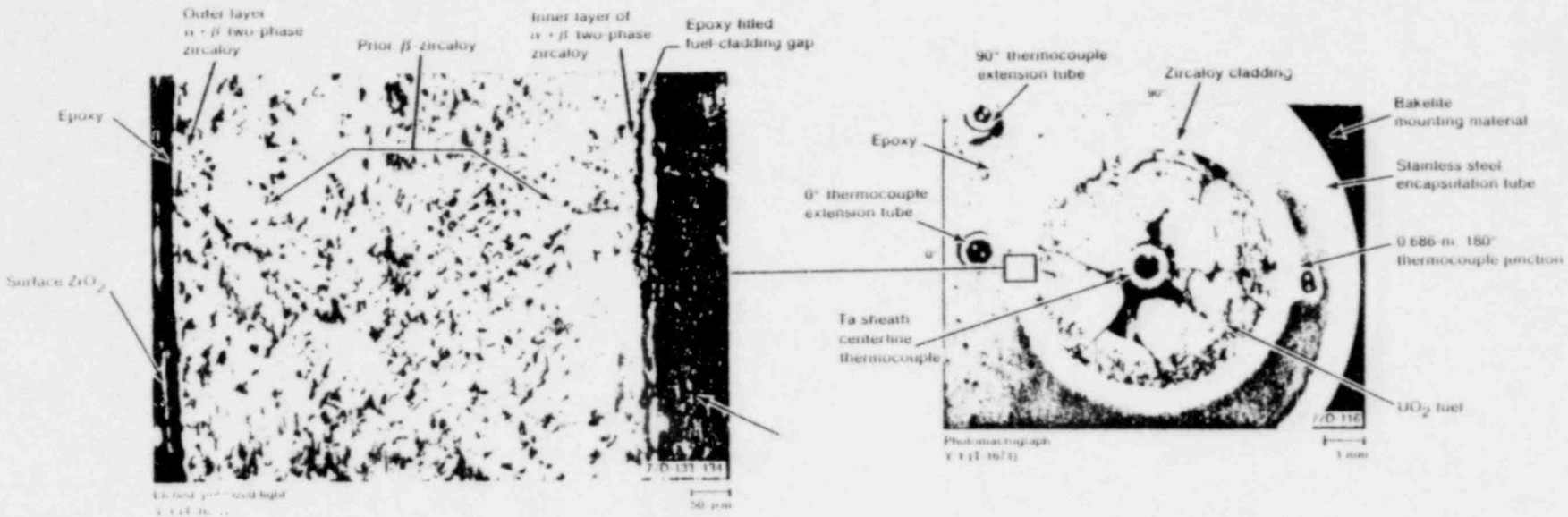

Fig. 3-1 Transverse section (Y-1) of Rod UTA-0014 at 0.686 m.

centerline thermocouple sheath as shown in Figure D-2. The UO_2 melt zone appeared to be related to a chemical reaction with the tantalum thermocouple sheath. Tantalum metal had segregated in spherical form in the UO_2 melt matrix, and as rod lamellae and inclusions at the boundaries of the primary UO_2-phase dendrite lobes.

Cladding microstructure observed in Sample Y-2 is illustrated in Figure D-3. The prior beta-phase structure bounded by outer and inner diameter layers of oxygen-stabilized alpha-zircaloy extends around the circumference of the transverse section. The cladding photomicrographs show a region where the cladding has collapsed onto the fuel near a fuel crack and deformed to conform to the fuel fracturing and fuel fragment repositioning. A duplex U-zircaloy reaction layer is present at the fuel-cladding interface[D-1,-2,-3]. The fuel restructuring is illustrated in Figure D-4 for this sample. Grain enlargement up to > 45 μm has occurred near the center of the fuel pellet. A melt zone associated with UO_2 reaction with the tantalum thermocouple sheath, and extending 350 to 400 μm into the fuel is observed. The tantalum-to-UO_2 diffusion couple is particularly apparent in the photomicrographs.

The cladding and fuel microstructures of Sample Y-3 are illustrated in Figures D-5 and D-6, respectively. The cladding has a prior beta structure bounded by outer and inner diameter layers of oxygen-stabilized alpha-zircaloy. Where the fuel and cladding are in contact around the circumference, a U-zircaloy duplex reaction layer has developed at the interface during testing. The fuel restructuring is similar to that described for Samples Y-1 and Y-2 with equiaxed grains up to ≥ 42 μm observed near the pellet center. Fuel melting associated with the reaction of the thermocouple sheath, and the tantalum-UO_2 diffusion couple described previously are also presented in Sample Y-3.

Cladding collapse into the interfacial gap between fuel pellets is illustrated in Figure D-7 for Sample Y-4. The cladding prior beta microstructure exhibits no variation along the length. A U-zircaloy duplex reaction layer is present at the fuel-cladding interface. No reaction layer is observed around the collapse tip at the fuel pellet gap where no contact with the fuel exists. The presence of a surface oxide flake attached to the contour of the collapse depression indicates that the collapse occurred prior to significant surface oxidation.

An additional region of fuel restructuring was observed in this sample compared to the limited equiaxed grain growth discussed in conjunction with the other samples. A zone of precursory grain elongation, mixed with equiaxed grains, developed near the center of the fuel pellet and was bounded by regions of equiaxed and unrestructured fuel. The molten zone at the center, associated with the reaction of the tantalum thermocouple sheath, appears to have slumped and extruded molten fuel into the disc-shaped gap between fuel pellets, as illustrated in Figure D-8. The tantalum-to-UO_2 diffusion couple associated with the centerline thermocouple sheath melting is illustrated in Figure D-9.

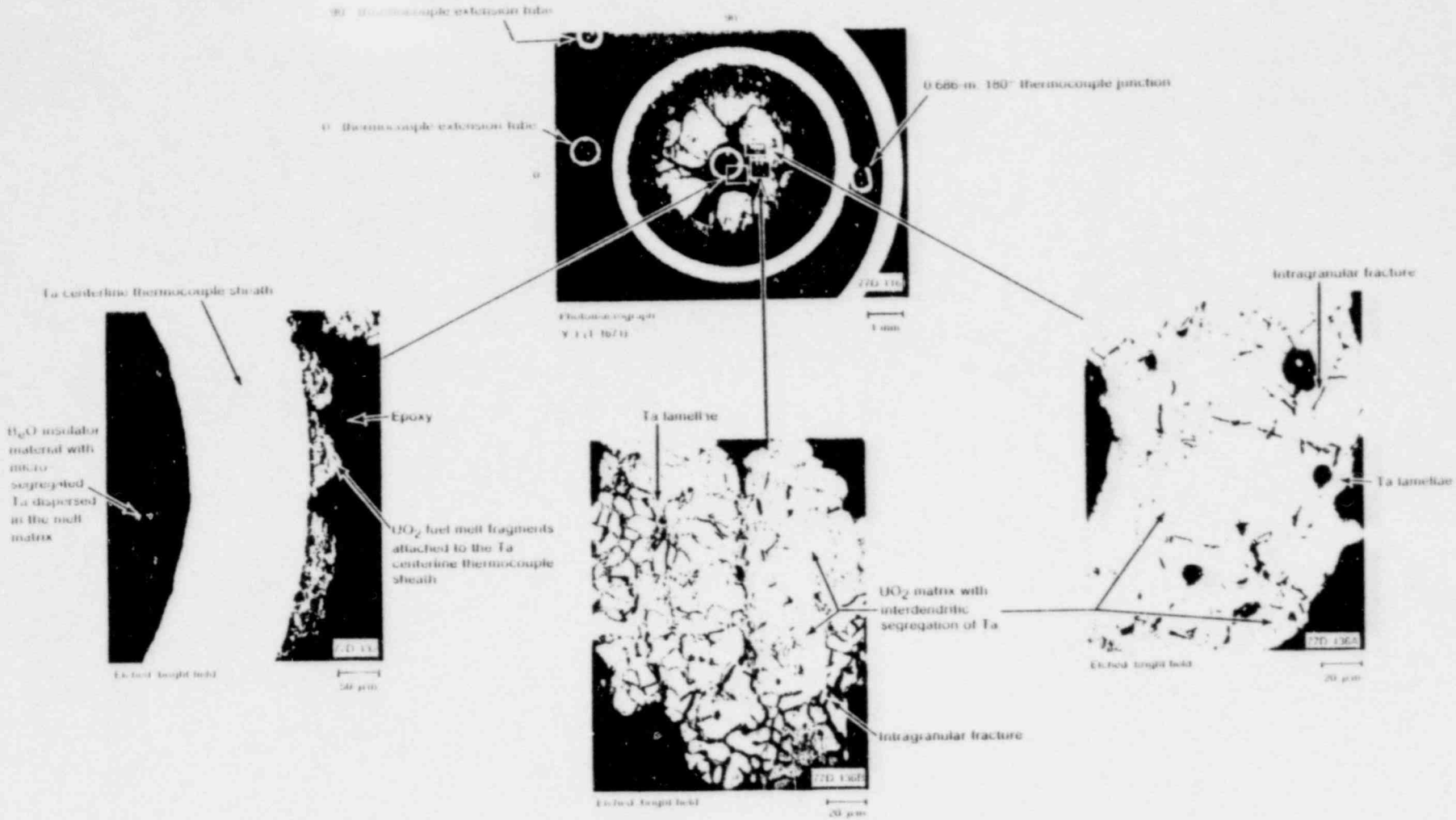

Fig. D-2 Transverse section (Y-1) of Rod UTA-0014 molten zone.

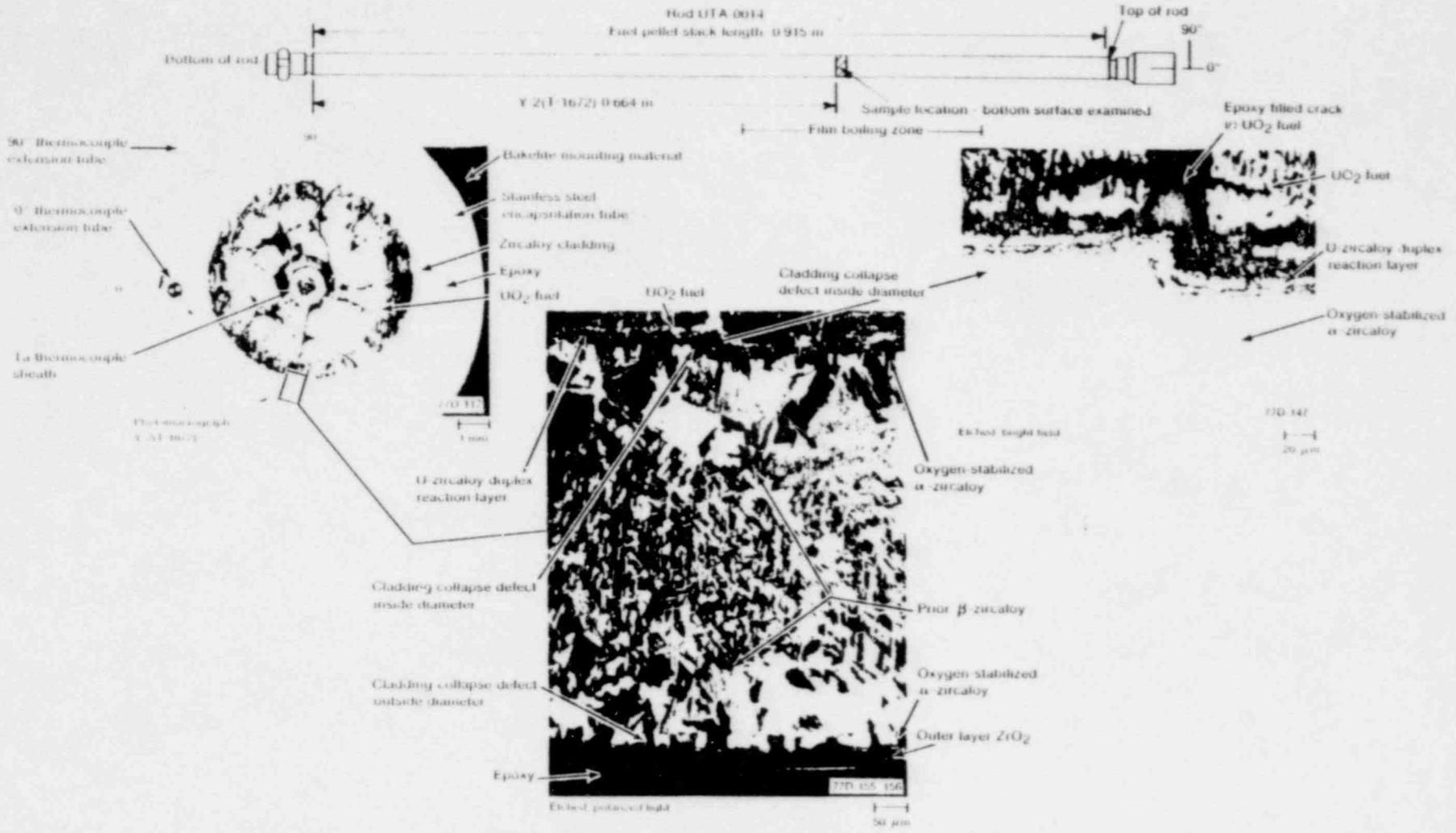

Fig. 4-3 Transverse section (Y-Z) of Rod UTA-0014 (0.664 m) showing cladding microstructure.

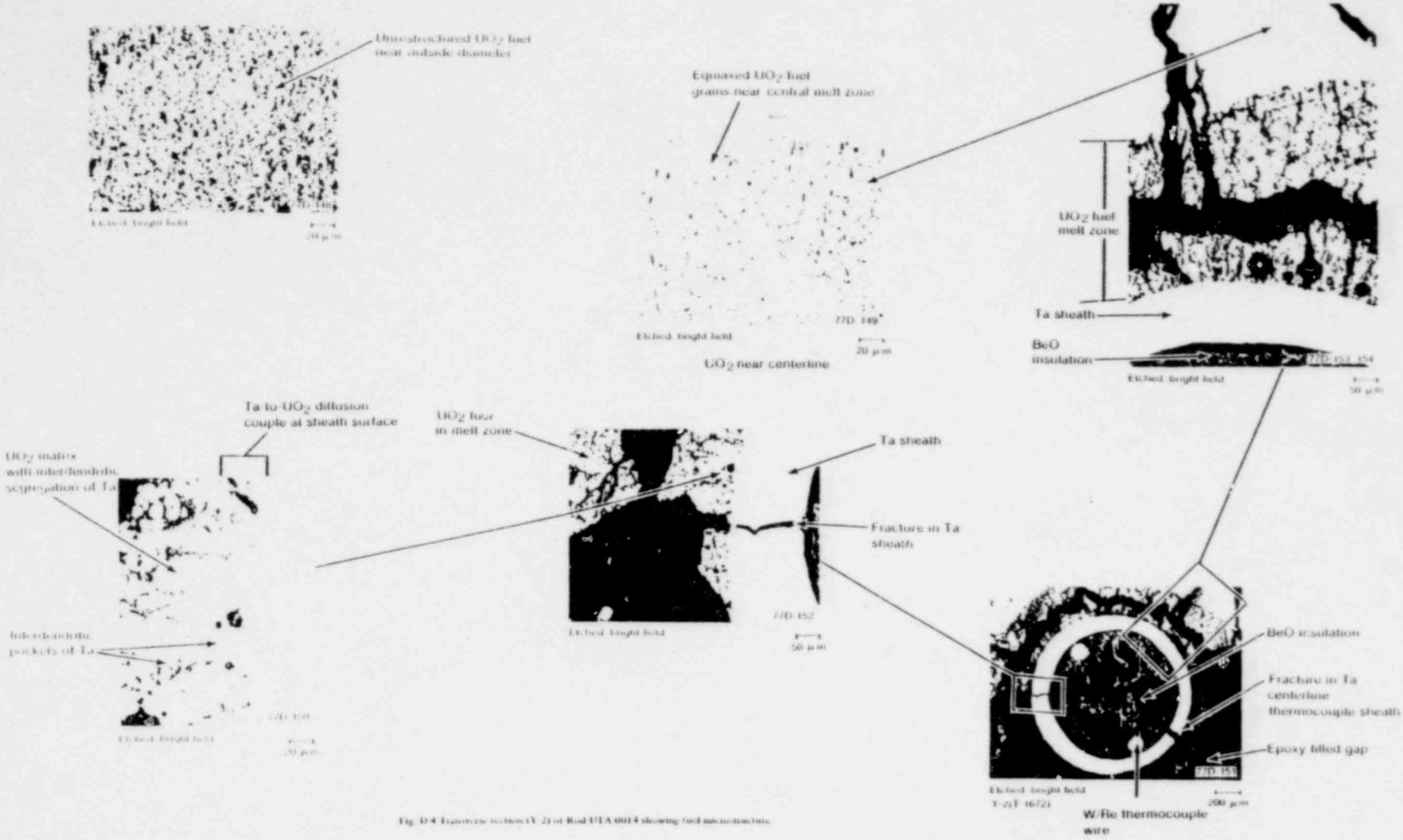

Fig. D-4. Transverse section (Y-21) of Rod UTA-6014 showing fuel microstructure.

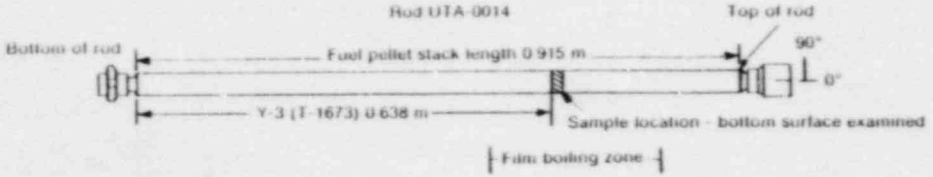

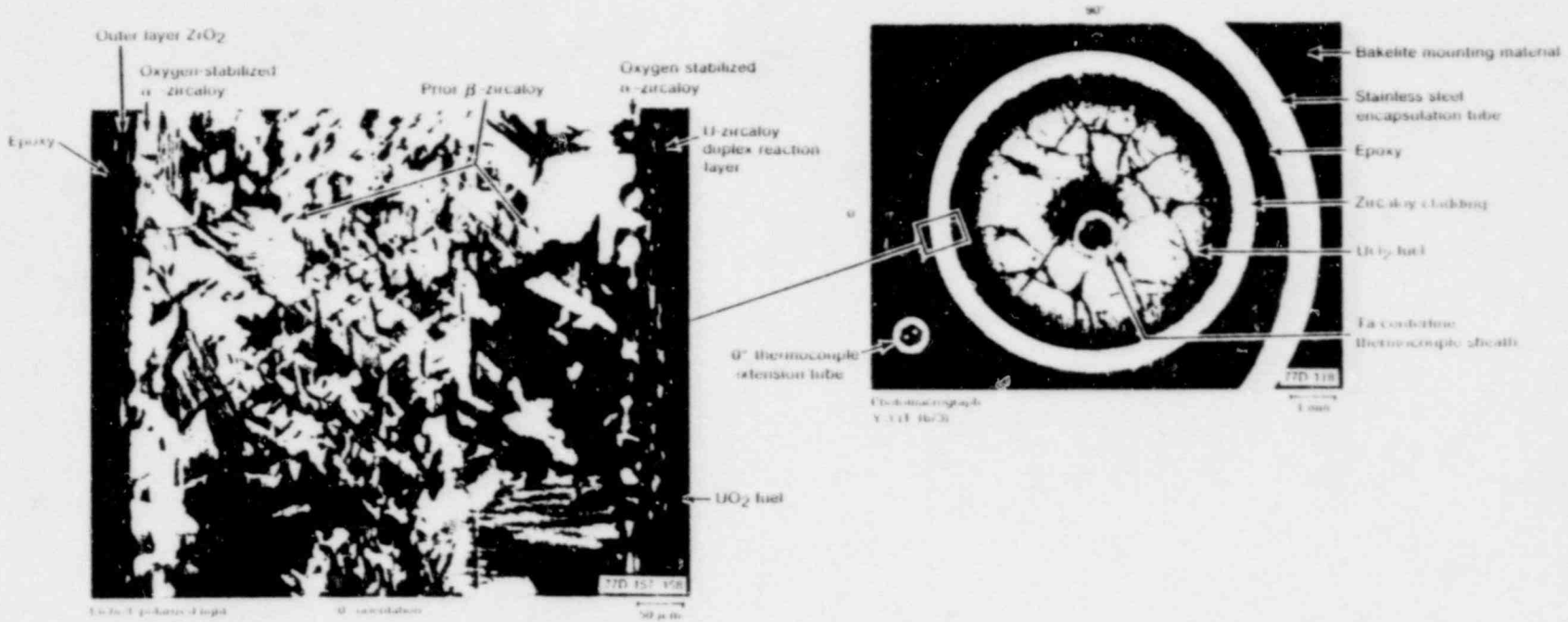

Fig. D-5 Transverse section (Y-3) of Rod UTA-0014 (0.638 m) showing cladding microstructure.

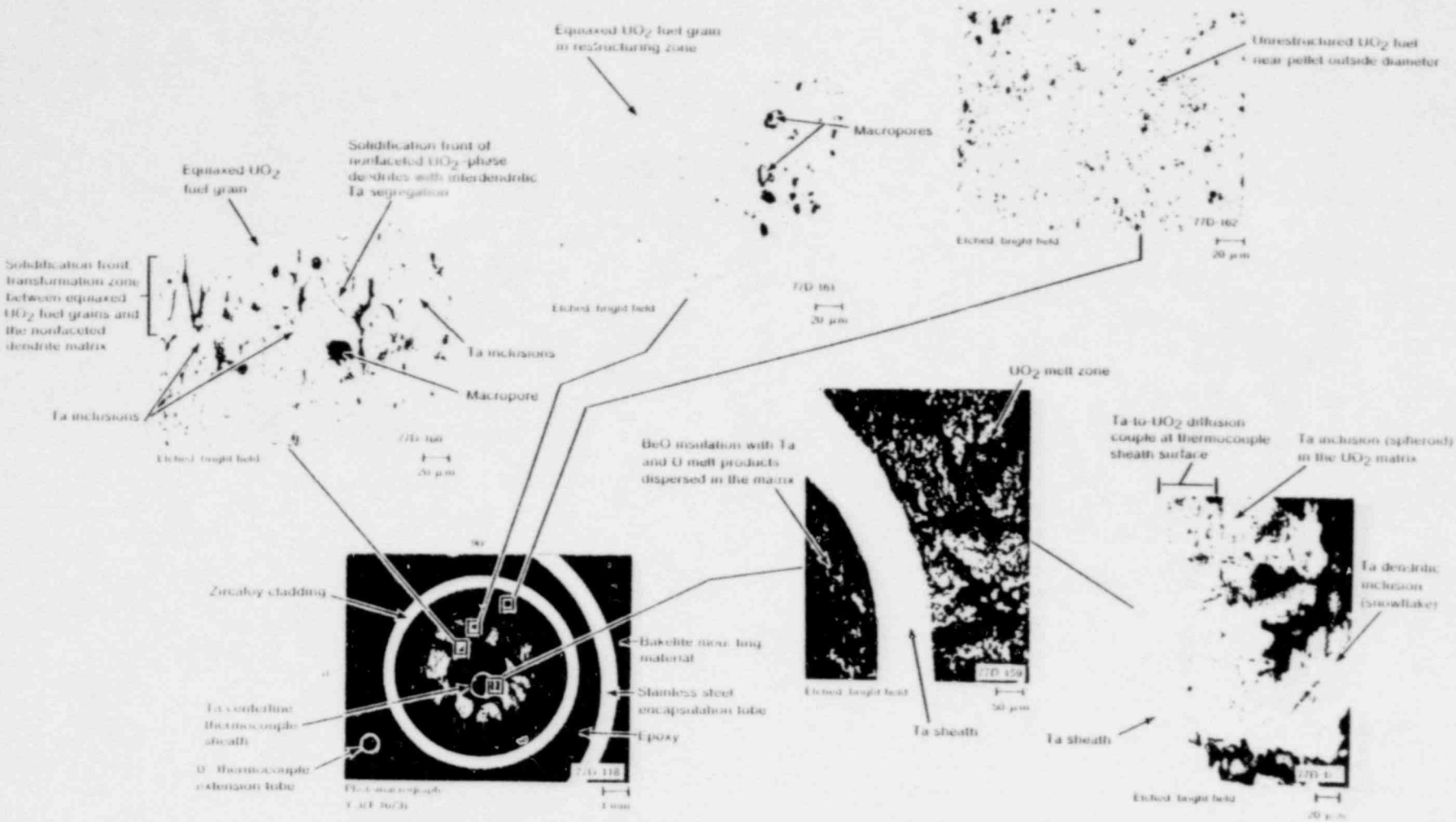

Fig. D-6. Transverse section (Y-3) of Rod UTA-4004 showing fuel microstructure.

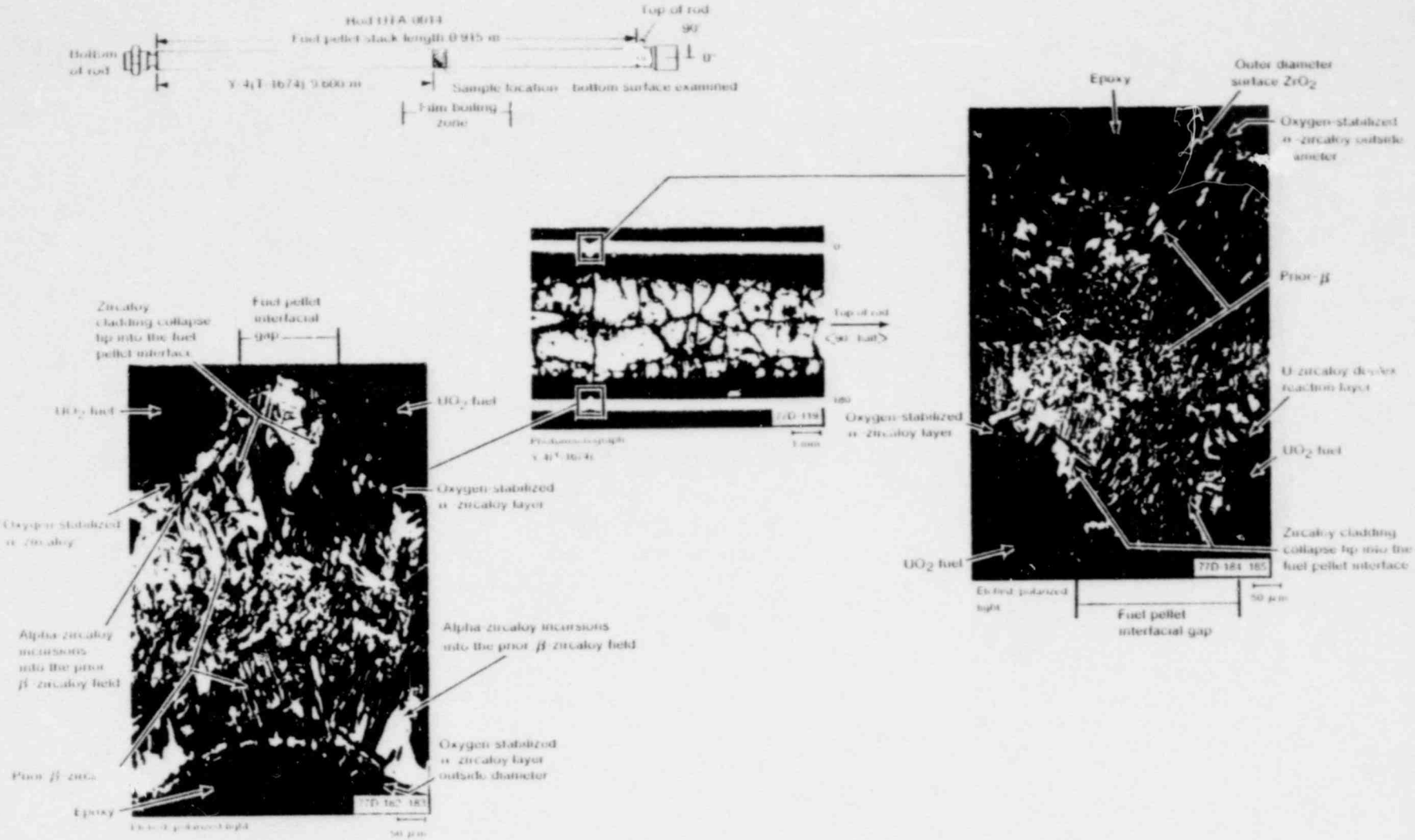

Fig. D-7 Longitudinal section (Y-4) of Rod 11I A-0014 between 0.600 and 0.619 m showing cladding wasting.

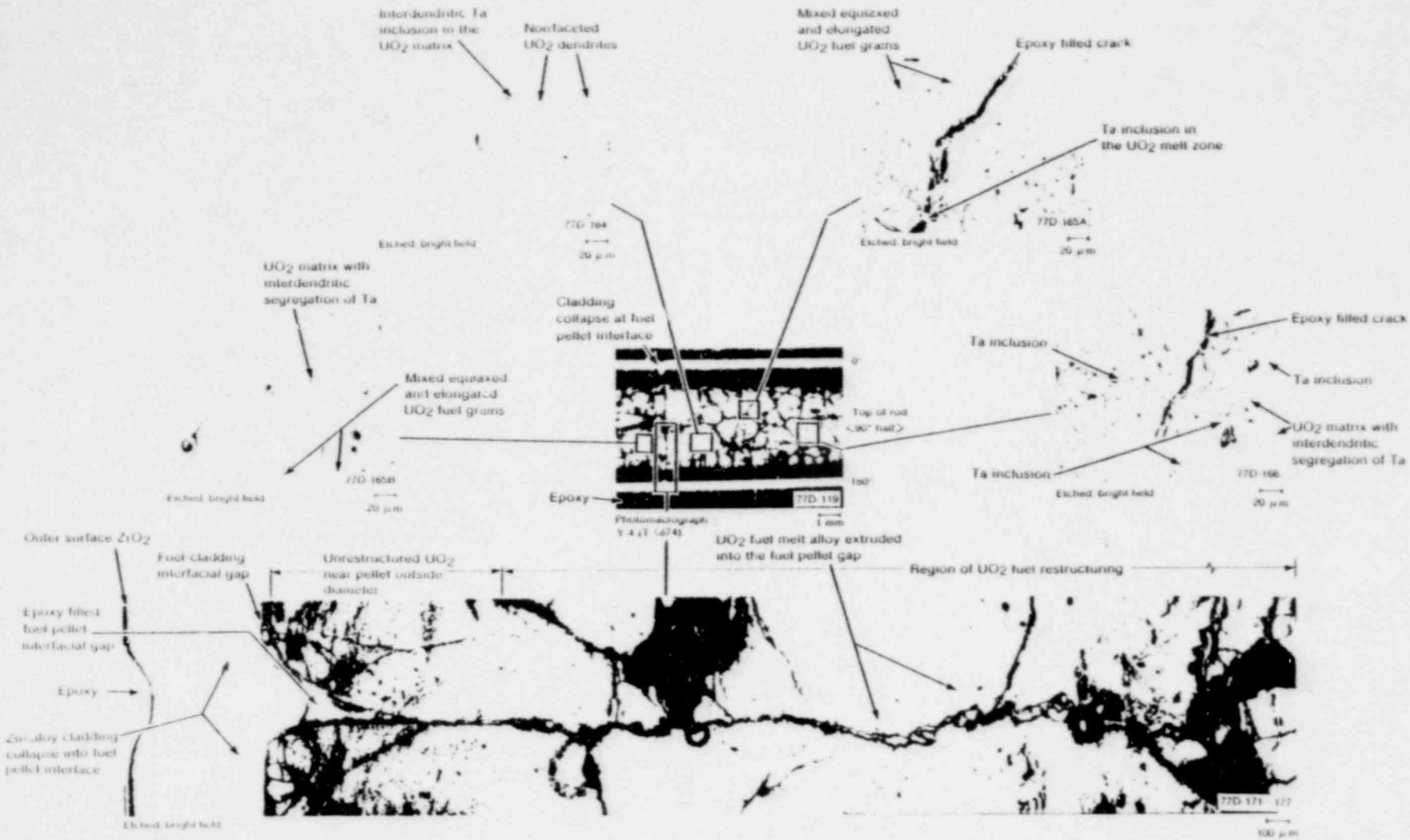

Fig. D.8 Longitudinal section (Y-4) of Rod UTA-0014 showing fuel-cladding interac

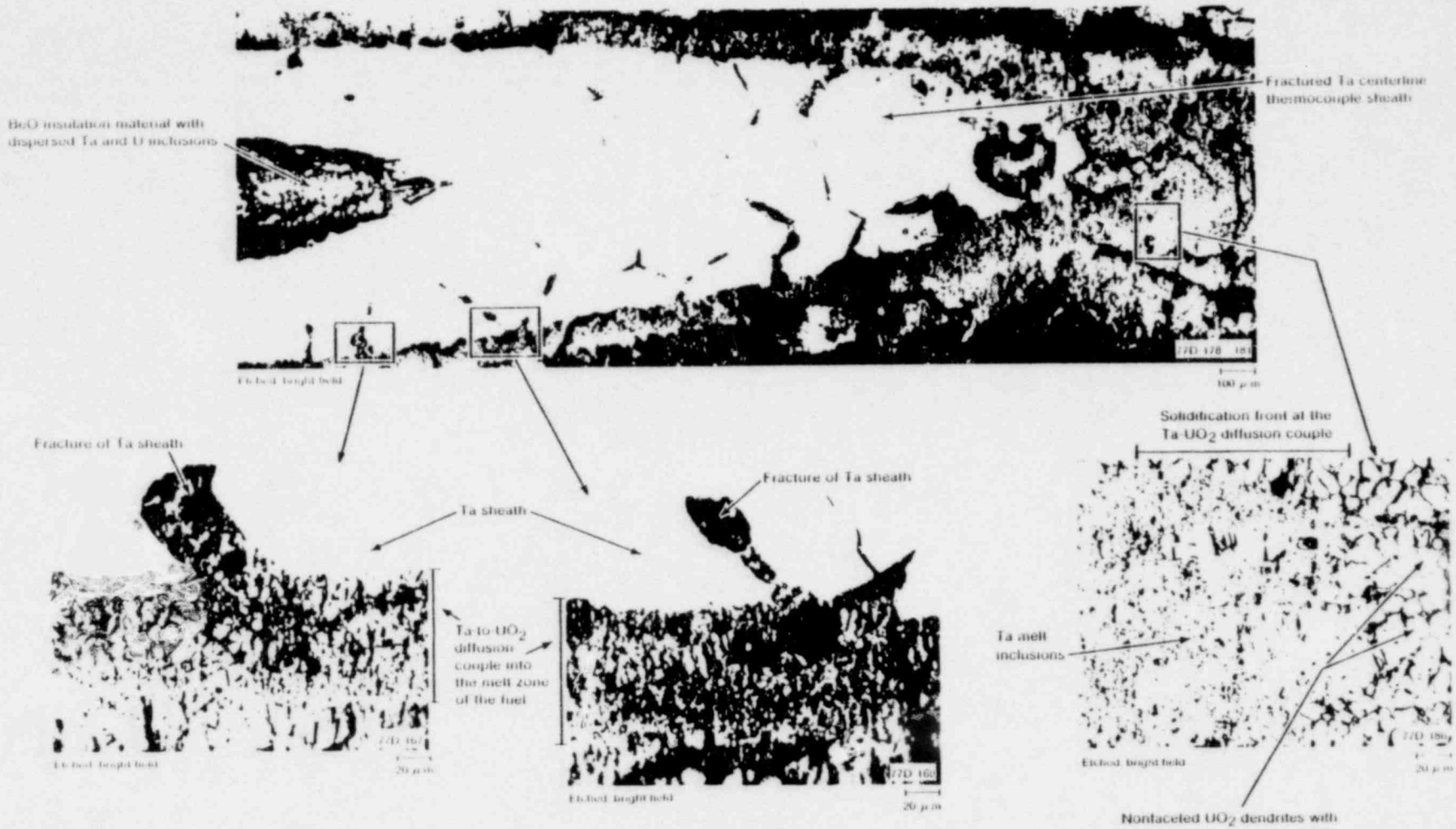

Fig. D.9 Longitudinal section LY-41 of Rod UTA-0014 showing fuel and tantalum thermocouple sheath melt zone diffusion couple.

2.2 Metallographic Examination Results for Rod UTA-0015

Metallographic samples sectioned from Rod UTA-0015 were taken from the central region that experienced cladding collapse between 0.50 and 0.84 m. A prior beta-phase zircaloy microstructure, bounded in the inside and outside diameters by layers of oxygen-stabilized alpha and alpha + beta two-phase zircaloy, was observed in the samples examined. Microstructural evidence of cladding hydriding was observed. The hydrides were found to be associated with the alpha + beta material in the prior beta field. A U-zircaloy duplex reaction layer was observed only in samples sectioned from 0.667 m and lower in the film boiling zone, close to the power peak near midlength of the rod. UO_2 fuel restructuring was limited to equiaxed grain growth near the center of the fuel pellets, with the exception of the sample sectioned from the lowest elevation examined. A column of fuel in the central region of the pellet in this sample was observed to have slumped into the gap between adjacent fuel pellets, indicating a previously molten condition.

Thermocouples on Rod UTA-0015 gave indications of DNB conditions ($T < 730$ K) during both test Cycles 3 and 4. DNB was indicated by the 0.686-m, 180° thermocouple for approximately 200 s during Cycle 3, with only transition nucleate boiling ($T < 730$ K) momentarily ($T < 10$ s) indicated at adjacent (0.889-m, 270° and 0.635-m, 90°) thermocouple locations. During Cycle 4, DNB was first indicated by the 0.635-m, 90° thermocouple and the linear variable differential transformer (LVDT). About 17 s later, the 0.686-m, 180° thermocouple indicated DNB. No DNB was indicated at the 0.889-m, 270° and 0.483-m, 0° thermocouple positions during the final test cycle. Maximum thermocouple readings during the test cycle were 1100 and 1030 K for the 0.686-m, 180° and 0.635-m, 90° thermocouples, respectively. These temperatures are 145 to 215 K below the 1245 K prior beta transformation temperature of the zircaloy microstructure observed metallographically. The individual samples examined are discussed in the following paragraphs.

A transverse section (Sample X-1) of the fuel rod, located 0.686 m from the bottom of the fuel stack is shown in Figure D-10. The cladding microstructure around the circumference was prior beta-phase zircaloy bounded by inside and outside diameter layers of oxygen-stabilized alpha-zircaloy. No reaction had developed at the fuel-cladding interface. The alpha incursions at some angular orientations occurred as equiaxed grains. Such morphology of the alpha material may be related to hydrogen solution in the presence of oxygenation of the cladding prior beta material[D-4].

Cladding hydriding is illustrated for this sample in Figures D-11 and D-12. The hydrides are precipitated away from the surface and appear in association with the alpha + beta interface within the prior beta field. The hydrides precipitated in the prior beta field appear along the boundaries of prior beta grains containing alpha material, and are no longer circumferentially oriented as typically observed in the PCM cladding[D-3]. Fuel restructuring observed in Figure D-13 varied from nominally 4 to 6 μm near the fuel pellet periphery up to about 18 μm near the center.

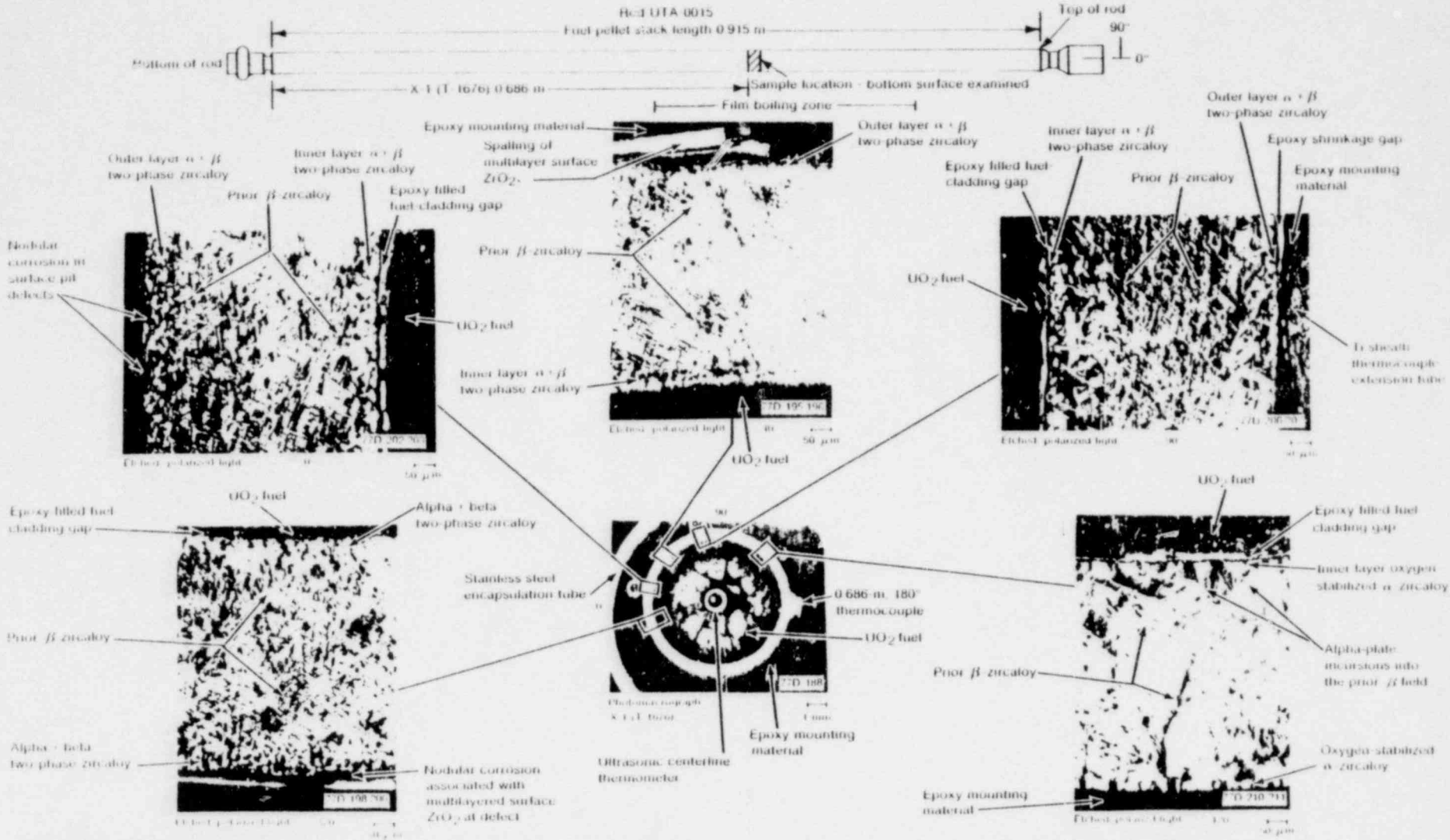

Fig. D-10. Transverse section (X-1) of Rod UTA-0015 (0.686 m) showing cladding microstructure.

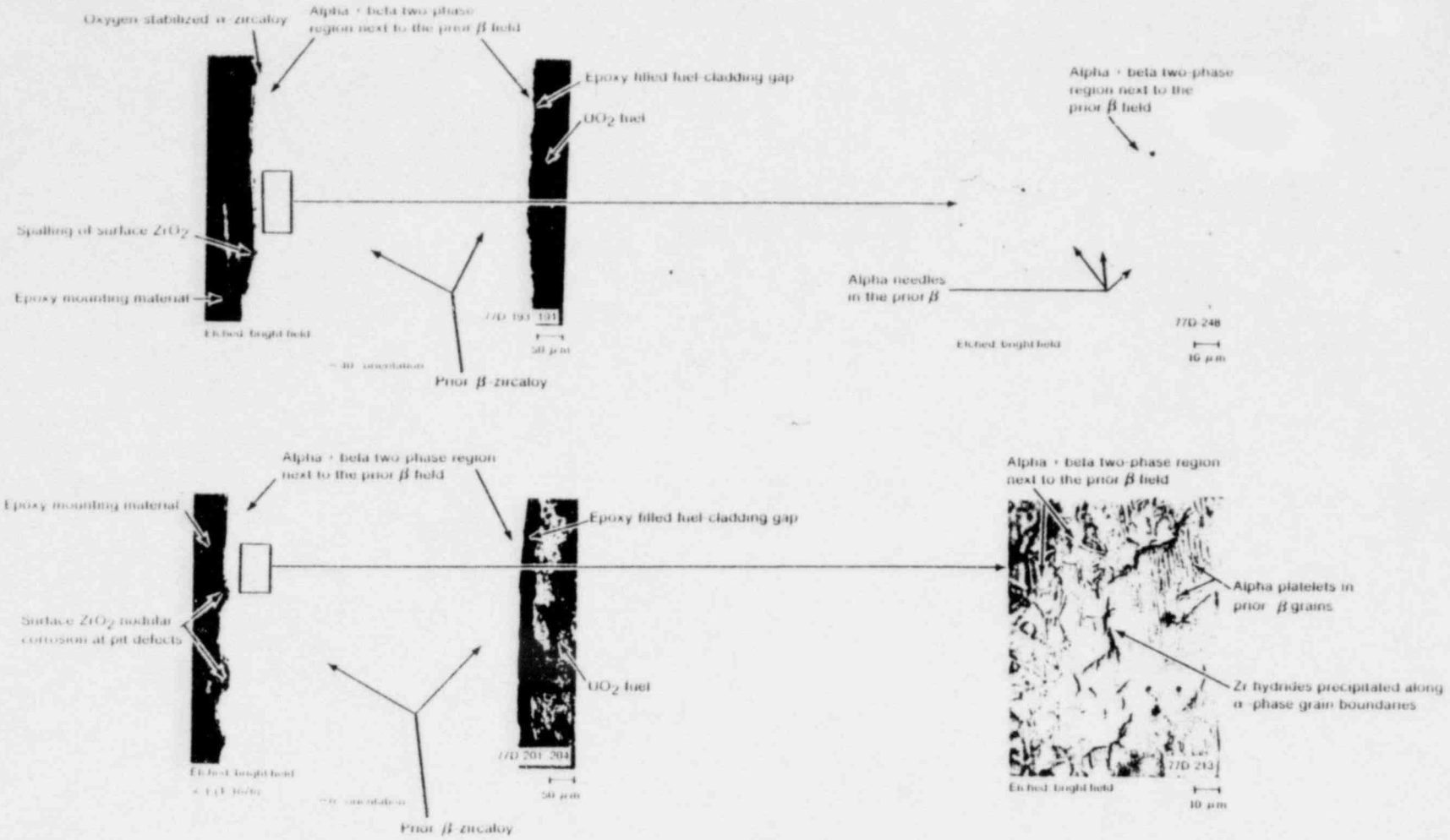

Fig. D-11 Transverse section (X-1) of Rod UTA-0015 showing cladding hydriding

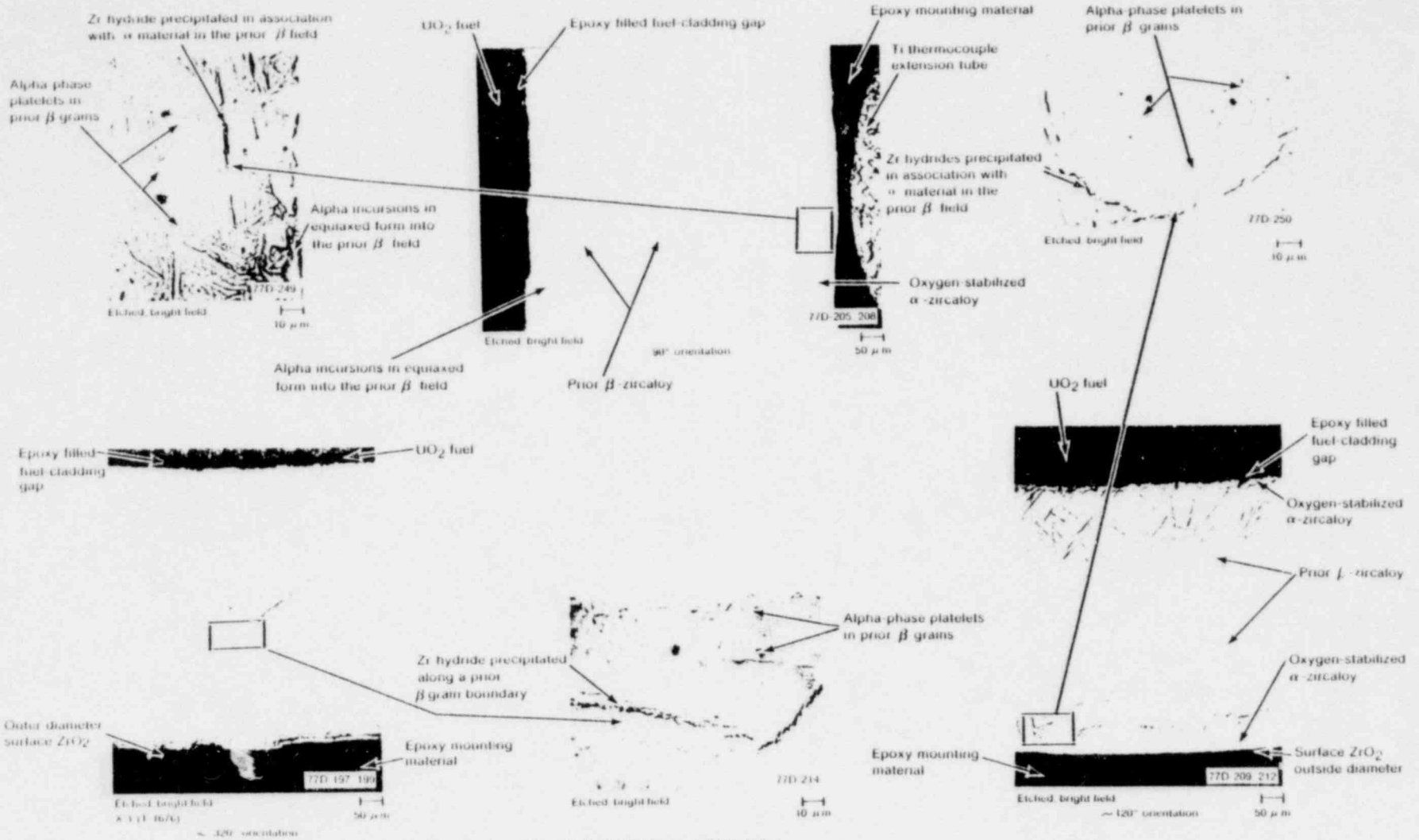

Fig. D-12 Transverse section (X-1) of Rod UTA-0015 showing cladding hydriding.

Etched, bright field

20 μ m

Equiaxed grain growth in the UO_2 fuel near the fuel pellet center

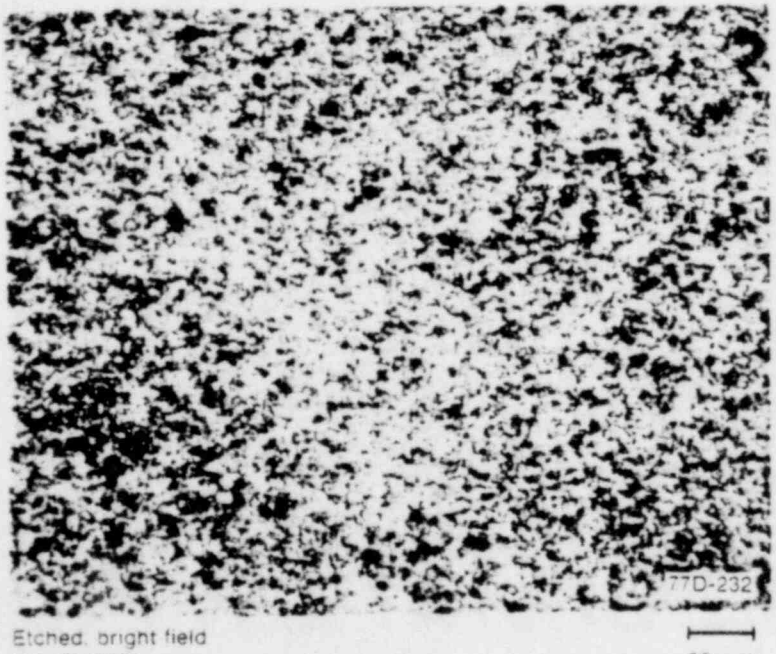

Etched, bright field
X-1 (T-1676)

20 μ m

UO_2 fuel near the outer periphery of the fuel pellet

Fig. D-13 Transverse section (X-1) of Rod UTA-0015 showing fuel restructuring.

The adjacent transverse sample (Sample X-2), sectioned at 0.667 m exhibits a circumferential variation in cladding microstructure as illustrated in Figure D-14. The cladding microstructure observed near the 0° thermocouple extension tube laser weld attachment and out to 50° on each side of the attachment is equiaxed alpha material ($920 < T < 1105$ K). A direct transition occurs from this lower temperature microstructure to prior beta zircaloy ($T \geq 1245$ K) microstructure over a circumferential distance of 0.1 to 0.2 mm.

The lower temperature microstructure near the extension tube attachment is attributed to a local cooling fin effect by the thermocouple relative to the adjacent cladding material. An alpha + beta region found adjacent to the prior beta field was similar to that discussed earlier. Hydrogen additions can produce variations in the observable proportions of alpha and alpha + beta phases[D-5]. The effect of hydrogen up-take with cladding oxygenation on the transformation temperature of the various microstructures present is not known. Hydride precipitation in the alpha + beta two phase field of the cladding is illustrated in Figure D-15.

Fuel restructuring was similar to that of the previously discussed sample. Metallic inclusions found in the periphery of the fuel pellet are shown in Figure D-16.

The transverse section (Sample X-3) from the 0.641-m fuel stack elevation is shown in Figures D-17 and D-18. The variation in microstructure around the cladding circumference is illustrated in the figures. Prior beta-phase microstructure was observed. A lower temperature prior beta structure ($T \sim 1245$ K) was present near the 0° circumferential orientation where the 0° thermocouple extension tube was located and had no reaction layer development at the fuel-cladding interface as seen in Figure D-17. Hydride precipitates oriented along the alpha-phase incursions were also observed. Cladding oxidation on the outer surface is illustrated for multilayer development. Layer separation and fragmenting of the surface ZrO_2 was observed. Silvery or white oxide occurred as the outermost layer on top of the mottled grey and black ZrO_2 layers in the cross section. Distortion of the centerline ultrasonic thermometer sheath seen in the photomacrograph of Figure D-17 occurred during the sectioning of the metallurgical sample when fragmented fuel fell out and left the sheath mechanically unsupported.

On the opposite side (180°) of the transverse sample, a higher temperature prior beta-phase ($T > 1245$ K) structure is present, as seen in Figure D-18. A reaction layer has formed at the fuel-cladding interface. Contact between the fuel and cladding at this higher temperature results in the development of a U-zircaloy alloy layer at the interface. Previous investigation of the UO_2-zircaloy reaction layer by electron microprobe analysis showed it to be composed of two principal layers[D-1,-2]. The intermittent and cavitated layer adjacent to the cladding layer of oxygen-stabilized alpha was demonstrated to be low in Zr, but contained a significant quantity of U, together with a measurable quantity of Sn. The layer adjacent to the fuel at the interface was demonstrated to be low in U, but contained primarily Zr. The state of development of the reaction layer illustrated in Figure D-18 shows pitting of the cladding oxygen-stabilized alpha layer where zircaloy material has been

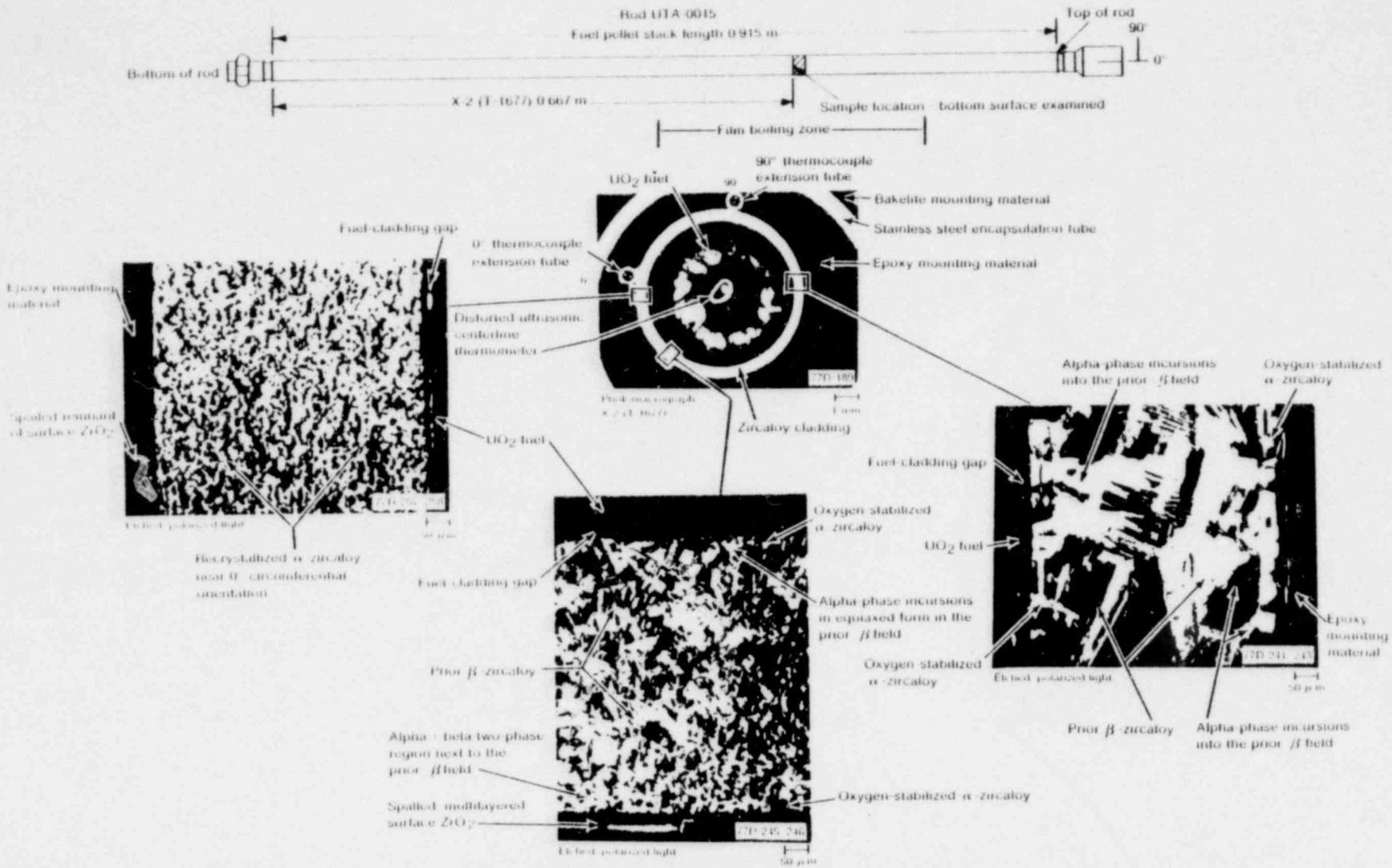

Fig. D-14 Transverse section (X-2) of Rod UTA-0015 (0.667 m) showing cladding microstructure.

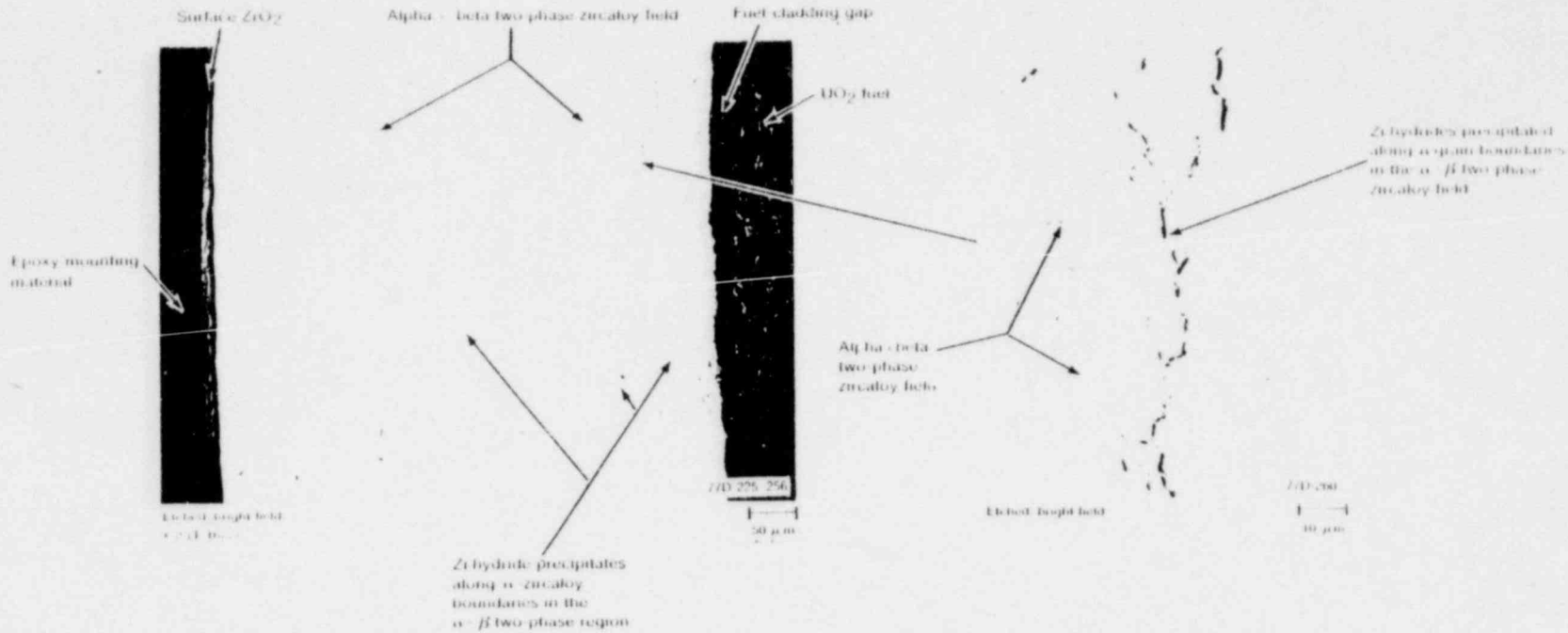

Fig. D-15 Transverse section (X-2) of Rod UTA-0015 showing cladding hydriding

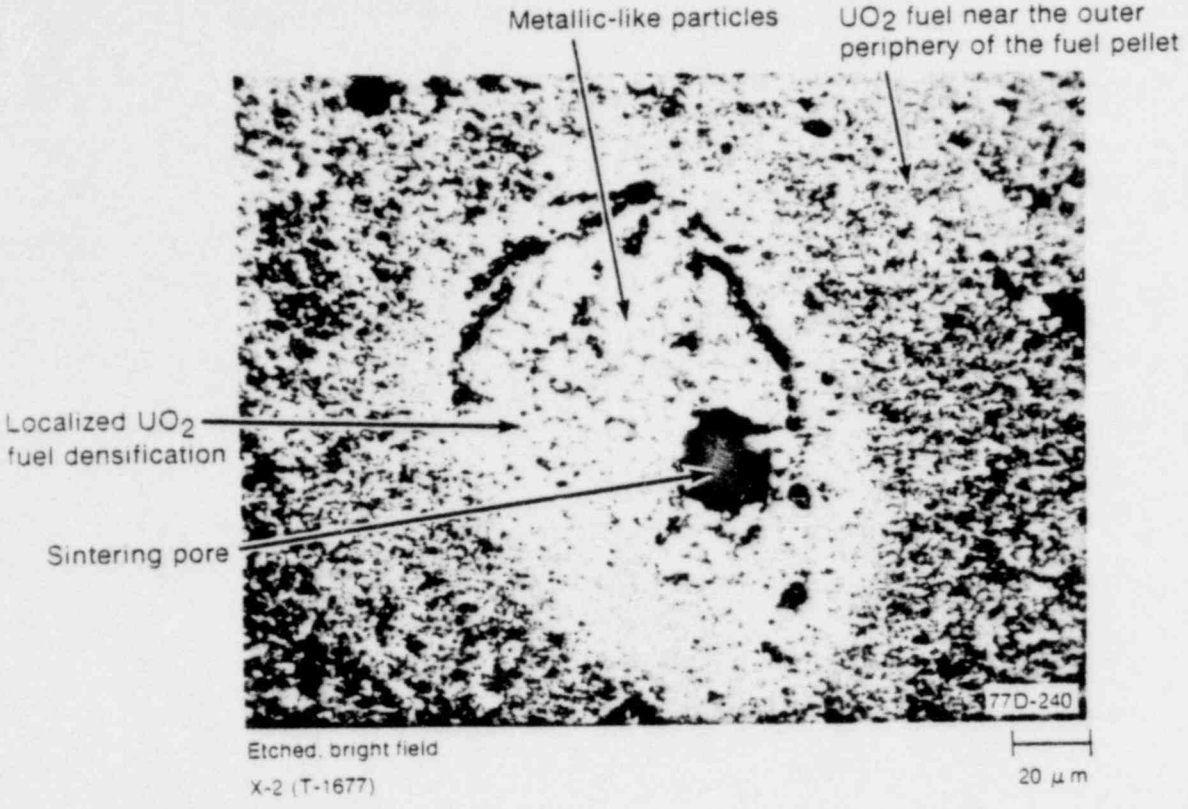

Fig. D-16 Transverse section (X-2) of Rod UTA-0015 showing metallic inclusions in the fuel.

transported into the fuel along a crack. Electron microprobe analysis of similar cavity formation showed that zircaloy and uranium exchange locations, with the cavity becoming U-rich while the zircaloy concentration in the fuel increases along the crack[D-3]. Near the interface, the composition is close to that of the Zr-rich UO_2-zircaloy reaction layer (U-Sn-Zr), whereas, farther out into the fuel the composition becomes a U-rich, U-Zr alloy with no detectable amounts of Sn.

Fuel microstructure near the outer pellet periphery resembled that of unirradiated fuel with average grain sizes of about 5 μm. Equiaxed UO_2 grain growth, illustrated in Figure D-19 for Rod UTA-0015, to grains greater than 60 μm in diameter was observed near the center of the fuel pellet.

Cladding collapse into the interface between fuel pellets was examined at 0.606 m in the longitudinal sample, Sample X-4 (90° half) shown in Figure D-20. Cladding microstructure in this sample was prior beta bounded on the inside and outside diameters by oxygen-stabilized alpha-zircaloy. In regions of fuel-cladding contact away from the collapse, a reaction layer developed at the interface. The reaction layer was brittle and fuel fracturing extended across the layer into the inner cladding layer of oxygen-stabilized alpha. Anomalously reacted material formed at the tip of the collapse indentation into the fuel

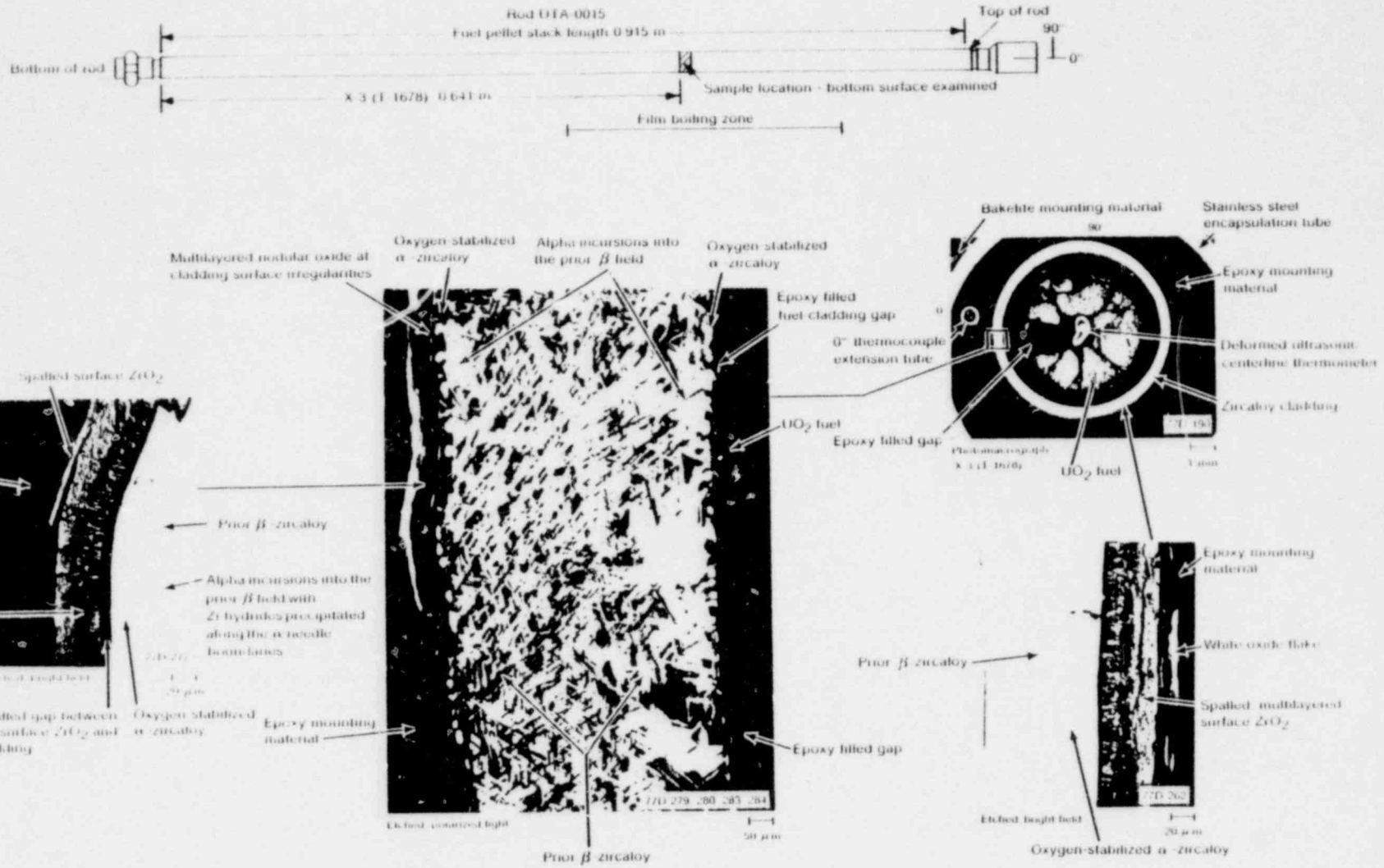

Fig. D-17. Transverse section (X-3) of Rod DFA-0015 showing cladding microstructure.

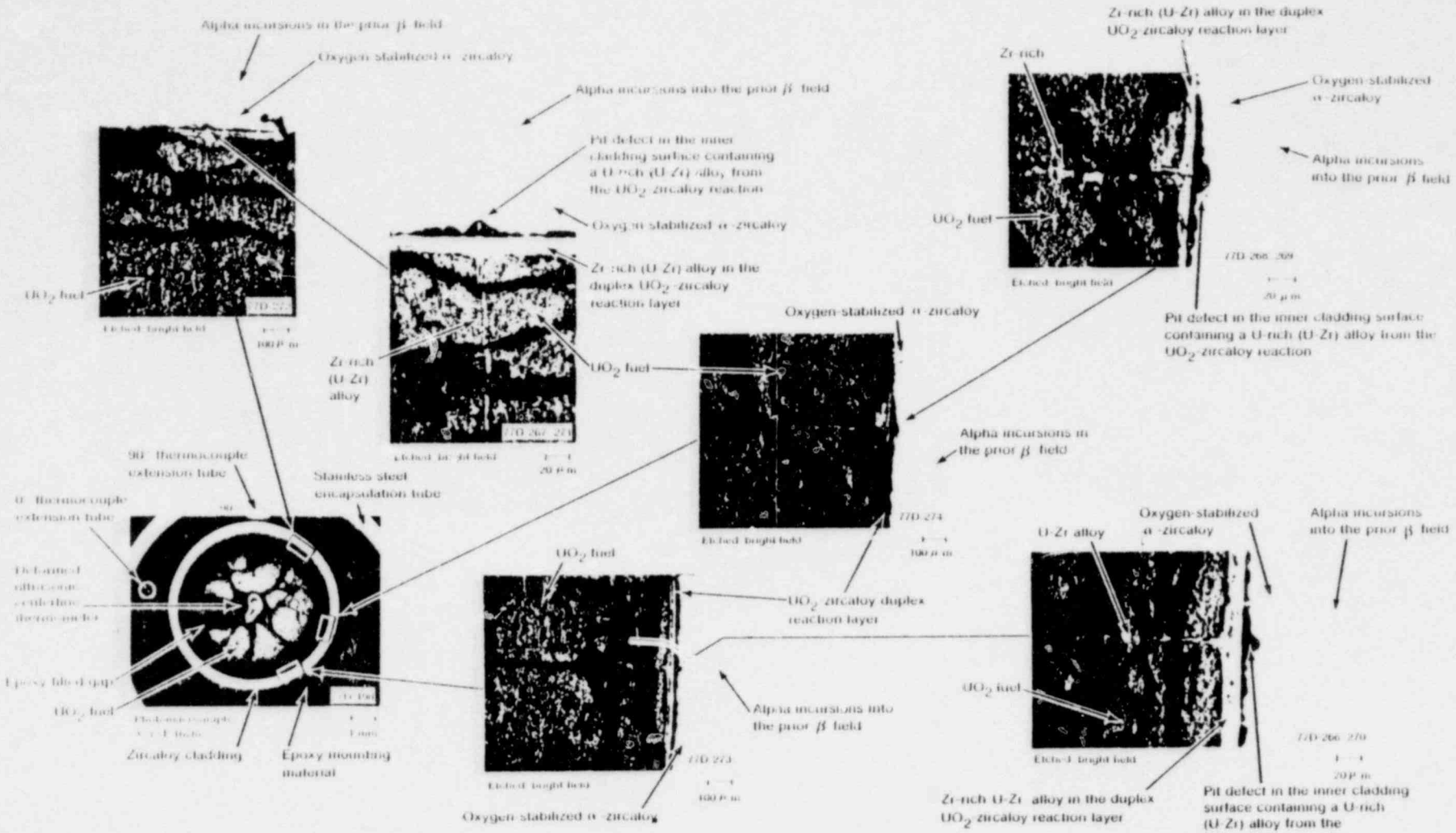

Fig. D-18. Transverse section (X-5) of Rod UTA-4015 showing fuel-cladding reaction layer material

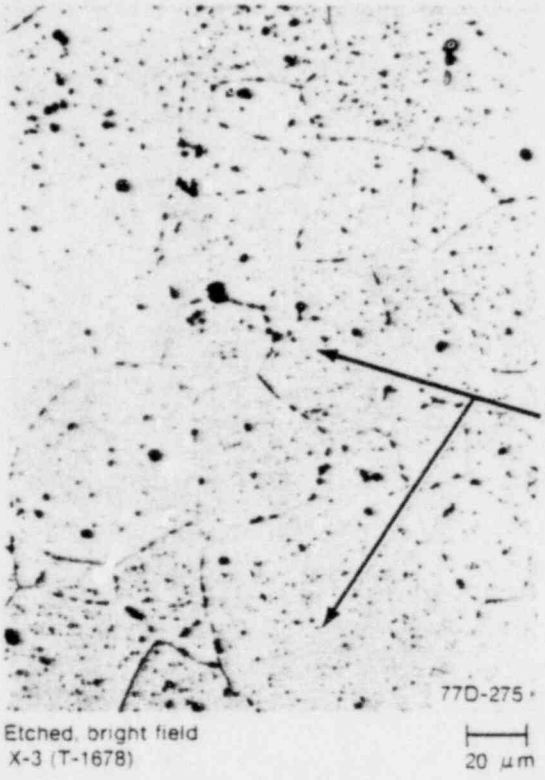

Fig. D-19 Transverse section (X-3) of Rod UTA-0015 showing fuel restructuring.

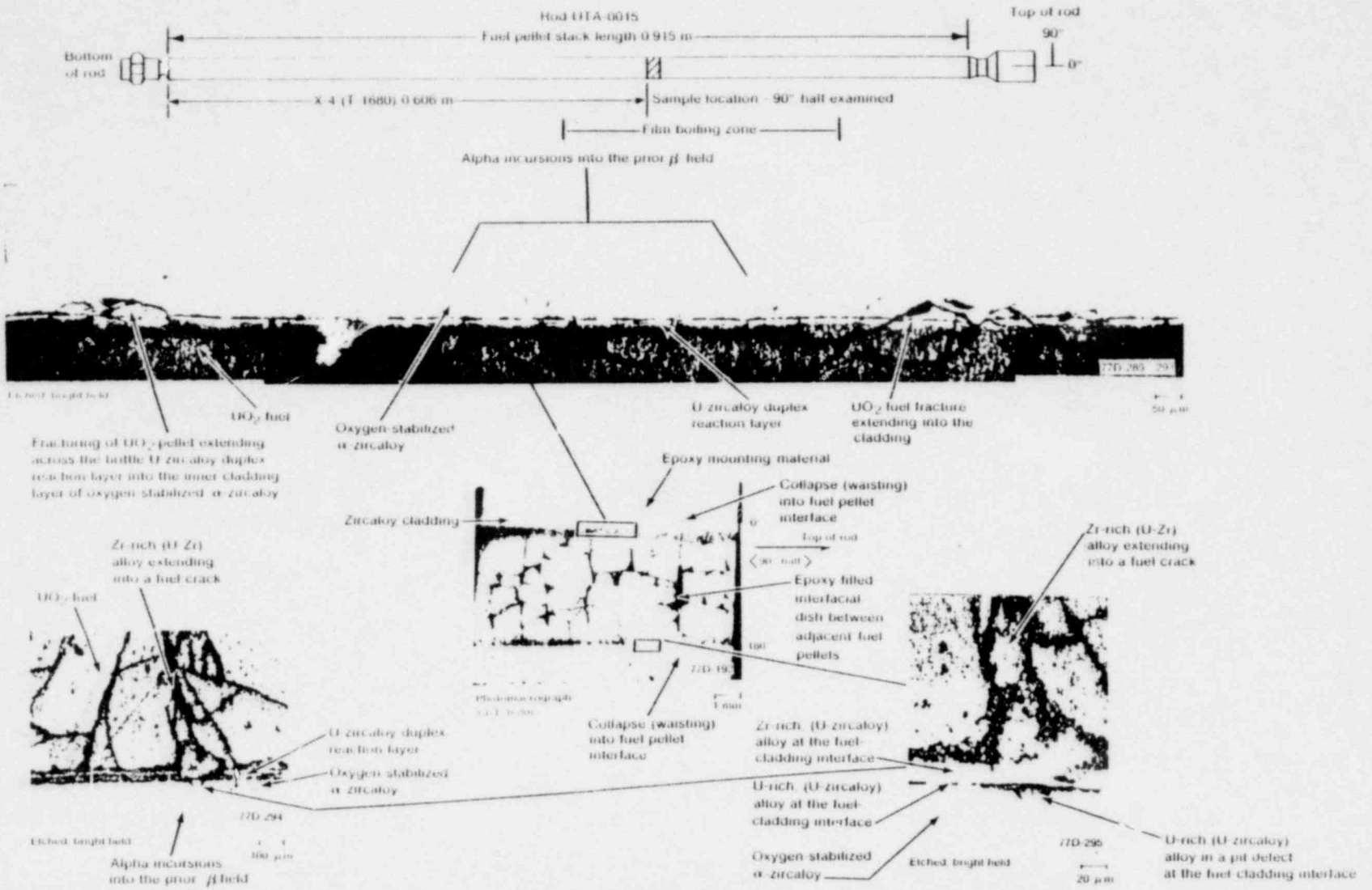

Fig. D-20 Longitudinal section (X-4) of Rod UTA-0015, between 0.606 and 0.625 m.

pellet gaps as shown in Figure D-21. Electron microprobe analysis of these anomalous reacted regions showed that the edges of the three-dimensional formation located at the collapse tip contain U and Zr with detectable, but not significant, quantities of Fe and Cr, and no measurable amount of Sn. The portion of material adjacent to the fuel contained a significant level of Zr. The central portion of the collapse tip reaction had a U content comparable to that of the UO_2 fuel pellet with essentially no Zr or Sn, but with irregular concentrations of Cr, Fe, and Ni. A similar composition was found by electron microprobe analysis of the reaction formation at the collapse tip into a fuel pellet gap of Rod UTA-0008 from Test PCM-2[D-2].

The fuel in Sample X-4 was extensively fractured as a result of the locking accomplished by the cladding collapse at the fuel pellet-to-pellet gap. Fuel restructuring is illustrated in Figure D-22. The central portion of the fuel pellet exhibited grain growth to an average grain size of 30 to 40 μm, with some individual grains up to > 60 μm. The fuel near the periphery of the pellet had grain sizes ranging from 6 to 8 μm.

Cladding collapse into the interface between fuel pellets was examined at 0.559 m in another longitudinal sample, Sample X-5 (90° half), as illustrated in Figures D-23 and D-24. Cladding microstructure was prior beta-zircaloy with inner and outer diameter layers of oxygen-stabilized alpha-zircaloy. Long, needle-like platelets of alpha material appeared inside the prior beta grains. Where the collapse brought the fuel into contact with the cladding, a UO_2-zircaloy bimetallic reaction layer developed.

Equiaxed grain growth up to 14 to 20 μm occurred in localized regions out to the periphery of the fuel pellets in this sample; otherwise, fuel grain sizes remained 4 to 6 μm in diameter near the periphery. This sample was located nearest the power peak (at 0.404 m) and had equiaxed grain growth and fuel slumping into the fuel pellet interfacial dish at the center of the pellet. Large grains to > 400 μm were observed in the central region where fuel slumping occurred. These large equiaxed grains near the centerline were present out to about 12% of the pellet radius. Equiaxed grain sizes in the adjacent regions, illustrated in Figure D-25, were only to 40 to 50 μm.

2.3 Metallographic Examination Results for Rod UTA-0016

Four samples were sectioned from Rod UTA-0016 for metallurgical examination. The samples were sectioned from locations within the film boiling zone which extended between 0.52 and 0.80 m along the fuel rod. The cladding microstructure found in these samples was prior beta bounded on the inside and outside diameters by oxygen-stabilized alpha-phase zircaloy. Some evidence of hydriding was observed in the cladding. The hydride precipitates were mostly identifiable in the lower temperature ($T \simeq 1245$ K) prior beta-phase material. The hydrides were dispersed and retained a general circumferential orientation where observable. A U-zircaloy duplex reaction layer was present on some samples but was not observed uniformly around the circumference of the fuel-cladding interface. Oxide spalling was observed at the outside diameter on some samples. UO_2 fuel restructuring was basically

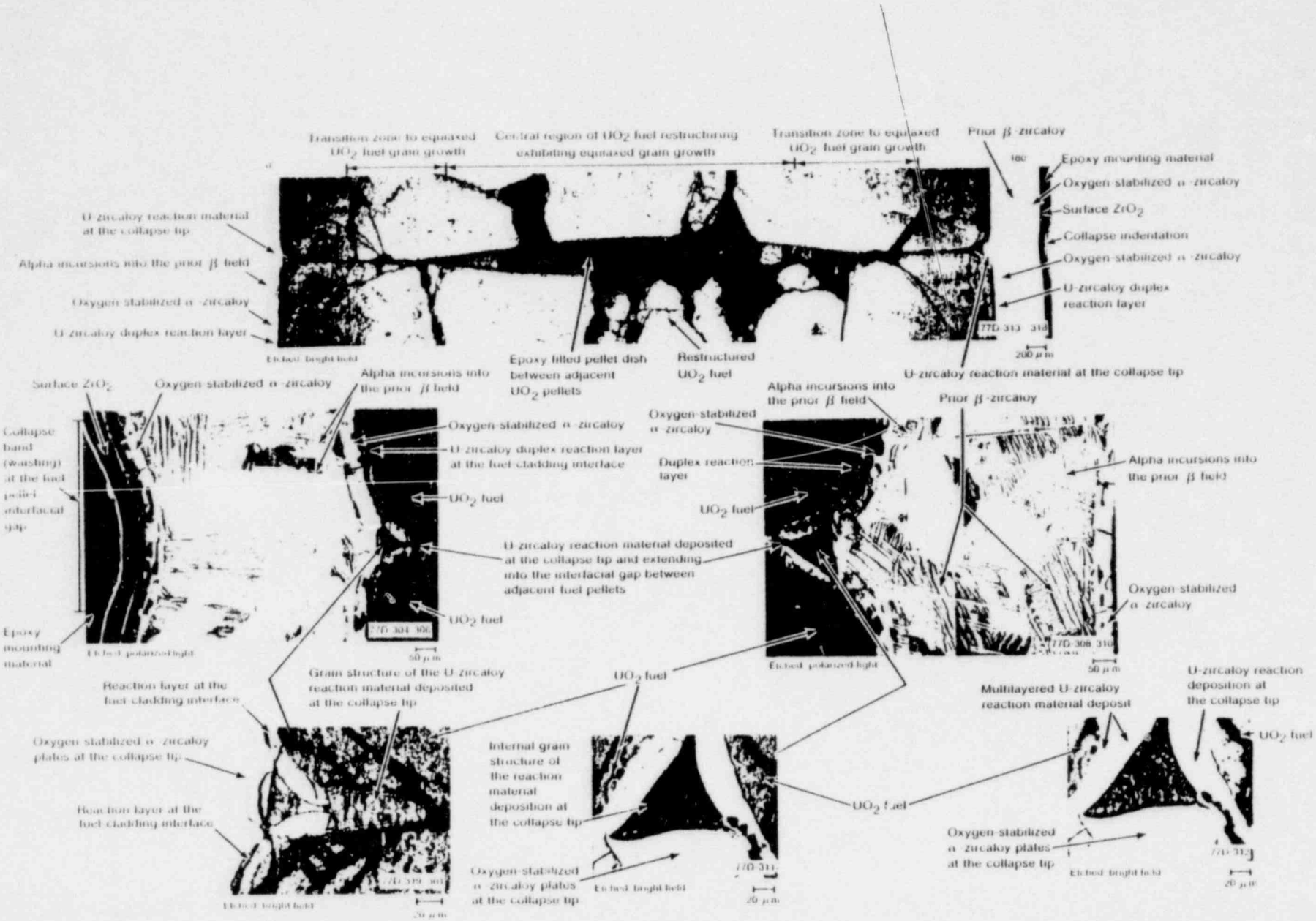

Fig. D-21 Longitudinal section (X-4) of Rod UTA-0015 showing fuel-cladding reaction

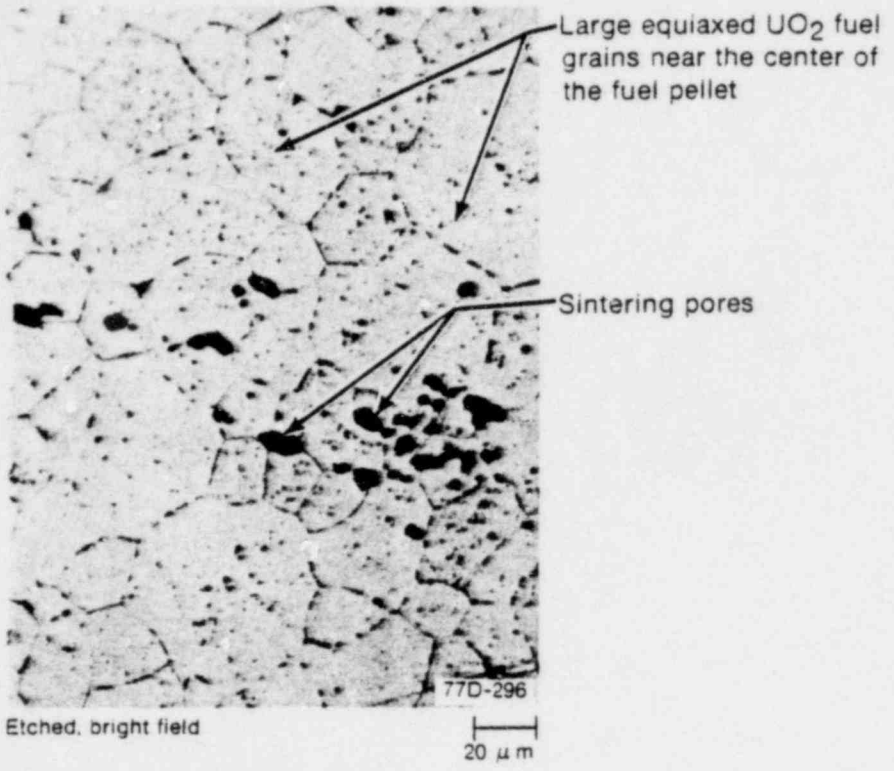

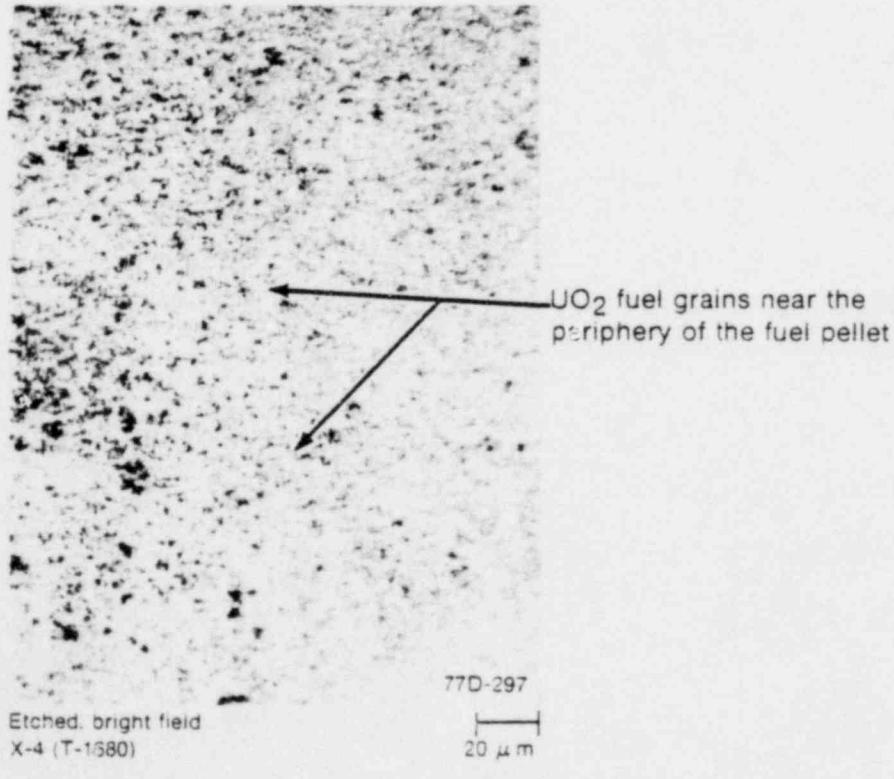

Fig. D-22 Longitudinal section (X-4) of Rod UTA-0015 showing fuel restructuring.

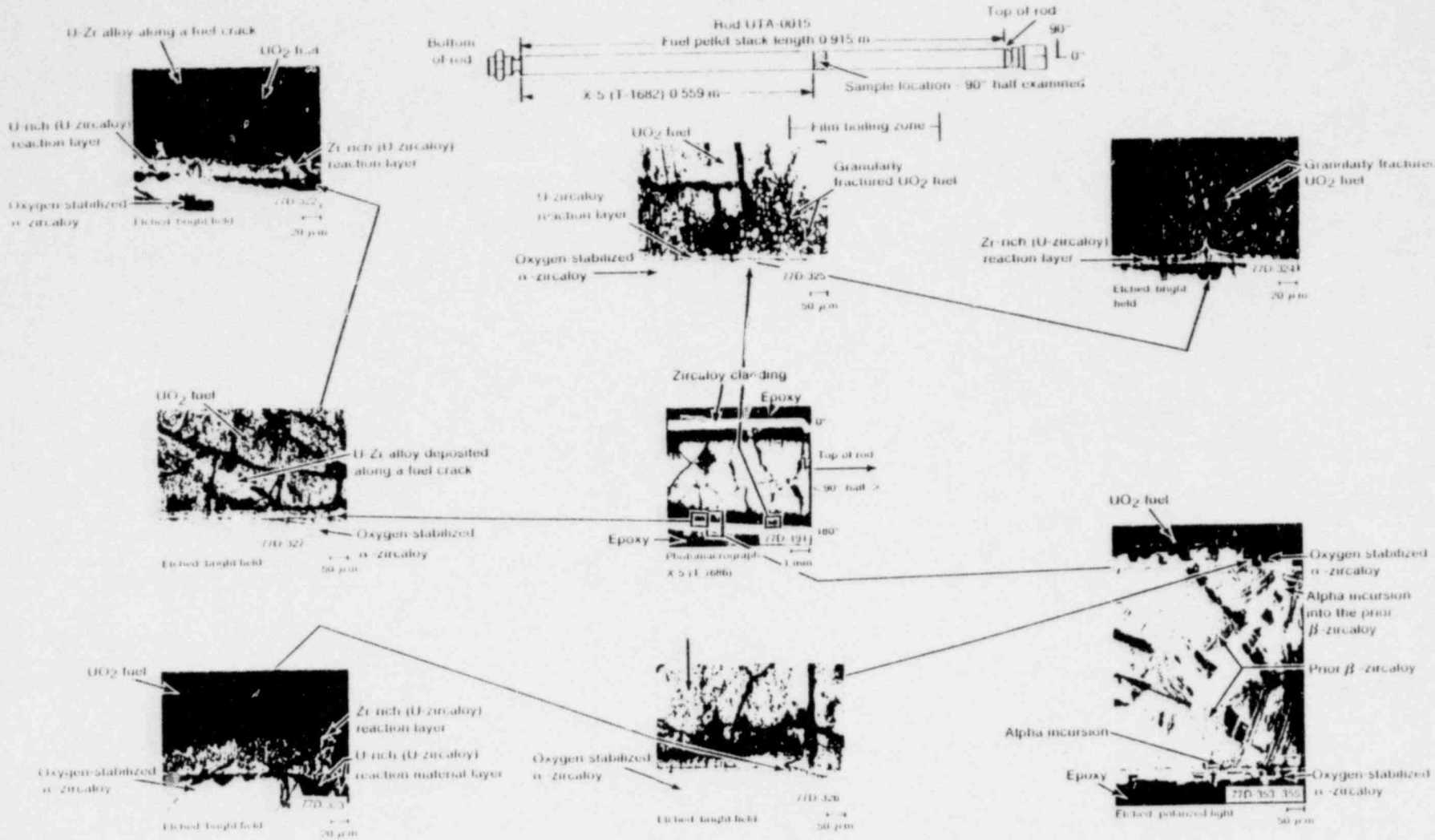

Fig. D-23 Longitudinal section (X-5) of Rod UTA-0015 between 0.559 and 0.571 m.

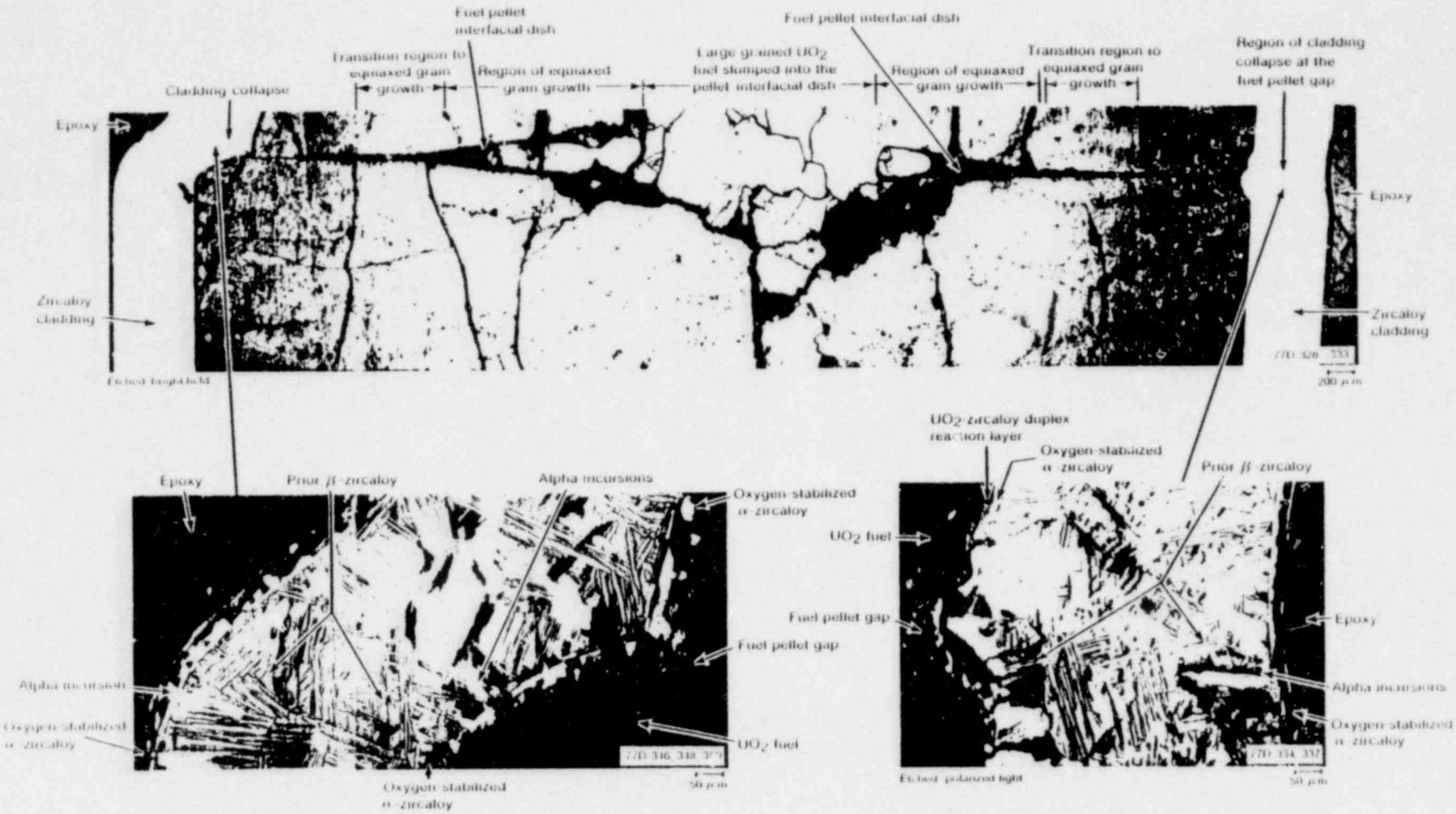

Fig. D-24 Longitudinal section (X-5) of Rod DEA-0015 showing cladding collapse and fuel restructuring.

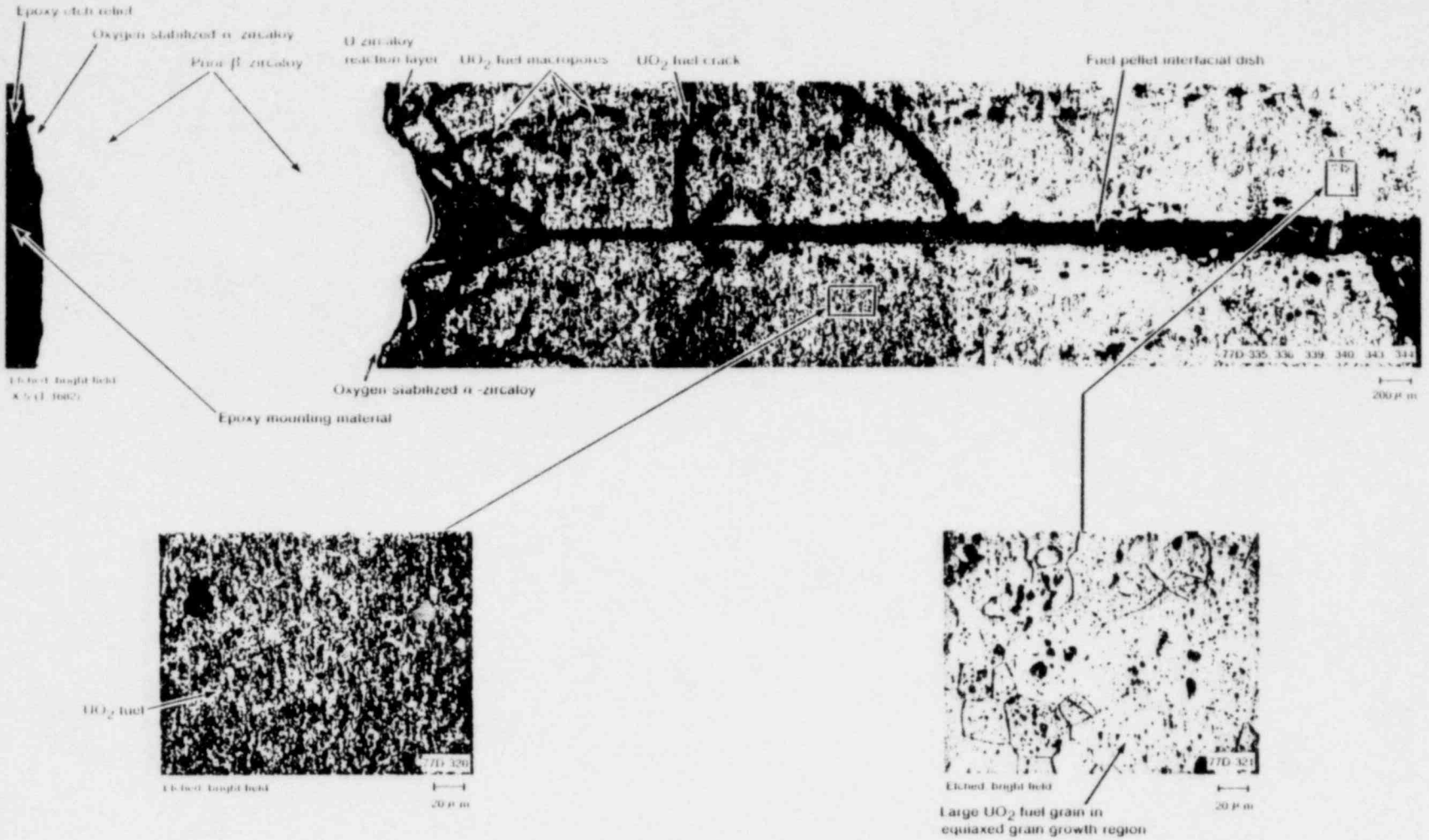

Fig. D-25 Longitudinal section (X-5) of Rod UEA-0015 showing fuel restructuring.

equiaxed grain growth toward the center. A small zone of melting at the center occurred in association with the oxidation of the tantalum sheathed centerline thermocouple.

Thermocouple readings of DNB conditions ($T > 730$ K) for Rod UTA-0016 were recorded during the fourth, and final test cycle. The 0.787-m, 270° thermocouple gave the first indication of DNB, followed by the 0.686-m, 180° thermocouple 30 s later, and the 0.584-m, 90° thermocouple 70 s later. No DNB was recorded during the test by the 0.483-m, 0° thermocouple. The 0.787-m, 270° thermocouple and the 0.686-m, 180°, and 0.584-m, 90° thermocouples indicated DNB conditions for 155, 140, and 80 s, respectively, during Cycle 4. Maximum thermocouple readings of 845, 1000, and 1005 K were recorded by the 0.787-m, 270°; 0.686-m, 180°; and 0.584-m, 90° thermocouples, respectively, during the test cycle. Such temperatures are from 240 to 400 K below the 1245 K transformation temperature of the zircaloy cladding to the prior beta-phase, verified metallographically. The microstructures of each sample are discussed below.

A transverse sample (Sample W-1), located 0.686 m from the bottom of the fuel stack, is presented in Figure D-26. The cladding microstructure around the circumference was prior beta-phase zircaloy with inside and outer diameter layers of oxygen-stabilized alpha-zircaloy. The UO_2-zircaloy duplex reaction layer at the fuel-cladding interface was present near the 270° orientation and extended around to 0°. No reaction layer was present at the other locations. Oxide spalling at the outer cladding surface is illustrated in the figure. The fuel microstructure near the outer pellet edge had grain sizes of about 5 to 6 μm, as seen in Figure D-27. Equiaxed grains up to ∼20 to 30 μm developed at the center of the fuel pellet.

The transverse sample (Sample W-2), sectioned 0.667 m from the bottom of the fuel stack, shown in Figure D-28, has a prior beta-phase microstructure around the circumference. The outer diameter band of oxygen-stabilized alpha is thinnest close to and beneath the 0° thermocouple extension tube weld. Hydride precipitates are also observed in the vicinity of the weld.

Fuel restructuring in this sample is illustrated in Figure D-29. The fuel grain size near the periphery of the pellet is about 4 μm, but near the center of the pellet, grain enlargement has occurred, resulting in an average grain size of 30 to 40 μm, with scattered grains exceeding 90 μm. A small melt zone is also observed near the centerline thermocouple sheath. Tantalum inclusions from reaction with the thermocouple sheath are found in the melt zone.

A prior beta microstructure was observed around the circumference of transverse Sample W-3, shown in Figure D-30. Inner and outer diameter layers of oxygen-stabilized alpha were present in the cladding.

Reaction layer development around the circumference of this sample is illustrated in Figure D-31. Pit defects formed at fuel cracks which intersect the fuel-cladding interfacial reaction layer. Microprobe analysis of the material deposited along the fuel cracks, some

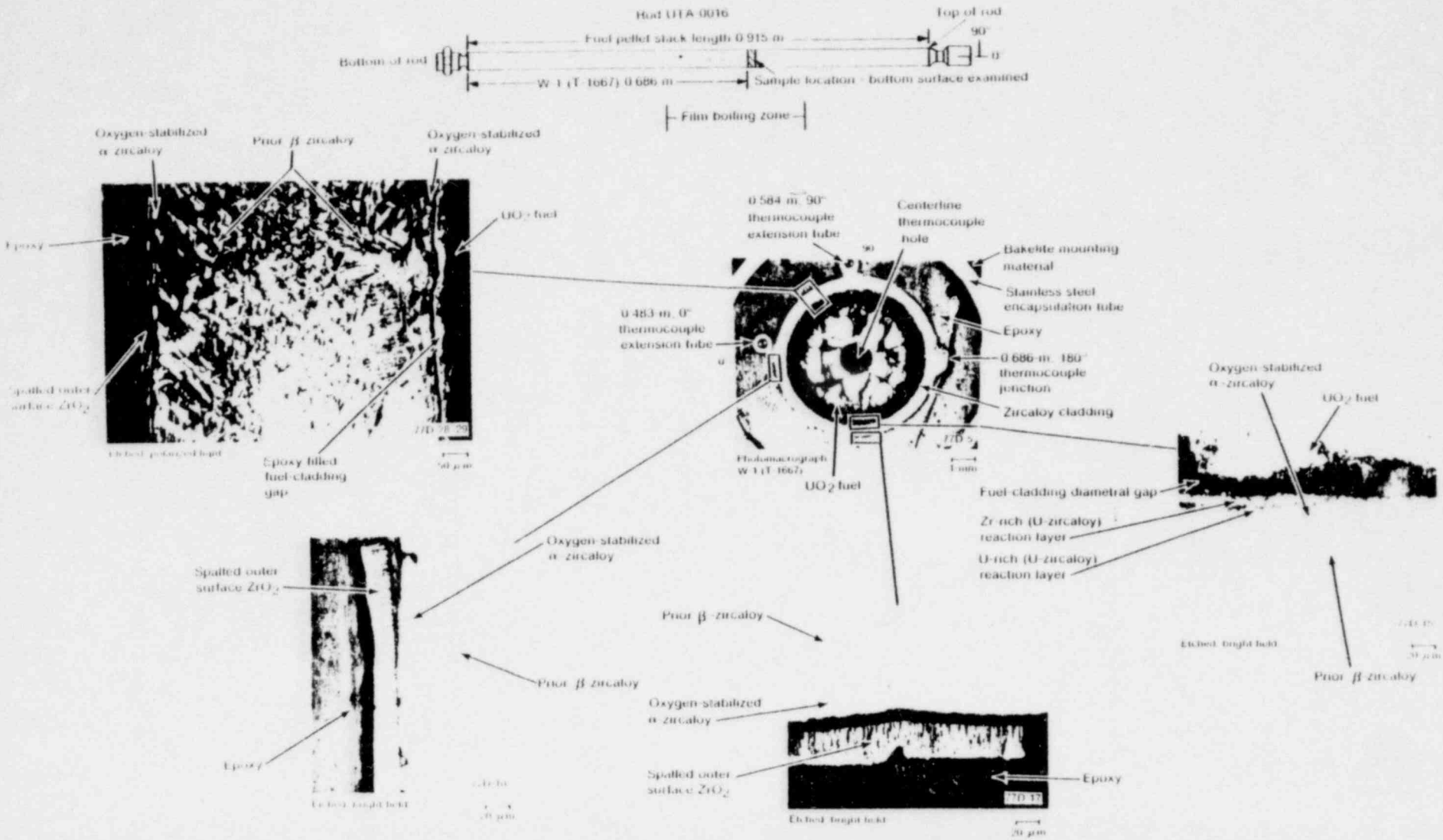

Fig. D-26 Transverse section (W-1) of Rod UTA-0016 (0.686 m) showing cladding microstructure

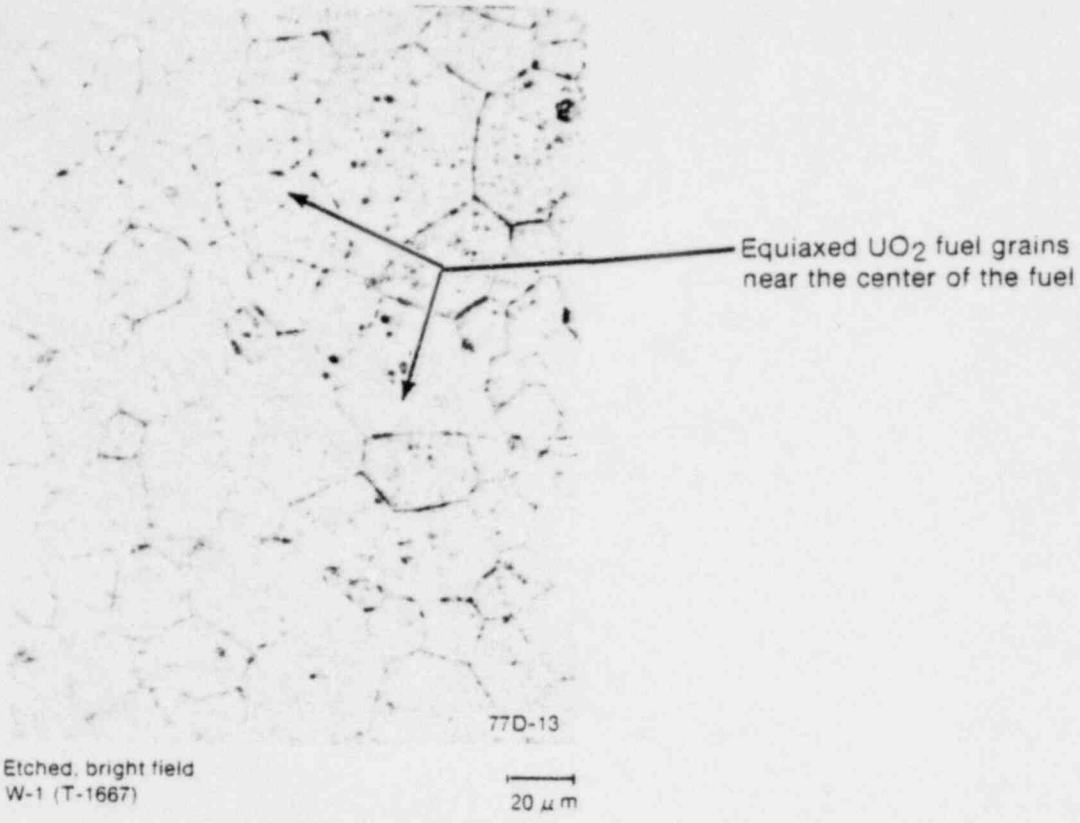

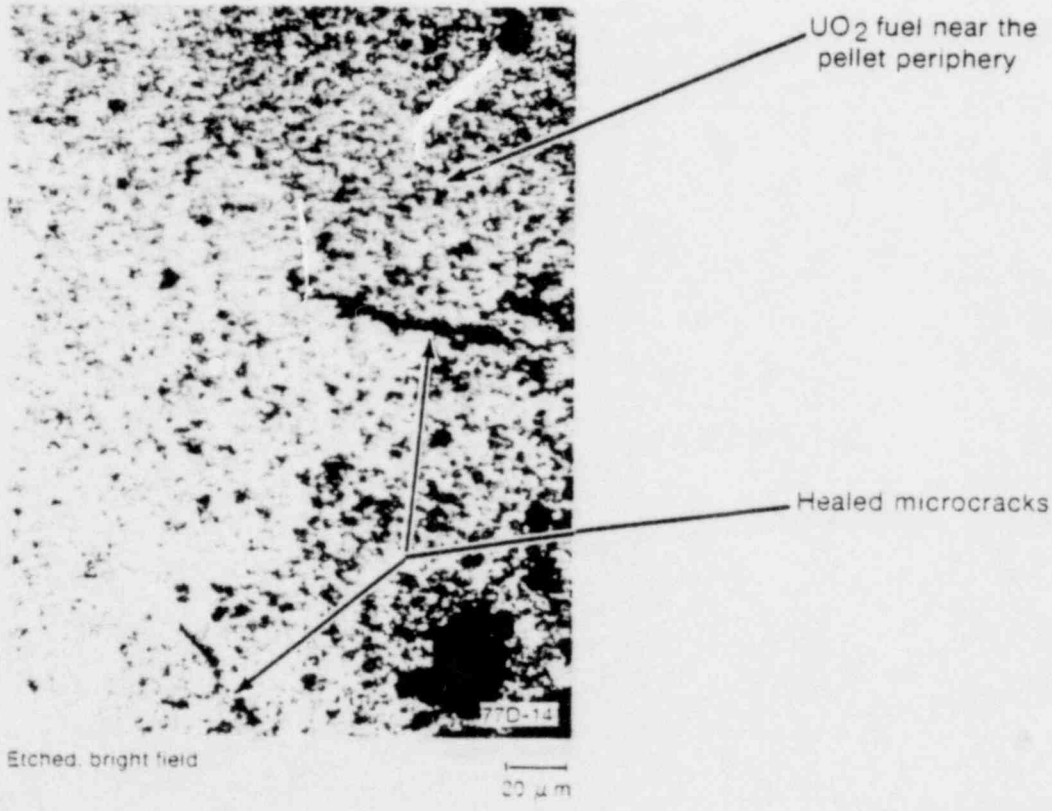

Fig. D-27 Transverse section (W-1) of Rod UTA-0016 showing fuel restructuring.

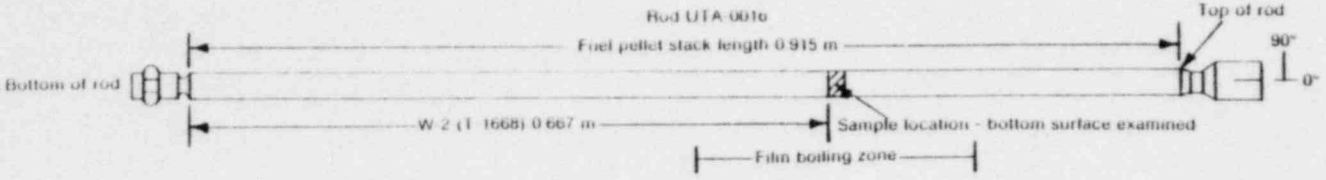

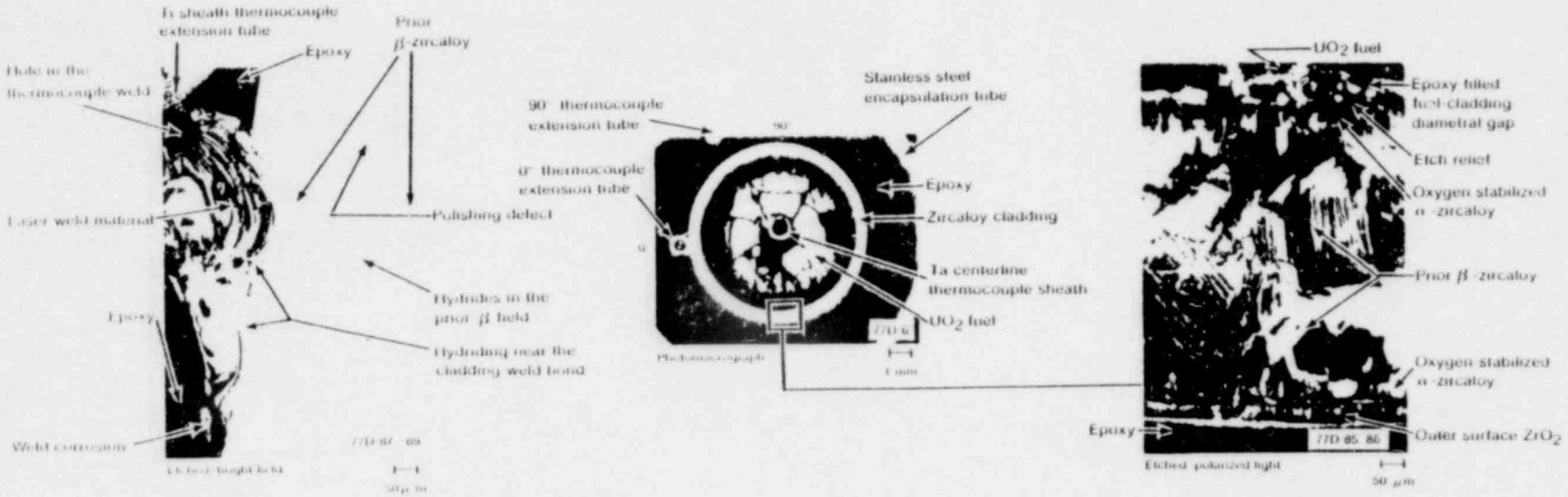

Fig. D-28. Transverse section (W-2) of Rod UTA-0016 (0.667 m) showing cladding microstructure

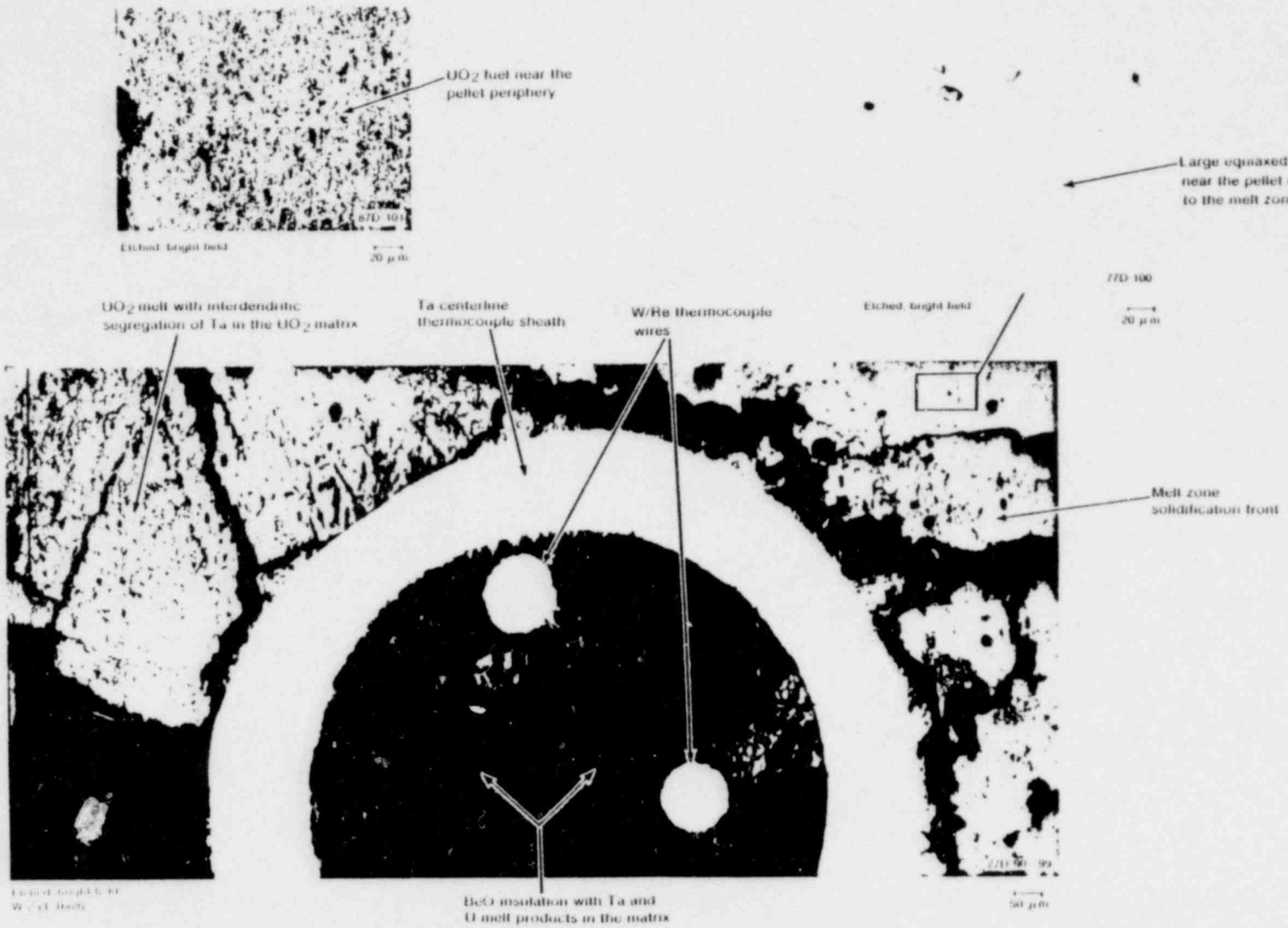

Fig. 4.29. Transverse section (W-2) of Rod UTA-0016 showing fuel restructuring and tantalum thermocouple sheath melting with the UO_2 fuel.

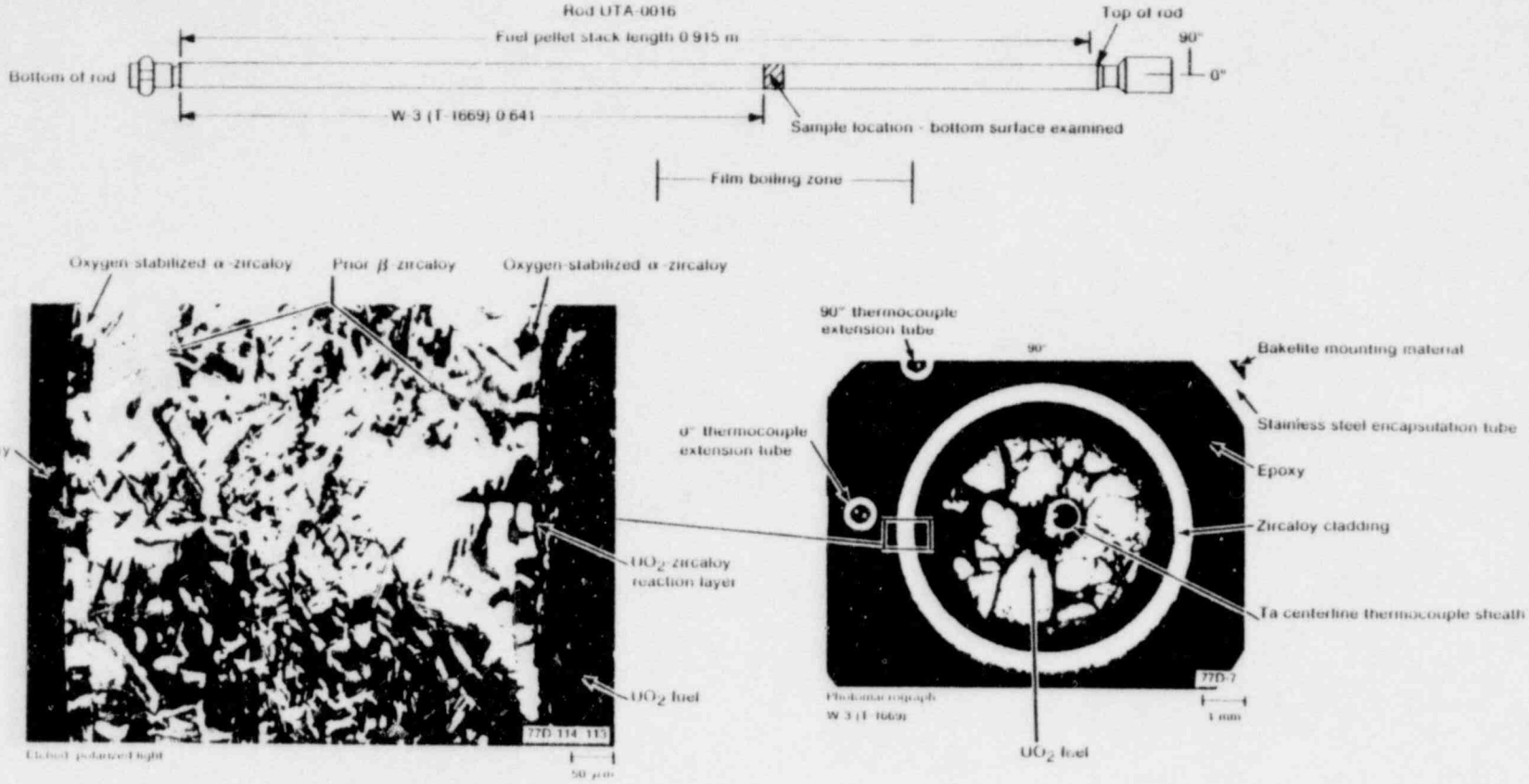

Fig. D-30 Transverse section (W-3) of Rod UTA-0016 (0.641 m) showing cladding microstructure.

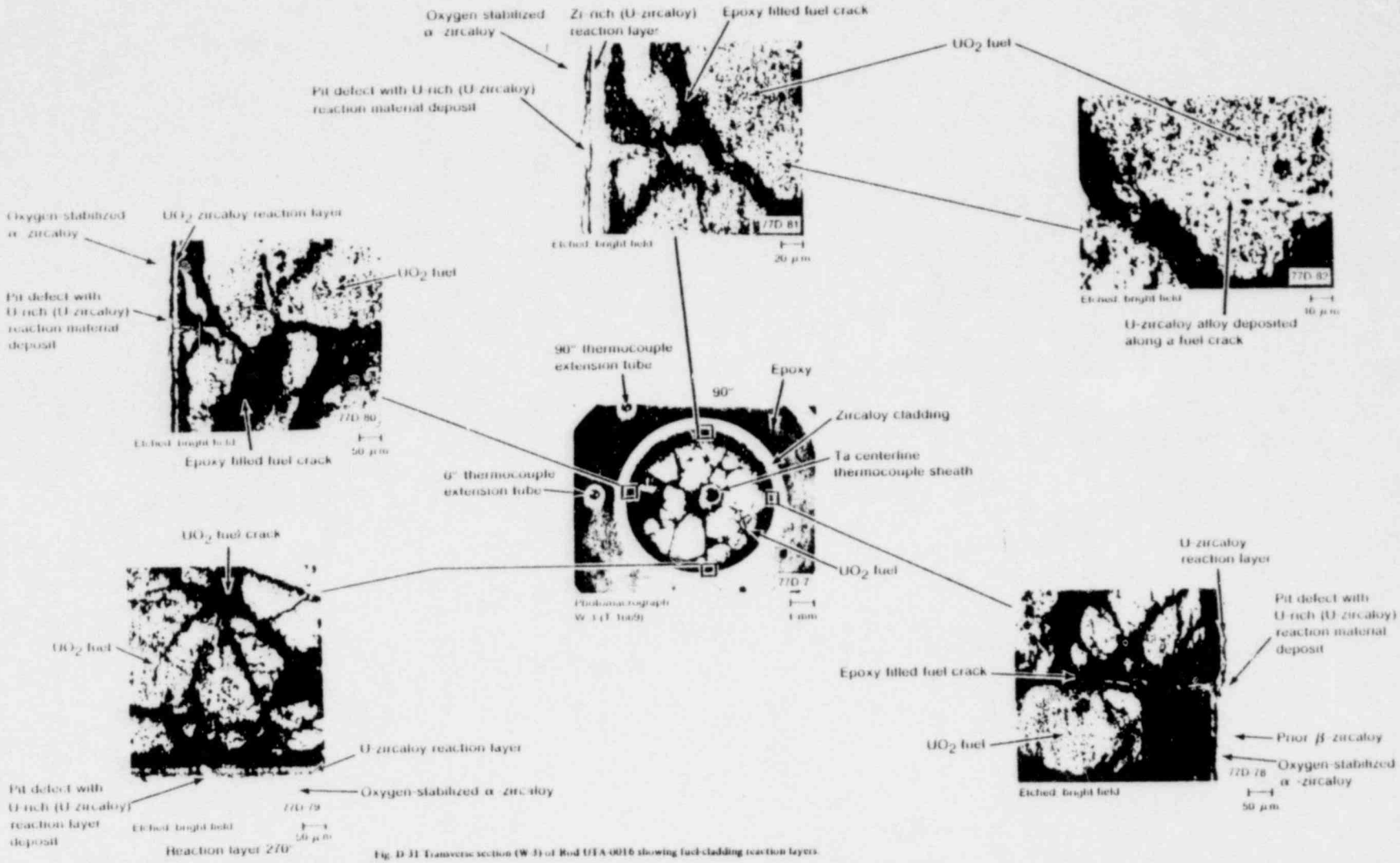

Fig. D 31 Transverse section (W-3) of Rod UTA-0016 showing fuel-cladding reaction layers

distance (100 to 200 μm) out into the pellet, has shown that the U-Sn-Zr reaction material near the fuel-cladding interface changed to essentially a U-Zr alloy rich in U[2].

UO_2 restructuring is similar to that discussed for the previous metallurgical sample. The melt zone near the tantalum thermocouple sheath is illustrated in Figure D-32.

The cladding and fuel microstructures from Sample W-4, located 0.587 m from the bottom of the fuel stack, are shown in Figures D-33 and D-34, respectively. The prior beta material, exhibiting a basket weave structure, is bounded at the inner and outer diameters by oxygen-stabilized alpha layers and extends around the circumference. An inner diameter fuel-cladding interfacial reaction layer is illustrated in Figure D-33.

Fuel microstructure was fine grained (< 4 μm) near the pellet periphery. The equiaxed grain growth near the center of the pellet had grain sizes of 30 to 40 μm, with scattered grains having sizes greater than 70 μm. The molten zone near the tantalum thermocouple sheath is illustrated in Figure D-34.

2.4 Metallographic Examination Results for Rod A-0017

Metallographic samples sectioned from Rod A-0017 were taken from the collapse zone extending from 0.50 to 0.80 m from the bottom of the fuel stack. Two longitudinal samples were examined. One sample was sectioned near the central region of the collapse zone, and the other was sectioned near the top of the collapse zone. Cladding from the center of the collapse zone exhibited a prior beta microstructure with inner and outer layers of oxygen-stabilized alpha. A fuel molten zone with central voids near the center of the pellet and fuel slumping were observed. Near the upper end of the film boiling zone, the cladding exhibited an alpha + beta two-phase zircaloy microstructure. The cladding in this region exhibited hydriding at both the inner and outer diameters. Fuel restructuring included a region of equiaxed grain growth and columnar grain development near the center of the fuel pellet. Pore segregation was observed in the grain boundaries of the large equiaxed and columnar grains.

Rod A-0017 was uninstrumented, and no cladding temperatures were obtained during the test. Based on the length change indication, Rod A-0017 initiated transition film boiling about 10 s before Rod UTA-0015 indicated DNB conditions (Rod UTA-0015 was directly across from Rod A-0017 in the test assembly). Rod A-0017 stabilized in film boiling about 20 s later than Rod UTA-0015. Based on the length change (from LVDT data) during the test, Rod A-0017 appears to have been in DNB conditions for approximately 235 s. The actual time in film boiling appears to be only approximately 116 s, as indicated by the leveling off of the change in length of the fuel rod prior to test termination.

The longitudinal sample (Sample Z-1) sectioned from the rod 0.629 m from the bottom of the fuel stack is shown in Figure D-35. The prior beta-phase zircaloy, bounded by inner and outer diameter layers of oxygen-stabilized alpha, extends along the length of the cladding sample at both the 0 and 180° sides. Reaction layer development at the fuel-cladding interface is also evident in the figure.

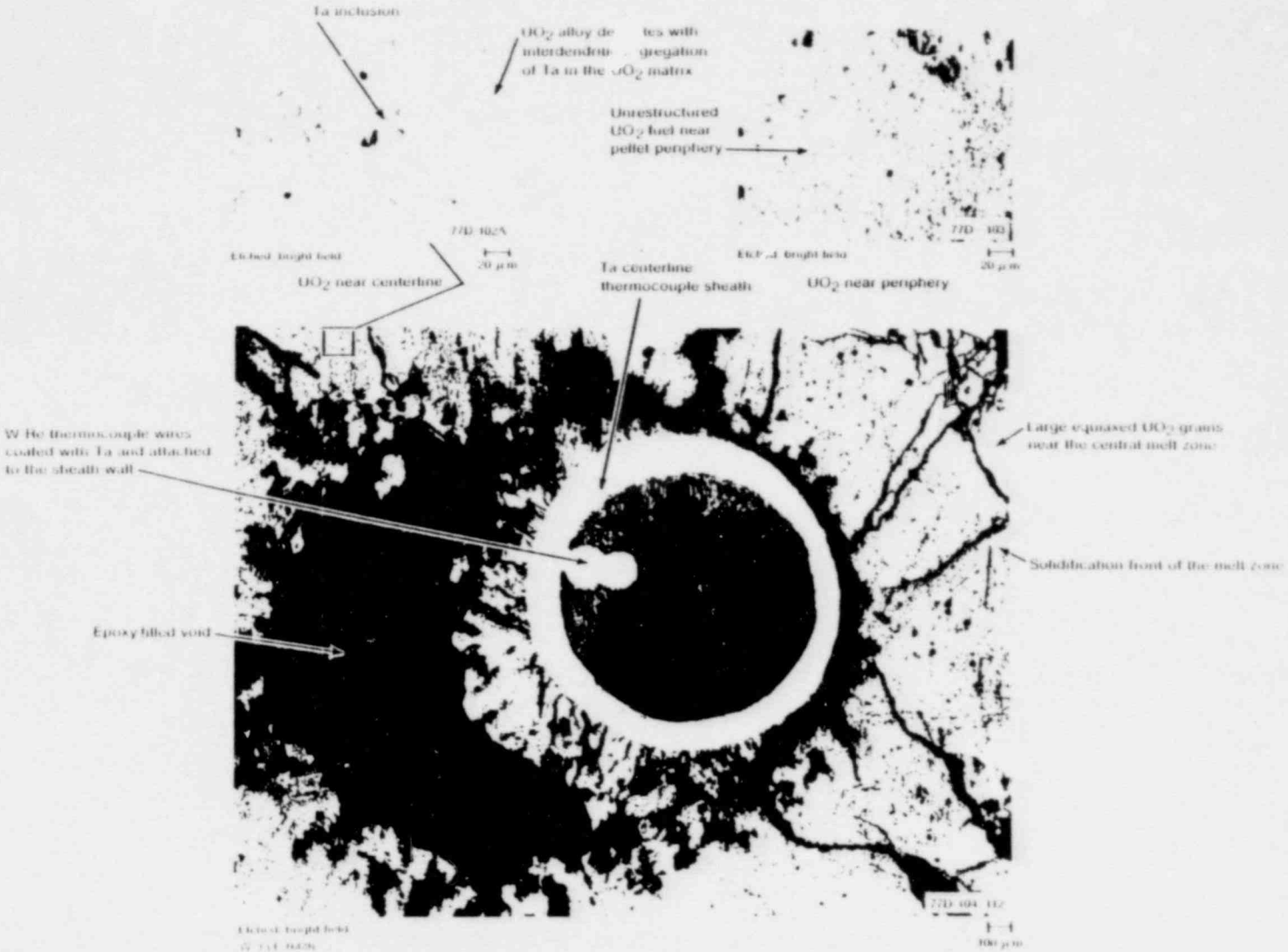

Centerline thermocouple

Fig. 4-12. Transverse section 6W-J1 of Rod DTA-0016 showing fuel restructuring and fuel melting with the tantalum centerline thermocouple sheath.

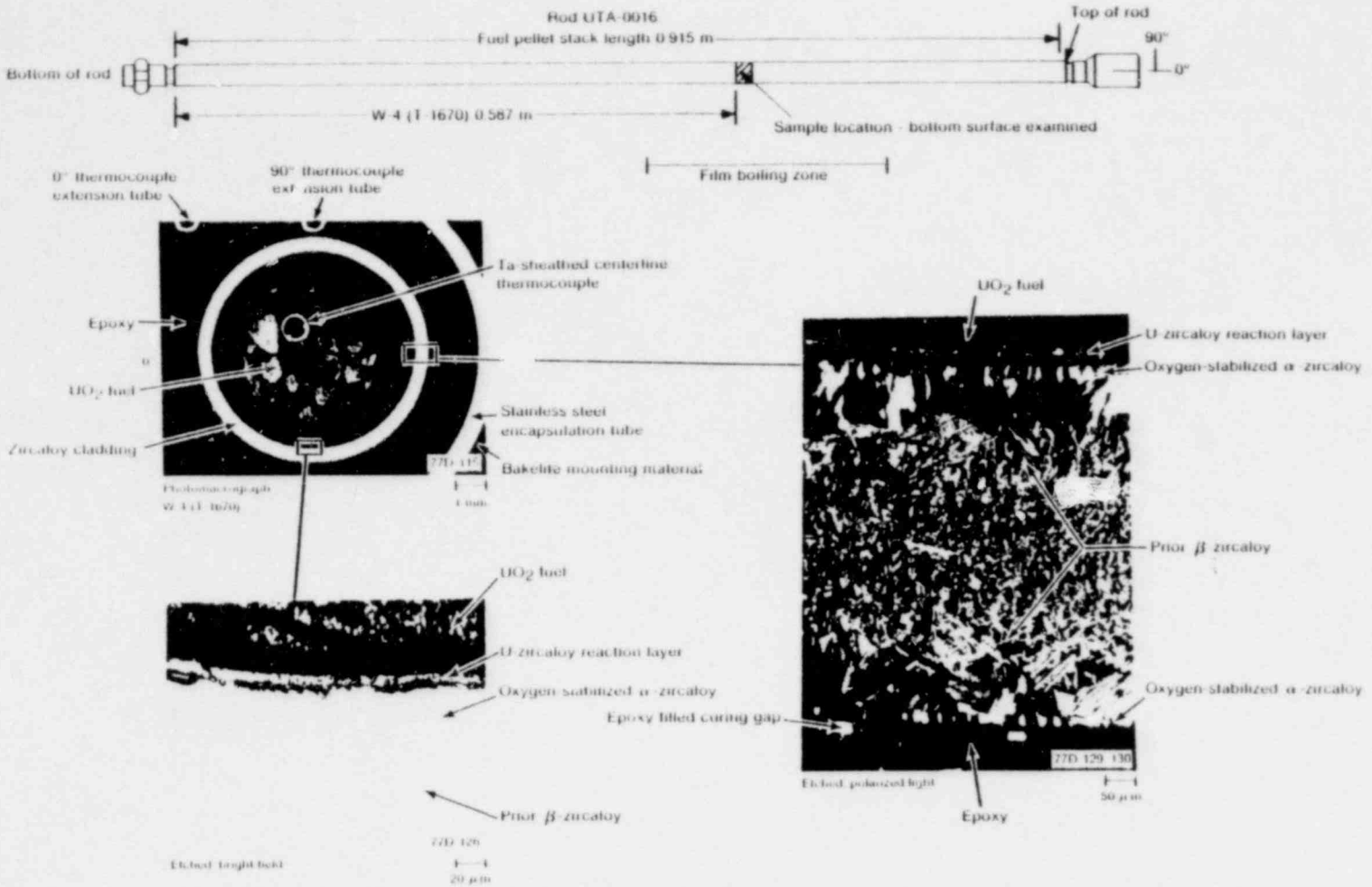

Fig. D-33. Transverse section (W-4) of Rod UTA-0016 (0.587 m) showing cladding microstructure.

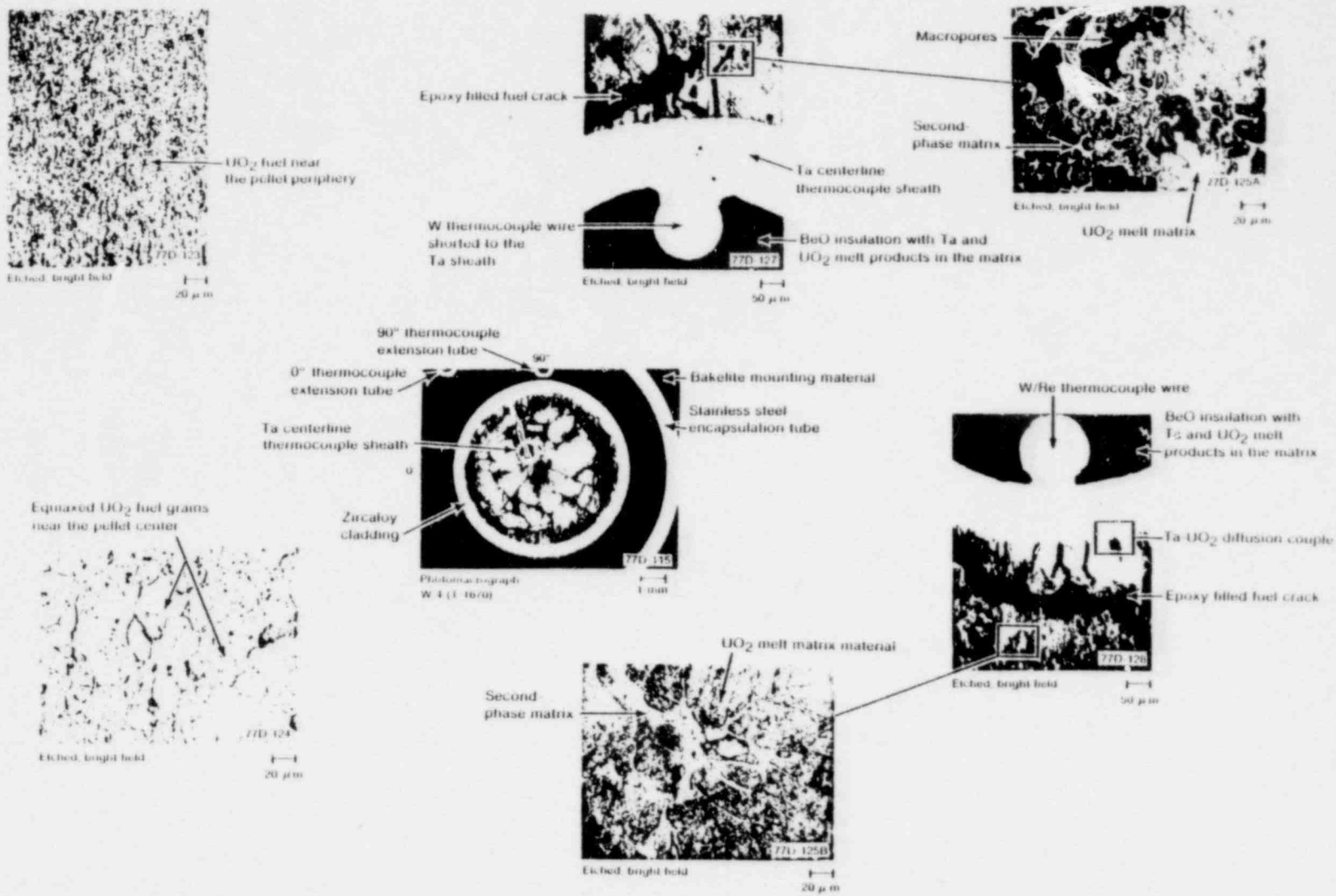

Fig. D-34 Transverse section (W-4) of Rod UTA-0016 showing fuel restructuring and fuel melting zone.

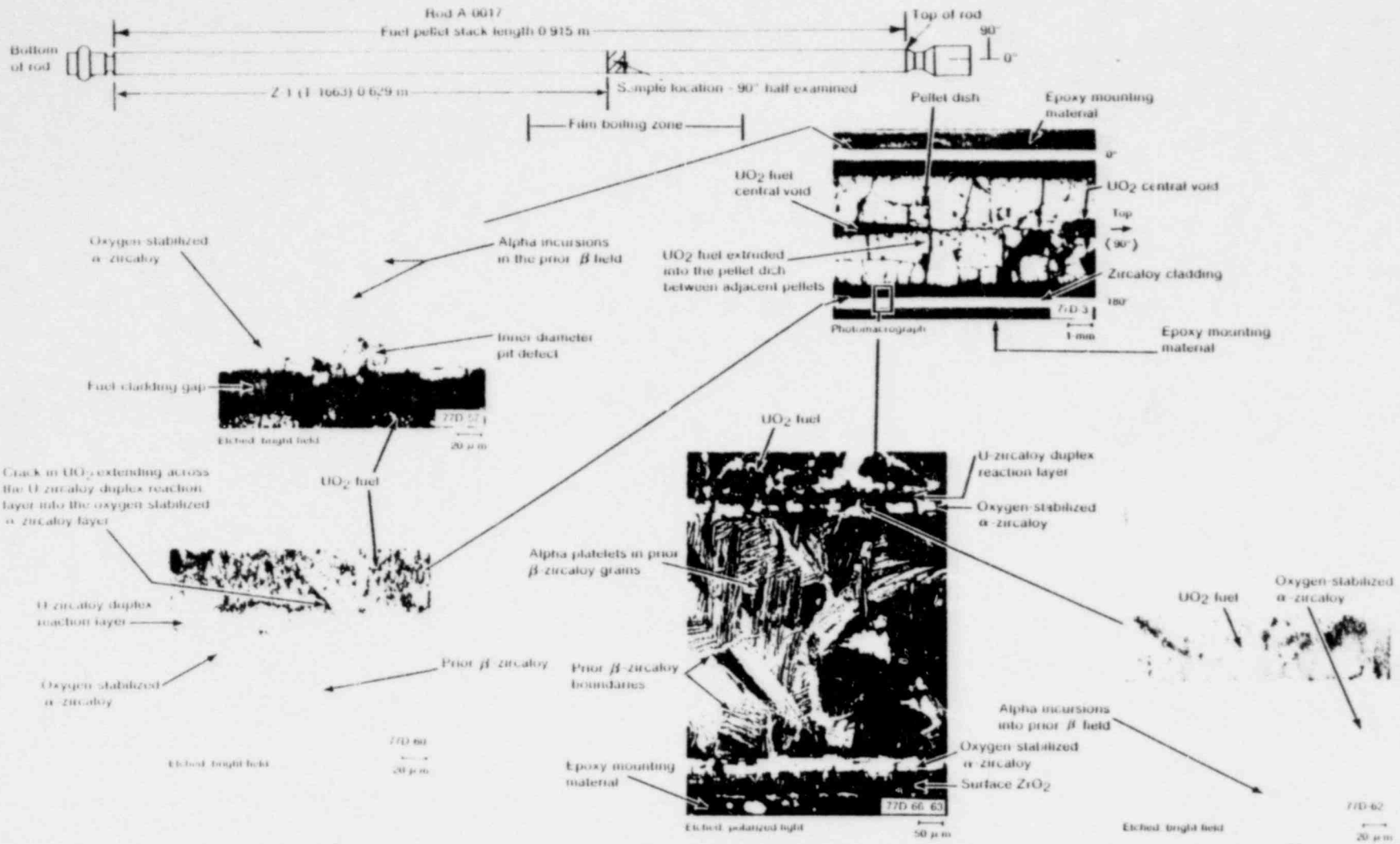

Fig. D-15 Longitudinal section (Z-1) of Rod A-0017 (between 0.629 and 0.648 m) showing cladding microstructure.

Various regions of the fuel restructuring seen in this sample are illustrated in Figure D-36. Fuel near the periphery of the pellet resembles that of unirradiated fuel (grain size ~ 4 μm). A region of equiaxed grain growth lies adjacent to and inside the region of fine grained fuel at the pellet periphery. Intermediate sized equiaxed grains (30 to 60 μm) are found in this zone with the grain size varying to greater than 100 μm adjacent to the central region of columnar grain growth. Sintering macro- and micropores have collected along the grain boundaries in the equiaxed and columnar grain growth regions near the center of the fuel pellet. Fuel in the central zone exhibiting long columnar grains contains coalesced pores near the central lenticular melt zone void. Fuel slumping into the interfacial pellet dish between adjacent fuel pellets is illustrated in the figure.

The longitudinal sample (Sample Z-2) located 0.768 m from the bottom of the fuel stack shows an alpha + beta two-phase zircaloy microstructure as illustrated in Figure D-37. The presence of the hydride precipitates in the alpha + beta two-phase field of the cladding suggests that hydrogen solution in the presence of dissolved oxygen may be responsible for this morphology, similar to that discussed for Rod UTA-0015. (As pointed out at the beginning of this section, both Rods A-0017 and UTA-0015 exhibited similar LVDT responses during the final test cycle and have similar thermal responses.) The form of hydriding in the sample is illustrated further in Figure D-38.

Fuel restructuring is shown in Figure D-39. In the photomacrograph of the longitudinal section, the region of limited equiaxed grain growth near the center of the fuel pellets appears as a lighter color than the background. The restructured region tapers to a small zone near the top of the sample, establishing the upper terminus of the higher fuel centerline temperatures (T $\sim$1900 K) for equiaxed grain growth[D-6]. Grain sizes ranged from < 4 μm near the pellet periphery to nearly 10 to 12 μm at the center of the fuel pellet. Bands of white material, illustrated in Figure D-40, were found in the fuel near the top end of the sample and close to the pellet edge. The composition is unknown, but this material may be remnants of grinding compound filling porous regions in the fuel.

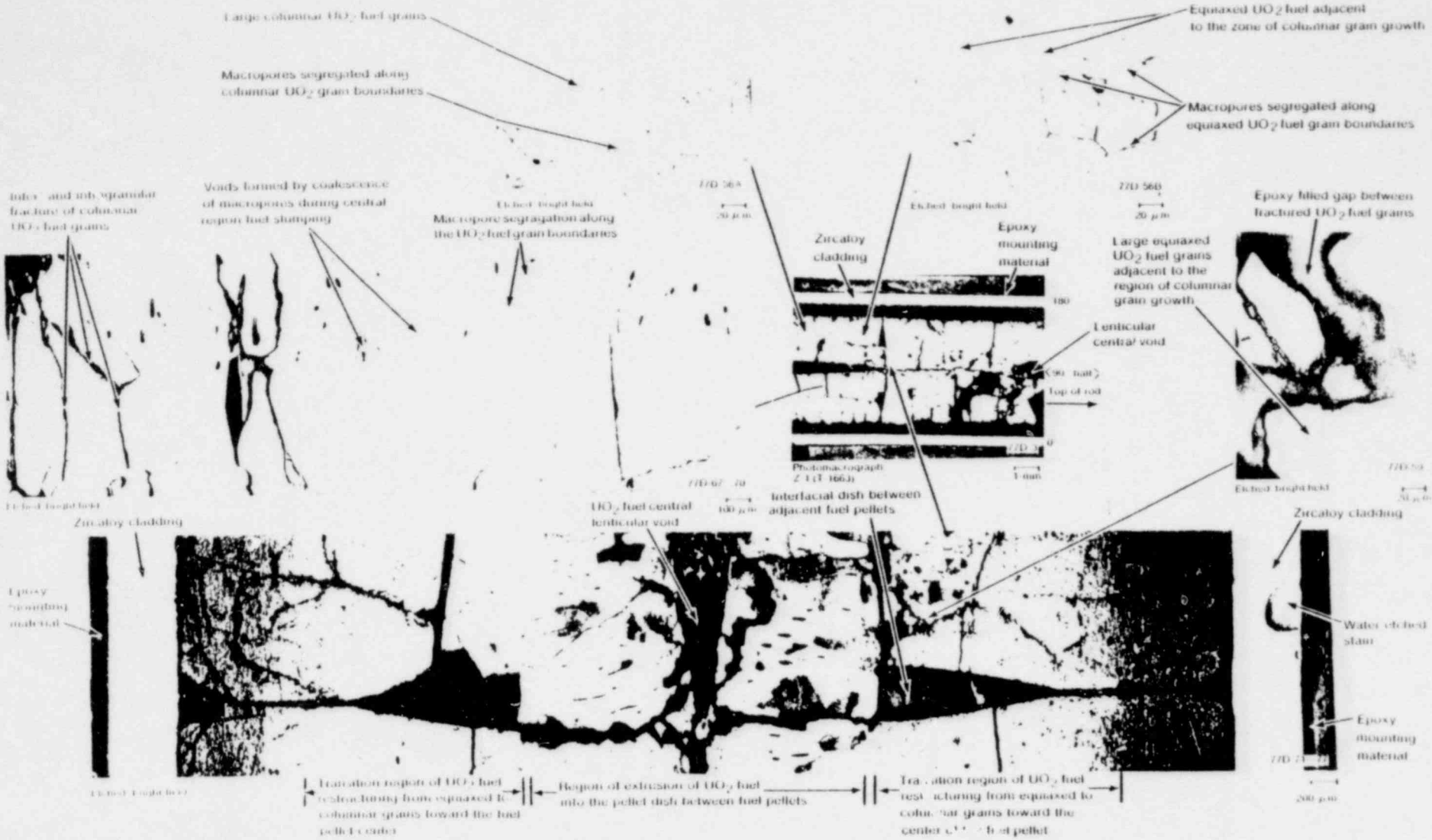

Fig. D-36 Longitudinal section (Z-11) of Rod A-0117 showing fuel restructuring and fuel melting zone

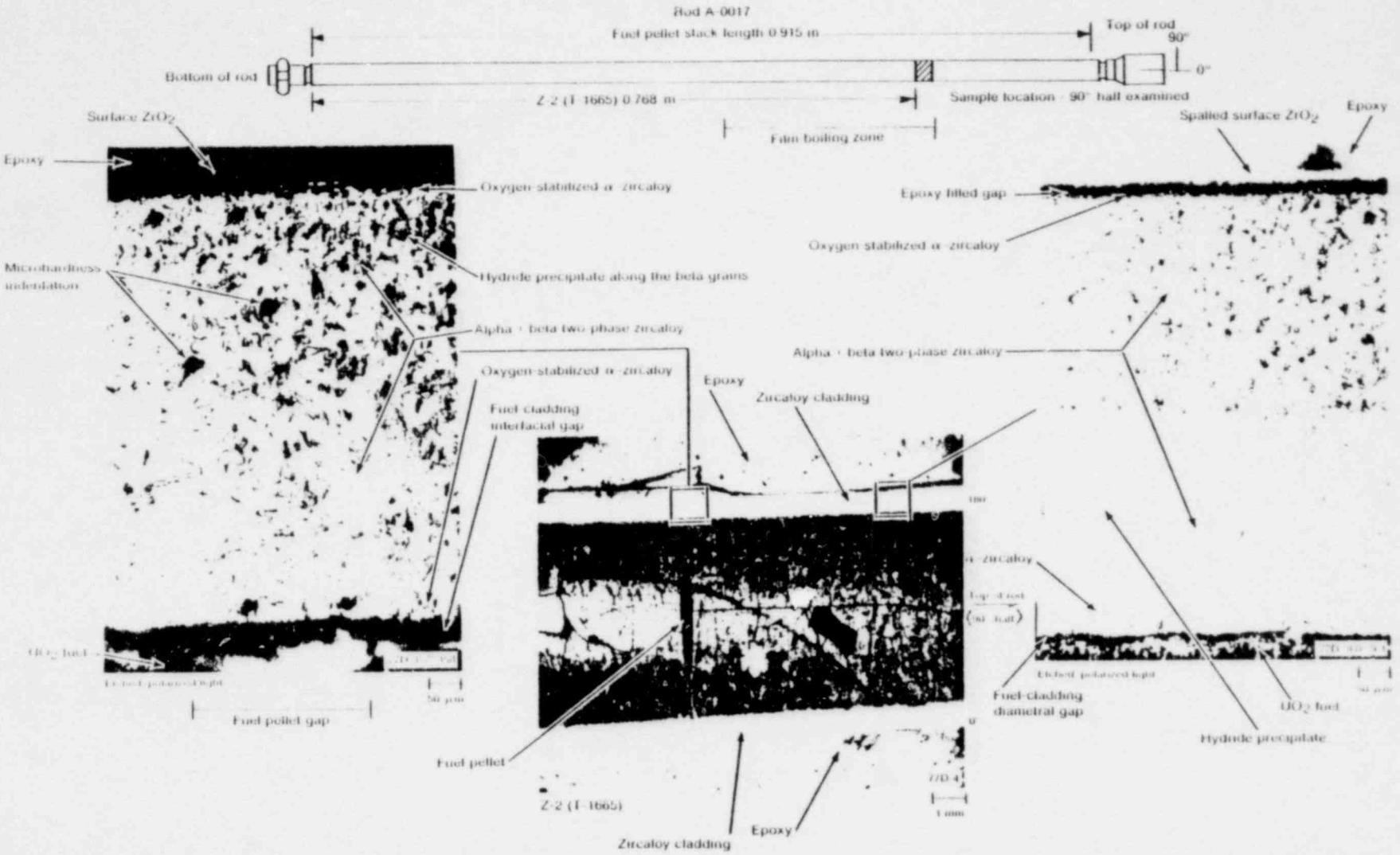

Fig. D-37 Longitudinal section (Z-2) of Rod A-0017 (between 0.768 and 0.87 m) showing cladding microstructure

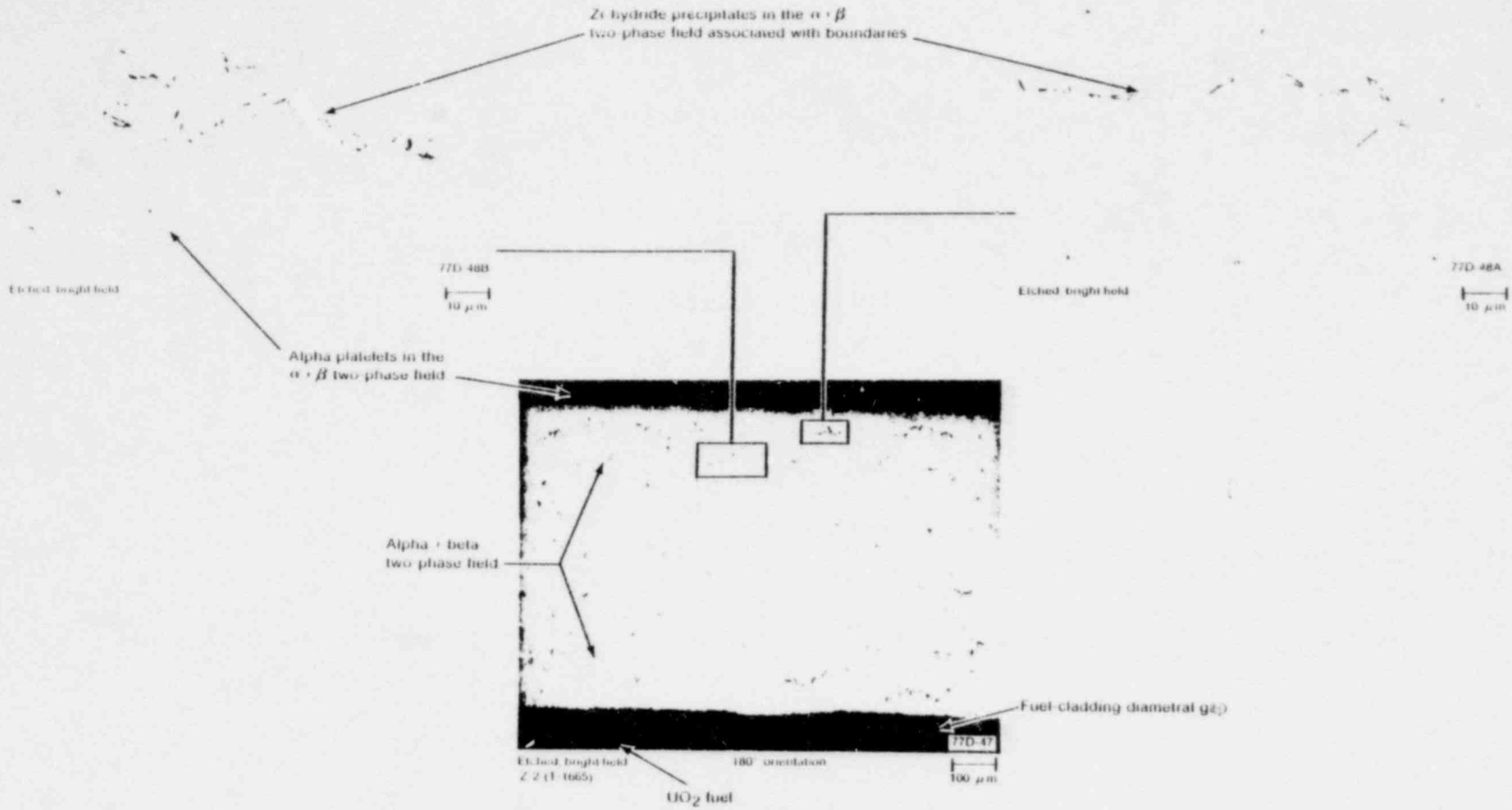

Fig. D-38. Longitudinal section (Z-2) of Rod A-0017 showing cladding hydriding.

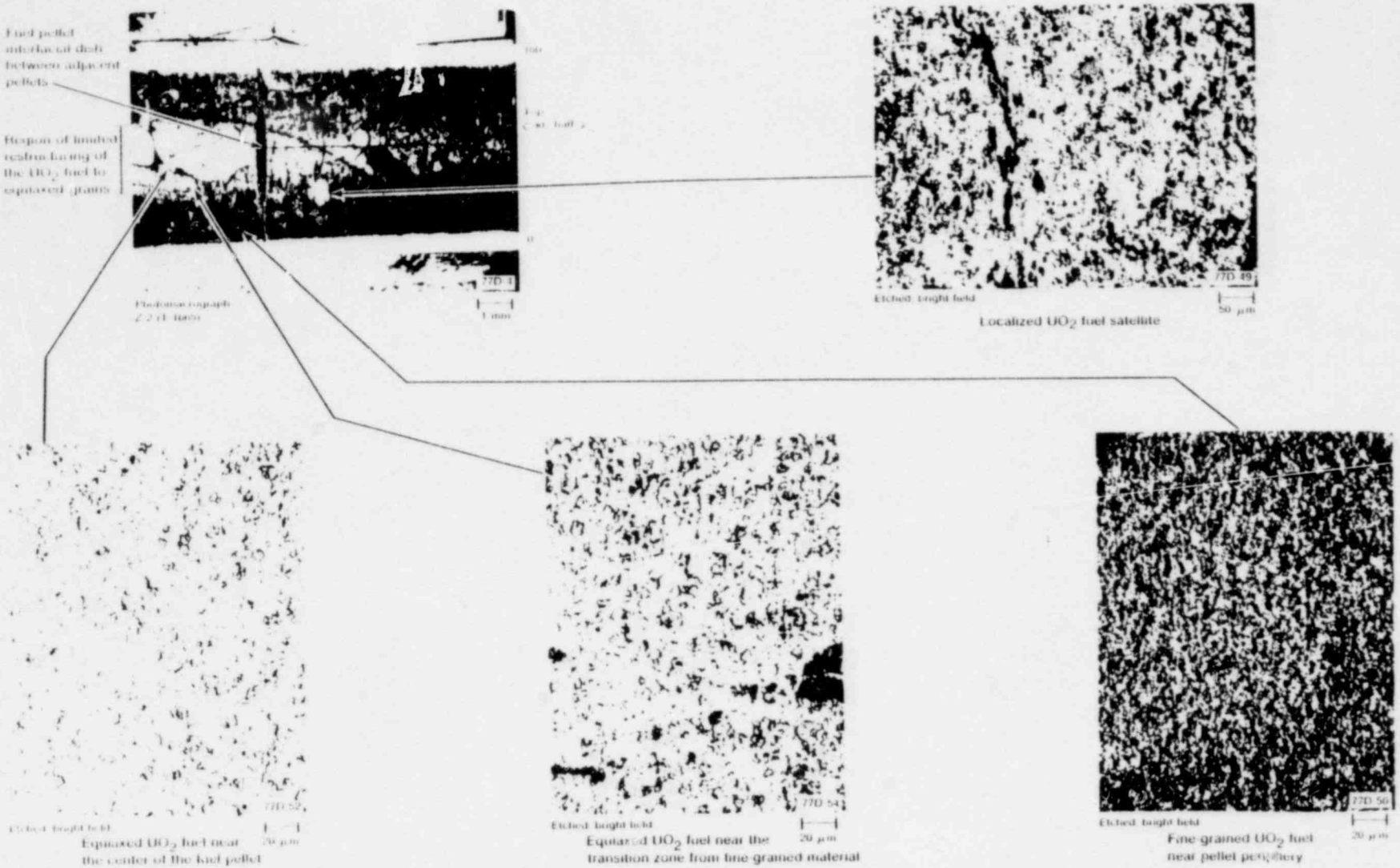

Fig. D-39 Longitudinal section (Z-2) of Rod A-0027 showing fuel restructuring

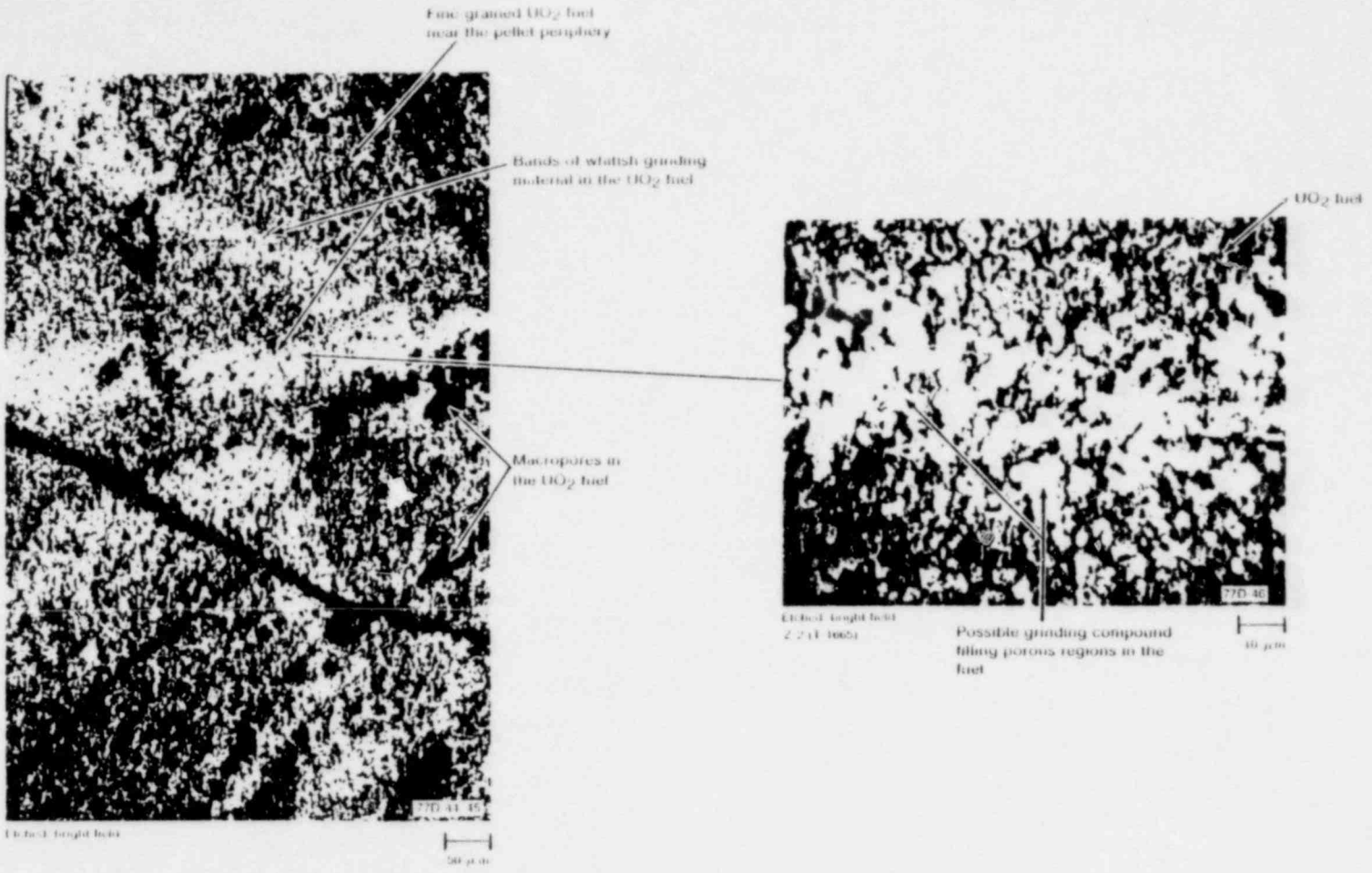

Fig. D-40 Longitudinal section (Z-2) of Rod A-001 showing grinding compound inclusions in the UO_2 fuel.

3. EXAMINATION OF SELECTED MICROSTRUCTURAL FEATURES FROM THE TEST FUEL RODS

Electron microprobe analysis and scanning electron microscopy (SEM) were used to supplement the optical metallographic examination of cladding and fuel microstructures.

Metallographic mounts were prepared for electron microprobe analysis by evaporating a carbon film onto the surface of the mount to provide a conductive path to prevent surface electric charge buildup during probe operation. Samples were transferred remotely into a shielded microprobe for examination. Line scans of U ($M\beta$), Zr ($L\alpha$), Ni ($K\alpha$), Fe ($K\alpha$), Cr ($K\alpha$), Ta ($L\alpha$), and Sn ($L\alpha$) were made at selected positions across the fuel-cladding interface in the fuel.

Scanning electron microscopy was used to analyze the hydride structures in the cladding. Room temperature vulcanizing (RTV) silicone rubber replicas were made of the etched cladding surfaces. Positive epoxy replicas were backcast from the RTV rubber molds of the hydrided surfaces and vacuum-shadowed with gold for the SEM examination.

3.1 Electron Microprobe Analysis of the Fuel-Cladding Interfacial Reaction Layers

The reaction layer at the cladding collapse protrusion into the gap between fuel pellets observed in Sample X-4 of Rod UTA-0015 was examined by electron microprobe. Several analysis scans were made across the interfacial reaction layers at various locations. The results of these scans for Zr ($L\alpha$), U ($M\beta$), Fe ($K\alpha$), and Cr ($K\alpha$) are presented in Figures D-41, -42, and -43. The scan of the reaction layer shown in Figure D-41, adjacent to the cladding and away from the collapse tip, exhibits characteristic uranium and zirconium composition with changes interpretable by the local fracturing across the region. No measurable quantity of Sn or Ni was found. Another region scanned is shown in Figure D-42. A significant quantity of Zr was recorded for the reaction material near the collapse tip. No uranium was detected in this region. Fe was found in the reaction material adjacent to the fuel. The reaction material showed an increase in U content and a decrease in Zr content with a trace of Cr in the Fe-rich region adjacent to the fuel. Scanning across the central region of the reaction deposit seen in Figure D-43 revealed a U-rich region with essentially no Zr except in the reaction layer near the fuel pellet. The reaction layer exhibited a significant quantity of Fe.

Electron microprobe analysis of similar reaction material from Rod UTA-0008 of Test PCM-2 showed a similar composition[D-2].

The presence of the Fe and Cr in the reaction material of Rod UTA-0015 is not readily explainable on the basis of the cladding zircaloy composition. Overall views of the fuel rod cladding surface in the 0 and 180° orientations showed some oxide and oxide spalling in the region of the sample. Posttest neutron radiographs of the fuel showed no anomalous features in the region of the sample. It was speculated previously[D-2] that the

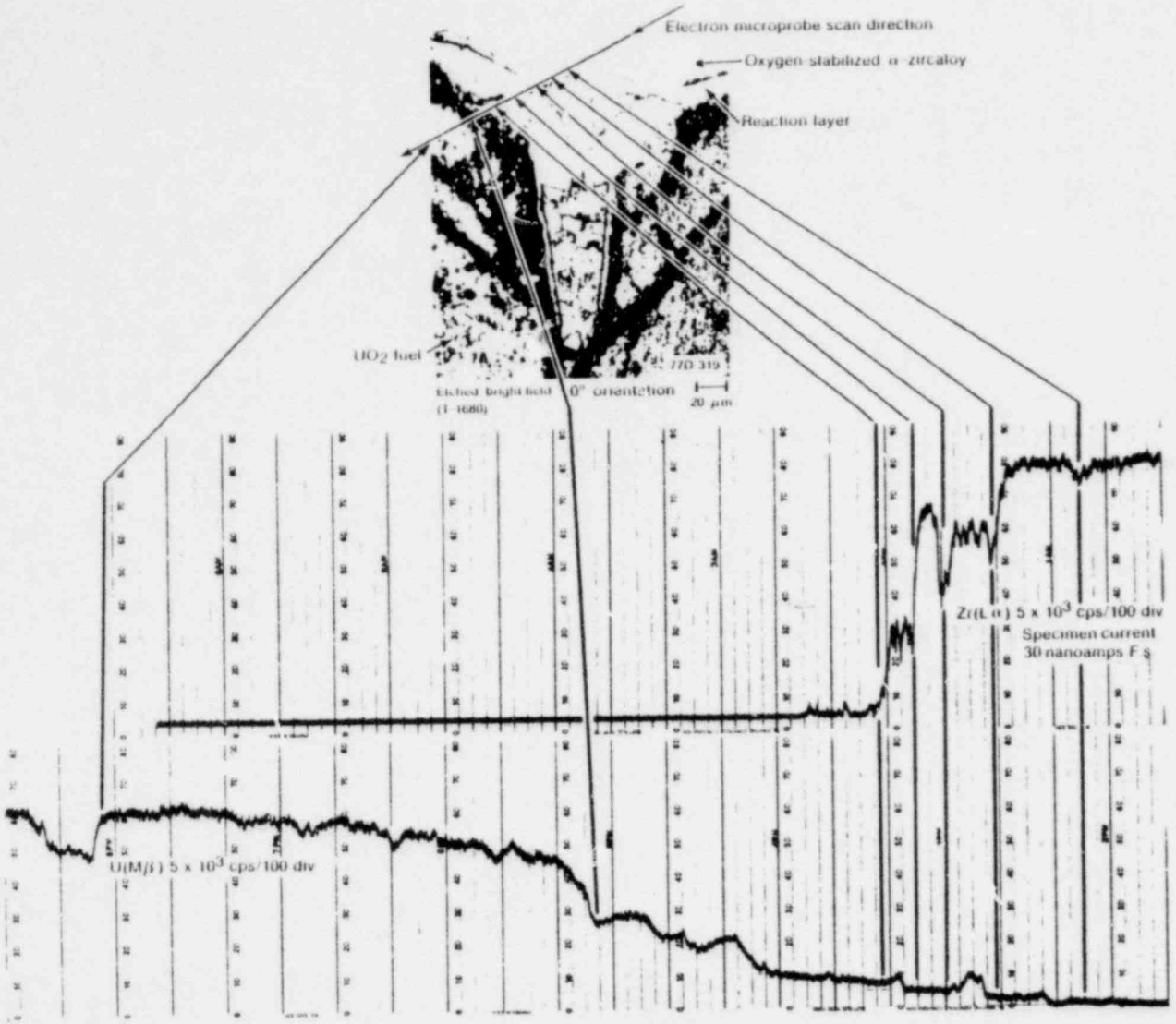

Fig. D-41 Electron microprobe scan of the fuel and cladding near a fuel pellet gap in Rod UTA-0015

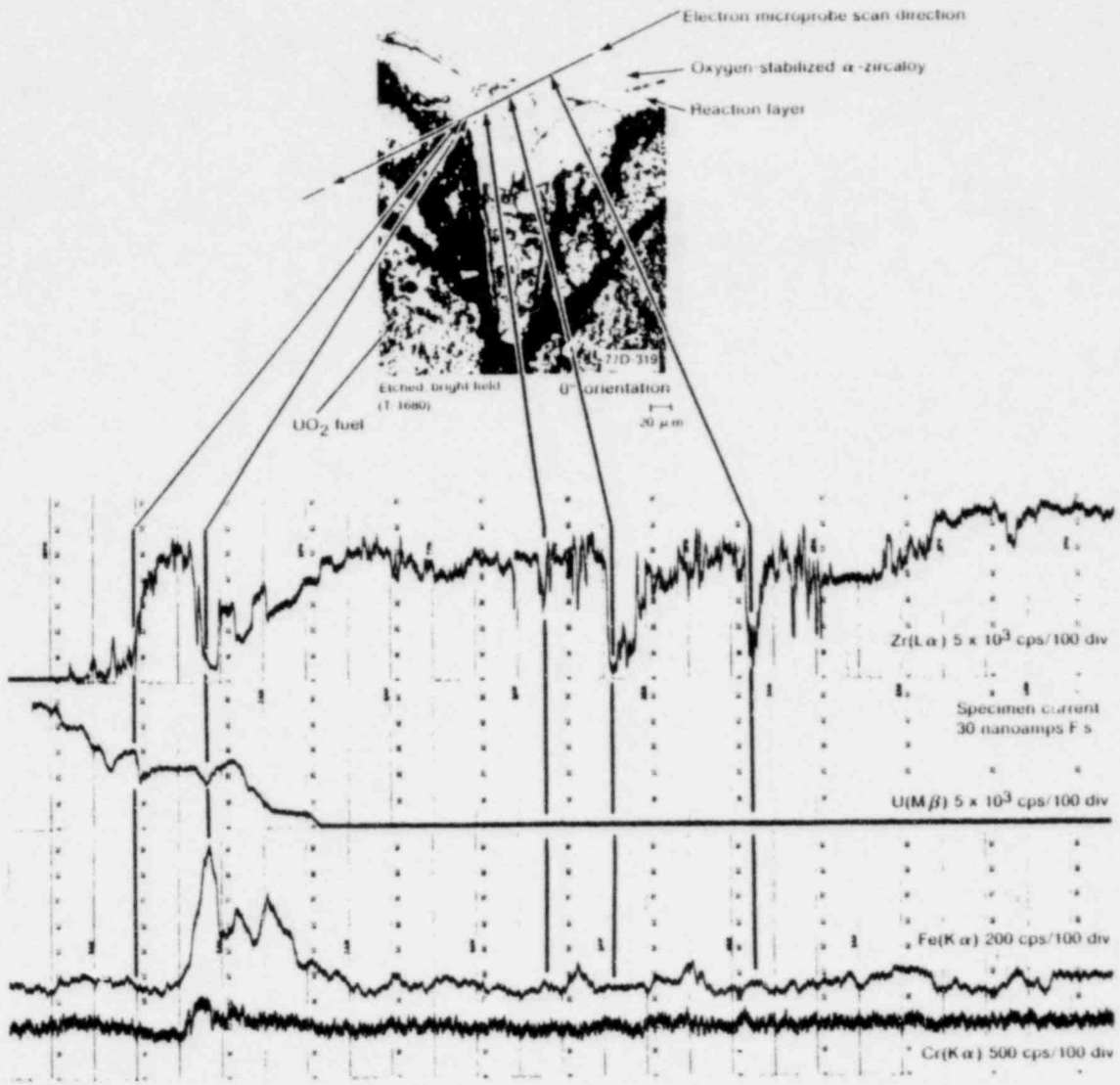

Fig. D.42 Electron microprobe scan across the collapsed cladding material at a fuel pellet interfacial gap in Rod UEA-0015.

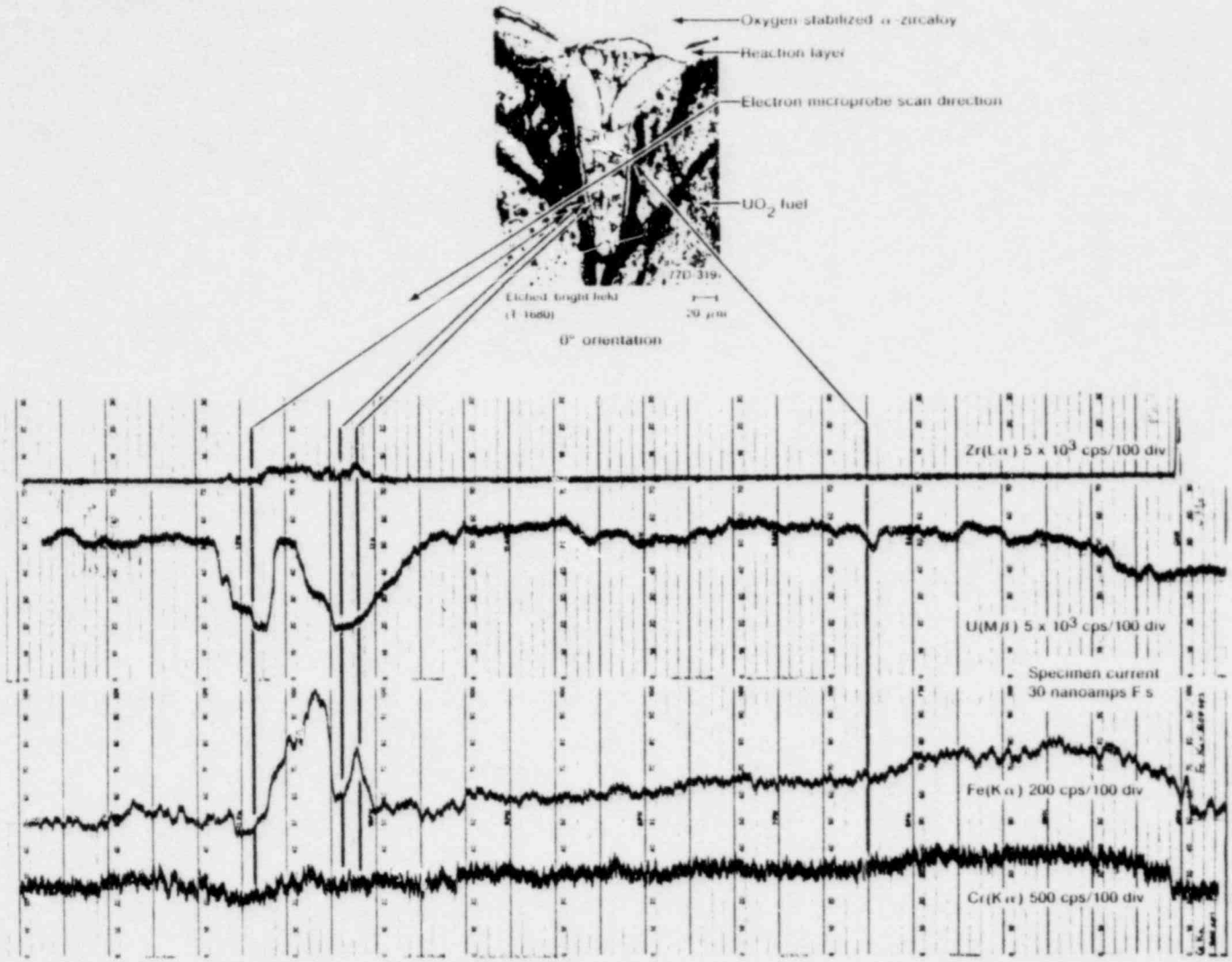

Fig. 1143 Electron microprobe scan across the reaction material associated with the cladding collapse at a fuel pellet interfacial gap in Rod UEA 0015

reaction composition was related either to the presence of an undetected metallic inclusion or to the possible penetration of a thermocouple weld. Association with weld penetration is not completely ruled out in the present case for Rod UTA-0015, but the 0.635-m, 90° thermocouple attachment was located about two fuel pellets (35 mm) above the sample location.

3.2 Thermal Reaction of Tantalum and UO_2

The fuel melting observed in Rods UTA-0014 and UTA-0016 was uncommon to the type of fuel restructuring normally encountered. The molten zone developed in the equiaxed grain region without significant grain enlargement. The melt zones of Rods UTA-0014 and UTA-0016 are illustrated in Figures D-44 through D-46.

The high temperature reaction between tantalum sheathed thermocouples and uranium dioxide has not been studied in detail. Early studies showed that a reaction was thermodynamically possible only with molten UO_2 and pure tantalum metal[D-7]. The melting point of tantalum metal is 3269 K and the melting temperature of UO_2 is near 3100 K. The thermodynamics of the stable form of tantalum oxide, Ta_2O_5, appear to exclude reaction of tantalum with uranium dioxide since uranium dioxide has a much greater free energy of formation than Ta_2O_5[D-7]. However, a high temperature reaction between tantalum and uranium dioxide has been verified metallographically, as described above, and elsewhere[D-7-D-12]. Amato et al[D-8] identified three phases metallographically: (a) a dark-grey phase of Ta_2O_5, (b) a light-grey phase of UO_2, and (c) a white phase of tantalum metal.

Several similar phases were identified in samples examined from Rods UTA-0014 and UTA-0016, containing tantalum sheathed centerline thermocouples. As illustrated in Figures D-47 through D-49, an interdendritic dark-grey phase, nonfaceted uranium dioxide primary phase dendrites (light-grey phase), interdendritic inclusions (white phase), and an interdendritic grey second phase were noted. The interdendritic inclusions (white phase) were confirmed as tantalum metal inclusions by electron microprobe analysis. Several analysis scans were made across the sheath section into the UO_2 fuel at various locations. The results of these scans for U ($M\beta$) and Ta ($L\alpha$) are presented in Figure D-50. The scans are interpretable as confirming a tantalum and UO_2 diffusion couple. The white-phase material is identified as essentially pure tantalum metal and the greyer-matrix-phase is identified as the U-rich UO_2. Intermediate phases of tantalum (or tantalum oxide) and UO_2 are not identifiable from the scans.

Several localized patterns and structures observed in the metallographic samples in Figures,D-46, D-48, and D-49 suggest simple eutectic-like morphologies. Fibrous-phase structures are shown in Figures D-47, and D-49. In eutectic alloys, fibrous phases tend to grow cooperatively, normal to the solid-liquid interface. The solid-liquid interface structure of eutectic phases is nonfaceted, with the separate phases freezing out side-by-side. A nonfaceted UO_2 dendritic primary matrix (light-grey phase) is observed metallographically

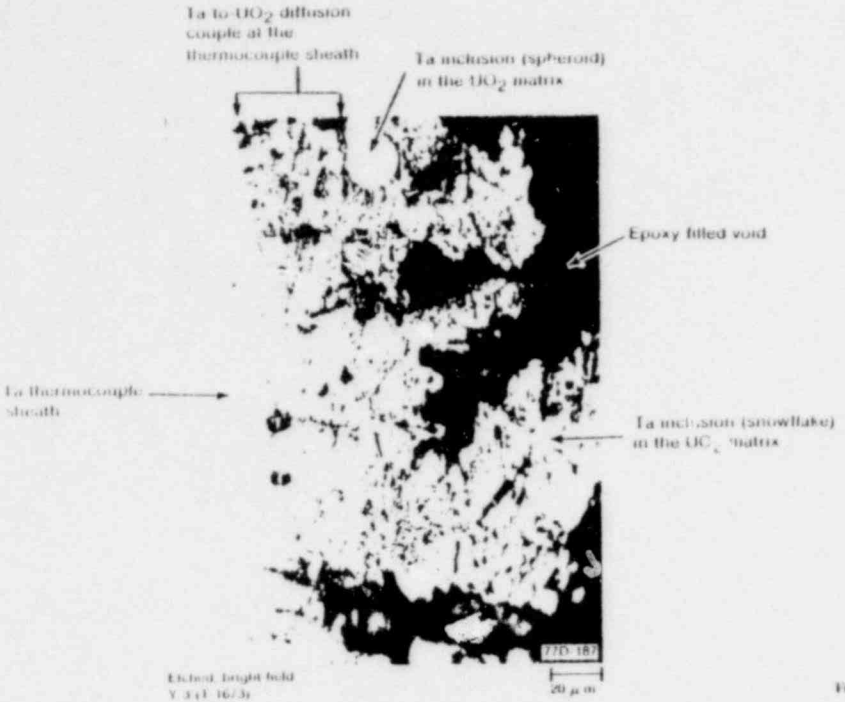

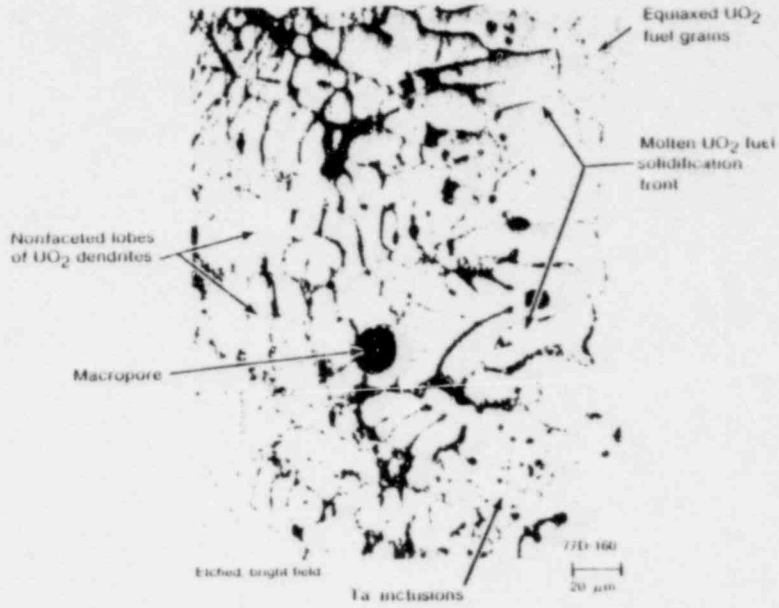

Fig. 5-44 Tantalum and UO_2 diffusion couple in Rod UTA-0014

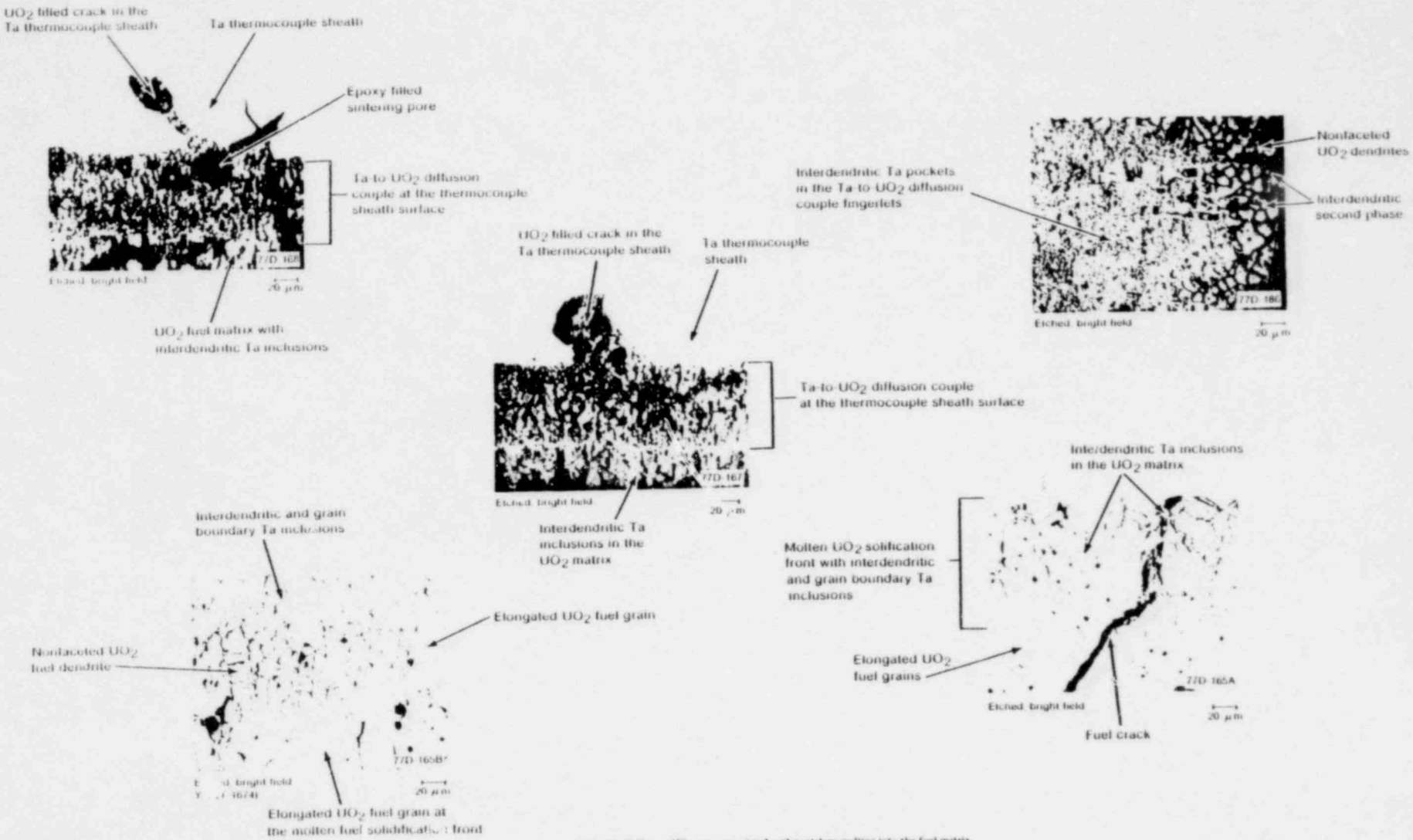

Fig. D-45 Molten UO_2 zone associated with tantalum melting into the fuel matrix.

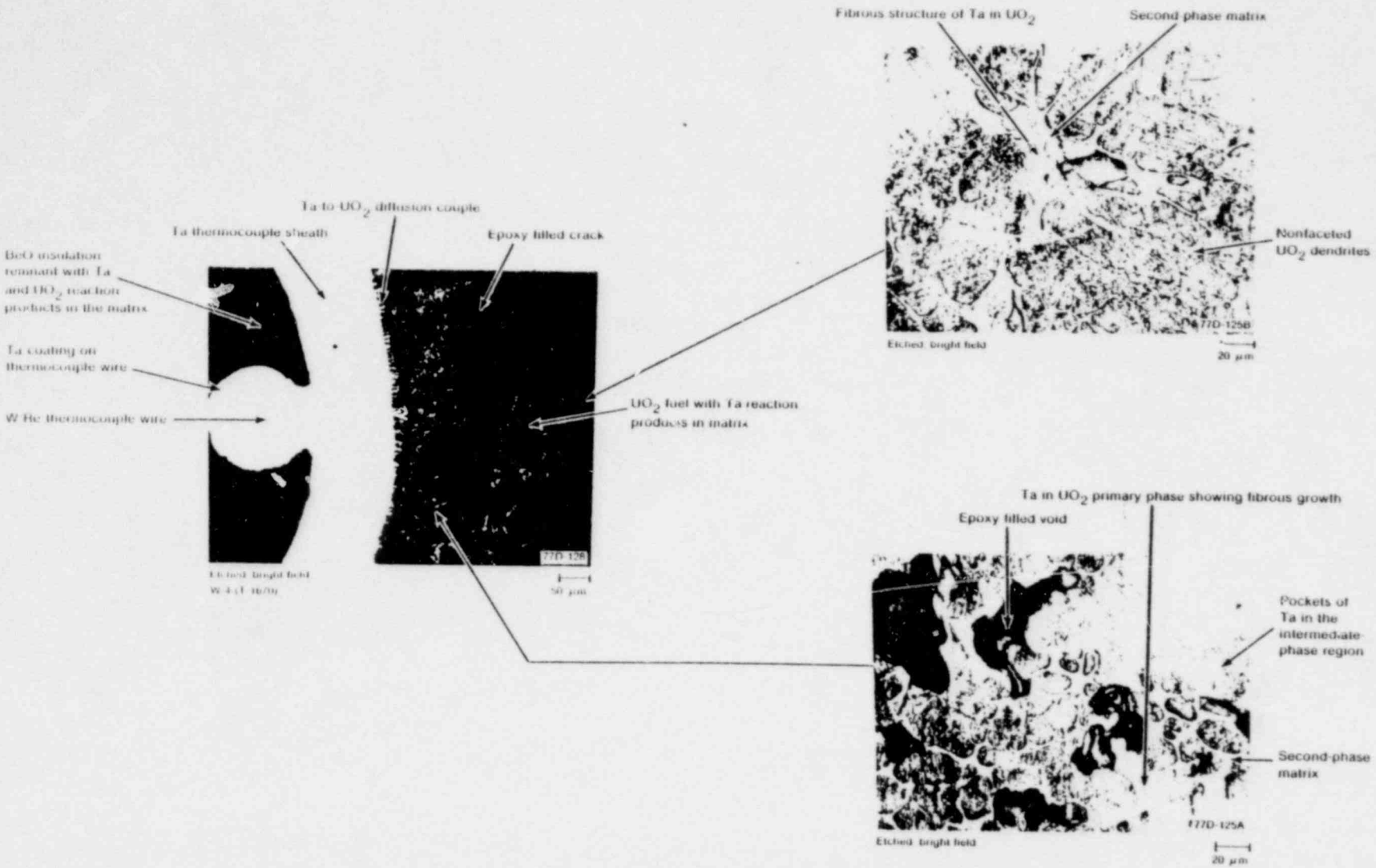

Fig. D-46. Tantalum and UO_2 diffusion couple with interdendritic tantalum inclusion and a second phase surrounding the UO_2 matrix dendrites in Run TFTA-6016.

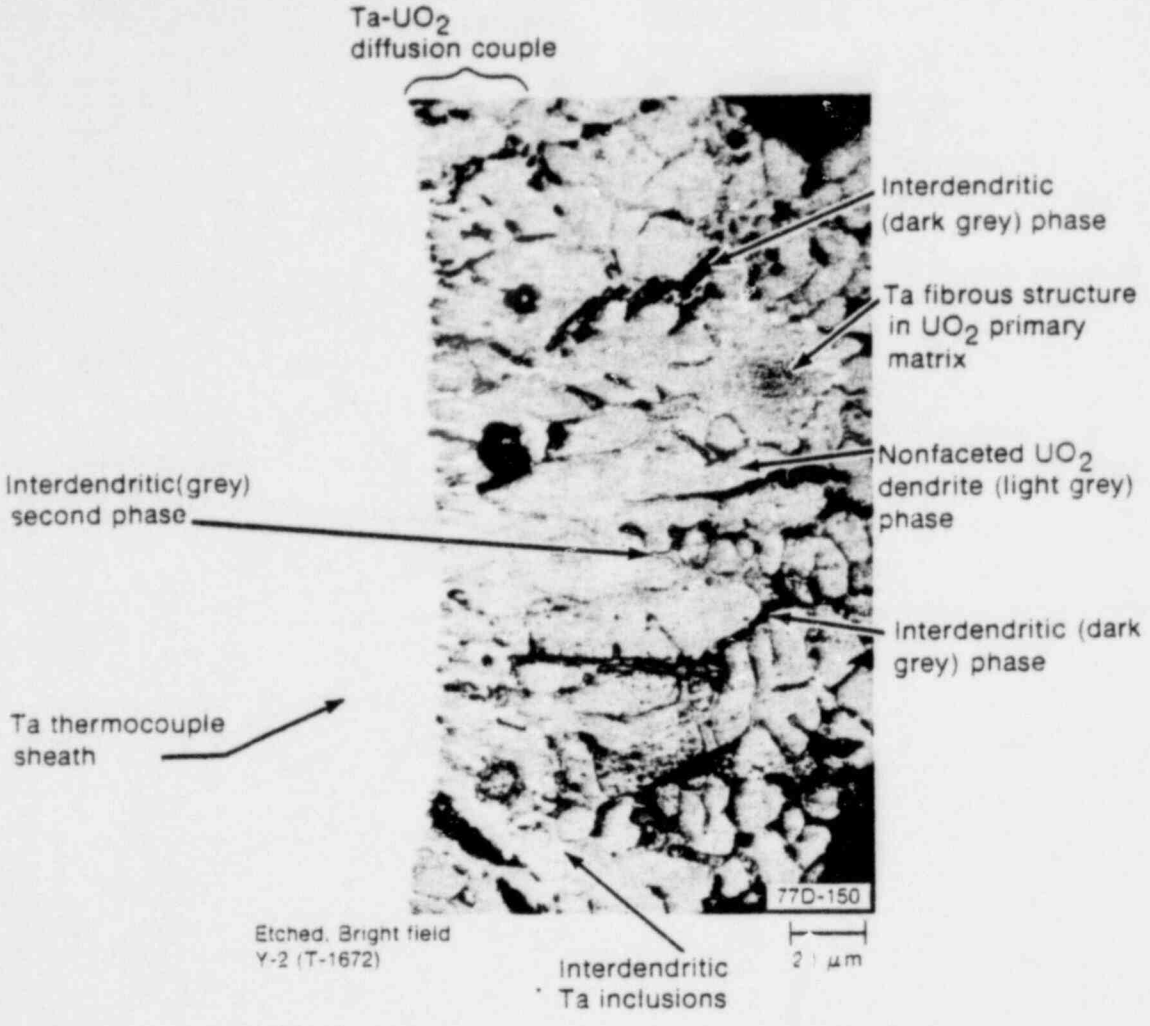

Fig. D-47 Tantalum and UO_2 diffusion couple with eutectic-like fibrous structures of tantalum in the UO_2 matrix.

in Test PCM-4 samples. The UO_2 dendrites are surrounded by a grey interdendritic second phase containing both dark-grey phase material and tantalum metal inclusions.

In eutectic alloys, the separate phases in the coupled region (stable cooperative growth zone) develop by short-range diffusion. As the primary phases nucleate, the free growth of nonfaceted dendrites becomes impaired and stops as the eutectic material surrounds the dendrites as a second phase.

Tantalum nodules, as seen in Figure D-45, provide additional evidence of eutectic-like composition in the examined metallurgical samples. The nodules have tantalum streaming from a central core similar to eutectic nodules. The interdendritic microsegregation of tantalum metal suggests incomplete miscibility similar to that noted by Sanders and Drell[D-9].

The oxidation of tantalum at temperatures above 800 K is characterized by the development of intermediate suboxide phases between Ta and Ta_2O_5[D-12-D-17]. Without

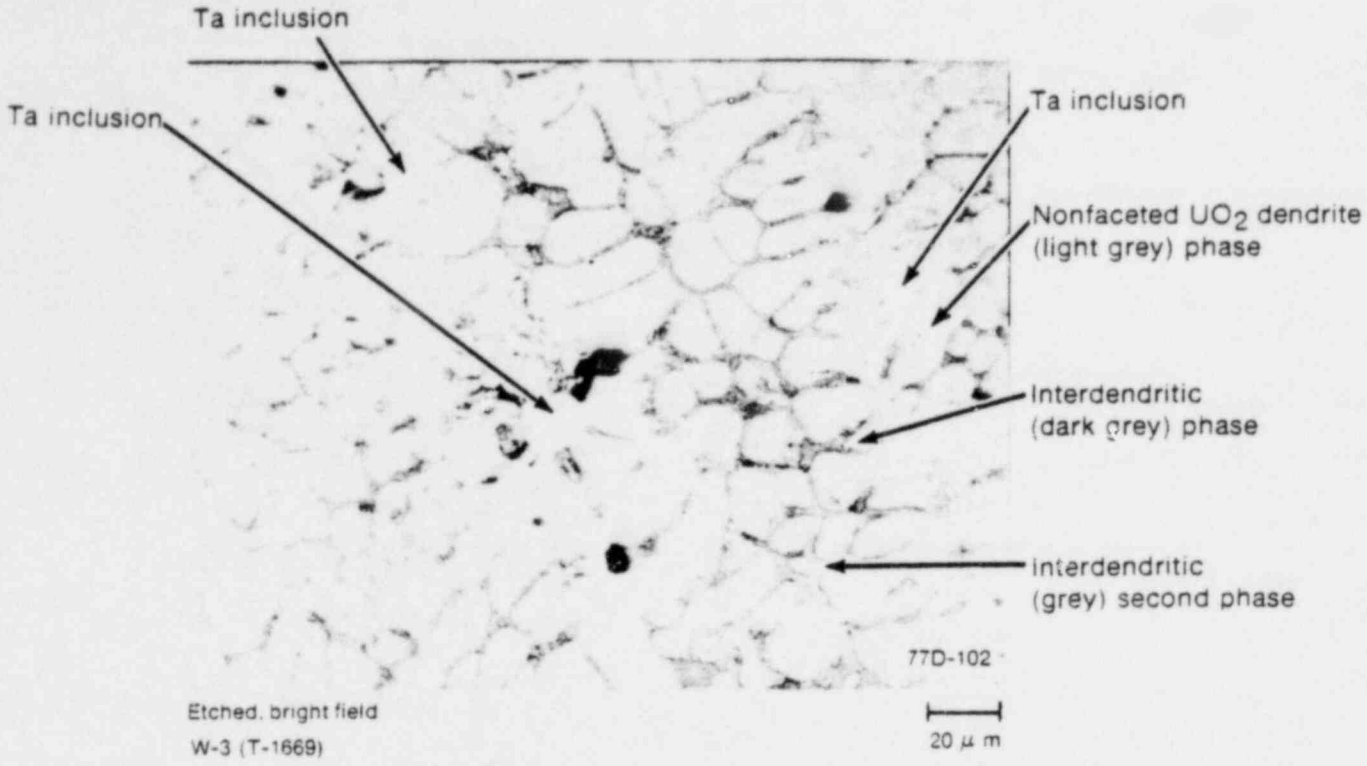

Fig. D-46 Nonfaceted UO_2 dendrites with interdendritic tantalum inclusions in the tantalum-UO_2 melt zone.

additional oxygenation, these suboxides decompose thermally above 625 K to form Ta_2O_5 and tantalum metal.

Several investigators indicate that the liquid phase formed in the high temperature reaction between tantalum metal and uranium dioxide is uranium tantalate, $U(TaO_3)^4$, which has a melting temperature of 1123 K[D-10,D-11,D-18] well within the temperature range experienced by the test rods. The oxygenation of the tantalum metal may occur with slightly hyperstoichiometric uranium dioxide where oxygen in excess of $UO_{2.00}$ in UO_{2+x} is loosely bound and can be released thermally. The released oxygen can react with the tantalum metal to form volatile intermediate tantalum suboxides which can thermally decompose into pentoxide and metal. The following tentative schedule is proposed:

$$[UO_{2+x}] + [Ta(m)] \rightarrow [\text{intermediate Ta suboxides} + Ta_2O_5] \cdot UO_{2-x}$$

$$\rightarrow [Ta(m)] \text{ white phase}$$

$$+ [Ta_2O_5] \text{ interdendritic dark-grey phase}$$

$$+ [Ta_2O_5 \cdot UO_{2-x} + U(TaO_3)_4] \text{ interdendritic grey second-phase}$$

$$+ [Ta_2O_5 + UO_2] \text{ light-grey phase (lobed dendrite)}$$

to account for the structures observed metallographically in the Test PCM-4 samples.

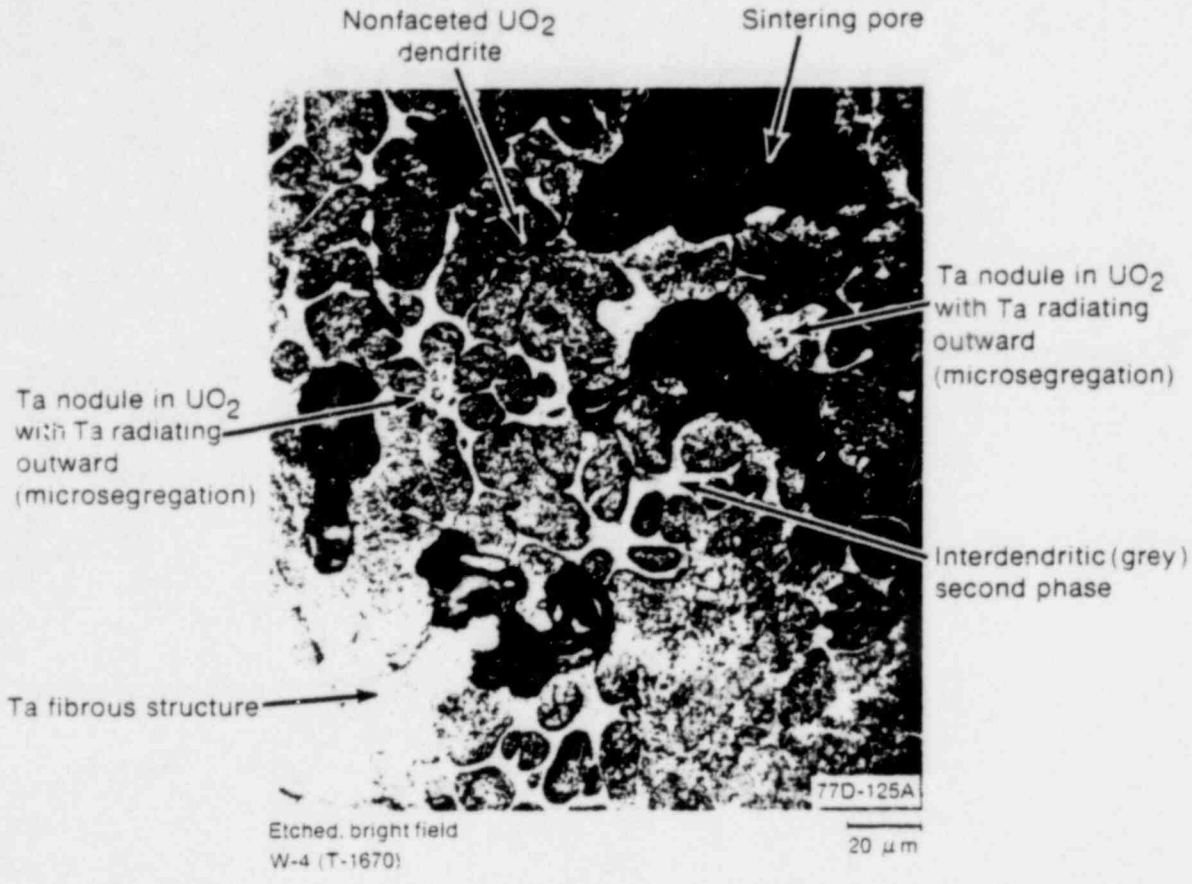

Fig. D-49 Tantalum and UO_2 molten zone with eutectic-like tantalum nodules in the UO_2 matrix.

3.3 Electron Microprobe Analysis of the Surface ZrO_2 Layer

The metal-water reaction layer of surface ZrO_2 at a cladding collapse indentation into the interfacial gap between fuel pellets of Rod UTA-0014 was examined by electron microprobe. An analysis scan was made across the surface layer of ZrO_2 into the zircaloy cladding. The results of this scan for Sn (Lα), Zr (Lα), and U (Mβ) are presented in Figure D-51. The scan indicates that both Sn and Zr occur in a layer of the oxide in approximately proportionally detectable amounts. The U activity trace was used only for a comparison. No U activity is indicated, as would be expected.

3.4 Cladding Hydriding

All four test fuel rods exhibited varying degrees of hydriding in the cladding. The hydriding is characterized in this subsection.

3.4.1 Hydride Characterization. Typical examples of the hydride structures in the cladding of various fuel rods are illustrated in Figures D-52 through D-58 for Rod

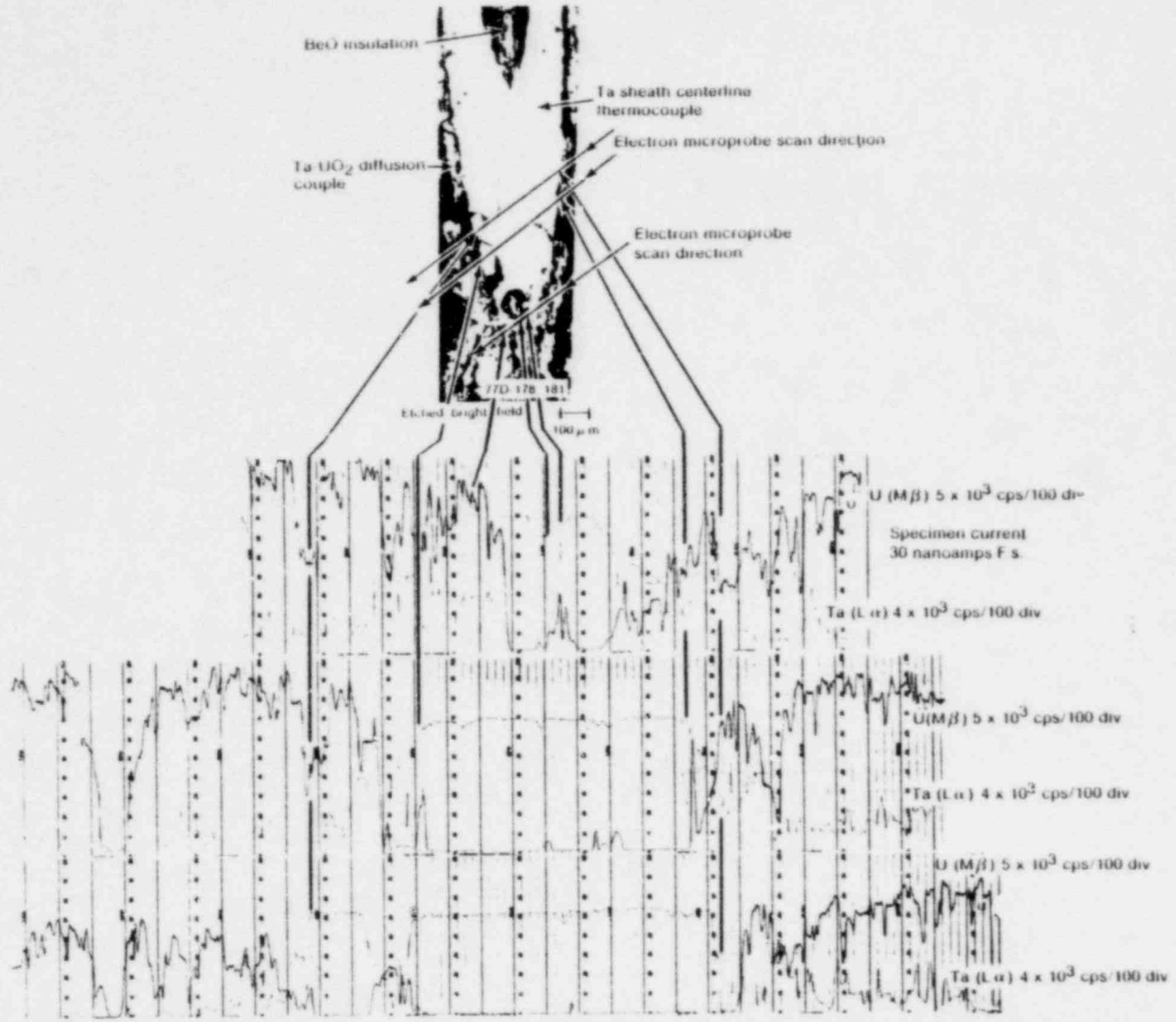

Fig. D-50 Electron microprobe scan across the tantalum thermocouple sheath and the tantalum-UO_2 diffusion couple of Run UTA 0014

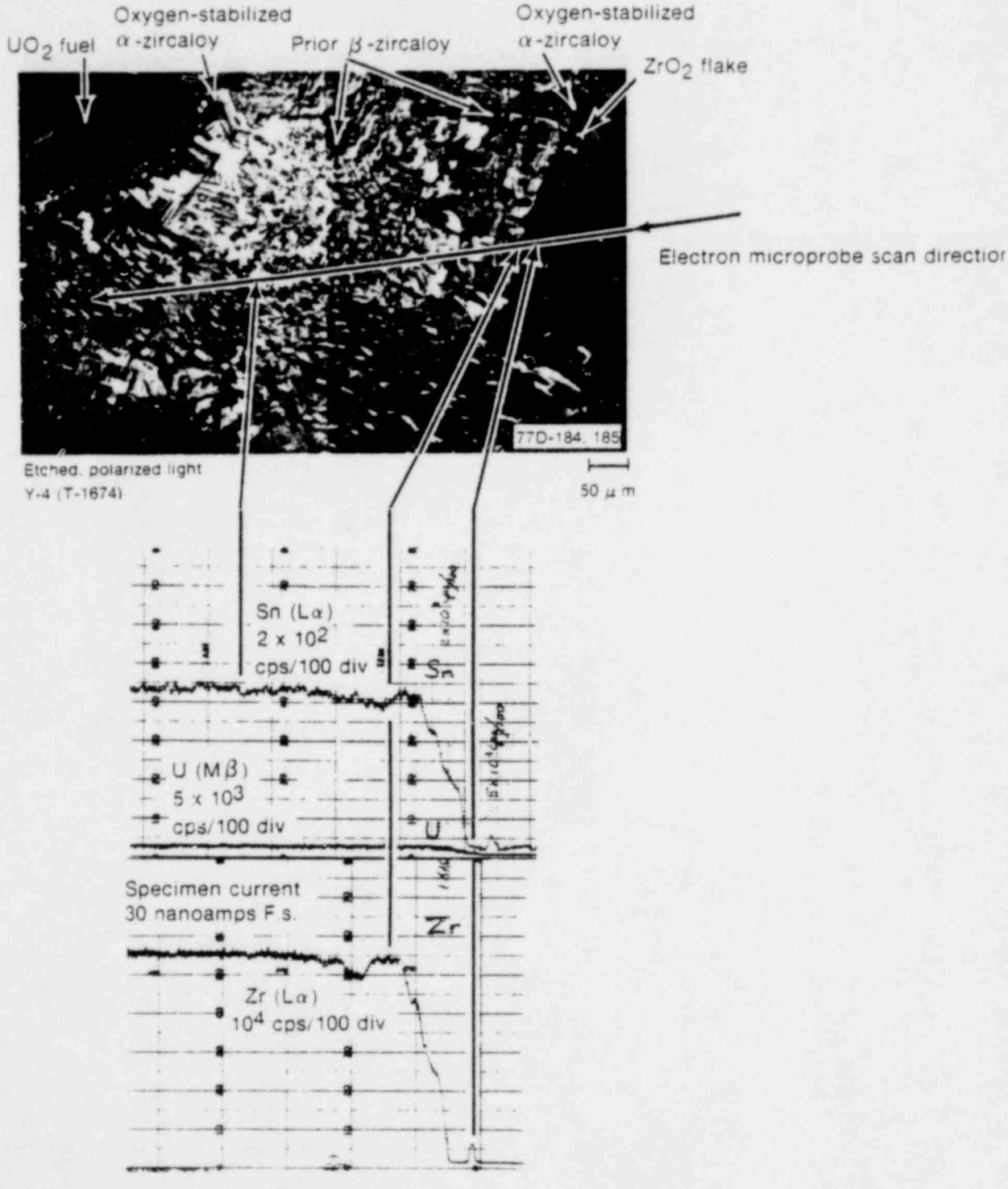

Fig. 51 Electron microprobe scan across the surface oxide and zircaloy cladding of Rod UTA-0014.

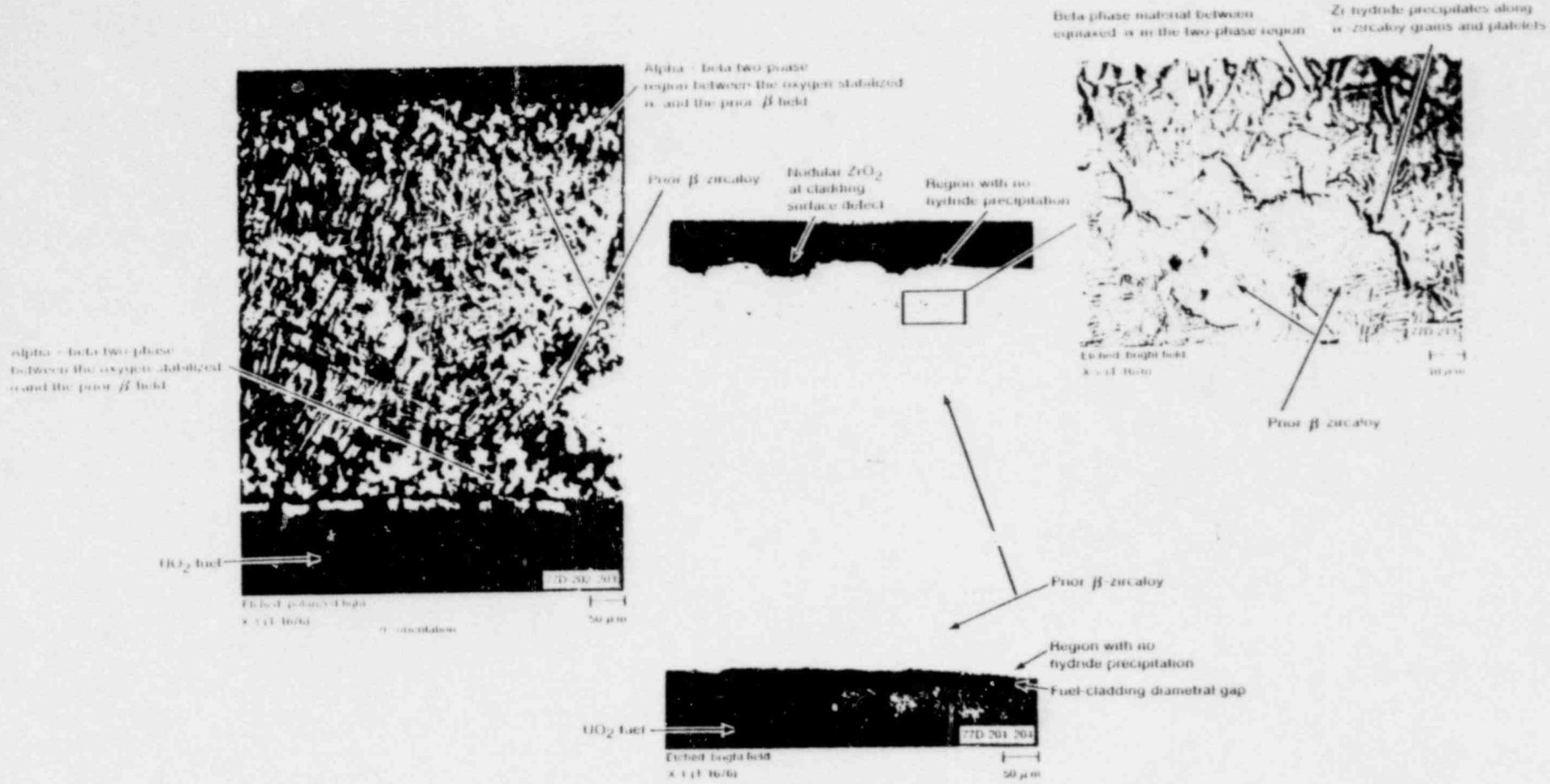

Fig D-5.2 Hydride precipitation at 0.686-m and 0° circumferential orientation in Sample X-1 of Rod UTA-0015.

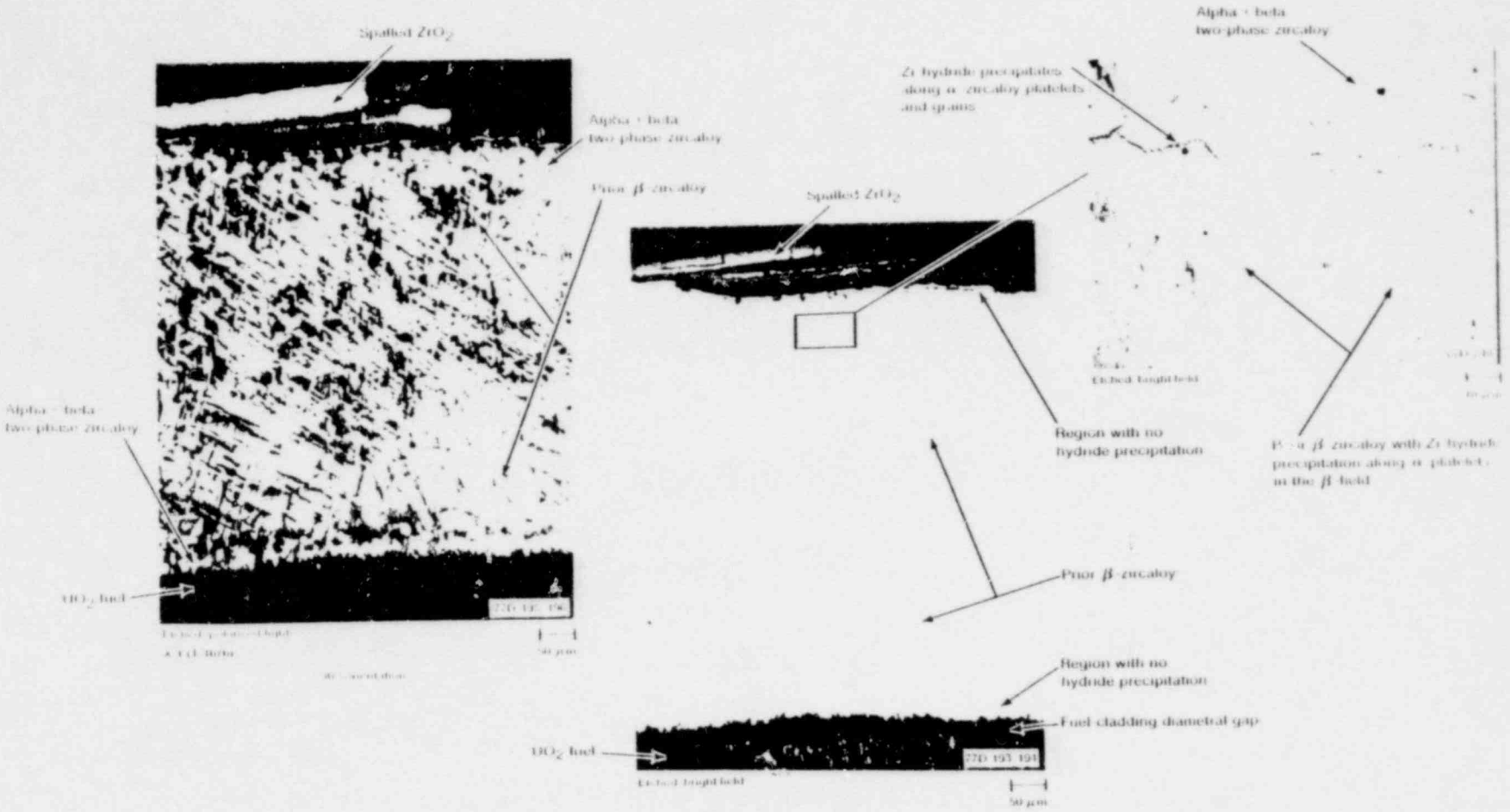

Fig. D-53 Hydride precipitation at 0.686 m and 45° circumferential orientation in Sample X-4 of Rod UTA-0015.

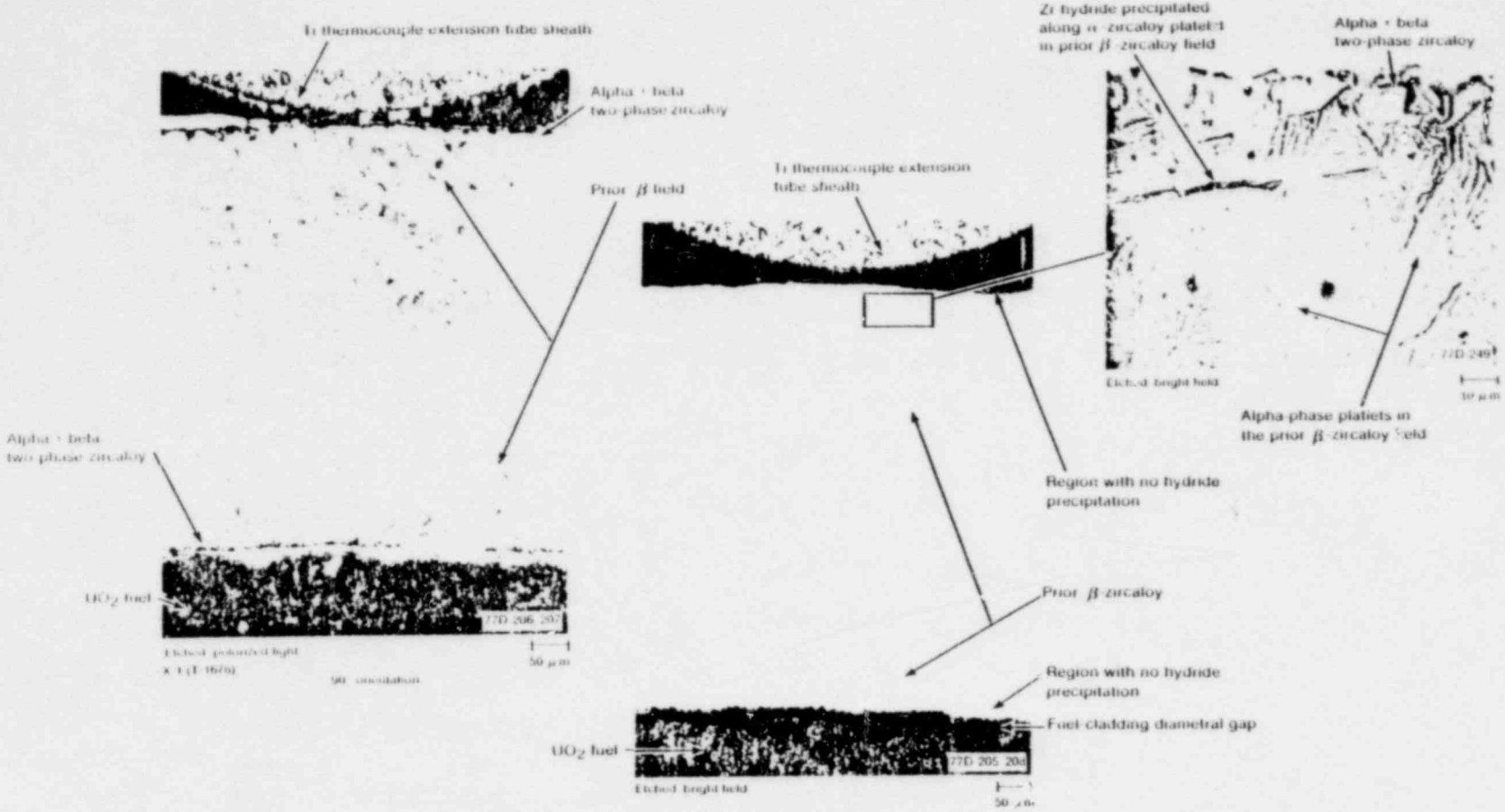

Fig. D-54 Hydride precipitation at 0.686 m and 90° circumferential orientation in Sample X-1 of Rod UTA-0015

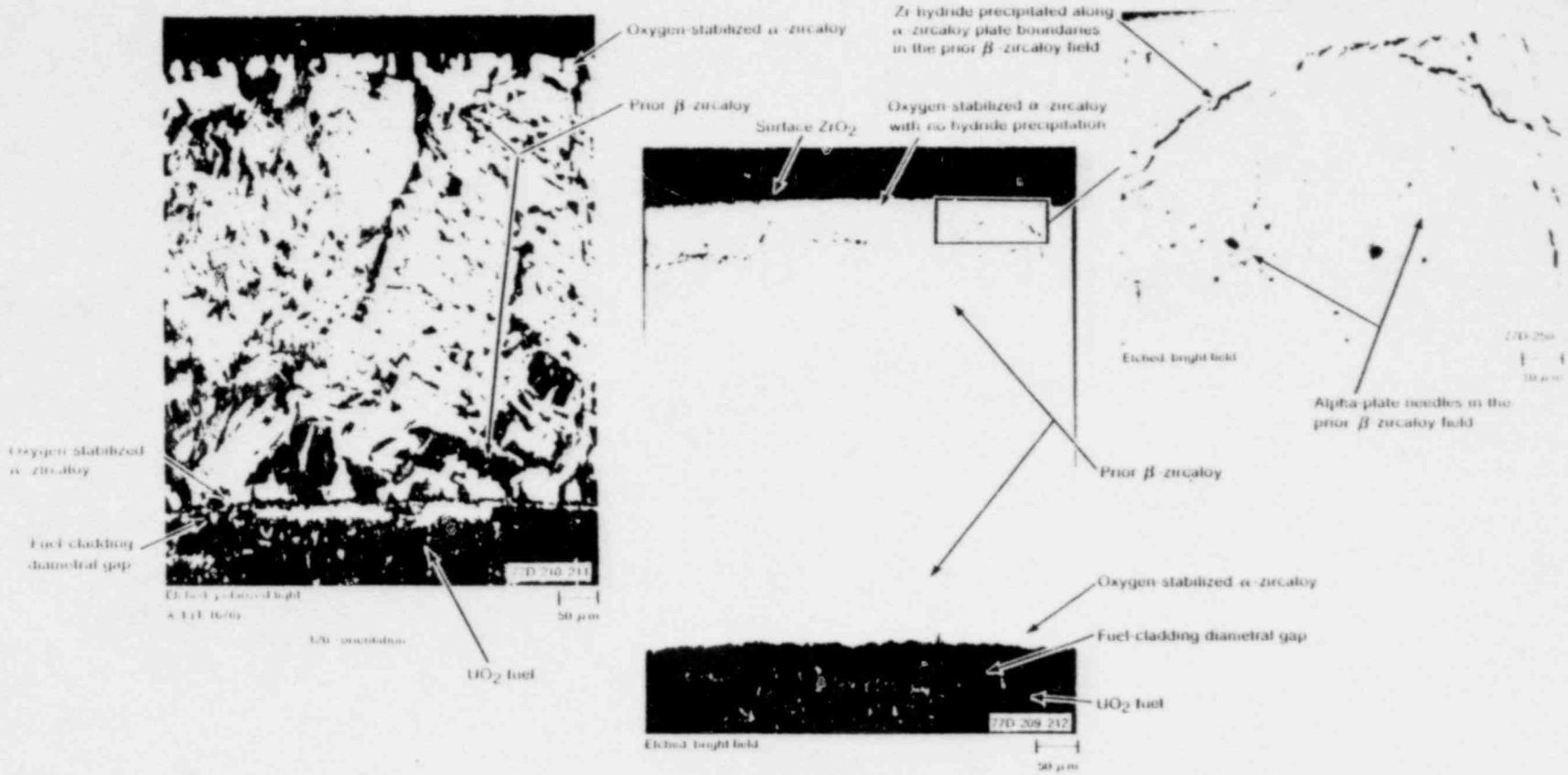

Fig. D-55 Hydrid[illegible] at 0.686 m and 120° circumferential orientation in Sample X-1 of Rod UEA-0015.

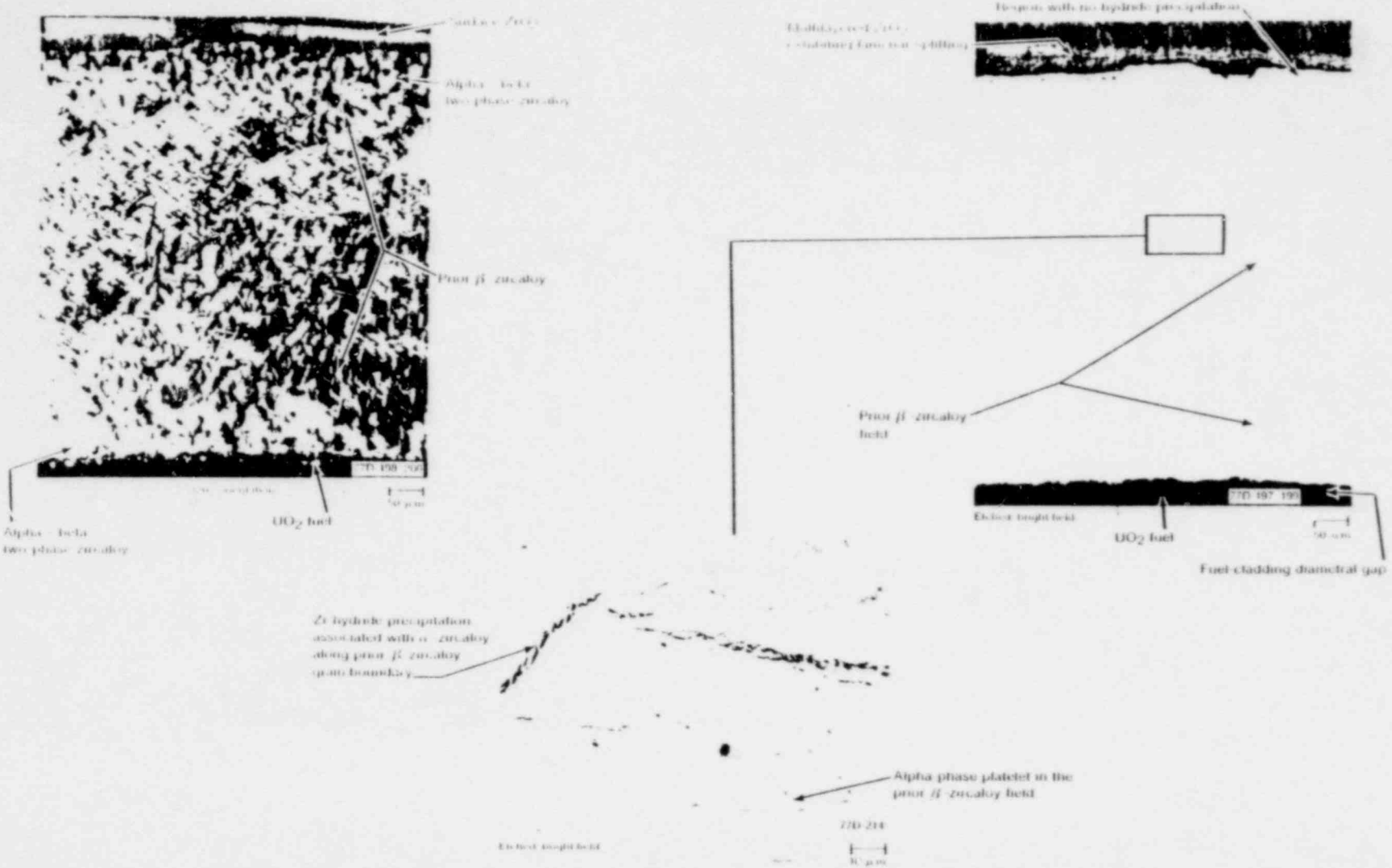

Fig. D-56 Hydride precipitation at 0.686 in and 120° circumferential orientation in Sample X-1 of Rod UTA 0015

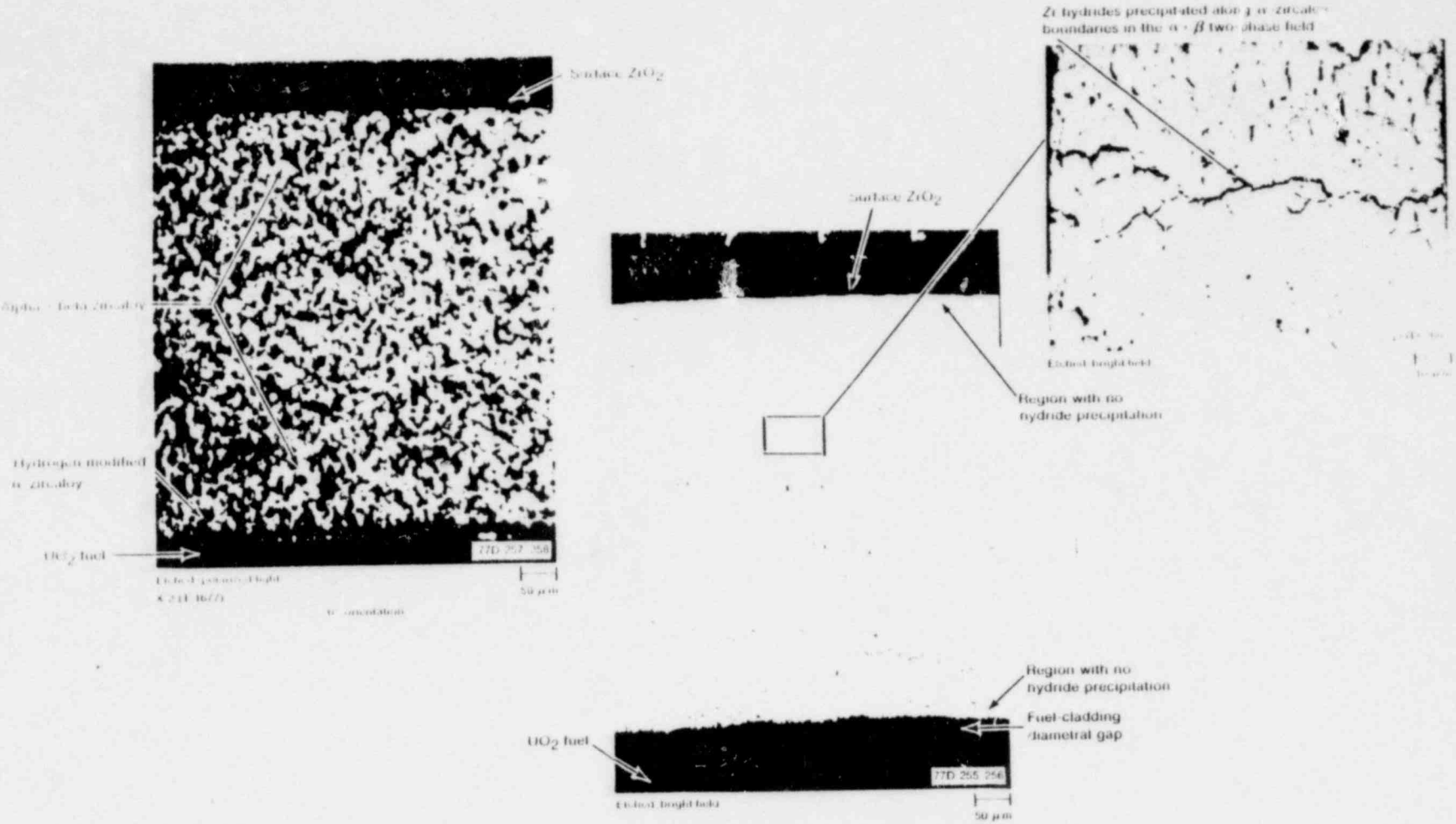

Fig. D-57 Dispersed hydriding at 0.667 m in Sample X-2 of Rod UTA-0015

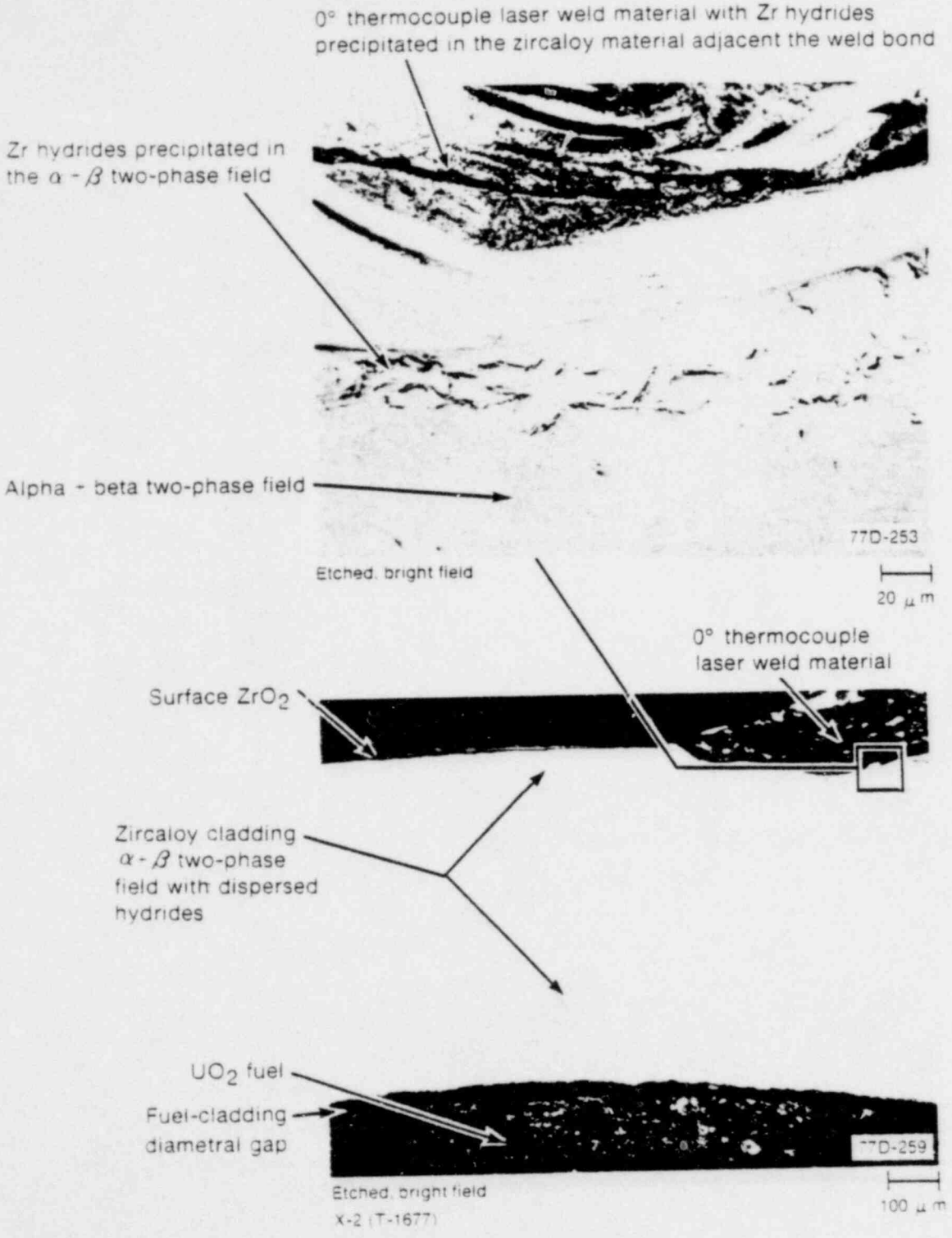

Fig. L 58 Dispersed hydriding at 0.667 m near the 0° thermocouple extension tube weld in Sample X-2 of Rod UTA-0015.

UTA-0015 and in Figures D-59 through D-61 for Rod A-0017. The cladding microstructures in these samples generally exhibit a prior beta-phase structure bounded on the outer and inner diameters by alpha + beta phase material. The hydrides tend to precipitate intergranularly in association with the alpha-phase material inside prior beta grains or along the prior beta grain boundaries, but, in general, precipitate away from the inner and outer cladding surfaces where oxygen-stabilized alpha forms.

The hydride structures from a transverse section (Sample X-1) located 0.686 m from the bottom of the fuel stack (peak cladding temperature 1410 K) are shown in Figures D-52 through D-58 for various circumferential orientations. The prior beta exhibits a basket weave structure composed of short, intersecting, alpha-phase needles within the beta grains.

Hydriding, illustrated in Figure D-57 for Sample X-2, is dispersed through the alpha + beta two-phase microstructure, in contrast with the beta-quenched hydride structures illustrated in the previous figure.

Examination of the hydriding near the thermocouple weld attachment revealed hydrides precipitated in the alpha + beta phase material adjacent to the weld bond, as shown in Figure D-58.

Samples X-1 and X-2 were tested for microhardness to determine the variation in hardness of hydrogen-modified structures in both the alpha- and beta-phase fields. The diamond-pyramid microhardness (DPH) test, using a 100-g load, provides an indication of the condition of the cladding in the various microstructural states.

In Sample X-1, microhardness measurements were made near the 180° thermocouple weld attachment. Hydrides were precipitated in the beta-quenched field adjacent to the weld bond. The hydrided beta material adjacent to the alpha + beta material near the outer cladding edge indicated a nominal hardness of 301 DPH. The prior beta field material at the center of the cladding wall had an average hardness of 210 DPH, and the alpha + beta material near the inner cladding diameter indicated an average hardness of 240 DPH.

Sample X-2 was examined at several circumferential locations near the thermocouple extension tube attachment position (0°) and at the transition zones (60 and 300° orientations) from alpha + beta two-phase region to prior beta-phase material. At the 0° thermocouple position, the nominal hardness of the hydrided alpha + beta material near the outer cladding edge was 230 DPH, whereas the material adjacent to the weld bond indicated an average hardness of 314 DPH. The two-phase field near the center of the cladding wall indicated a nominal hardness of 197 DPH and the alpha + beta two-phase band at the inner cladding edge measured 209 DPH. Across the transition zone near the 60° circumferential orientation, the nominal hardness ranged from about 201 to 211 DPH near the center of the cladding wall. The cladding on the alpha + beta two-phase field segment of the transition zone indicated an average hardness of 494 DPH, and the inner edge of the two-phase region indicated an average hardness of 334 DPH. The alpha material in the beta field of the transition zone indicated somewhat higher microhardness indexes at the outer edge

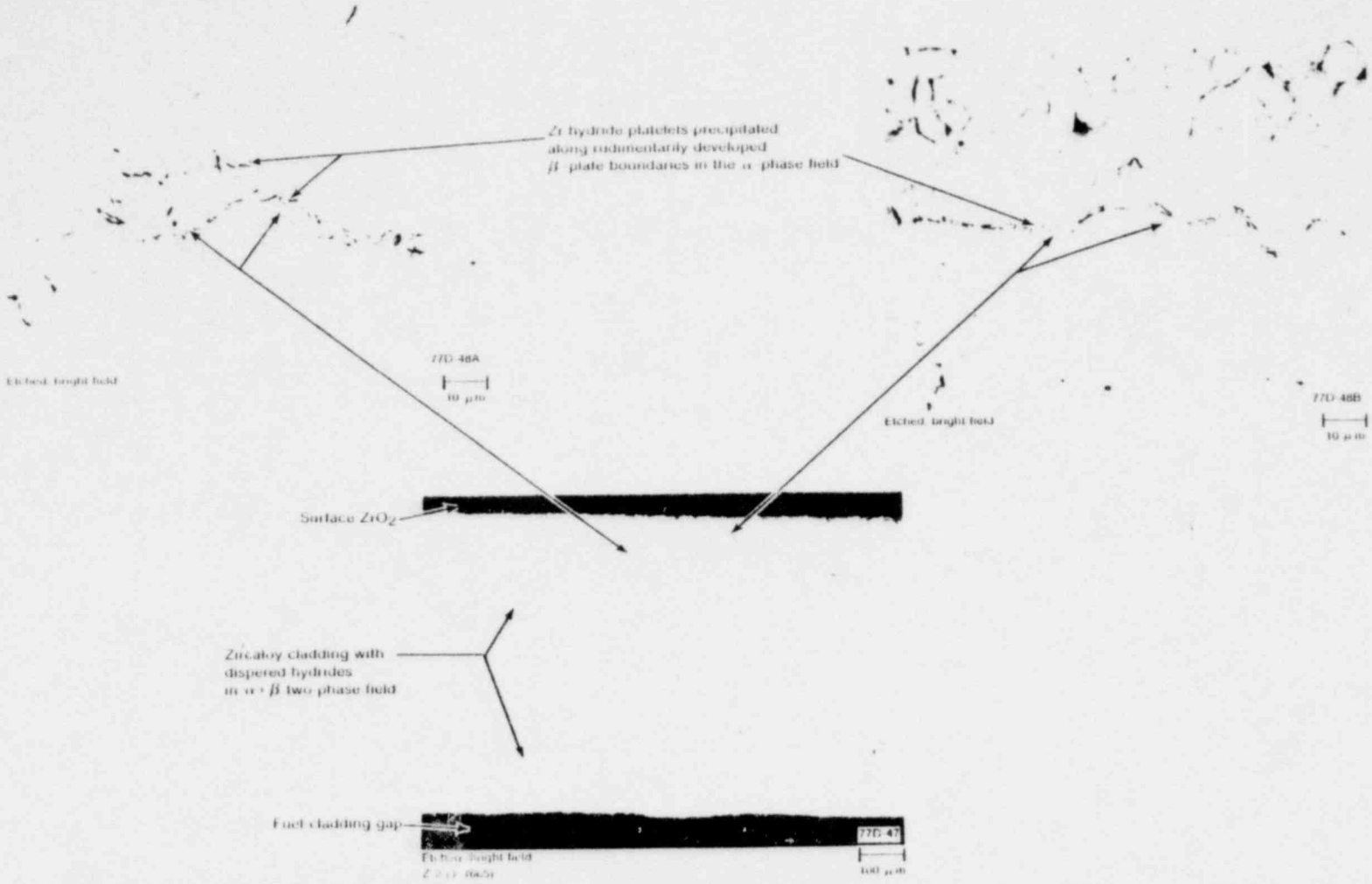

Fig. D-59 Hydride precipitation in the alpha + beta two phase field at 0.768 m in Sample Z-2 of Rod A-0017

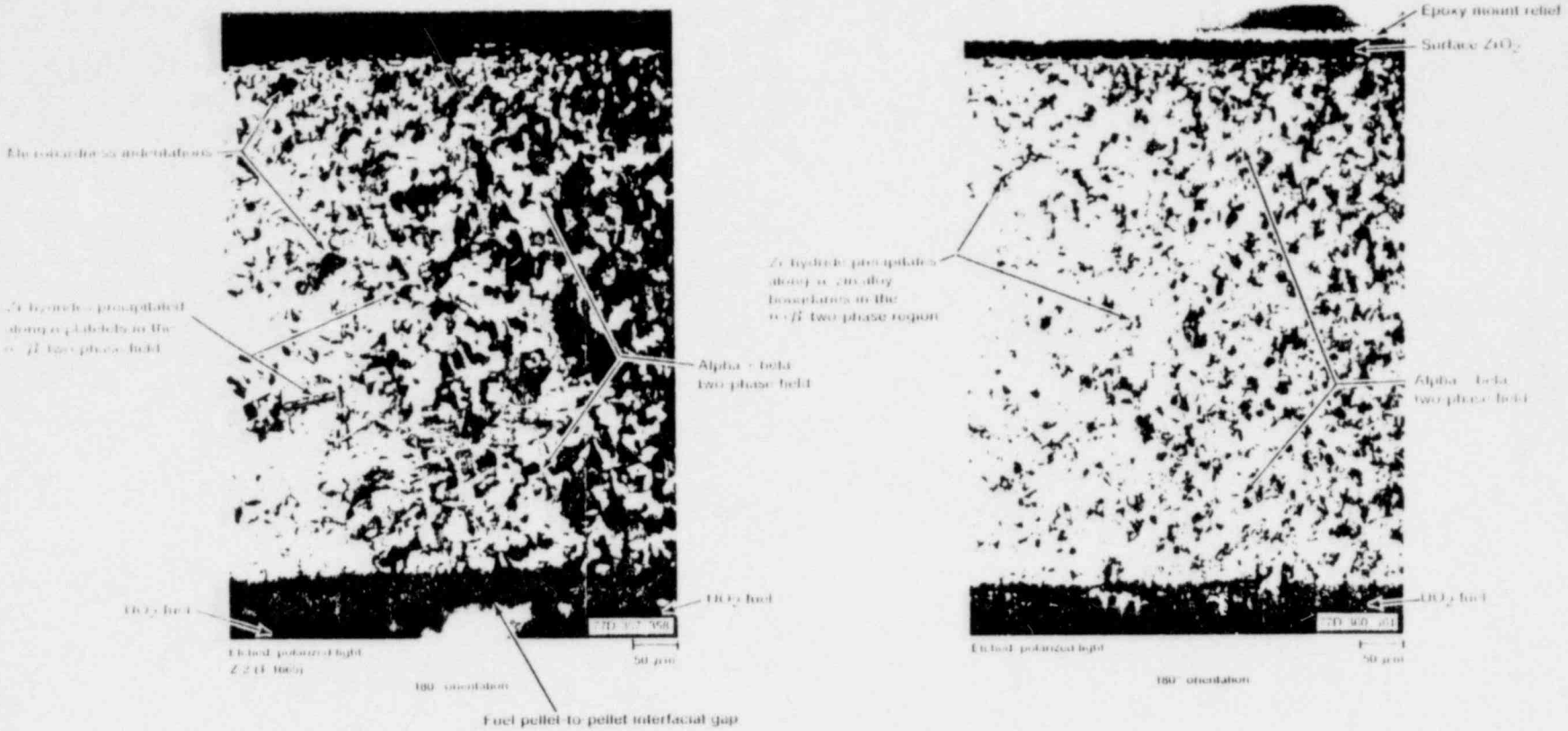

Fig. D-60 Hydriding in the alpha + beta two phase field in Sample Z-2 of Rod A-0017

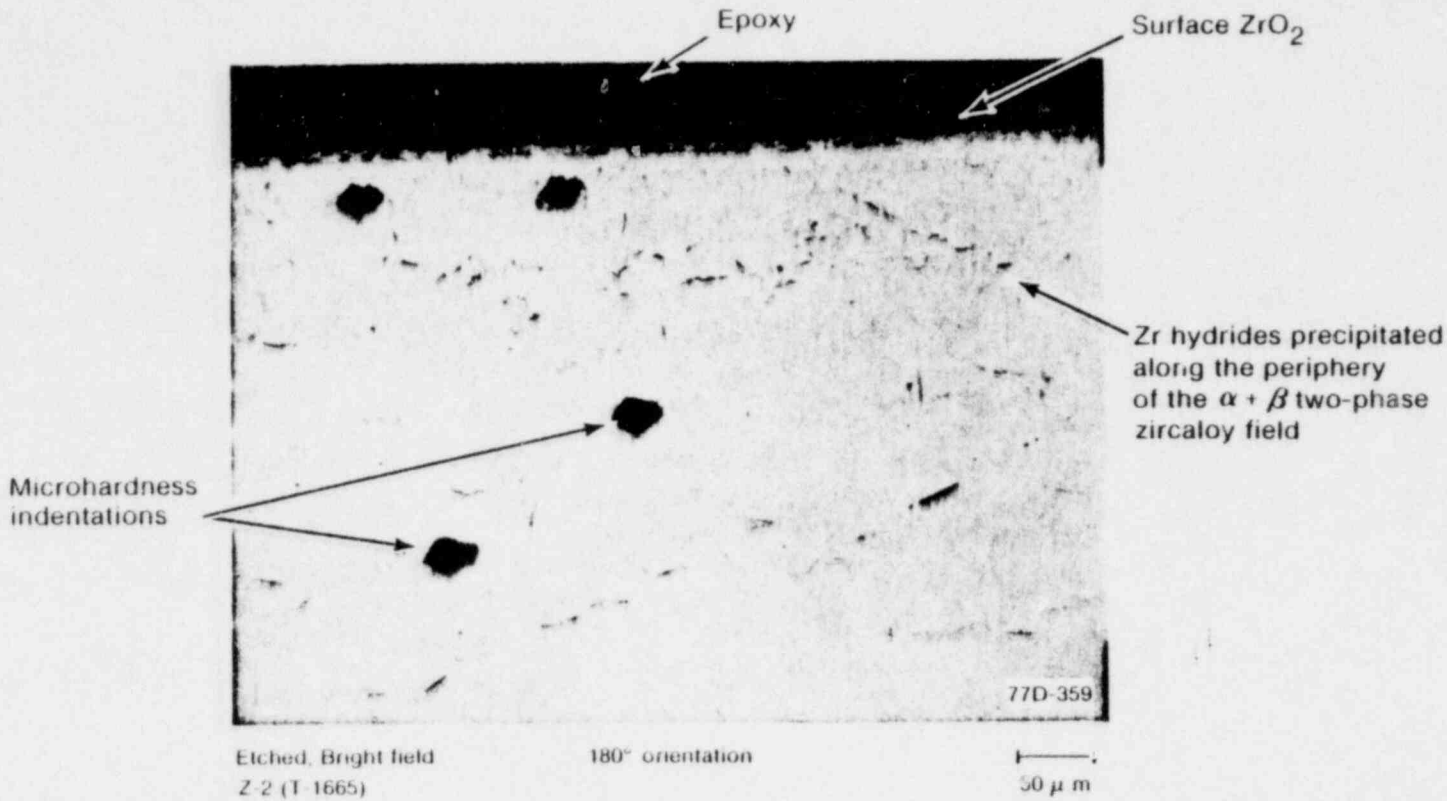

Fig. D-61 Microhardness indentations in the hydrided alpha + beta two-phase region of Rod A-0017.

(543 DPH) while the inner edge hardness values were somewhat lower (257 DPH) than those measured in the two-phase region. Similar microhardness variations were observed in the beta-phase to alpha + beta two-phase transition zone near the 300° circumferential orientation. The alpha + beta material at the outer cladding edge of the prior beta field indicated an average hardness of 625 DPH, lowering to 564 DPH across the transition region into the two-phase material. The inner edge values remained relatively close, ranging from 284 DPH to 249 DPH across the transition zone into the two-phase material.

The preceding microhardness indications are compared with typical average values for oxidized cladding of 425 and 312 DPH for alpha incursions and prior beta material, respectively, measured in previous cyclic DNB tests[D-6]. Oxygen-stabilized alpha-phase material was found to exhibit microhardness indexes in excess of 1500 to 2000 DPH. Microhardnesses reported by Hobson and Rittenhouse[D-19] ranged from 536, 455, and 300 DPH, corresponding to oxygen-stabilized alpha, alpha incursions, and prior beta, respectively, measured in oxidized zircaloy from single-cycle isothermal tests. The comparison of the microhardness values measured in the hydrogen-modified structures with microhardness values from oxidized cladding shows that the hydrogen embrittlement is not a significant influence to the structural integrity of the cladding in this test.

Hydriding in Rod A-0017 cladding material, illustrated in Figures D-59 through D-61, exhibits similar features in orientation-dispersion and extent compared with Rod UTA-0015. Sample Z-2, a longitudinal section, exhibited a transition zone from alpha + beta two-phase microstructure to a prior beta structure with bands of alpha + beta material at the outer and inner cladding edges. Microhardness measurements of these structures showed less variation across the transition zone than discussed for Rod UTA-0015. Microhardnesses measured on the 0° side of the sample ranged from 278 to 357 DPH across the transition zone along the outer diameter. The central region of the cladding wall exhibited no variation across the transition, measuring nominally 211 DPH. The inner diameter alpha + beta band material ranged from 233 to 295 DPH across the transition from two-phase to prior beta-phase field. At 180° microhardnesses at the outer diameter ranged near 300 DPH along the transition region. The central wall zone measured nominally 211 to 295 DPH across the transition from two-phase material to the prior beta-phase field.

Both in-pile and out-of-pile tests have shown that oxygen increases the terminal solubility of hydrogen in the alpha phase while it reduces the solubility of hydrogen in the beta phase[D-20-D-24]. Such results can be used to explain the modification of zircaloy microstructures observed metallographically and discussed in this section. The width of the alpha + beta regions found between the oxygen-stabilized alpha and the parent beta phase at the exterior and interior surfaces may be related to competition between the beta to alpha transformation induced by oxygen in solution and the quenching from test temperatures, as discussed by Sawatsky et al[D-25]. Hydrogen additions can produce variations in the proportions of alpha and alpha + beta phases. The microstructural variations change with test temperature and can occur at lower temperatures, depending on the hydrogen uptake during oxygenation. The DNB power-step increases, at nominally constant coolant conditions prior to quenching by test termination, may also be important to the hydrogen-oxygen pickup and subsequent changes in microstructure morphologies.

A thin zone of hydride-free alpha zircaloy is observed at both the inner and outer cladding edges, which is probably the result of greater hydrogen solubility than from the normal oxygenation of such regions by metal-water and fuel-cladding reaction. Hydrides are observed precipitated in the beta-quenched material away from the cladding surfaces where oxygen uptake reduces the hydrogen solubility. The bands of alpha + beta material with hydride precipitation at the boundary to the parent beta phase observed at the inner and outer cladding surfaces may then be interpreted as regions which develop with intermediate morphology. The hydrogen terminal solubility is increased in the presence of dissolved oxygen as the alpha-phase material nucleates and grows into the beta-phase field during quenching. Typical quench rates achieved in PCM tests are about 100 K/s.

3.4.2 Scanning Electron Microscopy (SEM). An attempt to analyze the cladding microstructures for Zr hydrides by SEM was largely unsuccessful due to the poor quality of the replicas obtained. The hydrided regions examined from metallurgical Sample X-1, from Rod UTA-0015 near 120°, revealed that the zirconium hydrides precipitated with platelet morphology. The hydrides in the prior beta field precipitated intragranularly along alpha-phase platelets. The hydride platelets illustrated in Figure D-62 are about 10 μm in length. Since no cladding hydrogen gas analysis was performed in the posttest investigation, the correlation of hydride platelet morphology with hydrogen concentration was not determined.

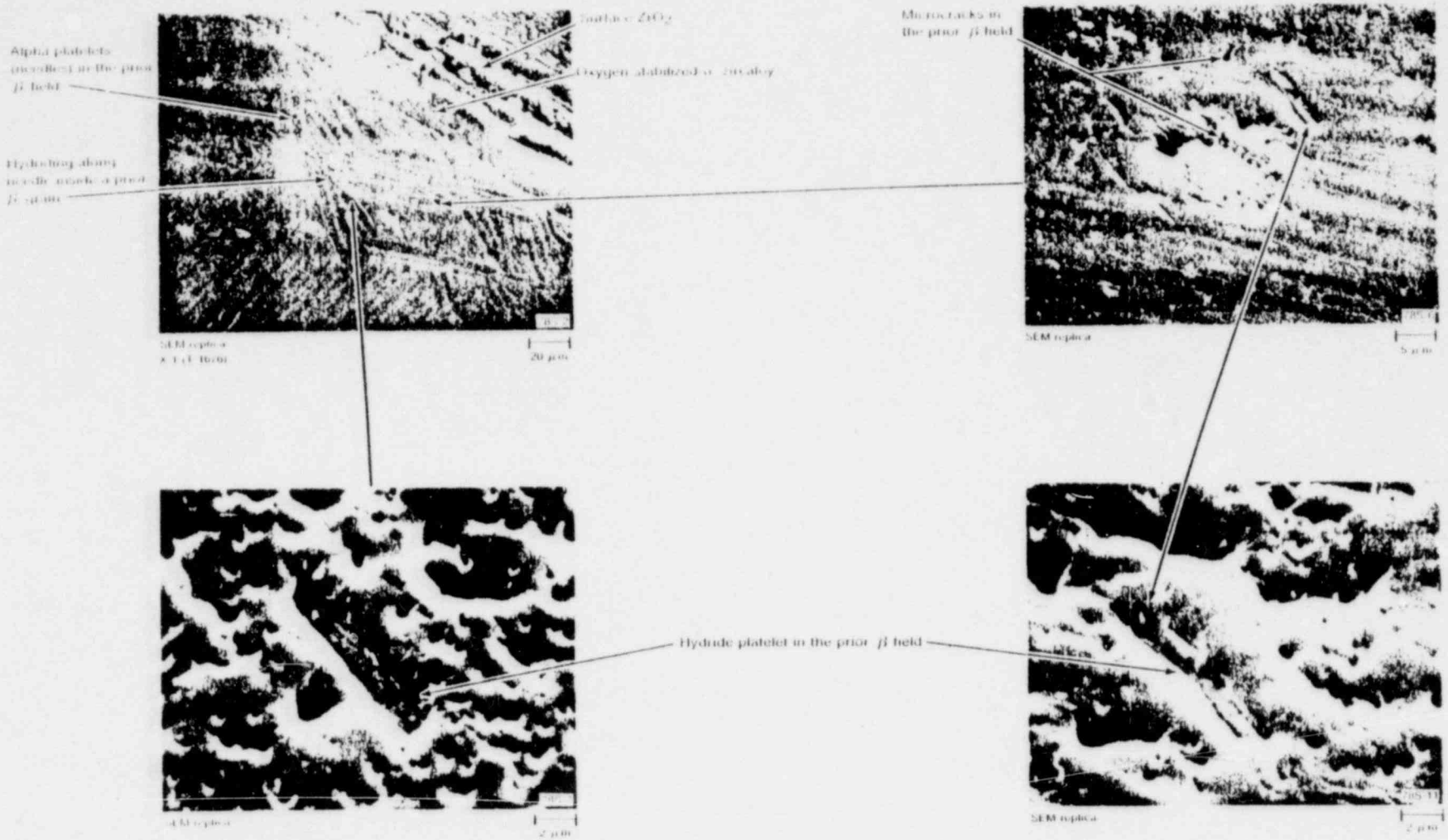

Fig. D-62 Hydride precipitation platelets in a replica of Sample X-1 of Rod UTA-0015 examined by scanning electron microscope

4. REFERENCES

D-1. S. L. Seiffert and G. R. Smolik, *Postirradiation Examination for the Power-Cooling-Mismatch Test-2A*, TREE-NUREG-1029 (February 1977).

D-2. S. L. Seiffert, *Power-Cooling-Mismatch Test Series, Test PCM-2 Postirradiation Examination*, TREE-NUREG-1069 (December 1977).

D-3. S. L. Seiffert, *Power-Cooling-Mismatch Test Series, Test PCM-3 Postirradiation Examination*, TREE-NUREG-1187 (December 1977).

D-4. A. Brown and D. Hardie, "The Effect of Dissolved Oxygen on the Terminal Solubility of Hydrogen in Alpha Zirconium," *Journal of Nuclear Materials, 4* (1961) pp 110-112.

D-5. J. J. Kearns, J. E. McCarley, F. A. Nichols, "Effects of Alpha/Beta Phase Constitution on Superplasticity and Strength of Zircaloy-4," *Journal of Nuclear Materials, 61* (1976) pp 169-184.

D-6. D. R. Olander, *Fundamental Aspects of Reactor Fuel Elements*, TID-26711-PI (April 1976).

D-7. J. J. Byerley, *The Compatibility of UO_2 with the Refractory Metals and Refractory Metal Thermocouples at Temperatures Above 1750°C*, CRFD-971 (October 1960).

D-8. I. Amato, R. L. Colombo, A. M. Petuccioli Balzari, "On the Reaction Between Tantalum Metal and Uranium Dioxide," *Journal of Nuclear Materials, 19* (1966) pp 190-192.

D-9. W. A. Sanders and I. L. Dell, *Compatibility of Molten Uranium Dioxide with Five Refractory Materials*, NASA-Technical Note D-1442 (January 1963).

D-10. D. Vollath, *Vertraglichkeit Hochschmelzender Metalle mit Urandioxide*, KFK-762, EUR-3952 d (April 1968).

D-11. O. Gotzmann and F. Thümmler, *Vergleich der Vetraglichkeit der Kernbremstoffe UN, UC, and UO_2 mit Metallen*, KFK-435 (June 1966).

D-12. P. Kofstad, "Oxidation of Tantalum in the Temperature Range 500-700°C," *Journal of the Institute of Metals, 90* (1961-62) pp 253-264.

D-13. J. N. Ong, Jr. and W. M. Fassell, Jr., "Kinetics of Oxidation of Columbian and Other Refractory Metals," *Corrosion, 18* (1962) pp 382t-389t.

D-14. M. G. Cowgill and J. Stringer, "Effect of Oxygen Pressure on the High Temperature Oxidation of Tantalum," *Journal of Less Common Metals, 3* (1960) p 233.

D-15. L. M. Adelsberg, G. R. St. Pierre, R. Speiser, "Kinetics of the Oxidation of Tantalum by Water Vapor," *Transactions of the Metallurgical Society of AIME, 239* (1967) pp 490-496.

D-16. W. J. Albecht et al, "Reaction of Pure Tantalum with Air, Nitrogen, and Oxygen," *Transactions of the Metallurgical Society of AIME, 221* (1961) pp 110-117.

D-17. S. G. Trevyatskiy and V. I. Kushakovskiy, "Melting Points of U-Binary Oxides," *Russian Nucleonics, 18* (1960) p 101.

D-18. E. Rothwell, "High Temperature Substoichiometry in Uranium Dioxide," *Journal of Nuclear Materials, 6* (1962) pp 229-236.

D-19. D. O. Hobson and P. L. Rittenhouse, *Embrittlement of Zircaloy-Clad Fuel Rods by Steam During LOCA Transients*, ORNL-4758 (January 1972).

D-20. C. E. Ells and A. D. McQuillan, "A Study of the Hydrogen-Pressure Relationships in the Zirconium-Hydrogen System," *Journal of the Institute of Metals, 85* (1956-57) pp 89-96.

D-21. W. J. Babyak, W. F. Bourgeois, G. J. Salvaggio, "Effect of Hydride Morphology on the Tensile Properties of Zircaloy-2," *Proceedings of the American Nuclear Society Symposium on Corrosion of Zirconium Alloys, New York, November 1963*, American Society for Testing and Materials Special Technical Publication No. 368 (1964) pp 76-100.

D-22. H. H. Klepfer and D. L. Douglass, "Factors Limiting the Use of Zirconium Alloys in Superheated Steam," *Corrosion of Zirconium Alloys*, American Society for Testing and Materials Special Technical Publication No. 368 (1964) pp 118-142.

D-23. E. Hillner, "Corrosion and Hydriding Performance of Zircaloy Tubing After Extended Exposure in the Shippingport Pressurized Water Reactor," *Proceedings of the Symposium on Zirconium in Nuclear Applications, Portland, Oregon, August 1973*, American Society for Testing and Materials Special Technical Publication No. 551 (1974) pp 449-462.

D-24. J. Kearns, J. E. McCauley, F. A. Nichols, "Effect of Alpha/Beta Phase Constitution on Superplasticity and Strength of Zircaloy-4," *Journal of Nuclear Materials, 61* (1976) pp 169-184.

D-25. A. Sawatsky, G. A. Ledoux, and S. Jones, "Oxidation of Zirconium During a High Temperature Transient," *Proceedings of the Third International Conference on Zirconium in the Nuclear Industry, Quebec City, Canada, August 1976,* American Society for Testing and Materials Special Technical Publication No. 633 (1977) pp 134-151.

APPENDIX E

THERMOCOUPLE EVALUATION

APPENDIX E

THERMOCOUPLE EVALUATION

The posttest visual inspection of the Test PCM-4 fuel rods indicated that some thermocouple weld attachment degradation occurred during testing. Since the thermocouple response data were an important test result parameter, the thermocouple junctions at selected locations were examined to evaluate performance relative to (a) the extent of attachment degradation (the thermocouple response depends strongly on the junction contact with the cladding surface), and (b) the establishment of adjacent cladding microstructures for temperature comparison with maximum thermocouple readings. The results of this examination are presented in the following paragraphs.

Three of the four fuel rods (Rods UTA-0014, UTA-0015, and UTA-0016) tested in-pile were instrumented to monitor cladding surface and fuel centerline temperatures. Rod A-0017 was not instrumented. Rods UTA-0014 and UTA-0016 each contained a fuel centerline thermocouple and four cladding surface thermocouples. The surface thermocouples were nominally 1.17 mm in diameter and the centerline thermocouples had nominally 1.57-mm outer diameters. Rod UTA-0015 contained a centerline ultrasonic thermometer to measure fuel temperatures, and four cladding surface thermocouples. The locations of instruments on the test fuel rods are presented in Table E-I.

Four titanium sheathed, magnesium-oxide-insulated, platinum/platinum-10% rhodium (Type S) thermocouples were laser welded at selected positions to the cladding surface of Rods UTA-0014 and UTA-0016. Rod UTA-0015 contained three platinum/platinum-10% rhodium thermocouples and one titanium sheathed, magnesium-oxide-insulated Chromel-Alumel (Type K) spaded junction thermocouple. The sheathed signal connection cables (extension tubes) for the cladding surface thermocouples were laser welded to the outer cladding surface at approximately 0.15-m intervals above the thermocouple junction positions. The fuel centerline thermocouple of Rods UTA-0014 and UTA-0016 consisted of tungsten-rhenium (W5%Re/W26%Re) junctions insulated with BeO and sheathed with tantalum.

The fuel centerline thermocouple junctions of Rods UTA-0014 and UTA-0016 were positioned at locations corresponding to the 0.584-m, 90° surface thermocouple junction positions as outlined in Table E-I. The fuel centerline holes for these rods, nominally 1.9 mm in diameter, penetrated 22 fuel pellets for a length of 0.339 m from the top end of the fuel stack. The thermocouple holes penetrated 24 fuel pellets in Rod UTA-0015 for a total length of 0.370 m from the top of the fuel column. The nominal fuel-cladding diametral gap was 0.203 mm for the rods.

Examination of the 0.686-m, 180° thermocouple junction attachment of Rod UTA-0014 revealed weld degradation. The junction was removed during grinding for sample

TABLE E-I

FUEL ROD INSTRUMENTATION FOR TEST PCM-4

Measured Variable:	Fuel Centerline Temperature	Cladding Temperature
Transducer:	Ultrasonic Thermometer or Grounded Junction W5%Re/W26%Re Thermocouple	Platinum-Rhodium (Type S) and Chromel-Alumel (Type K) Thermocouples
Rod UTA-0014	Thermocouple SN 523[a] 0.584-m[b]	0.483m- 0°:SN 13 0.584m- 90°:SN 6 0.686m-180°:SN 18 0.787m-270°:SN 2
Rod UTA-0015	Ultrasonic Thermometer SN 424[c] 0.635-m	0.483m- 0°:SN 11 0.635m- 90°:SN 17 0.686m-180°:SN 12 0.889m-270°:SN 24[d]
Rod UTA-0016	Thermocouple SN 533 0.584-m	0.483m- 0°:SN 1 0.584m- 90°:SN 10 0.686m-180°:SN 7 0.787m-270°:SN 19
Rod A-0017	None	None

[a] SN refers to serial number of instrument.

[b] Locations are referenced to the bottom of the fuel stack.

[c] Ultrasonic thermometer located in Rod UTA-0015 only.

[d] Type K cladding surface thermocouple located at the 0.889-m elevation on Rod UTA-0015 only.

preparation. A portion of the flattened (spaded) titanium sheath behind the junction is shown in Figure E-I. Weld penetration of up to 20% of the cladding wall thickness was observed during the examination. Corrosion of the weld material is also illustrated in Figure E-I.

Oxide thicknesses were uniform around the circumference of the cladding at this elevation, indicating little or no circumferential temperature gradient. Cladding microstructure around the circumference of the sample was prior beta-phase zircaloy with outer

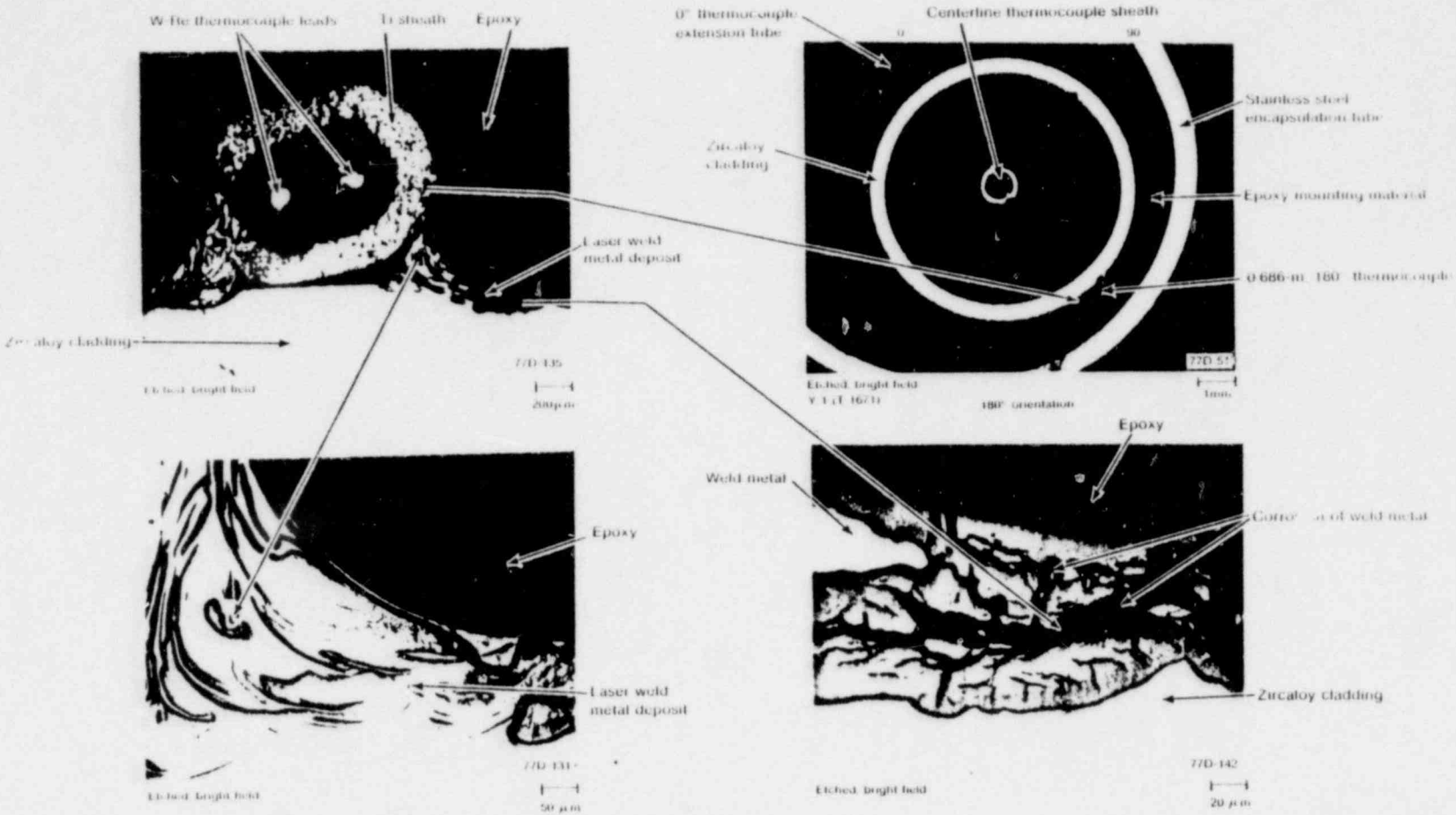

Fig. E-1 View of the 0.686-in. 180° thermocouple junction from Rod HTA-0014

and inner diameter layers of oxygen-stabilized alpha-phase zircaloy; microstructures form at $T \geq 1245$ K (calculated peak cladding temperature, 1360 K). Maximum thermocouple readings up to 815 K were measured by the 0.686-m, 180° thermocouple during testing. A temperature difference of 430 K was observed between the thermocouple reading and temperatures estimated from microstructure, compared with a 545 K difference with the calculated peak cladding temperature.

Similarly, examination of the 0.686-m, 180° thermocouple junction on Rod UTA-0015 revealed laser weld penetration and weld degradation as illustrated in Figure E-2. Weld penetration of up to 50% is shown in the figure, together with corrosion of the weld material as a result of test operation. This thermocouple indicated maximum readings up to 1090 K during testing. A temperature difference of up to 155 K between the maximum thermocouple indications and temperatures estimated from the prior beta cladding microstructures was noted. Comparison with the calculated 1400 K peak cladding temperature for this position shows a 310 K difference from the thermocouple reading. A prior beta cladding microstructure, bounded on the outer and inner diameter surfaces by layers of oxygen-stabilized alpha, was observed around the circumference. Little variation in the surface ZrO_2 layer thickness was noted around the cladding circumference, indicating only a small circumferential temperature gradient.

The 0° thermocouple extension tube laser weld attachment at 0.667 m was examined for weld penetration and degradation. Cladding microstructure in the region (about 50° on each side of the weld attachment) adjacent to the thermocouple was alpha + beta two-phase zircaloy ($1105 < T < 1245$ K). The remaining cladding microstructure was prior beta ($T \geq 1245$ K). The lower associated cladding temperature resulted in only a small amount of weld corrosion as illustrated in Figure E-3. Minimal weld penetration into the cladding wall was observed. Hydrides appearing in the cladding material are also illustrated in the figure.

The 0.686-m, 180° thermocouple from Rod UTA-0016 also exhibited a marked difference between the measured temperature and the temperature estimated from microstructure. The maximum temperature indicated by the thermocouple was 980 K at this elevation, whereas the microstructure (prior beta-phase material) indicated that the temperature was $T > 1245$ K (peak cladding temperature 1690 K). Oxide thicknesses were relatively uniform around the cladding circumference at this elevation, with the thickest layer near 270°. Only a small circumferential peak temperature gradient of about 100 K was indicated.

The thermocouple junction and the weld area are shown in Figure E-4. A large amount (> 75%) of weld penetration is evident in the macrophotographs and in the overall view of the thermocouple. Large areas of weld metal corrosion can also be seen in this figure.

The fuel centerline thermocouple from Rod UTA-0016 (located at 0.584 m from the bottom of the fuel stack) was examined. This thermcouple functioned well until the final DNB flow reduction step of Cycle 4, when the response became erratic and the thermocouple failed. The temperature indication prior to failure was about 2200 K.

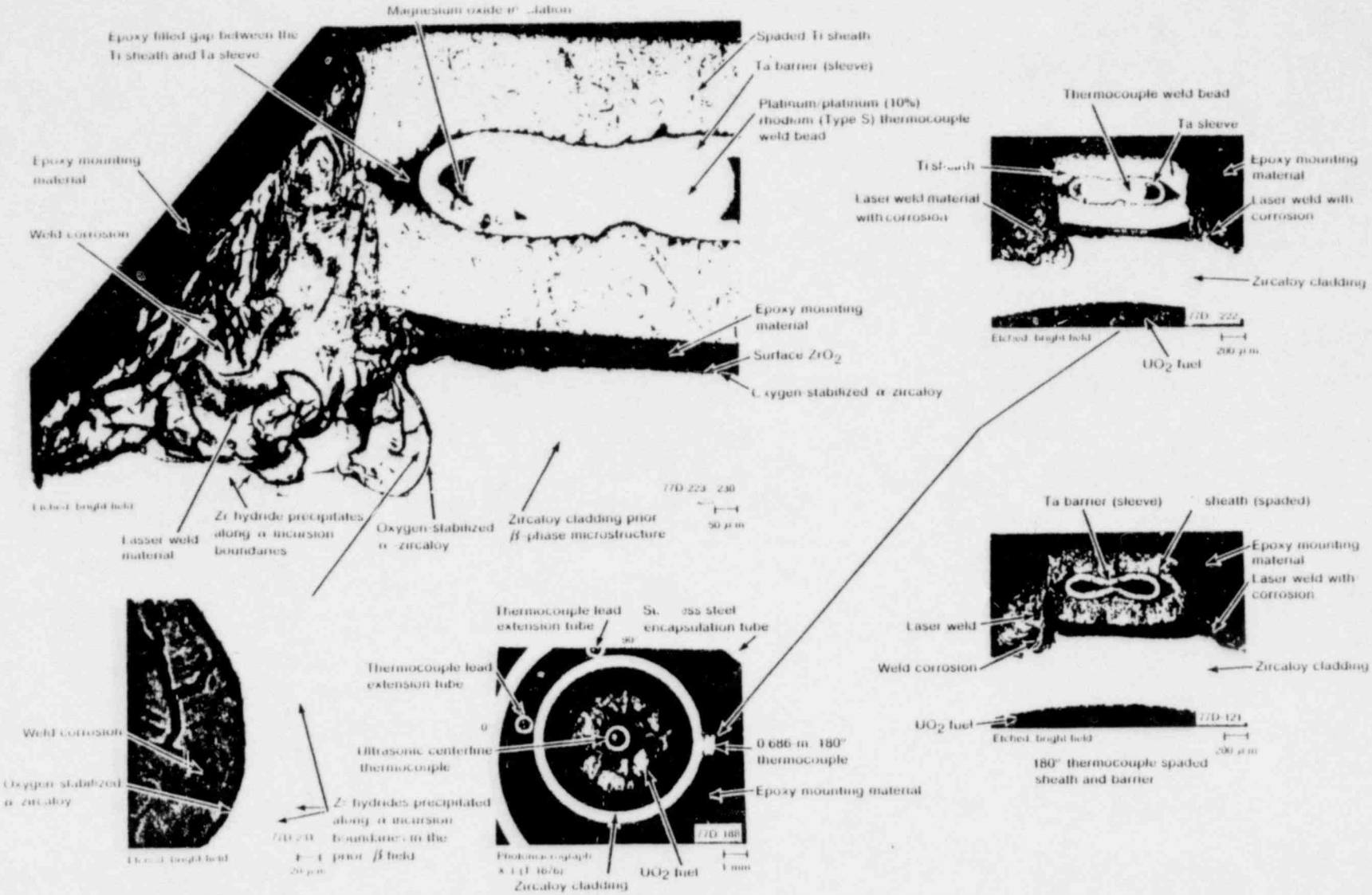

Fig. 4.2.4 Fuel/cladding surface thermocouple junctions at the 0.686-in. 180° position on Rod UTA-0015

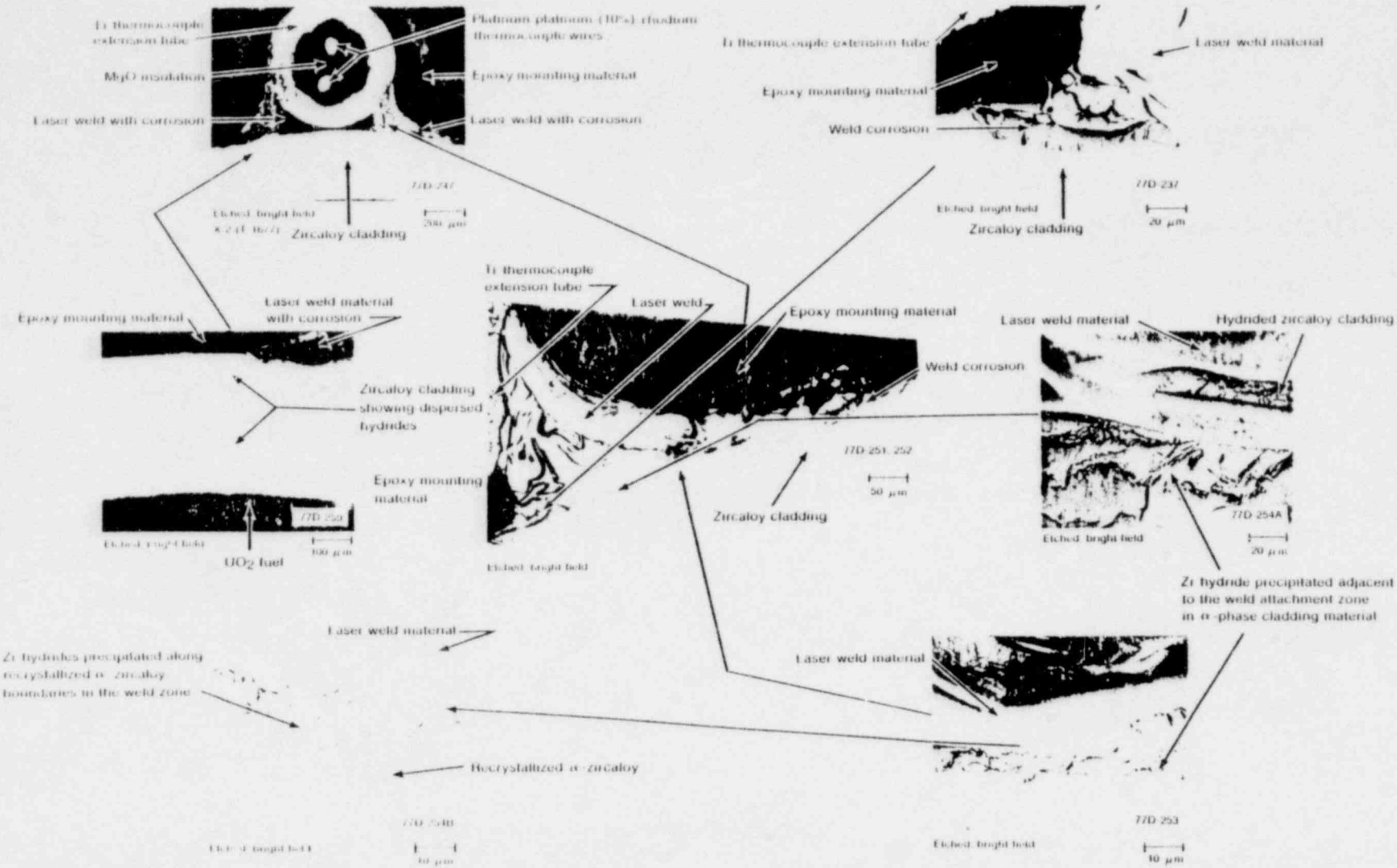

Fig. 4.3 The 0° thermocouple extension tube weld at 0.667 m on Rod UTA 0015.

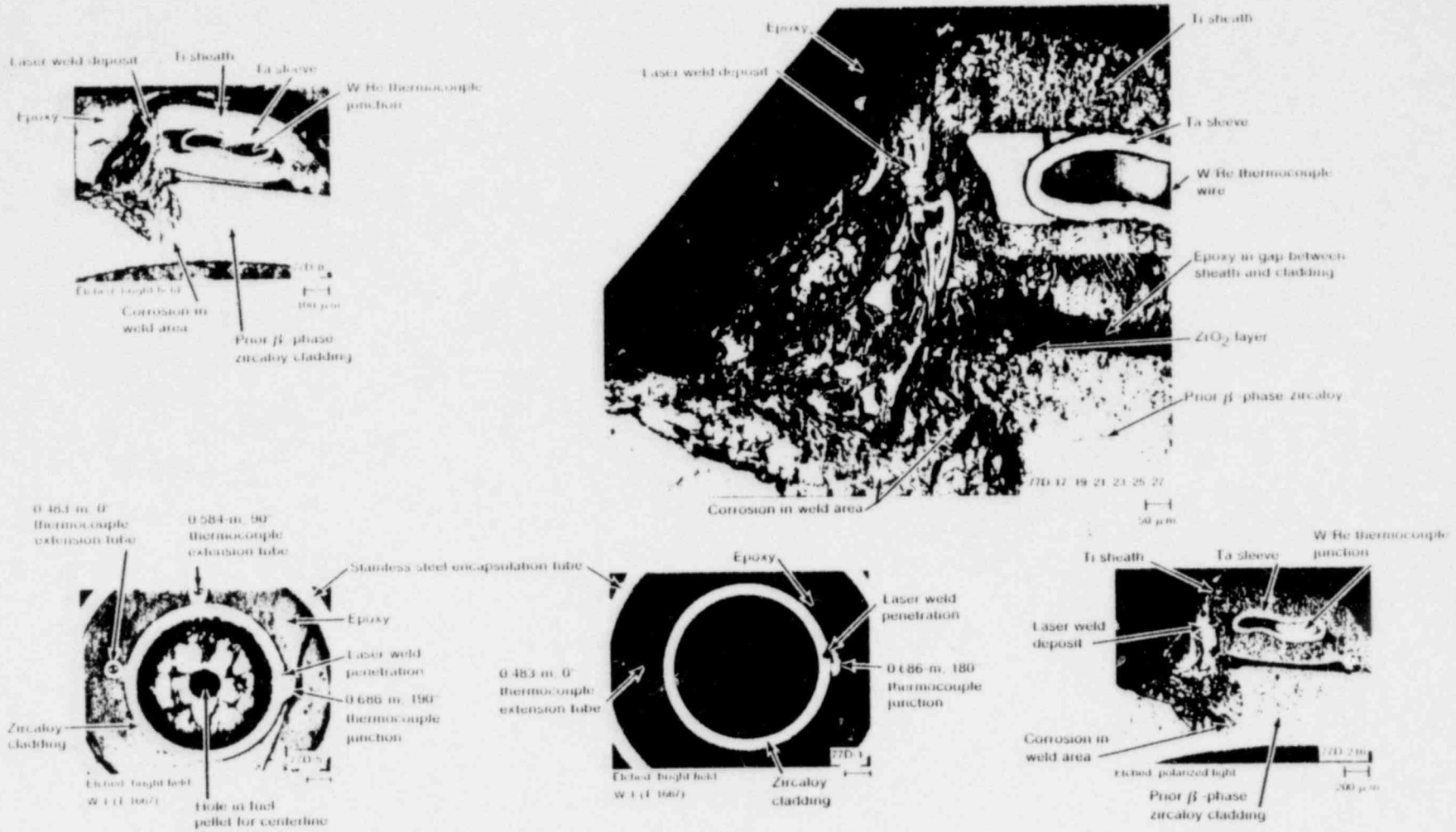

Fig F-4 View of the 0.686-in. 180° thermocouple junction from Rod UTA-0016

Previous experience with centerline thermocouples suggests this is a reasonably accurate indication of the test temperature near the fuel centerline[E-1]. The erratic behavior of the thermocouple prior to failure is attributed to the sheath deterioration by melting at this centerline temperature. The melting point of tantalum metal is 3269 K and the melting temperature of UO_2 is near 3100 K. Thermodynamic data indicate that tantalum metal will not directly reduce the UO_2, whereas intermediate tantalum oxides will readily melt with UO_2 at a lower melting temperature (near 2100 K)[E-2,-3,-4,-5]. Fusion of the W/Re thermocouple wires to the tantalum thermocouple sheath is illustrated in Figures E-5 and E-6 for the 0.587- and 0.641-m elevations, respectively. The band of molten UO_2 reacted with tantalum, shows tantalum streaming and inclusion microsegregation in the photomicrographs of the figures.

REFERENCES

E-1. S. L. Seiffert, *Power-Cooling-Mismatch Test Series, Test PCM-3, Postirratiation Examination*, TREE-NUREG-1187 (December 1977).

E-2. J. Belle, *Uranium Dioxide: Properties and Nuclear Applications*, Naval Reactors Division of Reactor Development, U.S. Government Printing Office, 1961.

E-3. S. G. Tresvyatskiy and V. I. Kushakovskiy, "Melting Points of U-Binary Oxides," *Nucleonics, 18* (1960) p 101.

E-4. C. E. Wicks and F. E. Block, *Thermodynamic Properties of 65 Elements – Their Oxides, Halides, Carbides, and Nitrides*, Bulletin 605, Bureau of Mines (1963).

E-5. B. A. Murdock, *Experiment Data Report, Gap Conductance Test Series, Test GC 1-3, Postirradiation Examination*, TREE-NUREG-1088 (September 1977).

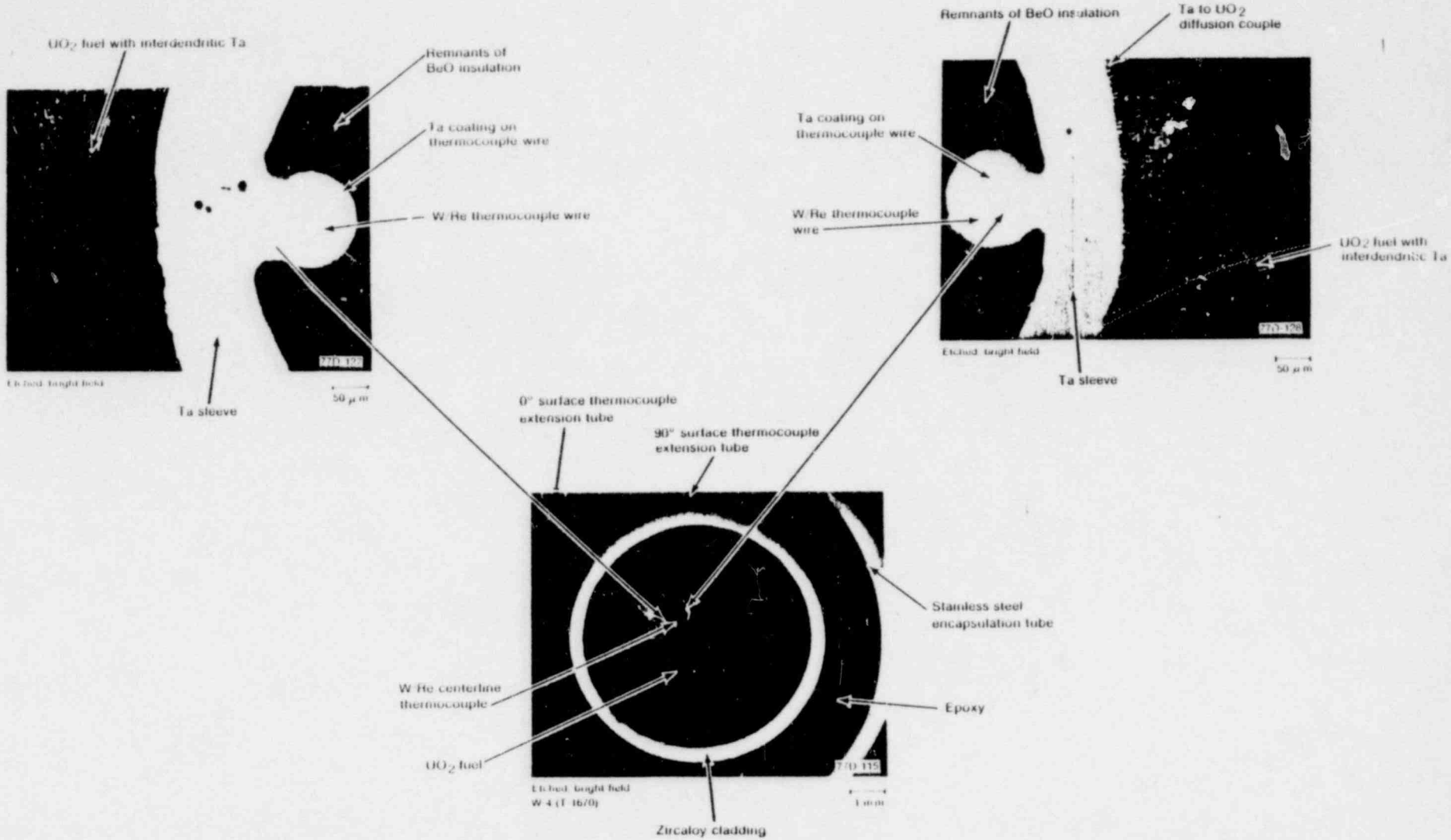

Fig. E-3 Centerline thermocouple near the junction in Rod UTA-0016.

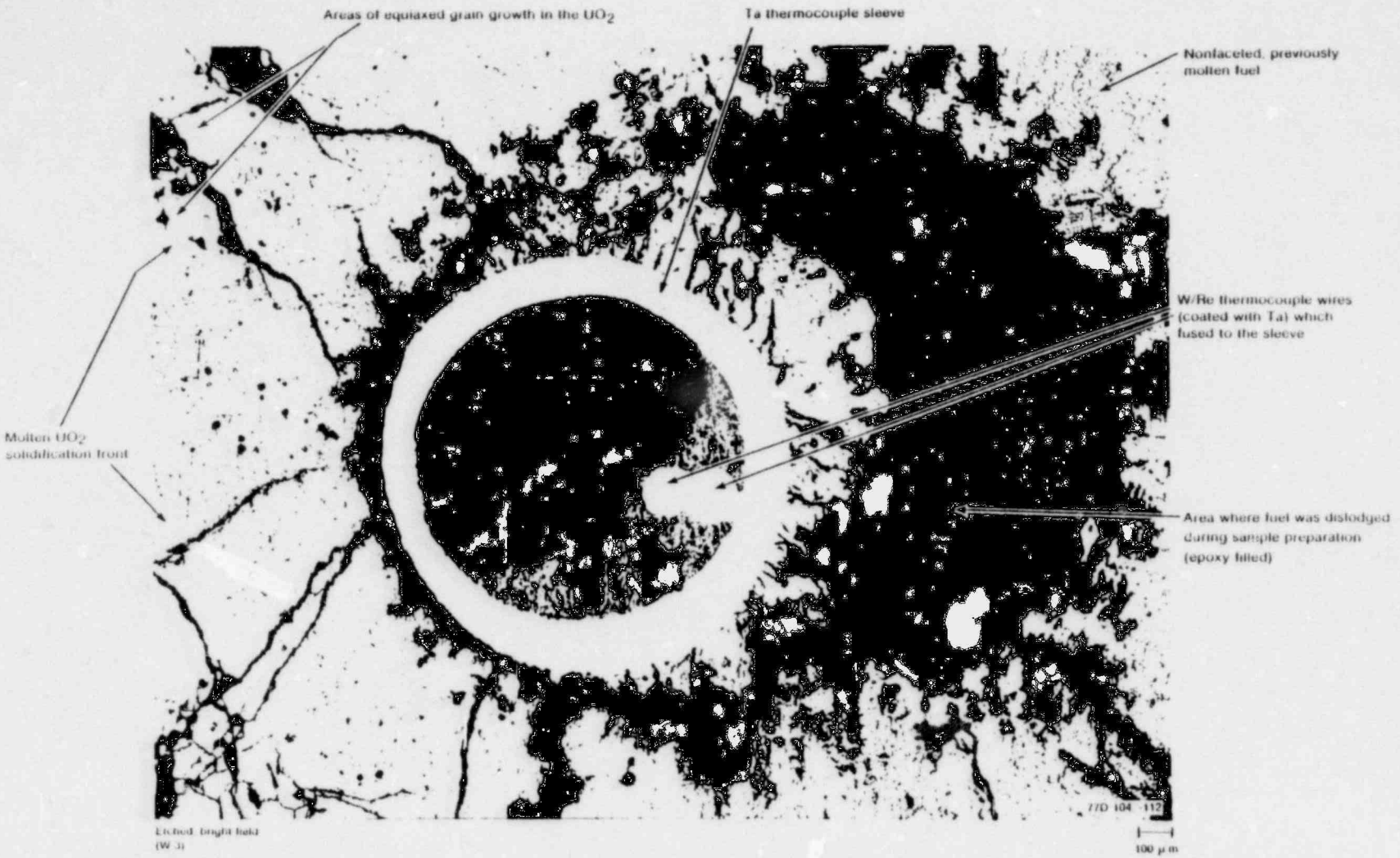

Fig. E-6 Centerline thermocouple above the junction in Rod UTA-0016

APPENDIX F

CLADDING SURFACE TEMPERATURE ESTIMATES

APPENDIX F

CLADDING SURFACE TEMPERATURE ESTIMATES

Cladding temperature is the most important single variable considered in the investigation of fuel rod behavior under simulated accident conditions. The cladding temperature essentially determines the mode of deformation and fuel rod failure. Thus, knowledge of the axial and circumferential temperature gradients along the region of film boiling is required to understand fuel rod behavior. The distribution data are especially required for model evaluation. Since cladding temperatures are only approximately known from test instrumentation, postirradiation analysis is necessary to determine the temperature distribution.

Cladding temperatures were determined by three techniques: (a) metallographic examination of cladding microstructures; (b) computation based on kinetic correlations that relate the sum of the external surface ZrO_2 layer thickness and the adjacent oxygen-stabilized alpha layer with the time in film boiling and the effective isothermal temperature of exposure; and (c) BUILD5 computer code[a] calculations adapted for use in determining peak cladding temperatures from linearized cladding thermocouple time-temperature response histories. Details of these techniques are presented and discussed in the following sections.

Microstructural changes observed in the zircaloy cladding material provide an indication, from phase changes, of the range of elevated temperatures achieved during test operation.

1. CLADDING MICROSTRUCTURES

Microstructures associated with the various phase changes established metallographically in the samples sectioned from Rods UTA-0014, UTA-0015, UTA-0016, and A-0017 are presented schematically in Tables F-I, F-II, F-III, and F-IV, respectively. Temperatures estimated from microstructures are presented in the tables, associated with the schematic microstructure descriptions. Rod UTA-0015 exhibited limited areas of equiaxed alpha zircaloy ($920 < 1105$ K) and alpha + beta zircaloy ($1105 < T < 1245$ K) near some thermocouple locations. The balance of the microstructure within the film boiling zone of Rod UTA-0015 and within the film boiling zones of Rods UTA-0014, UTA-0016, and A-0017 was prior beta bounded on the exterior and interior by oxygen-stabilized alpha-zircaloy layers. Such microstructures occur above 1245 K.

[a] The BUILD5 computer code was developed by R. Pawel at the Oak Ridge National Laboratory and is based on the mathematical analyses of oxygen diffusion in beta-zircaloy[F-1,F-2].

MICROSTRUCTURE KEY FOR TABLES F-I THROUGH F-IV.

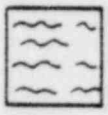

- The 'as-received' stress-relieved microstructure characterized by ropy (stringer) alpha structure

- Transition zone boundary

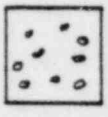

- Recrystallized (equiaxed) alpha-zircaloy

- Transformed prior beta-phase zircaloy

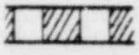

- Oxygen-stabilized alpha-zircaloy

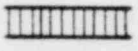

- Surface corrosion (oxide) ZrO_2

- UO_2 fuel pellet

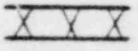

- UO_2-zircaloy duplex interaction layer

INEL-A-8682

TABLE F-I

OBSERVED MICROSTRUCTURES AND ESTIMATED TEMPERATURES AT VARIOUS LOCATIONS ALONG ROD UTA-0014

Sample	X-1	X-2	X-3	X-4	X-5
Distance from bottom of fuel stack (m)	0.686	0.667	0.641	0.606	0.559
Cladding microstructure	Prior beta-zircaloy	Prior beta with some alpha + beta two-phase zircaloy near 0°	Prior beta-zircaloy	Prior beta-zircaloy	Prior beta-zircaloy
	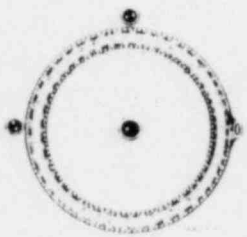	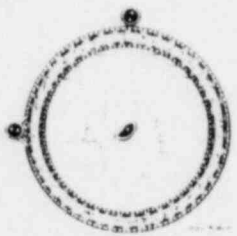	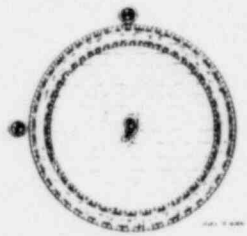	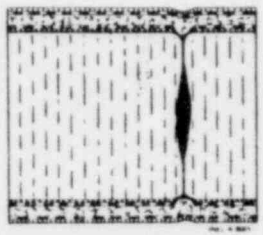	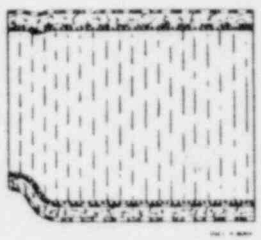
Circumferential cladding temperature range from microstructure (K)	< 1245	1105 < T < 1245 near 0°, > 1245 remainder	> 1245	> 1245	> 1245

TABLE F-II

OBSERVED MICROSTRUCTURES AND ESTIMATED TEMPERATURES AT VARIOUS LOCATIONS ALONG ROD UTA-0015

Sample	Y-1	Y-2	Y-3	Y-4
Distance from bottom of fuel stack (m)	0.686	0.664	0.638	0.600
Cladding microstructure	Prior beta-zircaloy	Prior beta-zircaloy	Prior beta-zircaloy	Prior beta-zircaloy
	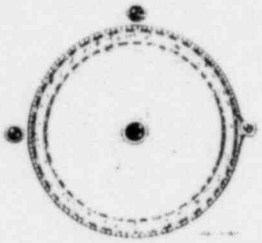	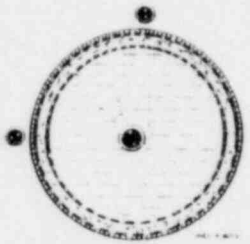	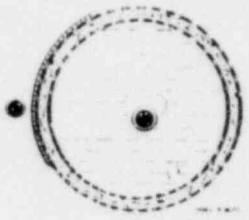	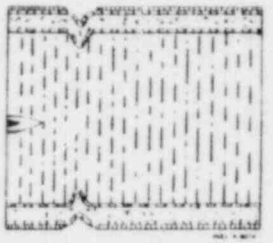
Circumferential cladding temperature range from microstructure (K)	>1245	> 1245	> 1245	> 1245

TABLE F-III

OBSERVED MICROSTRUCTURES AND ESTIMATED TEMPERATURES AT VARIOUS LOCATIONS ALONG ROD UTA-0016

Sample	W-1	W-2	W-3	W-4
Distance from bottom of fuel stack (m)	0.686	0.667	0.641	0.587
Cladding microstructures	Prior beta-zircaloy	Prior beta-zircaloy	Prior beta-zircaloy	Prior beta-zircaloy
	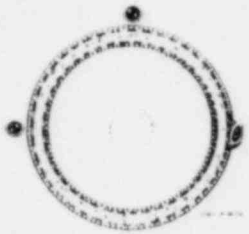	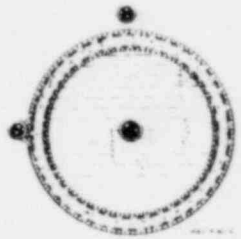	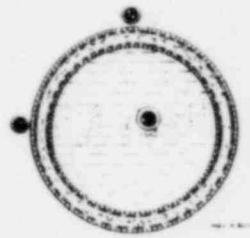	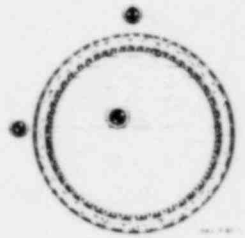
Circumferential cladding temperature range from microstructure (K)	> 1245	> 1245	> 1245	> 1245

TABLE F-IV

OBSERVED MICROSTRUCTURES AND ESTIMATED TEMPERATURES AT VARIOUS LOCATIONS ALONG ROD A-0017

Sample	Z-1	Z-2
Distance from bottom of fuel stack (m)	0.629	0.768
Cladding microstructures	Prior beta-zircaloy	Alpha + beta zircaloy
	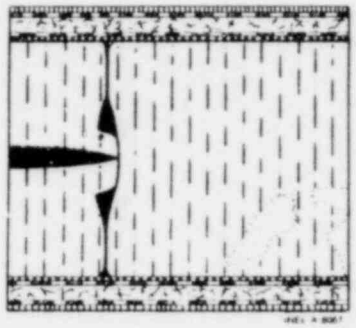	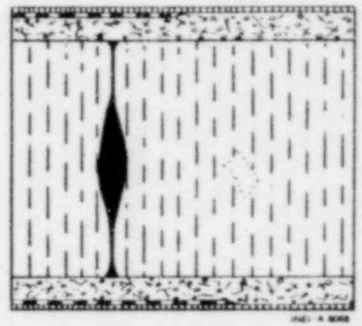
Circumferential cladding temperature range from microstructure (K)	> 1245	1105 < T < 1245

2. ISOTHERMAL TEMPERATURE CALCULATIONS

The cladding surface temperatures were calculated using several kinetic correlations found in the literature for reaction layer thicknesses at both the outside and inside diameters. The correlations are usually expressed by some form of the parabolic rate law

$$d\chi/dt = (1/\chi) \quad \kappa_p^2/2 \tag{F-1}$$

where

χ = the measured kinetic parameter (the thickness of the respective reaction layers in μm)

t = the reaction time in seconds at the test temperature

κ_p = a proportionality constant which is equal to the square root of the diffusivity of oxygen in zircaloy

$$\kappa_p^2 = D = D^* \exp (Q/RT) \tag{F-2}$$

where

D^* = the preexponential diffusion coefficient ($\mu m^2/s$)

Q = the activation energy or heat of activation of the reaction process (cal/mol)

R = the universal gas constant (1.987 cal/mol-K)

T = the temperature (K).

The correlations for reaction layer thicknesses are usually expressed in the integrated form of Equation (F-1)

$$\chi = \kappa_p t^{1/2}. \tag{F-3}$$

Temperatures were calculated from layer thicknesses measured at several circumferential positions in all metallographic mounts sectioned for examination. Lower cladding temperatures (below 1100 K) were based on microstructural evidence, since available kinetic data on oxide layer growth for such temperatures are marginal.

2.1 Kinetic Correlations

Cladding temperature estimates for the exterior cladding surface were based on the kinetic correlations developed by Cathcart[F-3]. The nearly steady state film boiling operation of the test rods in-pile is assumed to approximate isothermal metal-water oxidation conditions.

Similarly, the interior cladding wall temperatures were calculated on the basis of isothermal kinetic correlations developed by Grossman and Rooney[F-4] and by Mallett[F-5] for the growth of an inner cladding layer of oxygen-stabilized alpha-zircaloy.

2.1.1 External Kinetic Correlations. Cathcart has presented isothermal kinetic correlations for[F-3]:

(1) The surface layer of ZrO_2

$$\chi_o/t^{1/2} = 1500.67\ (^{+30\%}_{-23\%})\ \exp\ [-9031\ (\pm 2.2\%)/T] \qquad \text{(F-4)}$$

(2) The cladding (outer diameter) layer of oxygen-stabilized alpha

$$\chi/t^{1/2} = 12\ 340.99\ (^{+54\%}_{-35\%})\ \exp\ [-1211\ (\pm 2.6\%)/T] \qquad \text{(F-5)}$$

(3) The combined layer of ZrO_2 and oxygen-stabilized alpha

$$\chi\xi/t^{1/2} = 8260.75\ (^{+54\%}_{-35\%})\ \exp\ [-10\ 493\ (\pm 1.2\%)/T] \qquad \text{(F-6)}$$

where χ is measured in microns. Bracketed quantities refer to individual 90% confidence limits on the preexponential and activation energy terms.

2.1.2 Fuel-Cladding Interfacial Reaction. Cladding temperatures were calculated from reaction layer thicknesses at several inside diameter cladding locations for each of the four rods on all metallurgical mounts for which measurable layer thicknesses were observed. The computations were based on correlations presented by Grossman and Rooney[F-4] and by Mallett[F-5].

Grossman and Rooney found that the growth of oxygen-stabilized alpha-zircaloy in the cladding at the UO_2-zircaloy interface follows an equation of the form

$$\chi_\alpha/t^{1/2} = 20\ 000\ \exp\ (-12\ 582/T) \qquad \text{(F-7)}$$

where χ_α is measured in microns.

Mallett found that the growth of oxygen-stabilized alpha-zircaloy into the prior beta field from the interface between the fuel and cladding follows an equation of the form

$$\chi_\alpha/t^{1/2} = 2766.7\ \exp\ (-9311/T) \qquad \text{(F-8)}$$

where χ_α is also measured in microns.

2.2 Time Estimates

The times at temperature for each axial location along the fuel rods were adjusted to reflect the progression of film boiling as indicated from thermocouple response data obtained during the test. The axial positions of film boiling are plotted in Figures F-1, F-2, F-3, and F-4 for Rods UTA-0014, UTA-0015, UTA-0016, and A-0017, respectively, as a function of time in film boiling along each fuel rod. The heavy, dark arrows in Figures F-1, F-2, and F-3 for Rods UTA-0014, UTA-0015, and UTA-0016, respectively, correspond to

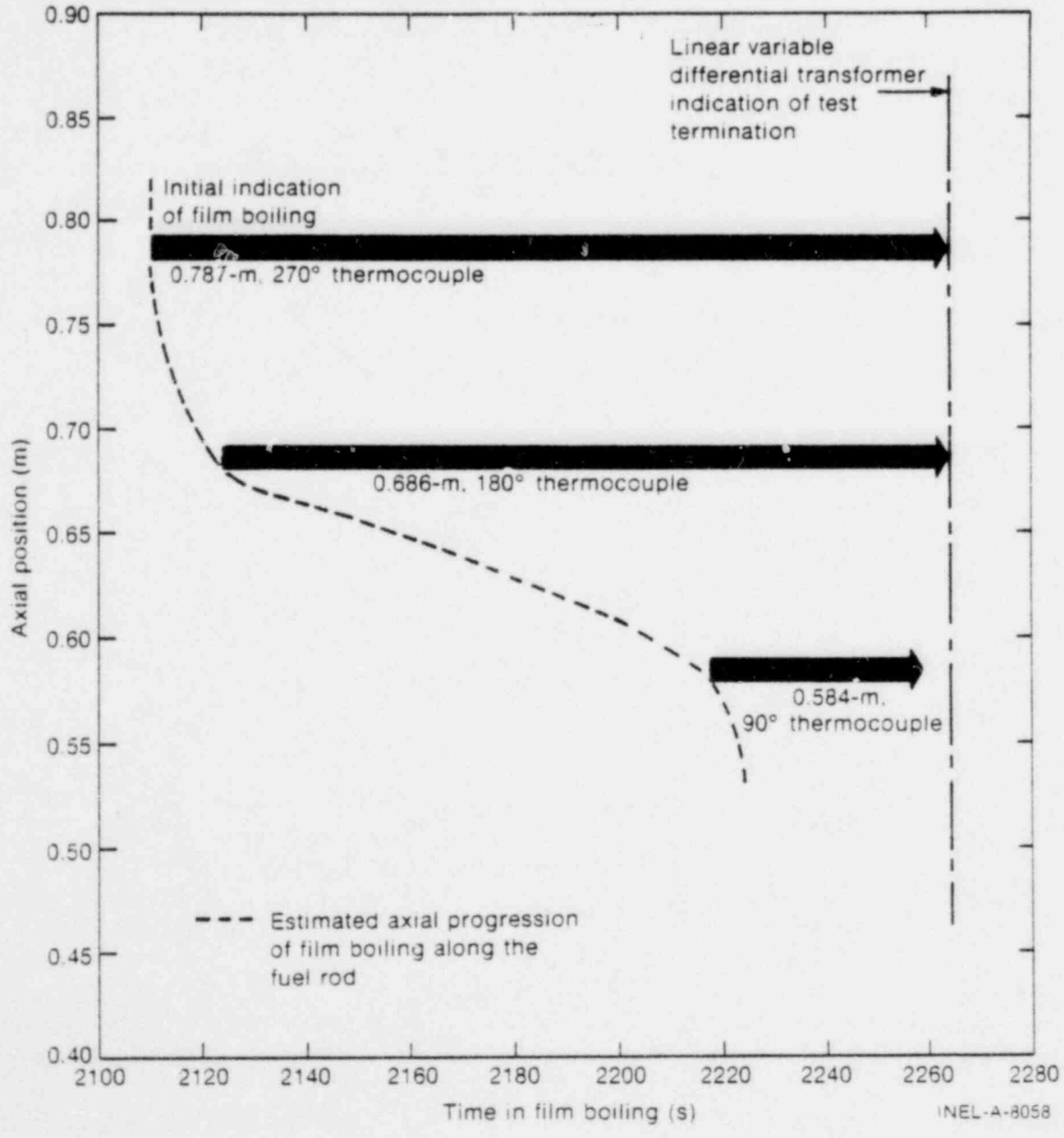

Fig. F-1 Axial progression of film boiling along Rod UTA-0014 from thermocouple response data.

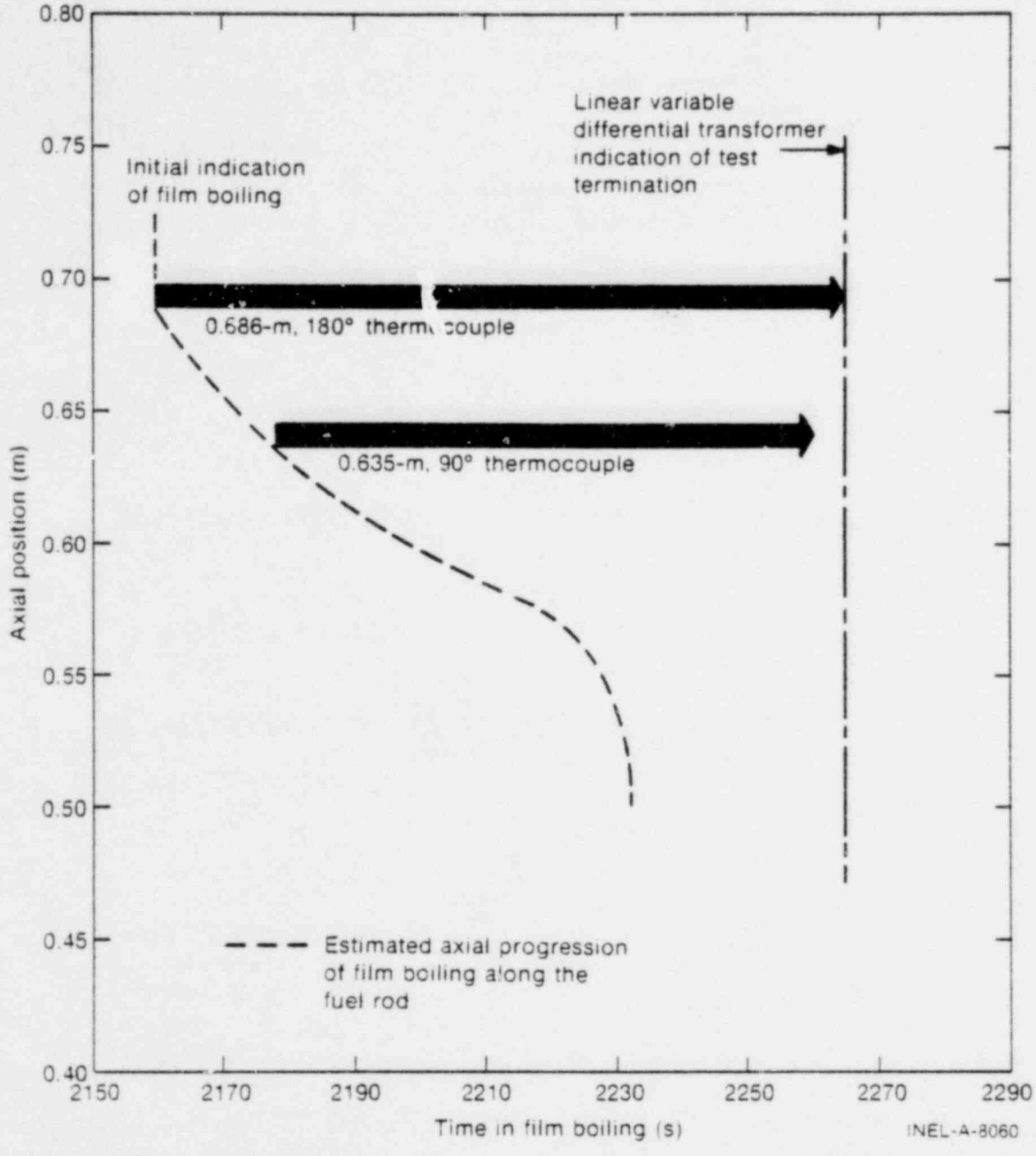

Fig. F-2 Axial progression of film boiling along Rod UTA-0015 from thermocouple response data.

actual thermocouple response times during film boiling operation. The dashed lines indicate an estimated progression of film boiling to lower axial positions along the rod, passing through known points. Since Rod A-0017 was uninstrumented, the estimated response times, as seen in Figure F-4 at several axial positions, were constructed by combining elongation information from the linear variable differential transformer (indicating initiation and termination of film boiling) with the thermocouple response history of the other test rods. The times at temperature for each rod are presented in Table F-V.

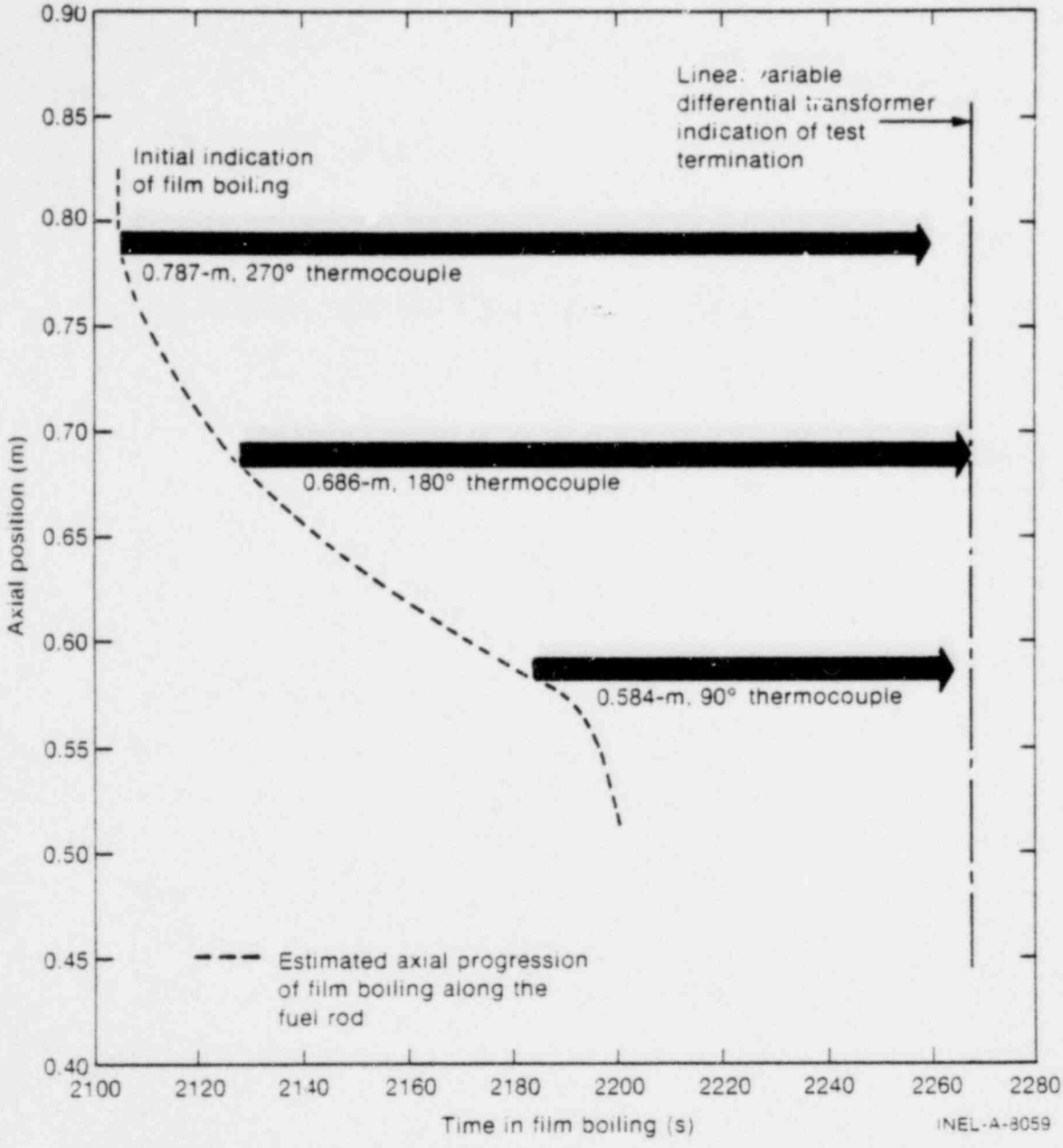

Fig. F-3 Axial progression of film boiling along Rod UTA-0016 from thermocouple response data.

2.3 Results of Isothermal Effective Temperature Estimate Calculations

The results of the isothermal cladding temperature estimate calculations using the film boiling times from Table E-V are presented in Tables F-VI, F-VII, F-VIII, and F-IX for Rods UTA-0014, UTA-0015, UTA-0016, and A-0017, respectively. The ξ-layer thicknesses give the most accurate temperature indication. These results are referred to as "effective" cladding temperatures in the remainder of this appendix.

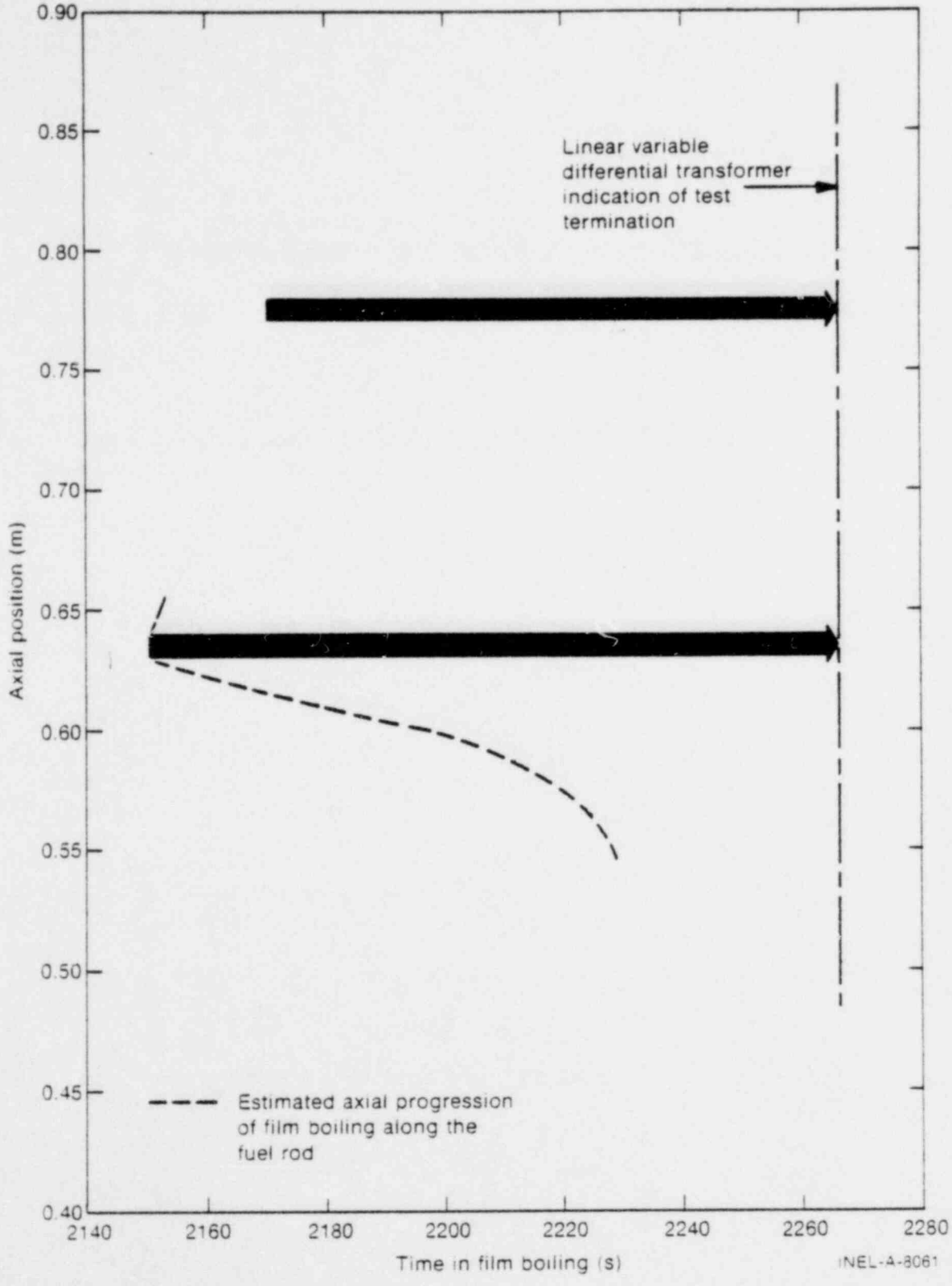

Fig. F-4 Estimated axial progression of film boiling along Rod A-0017 from linear variable differential transformer response data.

TABLE F-V

TIME IN FILM BOILING

Rod						
UTA-0014	Sample	Y-1	Y-2	Y-3	Y-4	
	Location (m)[a]	0.686	0.664	0.638	0.600	
	Time (s)	140	108	85	55	
UTA-0015	Sample	X-1	X-2	X-3	X-4	X-5
	Location (m)	0.686	0.667	0.641	0.606	0.559
	Time (s)	105	97	86	67	40
UTA-0016	Sample	W-1	W-2	W-3	W-4	
	Location (m)	0.686	0.667	0.641	0.587	
	Time (s)	140	127	112	82	
A-0017	Sample	Z-1	Z-2			
	Location (m)	0.629	0.768			
	Time (s)	96	116			

[a] All locations are distances from the bottom of the fuel stack.

Thermocouple data for the instrumented rods lie below the test temperature range. Calculated cladding temperatures are greater than the desired test temperature range (1105 to 1245 K), but are consistent with the prior beta cladding microstructures observed on the samples.

Results of the inner cladding wall temperature calculations are presented in Tables F-X through F-XIII. These temperatures generally are in good agreement with the calculated isothermal effective temperatures.

TABLE F-VI

ISOTHERMAL CLADDING TEMPERATURE ESTIMATES FOR ROD UTA-0014

Sample (Distance from Bottom of Fuel Stack, m)	Orientation (°)	Oxide Thickness (μm)[a]	Alpha Layer Thickness (μm)[a]	Oxide + Alpha Layer Thickness (μm)[a]	Temperature (K) Oxide[b]	Alpha[c]	Alpha + Oxide[d]	Temperature (K) Effective	Maximum	Minimum
Y-1	0	16	--	--	1287	--	--	1290		
(0.686)	90	16	--	--	1287	--	--	1290	1290	1210
	180	10	--	--	1207	--	--	1210		
	270	12	--	--	1237	--	--	1240		
Y-2	0	19	24	43	1345	1411	1380	1380		
(0.664)	90	20	25	45	1356	1417	1389	1390	1390	1380
	180	20	26	46	1356	1424	1393	1390		
	270	20	26	46	1356	1424	1393	1390		
Y-3	0	28	28	56	1459	1457	1454	1450	1460	1430
(0.638)	30	28	--	--	1455	--	--	1460		
	90	[e]	26	--	--	1445	--	1450		
	180	[e]	24	--	--	1431	--	1430		
	270	[e]	24	--	--	1431	--	1430		
Y-4	0	13	15	28	1337	1389	1364	1360	1480	1360
(0.600)	180	[e]	25	--	--	1476	--	1480		

[a] Uncertainties in these thicknesses average ± 1, μm due primarily to unevenness of the layers.

[b] Calculation based on the Cathcart correlation Equation (F-4) for oxide thickness.

[c] Calculation based on the Cathcart correlation Equation (F-5) for alpha-zircaloy layer thickness.

[d] Calculation based on the Cathcart correlation Equation (F-6) for the oxide plus alpha-zircaloy layer thickness (ξ layer).

[e] Oxide had spalled and was not measurable.

TABLE F-VII

ISOTHERMAL CLADDING TEMPERATURE ESTIMATES FOR ROD UTA-0015

Sample (Distance from Bottom of Fuel Stack, m)	Orientation (°)	Oxide Thickness (μm)[a]	Alpha Layer Thickness (μm)[a]	Oxide + Alpha Layer Thickness (μm)[a]	Temperature (K) Oxide[b]	Alpha[c]	Alpha + Oxide[d]	Temperature (K) Effective	Maximum	Minimum
X-1	0	24	10	34	1397	1282	1341	1340		
(0.686)	90	15	8	23	1302	1252	1277	1280	1340	1270
	180	14	8	22	1289	1252	1271	1270		
	270	22	6	28	1378	1216	1309	1310		
X-2	0	22	6	28	1387	1221	1315	1320		
(0.667)	90	11	14	25	1253	1335	1297	1300	1430	1300
	165	[i]	55	--	--	1572	--	--		
	180	24	30	54	1406	1458	1433	1430		
	270	24	28	52	1406	1446	1426	1430		
X-3	0	38	32	70	1529	1480	1499	1500		
(0.641)	90	20	32	52	1379	1480	1438	1440		
	180	[i]	33	--	--	1486	--	1490	1520	1440
	250	34	44	78	1501	1540	1522	1520		
	270	46	30	76	1581	1468	1517	1520		
X-4	0[e]	42	56	98	1590	1615	1605	1610		
(0.606)	0[f]	44	62	106	1603	1637	1624	1620	1620	1610
	0[g]	46	60	106	1616	1630	1624	1620		
	180[h]	[i]	53	--	--	1610	--	1610		
X-5	0[h]	[i]	30	--	--	1540	--	1540	1600	1540
(0.559)	180[h]	[i]	40	--	--	1598	--	1600		

[a] Uncertainties in these thicknesses average ± 1 μm, due primarily to unevenness of the layers.

[b] Calculation based on the Cathcart correlation Equation (F-4) for oxide thickness.

[c] Calculation based on the Cathcart correlation Equation (F-5) for alpha-zircaloy layer thickness.

[d] Calculation based on the Cathcart correlation Equation (F-6) for the oxide plus alpha-zircaloy layer thicknes (ζ layer).

[e] Longitudinal sample measured near the top end.

[f] Longitudinal sample measured near midlength.

[g] Longitudinal sample measured near the bottom end.

[h] Longitudinal sample measured nea the collapse at pellet interfaces.

[i] Oxide had spalled and was not measurable.

TABLE F-VIII

ISOTHERMAL CLADDING TEMPERATURE ESTIMATES FOR ROD UTA-0016

Sample (Distance from Bottom of Fuel Stack, m)	Orientation (°)	Oxide Thickness (μm)[a]	Alpha Layer Thickness (μm)[a]	Oxide + Alpha Layer Thickness (μm)[a]	Temperature (K) Oxide[b]	Alpha[c]	Alpha + Oxide[d]	Temperature (K) Effective	Maximum	Minimum
W-1	0	20	22	42	1330	1376	1353	1350		
(0.686)	90	20	22	42	1330	1376	1353	1350	1410	1350
	180	18	18	36	1309	1345	1327	1330		
	270	30	28	58	1414	1415	1412	1410		
W-2	0	--	--	--	--	--	--	--		
(0.667)	90	32	36	68	1440	1466	1452	1450	1490	1440
	180	38	44	82	1480	1503	1491	1490		
	270	[e]	31	--	--	1440	--	1440		
W-3	0	[e]	29	--	--	1440	--	1440		
(0.641)	90	36	38	74	1483	1487	1483	1480	1520	1440
	180	[e]	45	--	--	1519	--	1520		
	270	36	42	78	1483	1502	1494	1490		
W-4	0	[e]	27	--	--	1454	--	1450		
(0.587)	90	[e]	14	--	--	1348	--	1350	1450	1350
	180	[e]	20	--	--	1404	--	1400		
	270	[e]	25	--	--	1441	--	1440		

[a] Uncertainties is these thicknesses ± 1 μm, due primarily to unevenness of the layers.

[b] Calculation based on the Cathcart correlation Equation (F-4) for oxide thickness.

[c] Calculation based on the Cathcart correlation Equation (F-5) for alpha-zircaloy layer thickness.

[d] Calculation based on the Cathcart correlation Equation (F-6) for oxide plus alpha-zircaloy layer thickness.

[e] Oxide had spalled and was not measurable.

TABLE F-IX

ISOTHERMAL CLADDING TEMPERATURE ESTIMATES FOR ROD A-0017

Sample (Distance from Bottom of Fuel Stack, m)	Orientation (°)	Oxide Thickness (μm)[a]	Alpha Layer Thickness (μm)[a]	Oxide + Alpha Layer Thickness (μm)[a]	Temperature (K) Oxide[b]	Alpha[c]	Alpha + Oxide[d]	Temperature (K) Effective	Maximum	Minimum
Z-1 (0.629-0.648)	0[e]	32	50	82	1473	1555	1522	1520		
	0[f]	34	48	82	1488	1547	1522	1520	1530	1520
	0[g]	36	48	84	1502	1547	1527	1530		
	180[f]	[h]	28	--	--	1447	--	--		
Z-2 (0.768-0.787)	0[e]	16	14	30	1305	1323	1313	1310[i]		
	0[f]	14	15	29	1281	1333	1307	1310[i]		
	0[g]	13	16	29	1267	1342	1307	1310[i]	1320	1310
	180[e]	14	18	32	1281	1360	1323	1320[i]		
	180[f]	14	16	30	1281	1342	1313	1310[i]		
	180[g]	16	14	30	1305	1323	1313	1310[i]		

[a] Uncertainties in these thicknesses average ± 1 μm, due primarily to unevenness of the layers.

[b] Calculation based on the Cathcart correlation Equation (F-4) for oxide thickness.

[c] Calculation based on the Cathcart correlation Equation (F-5) for alpha-zircaloy layer thickness.

[d] Calculation based on the Cathcart correlation Equation (F-6) for the oxide plus alpha-zircaloy layer thickness.

[e] Longitudinal sample measured near the top end.

[f] Longitudinal sample measured near the pellet interface.

[g] Longitudinal sample measured near the bottom end.

TABLE F-X

CLADDING TEMPERATURE ESTIMATES FROM INNER REACTION LAYERS FOR ROD UTA-0014

Sample (Distance from Bottom of Fuel Stack, m)	Outside Diameter				Inside Diameter			Effective Temperature (K)		
	Orientation (°)	Oxide Thickness (μm)[a]	Alpha Layer Thickness (μm)[a]	Oxide + Alpha Layer Thickness (μm)[a]	Orientation (°)	Alpha Layer Thickness (μm)[a]	Reaction Layer Thickness (μm)[a]	[b]	[c]	[d]
Y-1	0	16	--	--	0	7.5	12.5	1210	1110	--
(0.686)	90	16	--	--	--	--	--	--	--	--
	180	10	--	--	--	--	--	--	--	--
	270	12	--	--	--	--	--	--	--	--
Y-2	0	19	24	43	--	--	--	--	--	1380
(0.664)	90	20	25	45	--	--	--	--	--	1380
	180	20	26	46	--	--	--	--	--	1390
	270	20	26	46	270	22	36	1370	1300	1390
Y-3	0	28	28	56	0	20	47.6	1380	1300	1450
(0.638)	90	[e]	46	--	--	25	34	1410	1340	--
	180	[e]	44	--	--	23	34	1400	1330	--
	270	[e]	44	--	--	25	34	1410	1340	--
Y-4	0	13	15	28	0	11	20	1320	1240	1360
(0.600)	180	[e]	25	--	180	17.5	30	1390	1320	--

[a] Uncertainties in these thicknesses average ± 1 μm, due primarily to unevenness of the layers.

[b] Calculation based on the Grossman and Rooney correlation Equation (F-7).

[c] Calculation based on the Mallett correlation Equation (F-8).

[d] Calculation based on the Cathcart correlation Equation (F-6) for the outer ε layer taken from Table F-VI.

[e] Oxide had spalled and was not measurable.

TABLE F-XI

CLADDING TEMPERATURE ESTIMATES FROM INNER REACTION LAYERS FOR ROD UTA-0015

Sample (Distance from Bottom of Fuel Stack, m)	Outside Diameter				Inside Diameter			Effective Temperature (K)		
	Orientation (°)	Oxide Thickness (μm)[a]	Alpha Layer Thickness (μm)[a]	Oxide + Alpha Layer Thickness (μm)[a]	Orientation (°)	Alpha Layer Thickness (μm)[a]	Reaction Layer Thickness (μm)[a]	[b]	[c]	[d]
X-1 (0.686)	0	24	10	34	0	16.5	22.5	1330	1250	1340
	90	15	8	23	40	25.5	32.5	1400	1330	1280
	180	14	8	22	90	26	32.5	1400	1330	1270
	270	22	6	28	120	17.5	30	1340	1260	1310
	--	--	--	--	320	20	27.5	1360	1280	--
X-2 (0.667)	0	22	6	28	0	7	7	1230	1130	1320
	90	11	14	25	--	--	--	--	--	1300
	180	24	30	54	165	42.5	60	1490	1440	1430
	270	24	28	52	340	12.5	22.5	1300	1210	1430
X-3 (0.641)	0	38	32	70	0	20	27.5	1380	1300	1500
	90	20	32	52	135	51	69	1530	1490	1440
	180	[e]	33	--	180	51	70	1530	1500	--
	270	46	30	76	210	34	48	1460	1410	1520
X-4 (0.606)	0	44	62	106	0	52	70	1560	1530	1620
	180	[e]	53	--	180	45	65	1530	1500	--
X-5 (0.559)	0	[e]	30	--	0	50	75	1610	1590	--
	180	[e]	40	--	180	47.5	60	1600	1580	--

[a] Uncertainties in these layers average ± 1 μm, due primarily to unevenness of the layers.

[b] Calculation based on the Grossman and Rooney correlation Equation (F-7).

[c] Calculation based on the Mallett correlation Equation (F-8).

[d] Calculation based on the Cathcart correlation Equation (F-6) for the outer ε-layer taken from Table F-VII.

[e] Oxide had spalled and was not measurable.

TABLE F-XII

CLADDING TEMPERATURE ESTIMATES FROM INNER REACTION LAYERS FOR ROD UTA-0016

Sample (Distance from Bottom of Fuel Stack, m)	Outside Diameter				Inside Diameter			Effective Temperature (K)		
	Orientation (°)	Oxide Thickness (μm)[a]	Alpha Layer Thickness (μm)[a]	Oxide + Alpha Layer Thickness (μm)[a]	Orientation (°)	Alpha Layer Thickness (μm)[a]	Reaction Layer Thickness (μm)[a]	[b]	[c]	[d]
W-1 (0.686)	0	20	22	42	0	24	24	1370	1290	1350
	90	20	22	42	80	28	41	1390	1320	1350
	180	18	18	36	180	10	--	1250	1150	1330
	270	30	28	58	270	25	40	1370	1300	1410
W-2 (0.667)	0	8	6	14	0	--	--	--	--	1190
	90	32	36	68	90	28	40	1400	1330	1450
	180	38	44	82	180	40	54	1460	1400	1490
	270	[e]	31	--	270	29	40	1405	1330	--
W-3 (0.641)	0	[e]	29	--	0	27.5	37.5	1410	1340	--
	90	36	38	74	90	35	52	1440	1380	1480
	180	[e]	45	--	180	35	55	1440	1380	--
	270	36	42	78	270	32.5	50	1430	1370	1490
W-4 (0.687)	0	[e]	27	--	0	25	37	1420	1350	--
	90	[e]	14	--	90	15	--	1340	1250	--
	180	[e]	20	--	180	20	35	1380	1310	--
	270	[e]	25	--	270	22	34	1400	1320	--

[a] Uncertainties in these layers average ± 1 μm, due primarily to unevenness of the layers.

[b] Calculation based on the Grossman and Rooney correlation Equation (F-7).

[c] Calculation based on the Mallett correlation Equation (F-8).

[d] Calculation based on the Cathcart correlation Equation (F-6) for the outer ε-layer taken from Table F-VIII.

[e] Oxide had spalled and was not measurable.

TABLE F-XIII

CLADDING TEMPERATURE ESTIMATES FROM INNER REACTION LAYERS FOR ROD A-0017

Sample (Distance from Bottom of Fuel Stack, m)	Outside Diameter				Inside Diameter			Effective Temperature (K)		
	Orientation (°)	Oxide Thickness (μm)[a]	Alpha Layer Thickness (μm)[a]	Oxide + Alpha Layer Thickness (μm)[a]	Orientation (°)	Alpha Layer Thickness (μm)[a]	Reaction Layer Thickness (μm)[a]	[b]	[c]	[d]
Z-1 (0.629)	0	34	48	82	0	38	57	1460	1400	1500
	180	[e]	28	--	180	38.5	57.5	1460	1400	--
Z-2 (0.768)	0	13	16	29	--	--	--	--	--	1310
	180	14	18	32	--	--	--	--	--	1320

[a] Uncertainties in these thicknesses average ± 1 μm, due primarily to unevenness of the layers.

[b] Calculation based on the Grossman and Rooney correlation Equation (F-7).

[c] Calculation based on the Mallett correlation Equation (F-8).

[d] Calculated based on the Cathcart correlation Equation (F-6) for the outer ε-layer taken from Table F-IX.

[e] Oxide had spalled and was not measurable.

3. MODIFIED BUILD5 COMPUTER CODE TEMPERATURE CALCULATIONS

The modified BUILD5 computer code was used to determine peak cladding temperature. The modified program is presented in Table F-XIV. Linearized time-temperature cladding thermocouple response histories of fuel rod temperatures above 730 K were used as input. The ZrO_2 buildup and oxygen-stabilized alpha-zircaloy layer formation were calculated by numerical integration over successive time-temperature steps using isothermal parabolic oxidation kinetic equations developed by Cathcart[F-3]. The input temperatures were augmented by a multiplicative factor (*FAC) in order to achieve calculated reaction layer development matching the actual microstructural thicknesses measured metallographically.

3.1 Modifed BUILD5 Code Analysis

The modified BUILD5 computer code calculations were extended to determine peak cladding temperatures and microstructural layer thicknesses at axial positions and angular orientations along the fuel rod at locations other than thermocouple positions. Thermocouple response histories were extrapolated to intermediate positions below the thermocouple attachments to determine the axial and circumferential temperature distribution along the fuel rod. Such computations are useful as input for model evaluation.

The constructed profiles are presented in Figures F-5 through F-8, together with the linearized thermocouple test response data. The response profiles are assumed to hold circumferentially at each axial position. The thermocouple response data used in Figures F-5 through F-8 are tabulated in Tables F-XV through F-XVIII for Rods UTA-0014, UTA-0015, UTA-0016, and A-0017, respectively.

3.2 Peak Cladding Temperature Results

Peak cladding temperatures were obtained from the BUILD5 data by comparing the calculated combined oxide and oxygen-stabilized alpha-zircaloy buildup with measured values of the combined reaction layer thicknesses for each time-temperature thermocouple response history. The results of this comparison are presented in Tables F-XIX through F-XXII. Also shown in these tables is the quantity (*FAC), which is the modified BUILD5 multiplicative factor for the input time-temperature data that adjusts the data to higher values so that the modified BUILD5 calculated layer thicknesses agree with the measured microstructural layer thicknesses. The calculated peak temperatures are plotted as a function of axial position in Figures F-9 through F-12 for Rods UTA-0014, UTA-0015, UTA-0016, and A-0017, respectively. Maximum and minimum peak cladding temperatures at each axial location are represented together with the maximum thermocouple temperatures for the instrumented fuel rods. The calculated values are compared with the temperature range sought during the test (represented by the hatched area bracketing the 1105 to 1245 K temperature range corresponding to the alpha + beta transition temperatures for zircaloy-4).

TABLE F-XIV

BUILD5 COMPUTER CODE MODIFIED TO CALCULATE PEAK CLADDING TEMPERATURES

```
      PROGRAM BUILD5 (INPUT,OUTPUT,TAPE5=INPUT,TAPE6=OUTPUT)
C
C     SUBCODE #BUILD5# FROM ORNL
C
C     THIS PROGRAM IS FOR **ONE-SIDE** OXIDATION.
C
C     THIS PROGRAM ACCEPTS LIN SEG INPUT AND USES ZWICK OY AND ALPHA
C     ARRHENIUS RATE CONSTANT EQUATION TO COMPUTE XI AND REMAINING BETA
C     VALUES FOR THE TRANSIENT.
C
C     OXYGEN PROFILES ARE COMPUTED ON THE BASIS OF A
C     FINITE DIFFERENCE METHOD ASSUMING THE TRANSIENT TO BE COMPOSED
C     OF A SERIES OF 174 SECOND ISOTHERMAL SEGMENTS.
C
      REAL AAYS
C
      DIMENSION AA(101), AB(101), AC(101), AD(101), AE(101),
     = AF(101), AG(101), AH(101), AI(101)
C
      DIMENSION AT(21),AP(21), AR(21)
C
  190 READ(5,199) AMS,AS3,AZ5,FAC
  199 FORMAT(4E20.5)
      WRITE(6,3080)
 3080 FORMAT(///16X,#**********************************************************
     =**********************************#)
      WRITE(6,197)
  197 FORMAT(////13X,#AMS#,17X,#AS3#,17X,#AZ5#,17X,#FAC#)
      WRITE(6,198) AMS,AS3,AZ5,FAC
C
C     AMS IS THE ORIGINAL SPECIMEN THICKNESS IN CM.
C     AS3 IS THE ORIG. OXYGEN CONCENTRATION (0.12 WT. % FOR BETA ZRY).
C     AZ5 IS THE PRINTOUT TIME INCREMENT.  (MUST BE AN INTEGRAL
C         MULTIPLE OF 0.25 SEC.)
C     FAC IS THE MULTIPLIER FOR THE THERMOCOUPLE TIME/TEMPERATURE CURVE.
C
  200 AA(1) = AS3
  201 AB(1) = AS3
  202 AC(1) = AS3
  203 AD(1) = AS3
  204 AE(1) = AS3
  205 AF(1) = AS3
  206 AG(1) = AS3
  207 AH(1) = AS3
  208 AI(1) = AS3
C
  225 AL2 = AMS
      AL2 = BETA THICKNESS AT 0 TIME/...(AND AT START OF EACH AZ4 INT.)
C
  270 AZ3 = 0.01
      AZ3 IS THE TIME INCREMENT FOR THE XI INTEGRATION
C
  290 AZ4 = 0.25
      AZ4 IS THE TIME INCREMENT FOR THE SUBROUTINE BEGINNING AT 3000,
          I.E. THE ISOTHERMAL SEGMENT LENGTH
C
      DO 345 I = 1,20
         READ(5,342) AT(I), AP(I)
  342 FORMAT(2F20.0)
C     AT(N), AP(N) ARE COORDINATES OF THE SEGMENT ENDS - SEC, DEG. K.
         I21 = I
         IF(AP(I) .EQ. 0.0) GO TO 346
C
C     THIS STEP FACTORS THE TEMP/TIME CURVE
      AP(I)=AP(I)*FAC
```

TABLE F-XIV (continued)

```
C
  345  CONTINUE
C
  346  IZ1 = IZ1 - 2
C      IZ1 IS THE NUMBER OF LINEAR SEGMENTS DESCRIBING THE TRANSIENT.
C
  355  AL3 = AT(1)
C      AL3 IS THE STARTING TIME. SEC./...(AND THE START OF EACH ATA
C      INT.)
C
       IZ11 = IZ1 + 1
 8000  CONTINUE
  360  DO 372 I = 1,IZ1
  370  AR(I) = (AP(I+1)-AP(I))/(AT(I+1)-AT(I))
C      AR(I) IS THE TEMP/TIME SLOPE OF THE I#TH SEGMENT.
C
  372  CONTINUE
       WRITE(6,5010)
 5010  FORMAT(1H0)
       WRITE(6,5010)
C
       WRITE(6,5070)
 5070  FORMAT(10X,#TIMES (SEC) AND CORRESPONDING TEMPS (K) FOR TRANSIENT
     # INPUT SHAPE#)
       WRITE(6,5010)
C
       AZ2 = AP(1)
       DO 380 I = 1,IZ11
       IF(AP(I) .GT. AZ2) AZ2 = AP(I)
C      AZ2 IS THE MAXIMUM TEMPERATURE OF THE TRANSIENT IN DEGREES K.
C
  373  WRITE(6,374) AT(I),AP(I)
  374  FORMAT(20X,2F10.2)
  380  CONTINUE
       WRITE(6,5010)
C
  381  W1 = 0.0
C      W1 IS THE INITIAL VALUE OF #OXYGEN CONSUMED#, GM2/CM**3.
C
  385  AM2 = 1.0E10
C
  387  Y8 = 0.0
  388  Y9 = 0.0
C      AM2 = ARTIFICIALLY LARGE MODULUS.
C      Y8 AND Y9 ARE INITIAL OXIDE AND ALPHA LAYER THICKNESSES.
C
  390  Y1 = 0.0
C      Y1 = INITIAL X1 VALUE, CM.
  400  Y2 = AM5
C      Y2 =  THE INITIAL SPECIMEN THICKNESS, CM.
C      Y1 = THE INITIAL Y VALUE AT START OF EXCURSION.
C
       WRITE(6,423) IZ1
  423  FORMAT(//20X,#NUMBER OF LINEAR SEGMENTS DESCRIBING THE TRANSIENT
     =#,I2)
       WRITE(6,5010)
C
  445  WRITE(6,446) AM5
  446  FORMAT(20X,#ONE-SIDE REACTION#,E15.5,# CM ORIGINAL WALL#)
C
  450  WRITE(6,460) AZ2
  460  FORMAT(/20X,#PEAK TEMP =#,E15.5,# DEG. K.#)
C
  492  IF(AL3 .EQ. 0.0) GO TO 500
  494  WRITE(6,495) AL3
  495  FORMAT(//20X,#T(1) =#, E15.5, # SEC#)
```

TABLE F-XIV (continued)

```
  500  CONTINUE
  510  Y3 = 1.0
       Y3 = COUNTER FOR NO. OF AZ3 INCREMENTS - ROUTES AT AZ4 SEC.
C
  520  I = 1
  530  Y4 = 1.0
       Y4 = COUNTER FOR AZ3 INC. IN EACH I STEP, FOR T CALC. - NO ROUTING
C
C
  540  Y5 = AT(I) + AZ3
       Y5 = TIME AT END OF H(T) INC. SEC.
C
  550  AZ8 = AP(I) + AR(I)*Y4*AZ3 - AZ3*AR(I)/2
       AZ8 = AV. TEMP DURING INCREMENT
C
  555  AZ7 = AP(I) + AR(I)*Y4*AZ3
       AZ7 = TEMP. AT END OF INCREMENT
C
C
  570  Y6 = 2.0*(1.12E69E-2)* EXP(-1.5890BFC4/(1.987*AZ8))
       Y6 = DEL**2, AS IN D(PHI)DT = (DEL**2)/(2*PHI), OXIDE LAYER, ZWOK
C
  572  Y7 = 2.00*0.76149* EXP(-4.8141*E04/(1.987*AZ8))
       Y7 = DEL**2, ALPHA LAYER, ZWOK
C
  575  Y8 =  SQRT(Y8**2 + Y6*AZ3)
       Y8 = OXIDE LAYER THICKNESS AFTER INCREMENT.
C
  577  Y9 =  SQRT(Y9**2 + Y7*AZ3)
       Y9 = ALPHA LAYER THICKNESS AFTER INCREMENT
C
  590  Y1 = Y8 + Y9
       Y1 = XI AFTER INCREMENT.
C
  600  Y2 = AMS - (2.0*Y8/3.2 + Y9)
       Y2 = REMAINING BETA AFTER INCREMENT
C
  602  W2 = 2.0*0.1660* EXP(-39870.3/(1.987*AZ8))
       W2 = DEL**2, TOTAL OXYGEN CONS., ZWOK DATA
C
  604  W1 =  SQRT(W1**2 + W2*AZ3)
       W1 = TOTAL OXY. CONS. AFTER INCREMENT
C
  606  AY6 = AZ4/AZ3 + .001
  607  IAY6 =   INT(AY6)
       Y33 = Y3 + .001
  608  IY3 =   INT(Y33)
  610  IF(IY3 .NE. IAY6) GO TO 650
       THE NUMERATOR IN 606 IS THE TIME INTERVAL FOR THE SUBROUTINE.
C
  630  GO TO 2000
C
  640  Y3 = 0.0
C      RESETS Y3 COUNTER FOR NEW ISOTHERMAL INCREMENT.
  650  Y4 = Y4 + 1.0
  660  Y3 = Y3 + 1.0
C
  670  IF(I - IZ1)671,675,680
  671  Y5 = Y5 + AZ3
       IF(Y5-AT(I+1)) 550,550,672
  672  I = I+1
  673  GO TO 530
```

TABLE F-XIV (continued)

```
C
  675   YS = YS + AZ3
        IF(YS-AT(I+1)) 550,550,680
  680   FACO=FAC
        FAC=FAC+0.01
        IF (FAC.GT.2.0) GO TO 3100
        DO 681 I=1,20
        AP(I) = (AP(I))*(FAC/FACO)
        IF (AP(I).LT.1(0.0) GO TO 682
  681   CONTINUE
C
  682   AA(1)=AS2
        AB(1)=AS2
        AC(1)=AS2
        AD(1)=AS2
        AE(1)=AS2
        AF(1)=AS2
        AG(1)=AS2
        AH(1)=AS2
        AI(1)=AS2
        AL3=AT(1)
C
        WRITE (6,197)
        WRITE (6,198) AM5,AS3,AZ5,FAC
        WRITE (6,5010)
C
        GO TO 8100
C
C
C       ENTER SUBROUTINE NEXT STEP.
 2001   CONTINUE
 2040   AL1 = AZ7
 2050   AL8 = Y2
        AL8 = THE REMAINING BETA, CM.
C
 2060   AJ1 = YS
        AJ1 = THE TIME AT END OF INTERVAL, (SEC.).
C
 2070   AZ8 = AL1
        AZ8 = THE TEMPERATURE DURING THE INTERVAL, (K).
C
 2100   AS1 = 0.12
          AS1 = C(S), THE SATURATION CONCENTRATION, (WT % OR CONSISTENT
                UNITS. (OXCOM BETA/ALPHA FROM ARGONNE #76 DATA.)
C
 2102   IF(AZ8 .LT. 1239.0)  GO TO 2106
 2103   AS1 = -8.0428C7 +  SQRT((AZ8/302.46)- 7.1417)
 2104   IF(AZ8 .LT. 1373.) GO TO 2105
 2105   AS1 = (AZ8 - 1061.7)/491.187
 2105   CONTINUE
C
 2200   AL6 = ( SQRT(9.E02/8.))*(2.48CE-2)* EXP(-2.8C0E04/(1.987*AZ8))
        AL6 = C(CX IN BETA), (CM**2/SEC), CICK PERKINS #76 DATA
C
 2210   AL4 = AL2 - AL6
        AL4 = DEL BETA DURING Z4 STEP, (MUST BE .LT. AL2/2.0)
C
 2215   AL7 = AL2/8.0
 2220   IF(AL4 .GT. AL7) GO TO 2770
 2222   AM3 = AL4/(2.*AL2)
 2224   AM4 = (AL4**2)/(2.0*(AL2**2))
 2240   AL5 = AL5/8.0
C       AL5 = F(X), THE DISTANCE INCREMENT FOR FD NETWORK.
```

TABLE F-XIV (continued)

```
C
 2250   AM1 = (AL6**2)/(AL5+0.(5)
        AM1 = MODULUS FOR P(T)   (TIME INCREMENT OF 0.05 SEC)
C
 2252   IF(AM2 .LT. AM1) GO TO 2256
 2254   AM2 = AM1
C       STORES SMALLEST MODULUS FOR STABILITY CRITERION CHECK.
 2256   CONTINUE
C
 2260   AA(1) = AS1
C
 2270   AB(1) = AB(1) + 7.*AM3*(4.*AC(1)-3.*AB(1)-AD(1)) +
     =          49.0*AM4*(AC(1)+AB(1)-2.*AC(1))
C
 2280   AC(1) = AC(1) + 6.*AM3*(4.*AD(1)-3.*AC(1)-AE(1)) +
     =          36.0*AM4*(AE(1)+AC(1)-2.*AC(1))
C
 2290   AD(1) = AD(1) + 5.*AM3*(4.*AE(1)-3.*AD(1)-AF(1)) +
     =          25.0*AM4*(AF(1)+AD(1)-2.*AF(1))
C
 2300   AE(1) = AE(1) + 4.*AM3*(4.*AF(1)-3.*AE(1)-AG(1)) +
     =          16.0*AM4*(AG(1)+AE(1)-2.*AF(1))
C
 2310   AF(1) = AF(1) + 3.*AM3*(4.*AG(1)-3.*AF(1)-AH(1)) +
     =           9.0*AM4*(AH(1)+AF(1)-2.*AG(1))
C
 2320   AG(1) = AG(1) + 2.*AM3*(4.*AH(1)-3.*AG(1)-AI(1)) +
     =           4.0*AM4*(AI(1)+AG(1)-2.*AH(1))
C
 2330   AH(1) = AH(1) + 1.*AM3*(4.*AI(1)-3.*AH(1)-AH(1)) +
     =           1.0*AM4*(AH(1)+AH(1)-2.*AI(1))
C
C       ABOVE ARE THE STARTING OXYGEN CONCENTRATION GRADIENTS, EACH AZ4
C       INTERVAL, FINAL BETA THICKNESS.
C2332   *** PARABOLIC INTERPOLATION PROCEDURE ***
C
 2350   AL9 = (AL6**2)/(AM1*AL5)
 2360   AQ1 = AS1+6.49*AL9/100.0
C       AQ1 IS THE MAXIMUM OXIDATION (AT SATURATION) IN THE BETA,GM/CM**3
C
 2375   AAZ4 = AZ4*2). + 1.1
 2380   IZ420 =    INT(AAZ4)
C
 2390   DO 2535 J = 2,IZ420
C       FOR FD INCREMENT OF .05 SEC.
C
 2400   AA(J) = AS1
 2410   AB(J) = (AA(J-1) + (AM1-2.)*AB(J-1) + AC(J-1))/(AM1)
 2420   AC(J) = (AB(J-1) + (AM1-2.)*AC(J-1) + AD(J-1))/(AM1)
 2430   AD(J) = (AC(J-1) + (AM1-2.)*AD(J-1) + AE(J-1))/(AM1)
 2440   AE(J) = (AD(J-1) + (AM1-2.)*AE(J-1) + AF(J-1))/(AM1)
 2450   AF(J) = (AE(J-1) + (AM1-2.)*AF(J-1) + AG(J-1))/(AM1)
 2460   AG(J) = (AF(J-1) + (AM1-2.)*AG(J-1) + AH(J-1))/(AM1)
 2470   AH(J) = (AG(J-1) + (AM1-2.)*AH(J-1) + AI(J-1))/(AM1)
 2480   AI(J) = ((AM1-2.)*AI(J-1)+2.*AH(J-1))/AM1
C
C       BUILDS NEW PROFILE FOR AZ4 INT. IN STEPS OF AZ3
C
 2490   AQ2    = (6.49*AL6)/300.0
 2491   AQ2 = AQ2*(AA(J) + AI(J) + 2.*(AC(J) + AE(J) + AG(J))
     = + 4.*(AB(J) + AD(J) + AF(J) + AH(J)))
C       AQ2 IS THE OXYGEN IN THE BETA,GM/CM**3,(BY SIMPSON'S RULE).
C
 2500   AQ4    = 100.0*AQ2/AQ1
 2535   CONTINUE
```

TABLE F-XIV (continued)

```
      AAY5 = (Y5 - AT(1))/(AZ5)
 2536 XXX = AINT(AAY5) - AAY5
 2539 YXX = 1.0 + XXX
 2540 IF(YXX .LT. .001) GO TO 2790
      YXX =  ABS(YXX)
      IF(YXX .LT. .001) GO TO 2790
C        ROUTE TO PRINTOUT AT TIME INTERVALS OF AZ5 SEC.
C
 2600 CONTINUE
 2620 AL2 = AL8
      START B THICK. FOR NEXT AZ4 INT. SET TO END VALUE FOR THIS INT.
C
 2630 AL3 = AJ1
      START TIME FOR NEXT AZ4 INT. SET TO END VAL. FOR THIS INT.
C
 2650 AA(1) = AA(IZ420)
 2660 AB(1) = AB(IZ420)
 2670 AC(1) = AC(IZ420)
 2680 AD(1) = AD(IZ420)
 2690 AE(1) = AE(IZ420)
 2700 AF(1) = AF(IZ420)
 2710 AG(1) = AG(IZ420)
 2720 AH(1) = AH(IZ420)
 2730 AI(1) = AI(IZ420)
      REASSIGNS CONC'S AT END OF THIS AZ4 INT. TO START VALUES FOR NEXT
C
 2740 IF(AL8 .EQ. 0.0) GO TO 3100
 2750 GO TO 64
 2760 GO TO 3100
 2770 CONTINUE
C
      WRITE(6,2771) AZ4
 2771 FORMAT(*CCL BETA IS TOO LARGE FOR*,E15.5,* SEC INCREMENTS-SORRY*)
 2780 GO TO 3100
C
 2790 WRITE(6,2800)
      WRITE(6,2810)
      WRITE(6,2810) Y5
 2810 FORMAT(//20X,*TIME IS*,E15.5,* SEC*)
C
      WRITE(6,2820) AZ7
 2820 FORMAT(20X,*TEMP IS*,E15.5,* DEG. K*)
C
      WRITE(6,2840) AL8
 2840 FORMAT(//20X,*FULL BETA THICKNESS =*,E15.5,* CM*)
      YXX = AL8/AME
      WRITE(6,2841) YXX
 2841 FORMAT(20X,*F(W)                    =*,E15.5)
C
      WRITE(6,2846) Y8
 2846 FORMAT(20X,*OXIDE THICKNESS         =*,E15.5,* CM*)
C
      WRITE(6,2848) Y9
 2848 FORMAT(20X,*ALPHA THICKNESS         =*,E15.5,* CM*)
C
      WRITE(6,2850) Y1
 2850 FORMAT(20X,*X1 (TOTAL, ONE SIDE) =*,E15.5,* CM*)
C
      YXX = 2.*Y9/3. + Y8
      WRITE(6,2860) YXX
 2860 FORMAT(20X,*X1 (FROM ORIG SURF) =*, E15.5,* CM*)
C
      WRITE(6,2861) Y1
 2861 FORMAT(20X,*TOTAL OXYGEN UPTAKE =*,E15.5,* GM/(M**2*)
```

TABLE F-XIV (continued)

```
C
      WRITE(6,2870) ALS
 2870 FORMAT(///20X,#TIME INC. =#,E15.5,# SEC#)
C
      WRITE(6,2871)  AM1, AM2
 2871 FORMAT(20X,#MOD        =#,E15.5,5X,#MIN MOD    =#,F15.5)
C
      WRITE(6,2880) ALS, ALS
 2880 FORMAT(20X,#DIST INC. =#,E15.5,5X,#D(O) IN B. =#,E15.5,# CM**2/SEC
     =.#)
C
      XXX= ALP/R.0
      WRITE(6,2900) XXX
 2900 FORMAT(//20X,#OXYGEN CONC. (WT :) ACROSS BETA IN#, E12.5,# CM INC
     =REMENTS#)
C
      WRITE(6,2910) YS
 2910 FORMAT(25X,#(#,E10.4,# SEC)#)
C
      WRITE(6,2930)AA(IZ420),AB(IZ420),AC(IZ420),AD(IZ420),AE(IZ420),AF
     =(IZ420),AG(IZ420),AH(IZ420), AI(IZ420)
 2930 FORMAT(//10X,9F12.4)
C
      WRITE(6,5010)
      WRITE(6,5050)
 5050 FORMAT(20X,#TOTAL OXYGEN IN FULL-BETA THICKNESS#)
      WRITE(6,2990)  AQ2
 2990  FORMAT(14X,E20.6,# GRAMS OXYGEN/CM**2#)
C
 3020 XXX = AQ4*(AS1/100.0)
      WRITE(6,3030) XXX
 3030 FORMAT(//20X,#AVERAGE CONCENTRATION IN BETA IS#,F23.3,# WT. :#)
C
      WRITE(6,3060) AQ4
 3060 FORMAT(//20X,#PER CENT FILLED /COMPARED TO SATURATION VALUE)#,
     = F9.3, #  :#)
C
      WRITE(6,3070)
 3090 GO TO 2600
C
 3100 CONTINUE
      STOP
      END
```

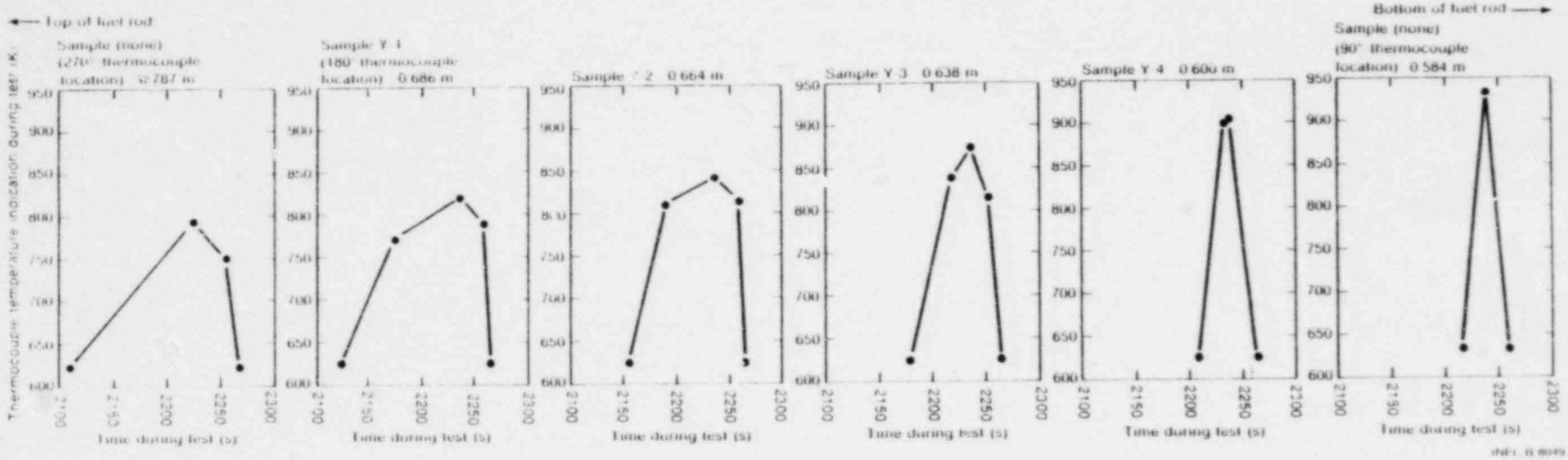

Fig. 4.5 Uncalculated time-temperature profile computer code input for Rod UTA-001S

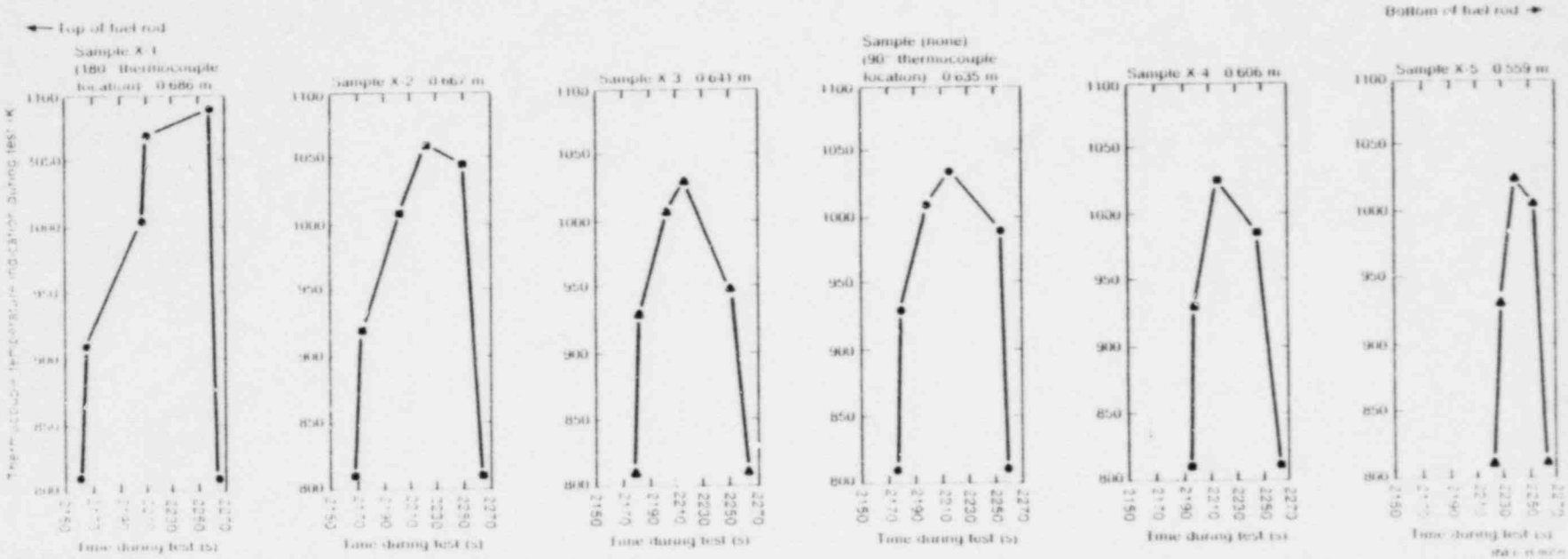

Fig. 4.6. Executed time-temperature profile computer code input for RodFEA (001).

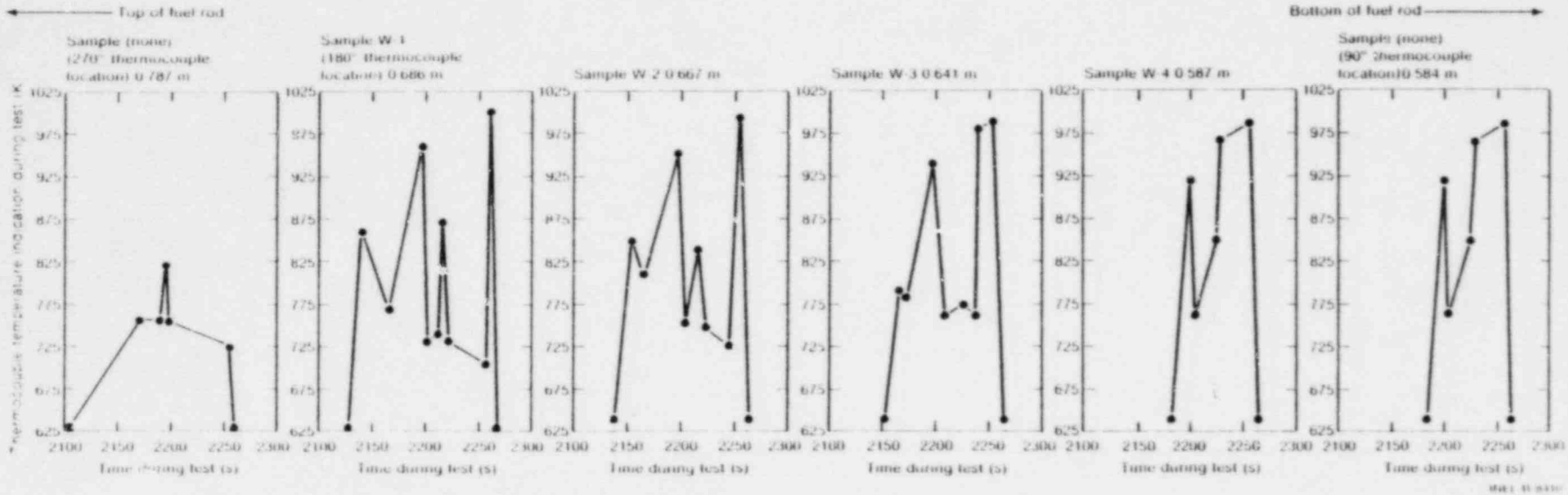

Fig. 4-7 Uncorrected true temperature versus computer code input for Rod UTA-0016

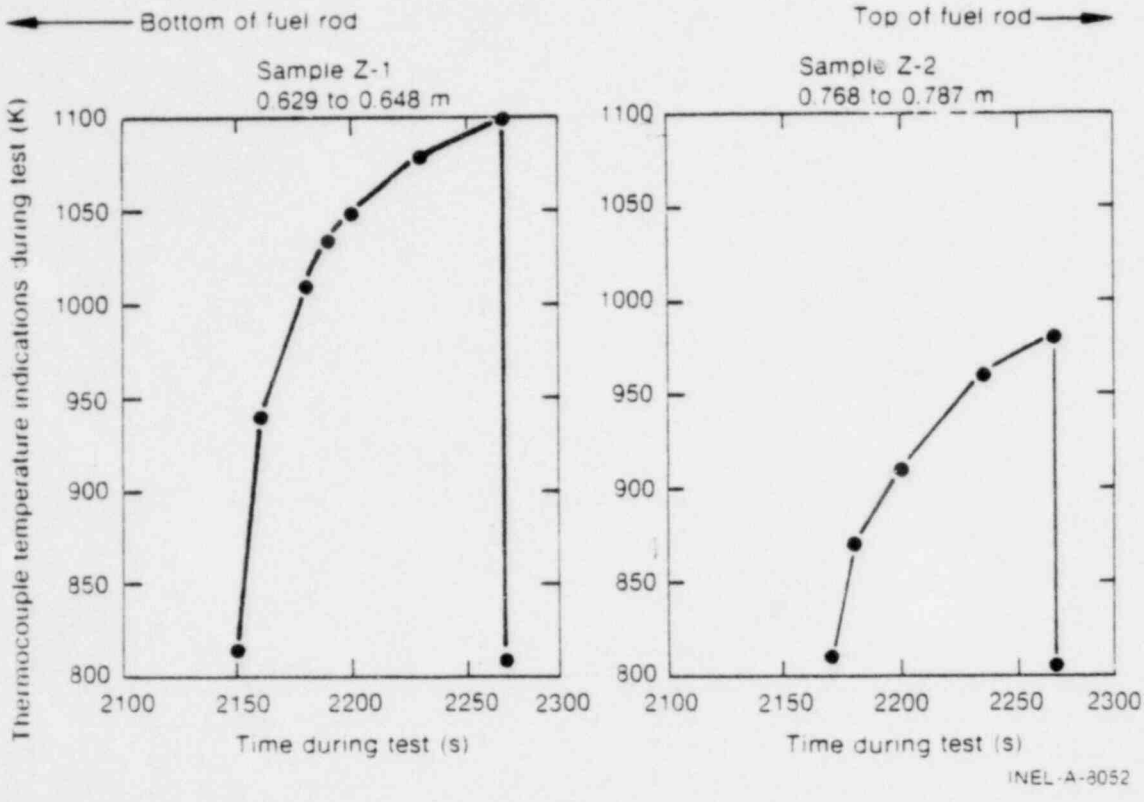

Fig. F-8 Linearized time-temperature profile computer code input for Rod A-0017.

TABLE F-XV

MODIFIED BUILD5 COMPUTER CODE TIME-TEMPERATURE PROFILE INPUT DATA FOR ROD UTA-0014

Sample	270° Thermocouple		Y-1 (180° Thermocouple)		Y-2[b]		Y-3[b]		Y-4[b]		90° Thermocouple[a]	
Distance from Bottom of Fuel Stack (m)	0.787		0.686		0.664		0.638		0.600		0.584	
	t[c] (s)	T (K)	t[c] (s)	T (K)	t (s)	T (K)	t (s)	T (K)	t (s)	T (K)	t[c] (s)	T (K)
	2109	622	2124	625	2156	625	2179	625	2209	626	2216	633
	2224	794	2174	772	2190	810	2218	840	2234	900	2239	933
	2254	750	2236	820	2236	843	2237	874	2238	904	2259	633
	2264	622	2258	790	2258	814	2252	816	2264	625		
			2264	625	2264	625	2264	625				

[a] Data taken from linearized time-temperature thermocouple response histories.

[b] Time-temperature profiles are constructed.

[c] Times represented are real times obtained from test output.

TABLE F-XVI

MODIFIED BUILD5 COMPUTER CODE TIME-TEMPERATURE PROFILE INPUT DATA FOR ROD UTA-0015

Sample	X-1 (180° Thermocouple)[a]		X-2[b]		X-3[b]		90° Thermocouple[a]		X-4[b]		X-5[b]	
Distance from Bottom of Fuel Stack (m)	0.686		0.667		0.641		0.635		0.606		0.559	
	t[c] (s)	T (K)	t (s)	T (K)	t (s)	T (K)	t[c] (s)	T (K)	t (s)	T (K)	t (s)	T (K)
	2160	810	2168	810	2179	810	2177	810	2198	810	2225	810
	2164	910	2173	920	2182	930	2180	930	2200	930	2230	930
	2206	1005	2202	1008	2203	1006	2200	1010	2218	1025	2240	1025
	2210	1070	2222	1060	2217	1030	2217	1035	2248	985	2255	1005
	2258	1090	2250	1045	2252	948	2255	990	2265	810	2265	810
	2265	810	2265	810	2265	810	2260	810				

[a] Data are taken from linearized time-temperature response histories.

[b] Time-temperature profiles are constructed.

[c] Times represented are real times obtained from the test output.

TABLE F-XVII

MODIFIED BUILD5 COMPUTER CODE TIME-TEMPERATURE PROFILE INPUT DATA FOR ROD UTA-0016

Sample	W-1 270° Thermocouple[a]		W-1 180° Thermocouple[a]		W-2[b]		W-3[b]		W-4[b]		90° Thermocouple[a]	
Distance from Bottom of Fuel Stack (m)	0.787		0.686		0.667		0.641		0.587		0.584	
	t[c] (s)	T (K)	t[c] (s)	T (K)	t (s)	T (K)	t (s)	T (K)	t (s)	T (K)	t[c] (s)	T (K)
	2105	630	2128	630	2137	640	2152	640	2182	640	2184	640
	2170	760	2140	860	2154	850	2166	792	2199	920	2199	920
	2188	760	2166	768	2165	810	2172	782	2204	763	2204	763
	2194	820	2196	960	2197	952	2197	941	2224	800	2224	800
	2198	760	2202	732	2204	752	2208	762	2228	968	2228	968
	2256	725	2212	740	2216	840	2226	775	2256	988	2256	988
	2260	630	2216	872	2224	748	2238	762	2264	640	2264	640
			2222	732	2246	725	2240	982				
			2258	704	2256	995	2254	990				
			2260	1000	2264	640	2264	640				
			2268	630								

[a] Data are taken from linearized time-temperature thermocouple response histories.

[b] Time-temperature profiles are constructed.

[c] Times represented are real times obtained from the test output.

TABLE F-XVIII

MODIFIED BUILD5 COMPUTER CODE TIME-TEMPERATURE PROFILE INPUT DATA FOR ROD A-0017

Sample	Z-1[a]		Z-2[a]	
Distance from Bottom of Fuel Stack (m)	0.629		0.768	
	t[b] (s)	T (K)	t[b] (s)	T (K)
	2150	815	2170	810
	2160	940	2180	870
	2180	1010	2200	910
	2190	1035	2235	960
	2200	1050	2265	980
	2230	1080	2266	805
	2265	1100		
	2266	810		

[a] Time-temperature profiles are constructed.

[b] Times represented are real times obtained from the test output.

Individual oxide and oxygen-stabilized alpha-zircaloy layer thickness calculated by the modified BUILD5 code exhibit up to a 30% variation in comparison with experimentally measured values, but the calculated ξ-layer thicknesses show a variation of less than 5% in comparison with experimentally measured values, confirming the ξ layer as the better measure for comparison. Peak temperatures taken from the modified BUILD5 data for each thermocouple location are greater than the maximum isothermal effective temperatures calculated at the same position. Differences of greater than 280 K were observed. Although such differences appear large, calculated peak temperatures agree with observed cladding microstructures. Peak temperatures calculated at each thermocouple location are up to 690 K greater than the corresponding maximum thermocouple reading.

TABLE F-XIX

MICROSTRUCTURE AND TEMPERATURE VARIATION FOR ROD UTA-0014

Sample	Distance from Bottom of Fuel Stack (m)	Orientation (°)	Oxide Thickness (μm)		Oxygen-Stabilized α-zircaloy Thickness (μm)		Oxide and Oxygen-Stabilized Thickness (μm)		Estimated Temperature			Differential Temperature (K)
			Measured[a]	Calculated	Measured[a]	Calculated	Measured[a]	Calculated	Peak[b] (K)	(*FAC)	Isothermal[c] (K)	
Y-1	0.686	0	16	16.2	--	--	--	--	1361	1.66	1290	71
	(180°	90	16	16.2	--	--	--	--	1361	1.66	1290	71
	thermo-	180	10	10.4	--	--	--	--	1279	1.56	1210	69
	couple)	270	12	12.0	--	--	--	--	1304	1.59	1240	64
Y-2	0.664	0	19	22.3	24	20.6	43	42.7	1442	1.71	1380	62
		90	20	23.1	25	21.4	45	44.6	1449	1.72	1390	59
		180	20	24.0	26	22.6	46	46.6	1458	1.73	1390	68
		270	20	24.0	26	22.6	46	46.6	1458	1.73	1390	68
Y-3	0.638	0	28	27.2	28	28.7	56	55.9	1564	1.79	1450	114
		90	--	--	26	26.2	--	--	1547	1.77	1450	97
		180	--	--	24	23.9	--	--	1530	1.75	1430	100
		270	--	--	24	23.9	--	--	1530	1.75	1430	100
Y-4	0.600	0	13	14.4	15	13.7	28	28.1	1500	1.66	1360	140
		90	--	--	--	--	--	--	--	--	--	--
		180	--	--	25	25.2	--	--	1618	1.79	1480	138
		270	--	--	--	--	--	--	--	--	--	--

[a] Uncertainty in these thicknesses average ± 1 μm, due primarily to unevenness of the measured layers.

[b] Peak temperatures were calculated with the modified BUILD5 computer code using time-temperature response data from Table F-XV as input.

[c] Calculation is based on the isothermal correlations.

TABLE F-XX

MICROSTRUCTURE AND TEMPERATURE VARIATION FOR ROD UTA-0015

Sample	Distance from Bottom of Fuel Stack (m)	Orientation (°)	Oxide Thickness (μm)		Oxygen-Stabilized α-zircaloy Thickness (μm)		Oxide and Oxygen-Stabilized Thickness (μm)		Estimated Temperature			Differential Temperature (K)
			Measured[a]	Calculated	Measured[a]	Calculated	Measured[a]	Calculated	Peak[b] (K)	(*FAC)	Isothermal[c] (K)	
X-1	0.686	0	24	17.7	10	15.6	34	33.6	1406	1.29	1340	66
	(180°	90	15	13.0	8	10.2	23	23.2	1340	1.23	1280	60
	thermo-	180	14	12.3	8	9.4	22	21.7	1330	1.22	1270	60
	couple)	270	22	15.3	6	12.7	28	28.0	1373	1.26	1310	63
X-2	0.667	0	22	15.5	6	12.8	28	28.3	1378	1.30	1320	58
		90	11	13.9	14	11.1	25	25.0	1357	1.28	1300	57
		180	24	27.4	30	27.4	54	54.8	1505	1.42	1430	75
		270	24	26.2	28	25.8	52	52.0	1495	1.41	1430	65
X-3	0.641	0	38	33.6	32	36.3	70	69.9	1575	1.53	1500	75
		90	20	26.3	32	26.3	52	52.6	1514	1.47	1440	74
		180	--	--	33	31.6	--	--	1205	1.17	--	--
		270	46	36.3	30	40.3	76	76.6	1596	1.55	1520	76
X-4	0.606	0	44	47.2	62	59.8	106	107.0	1700	1.66	1620	80
		90	--	--	--	--	--	91	--	--	--	--
		180	--	--	53	54.1	--	--	1281	1.75	1630	349
		270	--	--	--	--	--	--	--	--	--	--
X-5	0.559	0	--	--	30	30.5	--	--	1240	1.31	1540	300
		90	--	--	--	--	--	--	--	--	--	--
		180	--	--	40	38.9	--	--	1271	1.24	1600	329
		270	--	--	--	--	--	--	--	--	--	--

[a] Uncertainty in these thicknesses averages ± 1 μm, due primarily to unevenness of the layers.

[b] Peak temperatures were calculated by the modified BUILD5 computer code using time-temperature response data from Table F-XVI as input.

[c] Calculation is based on the Cathcart correlation Equation (F-6).

TABLE F-XXI

MICROSTRUCTURE AND TEMPERATURE VARIATION FOR ROD UTA-0016

Sample	Distance from Bottom of Fuel Stack (m)	Orientation (°)	Oxide Thickness (μm)		Oxygen-Stabilized α-zircaloy Thickness (μm)		Oxide and Oxygen-Stabilized Thickness (μm)		Estimated Temperature			Differential Temperature (K)
			Measured[a]	Calculated	Measured[a]	Calculated	Measured[a]	Calculated	Peak[b] (K)	(*FAC)	Isothermal[c] (K)	
W-1	0.686 (180° thermo-couple)	0	20	21.4	22	20.6	42	42.0	1620	1.62	1350	270
		90	20	21.4	22	20.6	42	42.0	1620	1.62	1350	270
		180	18	19.0	18	17.6	36	36.6	1590	1.59	1330	260
		270	30	27.9	28	29.1	58	57.0	1690	1.69	1410	280
W-2	0.667	0	--	--	--	--	--	--	--	--	--	--
		90	32	32.9	36	35.8	68	68.7	1701	1.71	1450	251
		180	38	37.7	44	42.8	82	80.5	1741	1.75	1490	251
		270	--	--	31	31.1	--	--	1672	1.68	1440	232
W-3	0.641	0	--	--	29	29.6	--	--	1604	1.62	1440	164
		90	36	33.8	38	39.3	74	73.1	1663	1.68	1480	183
		180	--	--	45	44.9	--	--	1693	1.71	1519	174
		270	36	36.2	42	43.0	78	79.2	1683	1.70	1490	193
W-4	0.587	0	--	--	27	27.7	--	--	1561	1.58	1454	107
		90	--	--	14	--	--	--	--	--	--	--
		180	--	--	20	20.8	--	--	1491	1.51	1400	224
		270	--	--	25	25.1	--	--	1541	1.56	1441	100

[a] Uncertainties in these thicknesses average ± 1 μm, due primarily to unevenness of the layers.

[b] Peak temperatures were calculated by the modified BUILD5 computer code using time-temperature response data from Table F-XVII as input.

[c] Calculation based on the Cathcart correlation Equation (F-6).

TABLE F-XXII

MICROSTRUCTURE AND TEMPERATURE VARIATION FOR ROD A-0017

Sample	Distance from Bottom of Fuel Stack (m)	Orientation (°)	Oxide Thickness (μm)		Oxygen-Stabilized α-zircaloy Thickness (μm)		Oxide and Oxygen-Stabilized Thickness (μm)		Estimated Temperature			Differential Temperature (K)
			Measured[a]	Calculated	Measured[a]	Calculated	Measured[a]	Calculated	Peak[b] (K)	(*FAC)	Isothermal[c] (K)	
Z-1	0.629-0.648	0	34	39.5	48	43.1	82	82.6	1573	1.43	1510	63
		90	--	--	--	--	--	--	--	--	--	--
		180	--	--	--	--	--	--	--	--	--	--
		270	--	--	--	--	--	--	--	--	--	--
Z-2	0.768-0.787	0	13	15.7	16	12.9	29	28.6	1382	1.41	1330	52
		90	--	--	--	--	--	--	--	--	--	--
		180	16	16.5	14	13.8	30	30.3	1391	1.42	1330	61
		270	--	--	--	--	--	--	--	--	--	--

[a] Uncertainties in these thicknesses average ± 1 μm, due primarily to unevenness of the layers.

[b] Peak temperature were calculated by the modified BUILD5 computer code using time-temperature response data from Table F-XVIII as input.

[c] Calculation based on the Cathcart correlation Equation (F-6).

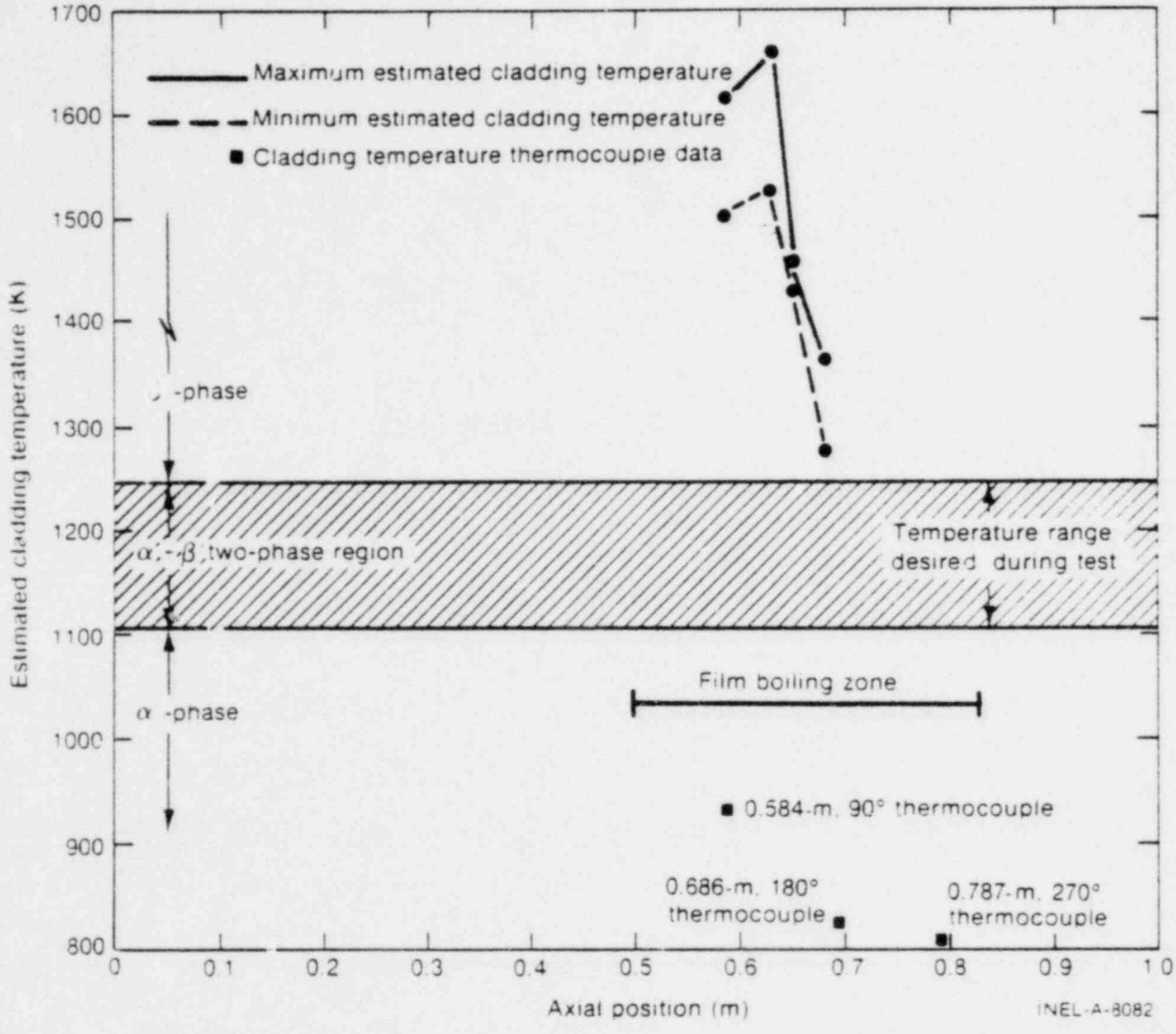

Fig. F-9 Cladding peak temperature axial profile for Rod UTA-0014.

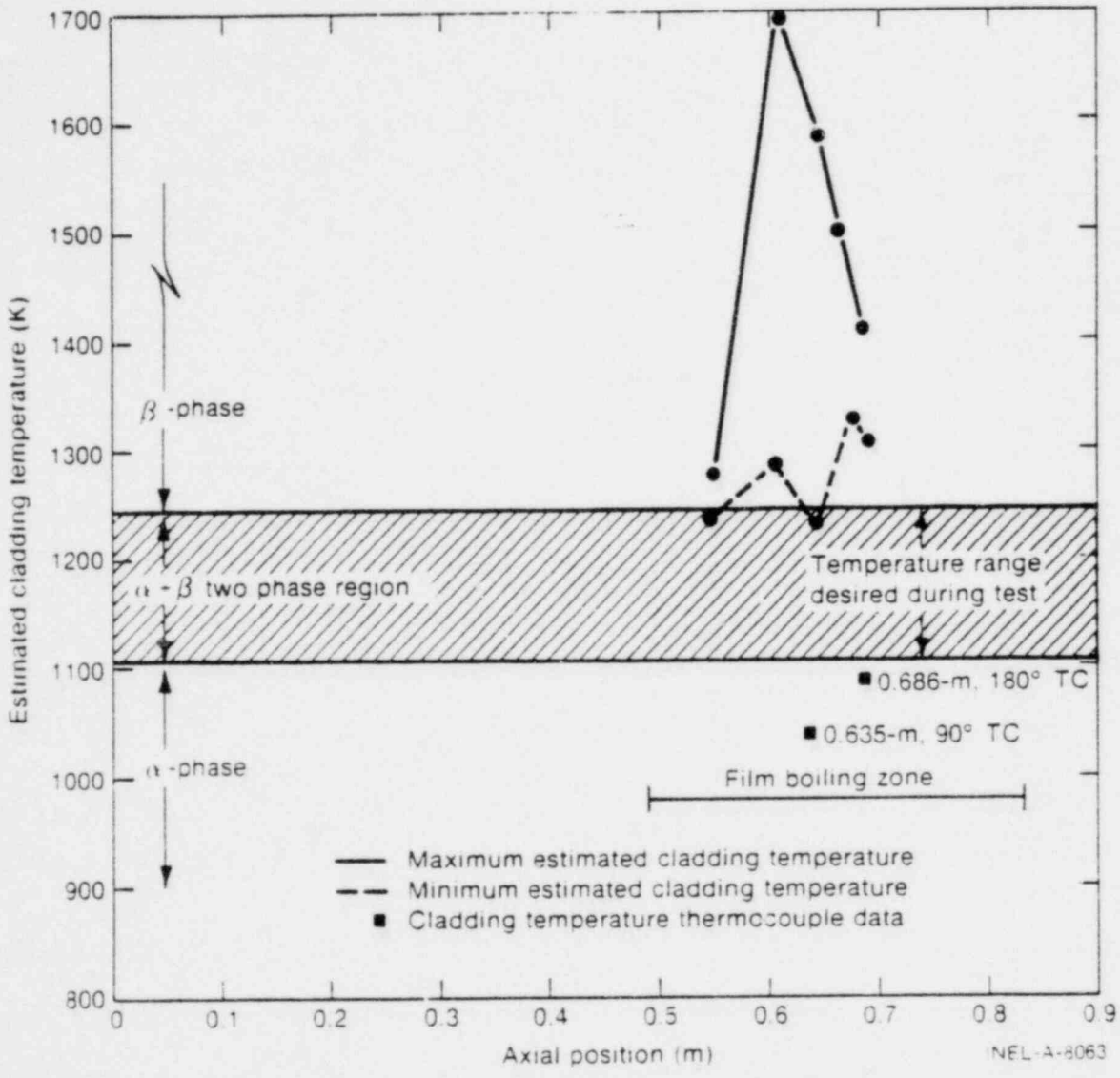

Fig. F-10 Cladding peak temperature axial profile for Rod UTA-0015.

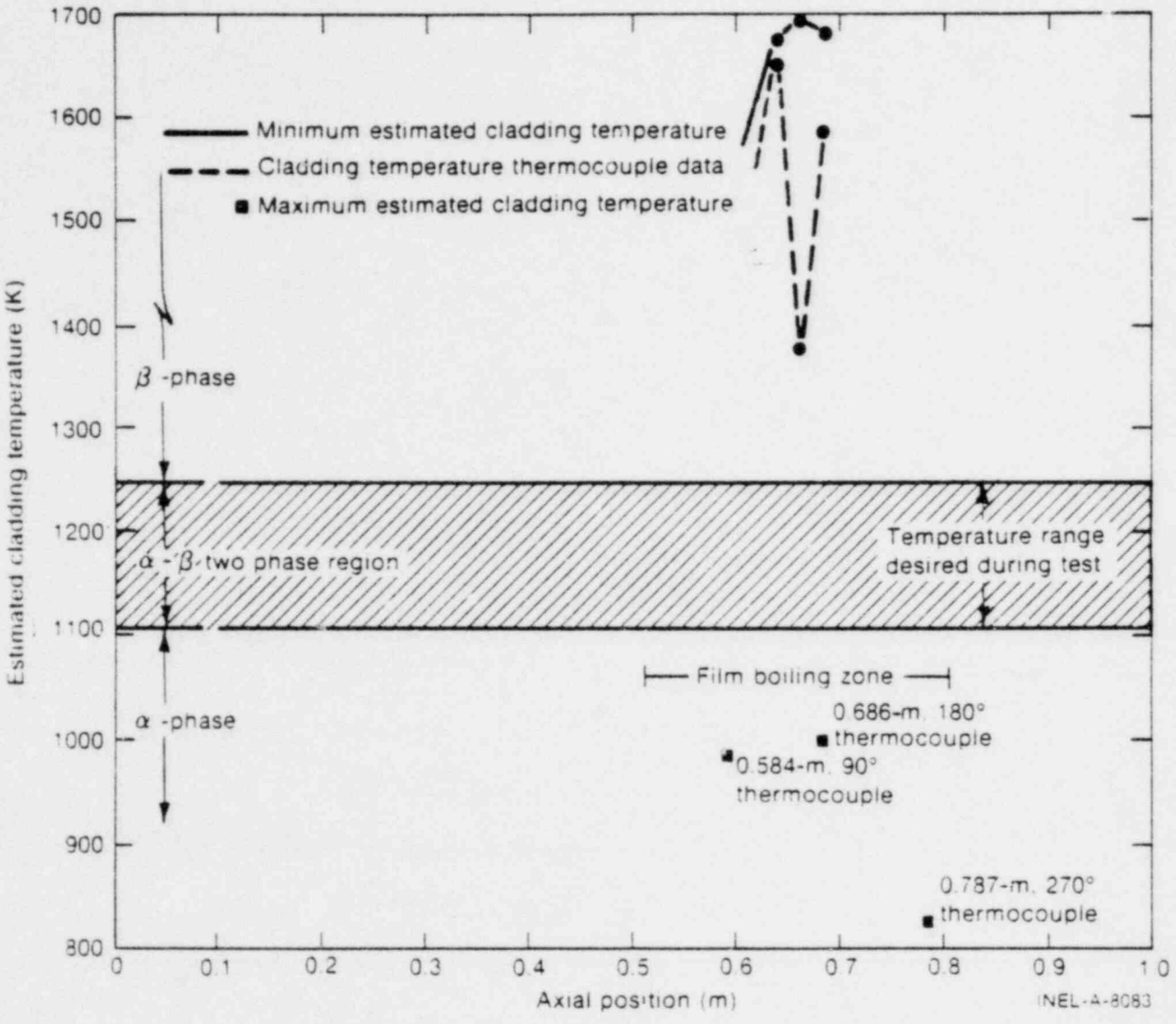

Fig. F-11 Cladding peak temperature axial profile for Rod UTA-0016.

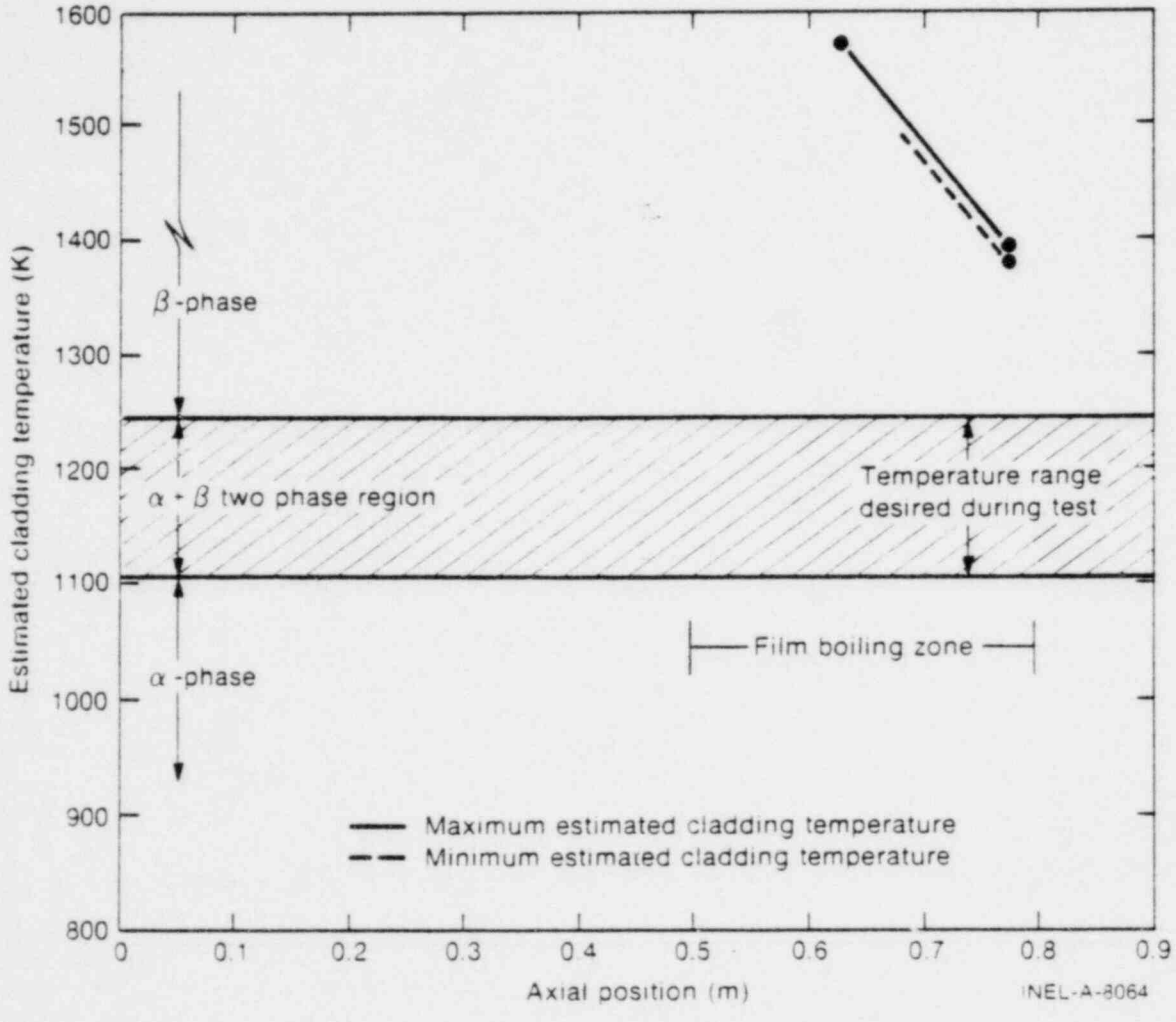

Fig. F-12 Cladding peak temperature axial profile for Rod A-0017.

4. REFERENCES

F-1. R. E. Pawel, "Diffusion in a Finite System with a Moving Boundary," *Journal of Nuclear Materials, 49* (1974) pp 281-290.

F-2. R. E. Pawel, "Oxygen Diffusion in Beta Zircaloy During Steam Oxidation," *Journal of Nuclear Materials, 50* (1974) pp 247-258.

F-3. J. V. Cathcart et al, *Zirconium Metal-Water Oxidation Kinetics IV Reaction Rate Studies.* ORNL/NUREG-17 (August 1977).

F-4. L. N. Grossman and D. M. Rooney, *Interfacial Reaction Between UO_2 and Zircaloy-2,* GEAP 4679 (EURAEC) (April 1965).

F-5. M. W. Mallett, "Solid State Reactions of Uranium Dioxide," in *Uranium Dioxide: Properties and Nuclear Applications,* Section 7.4, pp 342-371, J. Belle (Ed.) U.S. Government Printing Office, 1961.